

<https://doi.org/10.15388/vu.thesis.565>

<https://orcid.org/0000-0001-6387-7131>

VILNIUS UNIVERSITY

CENTER FOR PHYSICAL SCIENCES AND TECHNOLOGY

Mantas Jakučionis

Relaxation Theory of Quantum Systems
with Feedback:
Development of Methods Based on
Principle of Time-Dependent Variations

DOCTORAL DISSERTATION

Natural Sciences,
Physics (N 002)

VILNIUS 2023

The dissertation was prepared between 2019 and 2023 at the Institute of Chemical Physics, Vilnius University.

The research was supported by the Research Council of Lithuania with scholarship No. P-DAP-22-91 and projects No. S-MIP-20-47, No. S-MIP-23-48, the Lithuanian Academy of Sciences with project No. CERN-VU-2021-2022 and European Social Fund with project No. 09.3.3-LMT-K-712.

Academic supervisor – Prof. Dr. Darius Abramavičius (Vilnius University, Natural Sciences, Physics, N 002).

This doctoral dissertation will be defended in a public meeting of the Dissertation Defence Panel:

Chairman – Prof. Habil. Dr. Egidijus Anisimovas (Vilnius University, Natural Sciences, Physics, N 002).

Members:

Dr. Artūras Acus (Vilnius University, Natural Sciences, Physics, N 002),
Assoc. Prof. Dr. Jevgenij Chmeliiov (Vilnius University, Natural Sciences, Physics, N 002),

Dr. Lukas Razinkovas (Center for Physical Sciences and Technology, Natural Sciences, Physics, N 002),

Prof. Dr. Michael Thorwart (University of Hamburg, Natural Sciences, Physics, N 002).

The dissertation shall be defended at a public meeting of the Dissertation Defence Panel at 11:00 on January 8, 2024 in room B336 of the Center for Physical Sciences and Technology.

Address: Saulėtekio ave. 3, Vilnius, Lithuania

Tel. +370 5 264 9211; office@ftmc.lt.

The text of this dissertation can be accessed at libraries of Vilnius University and Center for Physical Sciences and Technology, as well as on the website of Vilnius University:

www.vu.lt/lt/naujienos/ivykiu-kalendorius

<https://doi.org/10.15388/vu.thesis.565>

<https://orcid.org/0000-0001-6387-7131>

VILNIAUS UNIVERSITETAS
FIZINIŲ IR TECHNOLOGIJOS MOKSLŲ CENTRAS

Mantas Jakučionis

Kvantinių sistemų relaksacijos teorija su
grįžtamuoju ryšiu:
nuo laiko priklausančio variacinio
principo metodų vystymas

DAKTARO DISERTACIJA

Gamtos mokslai,
Fizika (N 002)

VILNIUS 2023

Disertacija rengta 2019–2023 metais Vilniaus universiteto Cheminės fizikos institute.

Mokslinius tyrimus rėmė: Lietuvos mokslo taryba stipendija Nr. P-DAP-22-91 ir projektais Nr. S-MIP-20-47, Nr. S-MIP-23-48; Lietuvos mokslų akademija projektu Nr. CERN-VU-2021-2022; Europos socialinis fondas projektu Nr. 09.3.3-LMT-K-712.

Mokslinis vadovas – prof. dr. Darius Abramavičius (Vilniaus universitetas, gamtos mokslai, fizika, N 002).

Gynimo taryba:

Pirmininkas – prof. habil. dr. Egidijus Anisimovas (Vilniaus universitetas, gamtos mokslai, fizika, N 002).

Nariai:

dr. Artūras Acus (Vilniaus universitetas, gamtos mokslai, fizika, N 002),

doc. dr. Jevgenij Chmeliov (Vilniaus universitetas, gamtos mokslai, fizika, N 002),

dr. Lukas Razinkovas (Fizinių ir technologijos mokslų centras, gamtos mokslai, fizika, N 002),

prof. dr. Michael Thorwart (Hamburgo universitetas, gamtos mokslai, fizika, N 002).

Disertacija ginama viešame Gynimo tarybos posėdyje 2024 m. Sausio mėn. 8 d. 11:00 val. Nacionaliniame fizinių ir technologijos mokslų centro B336 auditorijoje. Adresas: Saulėtekio al. 3, Vilnius, Lietuva, tel. +370 5 264 9211; el. paštas office@ftmc.lt.

Disertaciją galima peržiūrėti Vilniaus universiteto ir Fizinių ir technologijos mokslų centro bibliotekose ir VU interneto svetainėje adresu:

<https://www.vu.lt/naujienos/ivykiu-kalendorius>

Contents

INTRODUCTION	7
Layout of the dissertation	11
List of articles	11
Author's contribution	12
Goals of the dissertation	12
Statements to be defended	13
List of abbreviations	15
1 THEORY	16
1.1 Hamiltonian of the system-bath model	16
1.1.1 Non-linear displaced oscillator model	20
1.2 Time-dependent variational principle	20
1.3 Davydov's ansätze	21
1.3.1 Davydov D_2 ansatz	22
1.3.2 Squeezed-Davydov D_2 ansatz	24
1.3.3 Multiple-Davydov D_2 ansatz	26
1.3.4 Superposition-Davydov D_2 ansatz	28
1.4 Solving implicit EOM of the mD_2 ansatz	29
1.5 Modelling thermal effects	32
1.5.1 Observable of an operator	33
1.6 Simulating absorption and fluorescence spectra	33
1.6.1 Transitions between electronic manifolds	33
1.6.2 Absorption and fluorescence response functions	36
2 EXCITATION RELAXATION USING DAVYDOV'S ANSATZE	38
2.1 Absorption spectrum of β -carotene with fully resolved vibrational modes	38
2.1.1 Mixing of vibrational modes upon electronic excitation	39
2.1.2 Absorption spectra of the β -carotene	40
2.1.3 Main outcomes of the Article [A1]	43

2.2	Molecular internal conversion	44
2.2.1	Setup of the model	45
2.2.2	Excitation energy relaxation dynamics	46
2.2.3	Wavepacket evolution	46
2.2.4	Main outcomes of the Article [A2]	48
2.3	Excitation relaxation in molecular aggregates	49
2.3.1	Absorption spectra convergence using the mD ₂ ansatz	49
2.3.2	The mD ₂ ansatz depth dependence on model parameters	51
2.3.3	Main outcomes of the Article [A3]	52
2.4	Vibrational frequency shift	54
2.4.1	Numerical optimization approach for simulating fluorescence spectra	54
2.4.2	Absorption and fluorescence spectra with frequency shifts	56
2.4.3	Fluorescence spectra temperature dependence	58
2.4.4	Main outcomes of the Article [A4]	60
3	THERMALIZATION OF SYSTEM-BATH MODEL	61
3.1	Thermalization algorithm for the D ₂ ansatz	62
3.1.1	Time evolution of the thermalized primary bath	63
3.1.2	Thermalized excitation relaxation using the D ₂ ansatz	65
3.1.3	Main outcomes of the Article [A5]	68
3.2	Thermalization algorithm for the mD ₂ ansatz	69
3.2.1	Thermalized excitation relaxation using the mD ₂ ansatz	72
3.2.2	Thermalized fluorescence spectra	74
3.2.3	Main outcomes of the Article [A6]	78
	SANTRAUKA	79
	Įvadas	79
	Disertacijos tikslai ir užduotys	83
	Ginamieji teiginiai	84
	Pagrindinių rezultatų apžvalga	84
	BIBLIOGRAPHY	96
	CURRICULUM VITAE	97
	COPIES OF ARTICLES	99

INTRODUCTION

The function of many biological molecular systems is closely tied to the process of energy relaxation in their electronic and/or vibrational manifolds. Understanding the pathways and rates of energy relaxation induced by photoexcitation is relevant across a range of molecular spatial scales. From the smallest, on the level of energy states of a single molecule¹⁻⁴, to the intermediate-sized molecular aggregates consisting of a few interacting molecules⁵⁻⁸, and to the largest photosynthetic complexes found in Nature⁹⁻¹³, which involve physical processes of molecular energy relaxation, charge transfer, spatial energy transfer and others in structures composed of tens or hundreds of molecules.

Analytical solution of all but the most primitive theoretical models of molecular systems is intractable. For sufficiently complex models, due to a high number of interacting degrees of freedom involved, brute-force numerical simulations of non-equilibrium dynamics in even the smallest systems are also challenging, because of the exponential numerical effort scaling.

The standard theoretical approach to proceed for molecular systems is to treat it as an open quantum system^{14,15}. In this description, only those molecular electronic and vibrational degrees of freedom that participate in a relaxation process of interest, constitute the observable system, while less relevant degrees of freedom are treated as part of a larger than system thermal reservoir (the bath), which is fully characterized by a continuous fluctuation spectral density function^{16,17}. Generally, separation into the system and the bath is only formal as the interaction between the two remains.

The prominent mathematical tool to simulate the time evolution of open quantum systems is the reduced density operator, i.e., an outer product of wavefunctions. If the system-bath interaction strength is small, relative to the intra-system coupling strength, comparably straightforward perturbative approaches of the Redfield theory¹⁸⁻²¹ can be used with great success. When the opposite is true, i.e., the system-bath coupling is stronger than the intra-system coupling, perturbative theories of the Förster²²⁻²⁴ become applicable. These methods solve coupled equations of motion of both the system and the bath with an intent to average over the influence of the fluctuating bath on the system,

reducing the full system-bath dynamics to only the relevant dynamics of the system. The accuracy of these methods heavily relies on the clear separation between the system-bath and the intra-system coupling strengths. If strengths are of a similar magnitude, energy relaxation dynamics must be modelled non-perturbatively since the timescales of the system and bath dynamics essentially become inseparable. This regime is the most challenging to simulate, yet, a range of formally exact approaches, though, numerically expensive, have been developed such as hierarchical equations of motion²⁵, density matrix renormalization group²⁶, chain-mapping approaches^{27–29}, path integral formulations³⁰.

These techniques are based on the reduced density operator description. However, for the same purposes, one can also directly utilize the wavefunction itself using methods of, e.g., the multi-configuration time-dependent Hartree^{31,32}, surface hopping³³, quantum jumping³⁴, stochastic Schrödinger equation³⁵, hierarchy of pure states³⁶, thermofield dynamics^{37,38}. The principal idea behind most wavefunction approaches is to expand states of the entire system-bath model in a chosen state basis. Such approaches are well suited for the non-perturbative parameter regime as they explicitly and on an equal footing treat both the system and bath degrees of freedom. The accuracy depends on how well the chosen state basis can approximate eigenstates of the system-bath model or, at least, the eigenstates that participate in the relaxation process of interest the most.

The family of trial wavefunctions (ansätze) considered in this work is named after Alexander Davydov. It is based on an innovative mechanism^{39,40} for vibrational energy transport and localization in α -helix proteins proposed by Davydov in 1973, where the energy carrier quasiparticle was termed the Davydov’s soliton^{41,42}. The main idea behind the Davydov’s ansätze^{43,44} is to expand the system-bath vibrational eigenstates in terms of the time-dependent coherent states^{45–47} with Gaussian wavepackets in their phase space. During time evolution of the system-bath model, which propagate according to the equations derived by applying the time-dependent variational principle to an ansatz, coherent states continuously adjust to align with the most relevant eigenstates at any given moment. This adaptation aims to minimize the discrepancy between the ansatz and the solution of the Schrödinger’s equation.

The simplest variant and backbone of the family of Davydov’s ansätze is called the D₂ ansatz^{48–53}. It assigns a single coherent state to each vibrational degree of freedom of the model, independent of the electronic state the system is in. Various alterations have been proposed^{49,54} to improve accuracy

of the D_2 ansatz. The D_1 ansatz^{55–57} assigns a coherent state to each vibrational degree of freedom per every electronic state. This expands the state basis set in an attempt to uncouple movement of wavepackets in different electronic states. The $D_{1.5}$ ansatz has an intermediate sophistication between the two and is constructed for a specific case of initial conditions⁵⁴. Alternatively, instead of packing more coherent states, modifications to the coherent states themselves have been proposed. Suggestions of applying squeeze operators⁴⁷ to coherent states have been made in order to enhance the representation of non-Gaussian eigenstates. It contracts Gaussian wavepackets along a direction in the coordinate-momentum phase space, while simultaneously expanding wavepacket along the perpendicular direction. The resulting wavefunctions are termed the squeezed-Davydov D_2 and D_1 ansätze^{58–62}. While these alterations broaden the range of representable states, they also increase the numerical effort and may introduce numerical instabilities. These ansätze have been used to model relaxation dynamics and compute spectroscopic signals of molecules and their aggregates in perturbative regimes with great success, however, they become insufficient in the non-perturbative parameter regime^{63,64}, especially at low temperatures.

The idea that leads to further progress was to consider the trial wavefunction as a superposition of D_2 ansätze, termed the multiple-Davydov D_2 ansatz^{63–65}. In theory, by considering an infinite number of superposition terms, the multiple-Davydov D_2 ansatz is an exact expansion of any system-bath model’s eigenstates. However, in practice, due to the complicated structure of the resulting equations of motion, the number of terms is limited by the scaling of numerical cost with respect to the number of vibrational degrees of freedom^{66,67}. Still, due to the time-dependent adaptive basis set of the multiple-Davydov D_2 ansatz, the numerical effort scaling is reduced^{68,69} from exponential to polynomial with a power in the range of 2 – 3. Therefore, even when the number of vibrational modes is large, it can match the results of other state-of-the-art methods such as hierarchical equations of motion^{63,64,70}, quasiadiabatic path integral⁷¹, and multi-configuration time-dependent Hartree^{72,73,69}.

While density operator approaches are able to account for the influence of an infinitely-sized bath on the system by tracing over fluctuations of vibrational modes, the variational approach is unable to do the same. Therefore, a finite-sized bath has to be considered. Most often, the continuous spectral density function of the bath is linearly or logarithmically⁷⁰ discretized along the frequency domain in hopes to accurately mimic effects of the continuous function.

The resulting finite number of discretized frequencies and their corresponding fluctuation magnitudes are then assigned to quantum harmonic oscillators, which are modelled explicitly along the electronic states.

The wavefunction approach, involving a finite number of electronic states and vibrational modes, is technically a closed quantum system rather than an open one, in a sense that there is no external drain or source with which the model could exchange energy and particles. To retain equivalence between the open quantum systems of the reduced density operator and the closed quantum systems of wavefunction-based methods, the discretized bath should behave as a true thermostat, having a much larger heat capacity than the system. However, including enough quantum harmonic oscillators to represent a bath with a sufficiently high heat capacity can be numerically expensive.

As the excitation energy relaxation takes place in the system-bath model, the energy is primarily absorbed from the system by a few in-resonant bath oscillators, leading to a divergence from the equilibrium. Therefore, the temperature at which dynamics of the system-bath model occur no longer matches the initial temperature, this process is called local heating⁷⁴. The bath most often is modelled as a collection of independent harmonic oscillators, therefore it lacks any direct energy exchange mechanism between oscillators. This means that the only pathway for the hot bath to dissipate thermal energy is to transfer it back to the system, which violates assumption of the constant temperature thermostat and introduces unwanted feedback to dynamics of the system.

The theoretical problem of bath heating resembles a process in Nature called molecular local heating^{75,76}, where if a molecule quickly dissipates a large amount of thermal energy to its immediate surroundings during, e.g., exciton-exciton annihilation⁷⁷⁻⁷⁹ or ultrafast molecular internal conversion^{4,80}, the temperature of molecule's nearest surrounding increases. Naturally, the subsequent colling process^{81,82} – thermalization, occurs where the excess heat is dissipated away from the molecule's immediate surrounding into deeper layers of the environment.

The issues of bath heating persist throughout the entire family of Davydov's ansätze. While, for non-multiple ansätze, it is possible to explicitly model hundreds or even thousands of bath oscillators, such that each oscillator absorbs a negligible amount of energy from the system, this approach is unfeasible for multiple-type ansätze. A more sophisticated solution is required.

Layout of the dissertation

The doctoral dissertation is based on 6 articles published in journals indexed in the Clarivate Analytics Web of Science (CA WoS) database. The reader is encouraged to read articles in full for more details, they are attached in Section (3.2.3). The articles are listed in the order of their appearance in the dissertation.

The main body of the dissertation is structured as follows:

Chapter (1) provides the theoretical background on the system-bath model, discusses various Davydov's ansätze and other necessary topics.

Chapter (2) presents an overview of the main results of Articles [A1], [A2], [A3], [A4], which focuses on comparing Davydov's ansätze by modelling energy relaxation processes and spectra.

Chapter (3) summarizes results from Articles [A5] and [A6], which introduce the thermalization algorithm and showcase its capabilities.

List of articles

Articles included in doctoral dissertation

- [A1] **M. Jakučionis**, I. Gaižiūnas, J. Šulskus, D. Abramavičius, Simulation of Ab Initio Optical Absorption Spectrum of β -Carotene with Fully Resolved S0 and S2 Vibrational Normal Modes, *The Journal of Physical Chemistry A*, **126**, 180–189, 2022
- [A2] **M. Jakučionis**, T. Mancal, D. Abramavičius, Modelling irreversible molecular internal conversion using the time-dependent variational approach with sD2 ansatz, *Physical Chemistry Chemical Physics*, **22**, 8952-8962, 2020
- [A3] **M. Jakučionis**, A. Žukas, D. Abramavičius, Modelling Molecular J and H Aggregates using Multiple-Davydov D2 Ansatz, *Physical Chemistry Chemical Physics*, **24**, 17665-17672, 2022
- [A4] **M. Jakučionis**, A. Žukas, D. Abramavičius, Inspecting molecular aggregate quadratic vibronic coupling effects using squeezed coherent states, *Physical Chemistry Chemical Physics*, **25**, 1705-1716, 2023

- [A5] **M. Jakučionis**, D. Abramavičius, Temperature-controlled open-quantum-system dynamics using a time-dependent variational method, *Physical Review A*, **103**, 032202, 2021
- [A6] **M. Jakučionis**, D. Abramavičius, Thermalization of open quantum systems using the multiple-Davydov-D2, *Physical Review A*, **107**, 062205, 2023

Articles not included in doctoral dissertation

- [A7] **M. Jakučionis**, V. Chorošajev, D. Abramavičius, Vibrational damping effects on electronic energy relaxation in molecular aggregates, *Chemical Physics*, **515**, 193-202, 2018
- [A8] O. Rancova, **M. Jakučionis**, L. Valkūnas, D. Abramavičius, Origin of non-Gaussian site energy disorder in molecular aggregates, *Chemical Physics Letters*, **674**, 120-124, 2017

Author's contribution

The author has solely developed the numerical computation package Vari-Davy⁸³, formulated and performed most[†] numerical simulations, derived most[‡] equations of motion for the considered Davydov's ansätze.

[†] Prof. Dr. Juozas Šulskus and Ignas Gaižiūnas performed quantum chemistry calculations of β -carotene, whose results were then used for the simulation of absorption spectra in Section (2.1).

[‡] Agnius Žukas co-derived the equations of motion of the squeezed-Davydov D₂ ansatz in Section (1.3.2).

Goals of the dissertation

The goals of this research project are (1) to understand which Davydov's ansätze are suitable for different types of system-bath models and (2) to develop theoretical and numerical methods for more efficient and accurate simulations of relaxation dynamics and spectroscopic signals using Davydov's ansätze.

To achieve the first (1) goal, the following tasks were set:

- Create a numerical computation package to simulate the time dynamics and spectroscopic signals of system-bath models using the time-dependent variational method with Davydov's family of ansätze.
- Develop a theoretical description and investigate the applicability of the D_2 ansatz for modelling the dynamics of a system-bath model including the mixing of normal modes of different electronic states.
- Investigate the applicability of representing excited states of quantum harmonic oscillators with a superposition of coherent states.
- Examine the applicability and convergence of the multiple-Davydov D_2 ansatz for simulating the absorption spectra of H and J-type molecular aggregates.
- Compare the accuracy of the regular, squeezed and multiple-Davydov D_2 ansätze for simulating the absorption and fluorescence spectra of a system-bath model with the frequency shift of the quantum harmonic oscillators upon the electronic excitation of the system.

To realize the second (2) goal, the tasks were:

- Develop a theoretical description and a numerical method to deduce the ensemble of thermal equilibrium states of excited system-bath model.
- Develop and investigate effects of the D_2 ansatz thermalization algorithm on the quantum harmonic oscillators and excitation relaxation dynamics.
- Extend the description of the D_2 ansatz thermalization algorithm to be used with the multiple-Davydov D_2 ansatz.
- Examine the optimization and thermalization algorithms as the tools for simulation of the spectroscopic signals.

Statements to be defended

1. The multiple-Davydov D_2 ansatz is capable of accurately simulating excitation relaxation dynamics and spectroscopic signals of molecular aggregates, while the less sophisticated non-multiple ansätze can capture only certain aspects of the aggregate's model.

2. To simulate the energy exchange between quantum harmonic oscillators induced by the non-linear coordinate coupling term $\propto x_p x_q^2$ using Davydov's family ansätze, the eigenstates of quantum harmonic oscillator can be represented by a superposition of coherent states.
3. The numerical thermalization algorithm for the regular and multiple D_2 ansätze allow to reduce the required number of quantum harmonic oscillators in the bath and, in turn, the numerical cost of simulations.
4. An ensemble of thermal steady states of the excited system-bath model can be obtained using either the numerical optimization or thermalization approach. The thermalization method is better suited for models with many degrees of freedom.

List of abbreviations

SB	System-bath
TDVP	Time-dependent variational principle
EOM	Equations of motion
DOF	Degrees of freedom
CS	Coherent state
QHO	Quantum harmonic oscillator
PES	Potential energy surface
HR	Huang-Rhys
sD ₂	Superposition-Davydov D ₂
sqD ₂	Squeezed-Davydov D ₂
mD ₂	Multiple-Davydov D ₂
RHS	Right-hand side
LHS	Left-hand side
TF	Thermalized fluorescence
TRF	Time-resolved fluorescence
TTRF	Thermalized time-resolved fluorescence
GMRES	Generalized minimal residual method

1 THEORY

This chapter presents a theoretical description of the standard system-bath (SB) model and outlines the prerequisites for using the time-dependent variational principle (TDVP) with the ansätze of the Davydov’s family. It is useful to have a specific physical model in mind when speaking about the theory. Therefore, we will present the SB model within the context of molecular aggregates. As we will see later, by appropriately renaming theoretical variables of the SB model formulated for molecular aggregates, it can be used to describe other physical systems as well.

In Section (1.1), the standard SB model Hamiltonian is formulated as well as the non-linear SB coupling term. Then, Section (1.2) introduces the TDVP and how it is used to derive equations of motion (EOM) of an ansatz. Section (1.3) presents and discusses various Davydov ansätze, which are used in this research work, along with their respective EOMs. Section (1.4) discusses numerical aspects of solving EOMs of Davydov’s ansätze. Then, Section (1.5) describe how the temperature effects are included as well as the concept of the ensemble of wavefunction trajectories. Lastly, Section (1.6.1) formulates the response functions of absorption and fluorescence spectroscopic signals.

1.1 Hamiltonian of the system-bath model

The SB model consists of a collection of electrostatically interacting molecules. Each molecule can further be coupled to both: the vibrational modes originating from the molecules themselves (intramolecular), and vibrational modes due to the motion in the surroundings of these molecules (intermolecular). The intramolecular modes are typically high frequency, whereas intermolecular modes are overdamped with low frequency and arise due to fluctuations in the nearest environment of molecules, such as the motion of solvent molecules, phonon modes of the molecular matrix, polymers.

The standard SB model Hamiltonian^{84,85,9,17}

$$\hat{H} = \hat{H}_S + \hat{H}_B + \hat{H}_{S-B}. \quad (1.1.1)$$

is made up of three terms: the system Hamiltonian \hat{H}_S , the bath Hamiltonian \hat{H}_B and a linear SB interaction Hamiltonian \hat{H}_{S-B} .

In this model, we consider the system as N coupled molecules, where each n -th molecule is modelled as a bosonic two-electronic-level system with a ground state $|0_n\rangle$ and an excited state $|1_n\rangle$. We construct the global electronic ground state as a product of each molecule ground state, given by

$$|0\rangle = \otimes_n^N |0_n\rangle. \quad (1.1.2)$$

We take the global electronic ground state energy E_G as a reference point for all energy values, hence we set $E_G = 0 \text{ cm}^{-1}$.

Using the Heitler-London approach^{86,84}, we construct the single electronic excitation states as

$$|n\rangle = |1_n\rangle \otimes_{m \neq n}^N |0_m\rangle, \quad (1.1.3)$$

with ground-to-excited transition energy ε_n , where the n -th two-level system is excited and all the rest of two-level systems are in their ground state. Transitions between the global ground state and excited system states are given by action of bosonic creation \hat{a}_n^\dagger and annihilation \hat{a}_n operators:

$$\hat{a}_n^\dagger |0\rangle = |n\rangle, \quad (1.1.4)$$

$$\hat{a}_n |n\rangle = |0\rangle. \quad (1.1.5)$$

The Coulomb electrostatic interaction strength J_{nm} between the n -th and m -th molecule can be expressed as an integral of interaction between respective molecules' transition charge distributions $\rho_n(\mathbf{r}_n)$ given by

$$J_{nm} = k_e \iint d\mathbf{r}' d\mathbf{r}'' \frac{\rho_n(\mathbf{r}') \rho_m(\mathbf{r}'')}{|\mathbf{r}' - \mathbf{r}''|}, \quad (1.1.6)$$

where k_e is the Coulomb constant.

If the distance between molecules' center of masses \mathbf{R}_n is larger than charge distributions, then the double integral can be evaluated numerically to the desired precision using the multipole expansion series. In the case of molecules with an overall non-zero charge or those involving charge transfer states, the Eq. (1.1.6) can be sufficiently approximated by the dipole-dipole expansion terms

$$J_{nm} = k_e \left(\frac{q_n q_m}{|\mathbf{R}_n - \mathbf{R}_m|} + \frac{q_n (\boldsymbol{\mu}_m \cdot \mathbf{R}_0) - q_m (\boldsymbol{\mu}_n \cdot \mathbf{R}_0)}{|\mathbf{R}_n - \mathbf{R}_m|^2} \right), \quad (1.1.7)$$

where q_n is the total charge, $\boldsymbol{\mu}_n$ is the transition dipole moment and \mathbf{R}_0 is the unit vector. They account for the majority of the interaction strength; the higher order expansion terms quickly decay with the distance and are of limited importance. However, if the distance between molecules' center of masses is of similar order as the molecular size, then the multipole expansion is invalid and Eq. (1.1.6) must be computed in full.

The system Hamiltonian can be expressed as

$$\hat{H}_S = \sum_n^N \varepsilon_n \hat{a}_n^\dagger \hat{a}_n + \sum_{n,m}^{n \neq m} J_{nm} \hat{a}_n^\dagger \hat{a}_m, \quad (1.1.8)$$

and is called the Frenkel exciton Hamiltonian⁸⁶.

When the electronic coupling between molecules of the system is sufficiently large, it is often convenient to analyze excitation dynamics of the SB model in terms of the eigenstates Φ_n^{exc} of the system Hamiltonian \hat{H}_S with corresponding eigenenergies $\varepsilon_n^{\text{exc}}$, which satisfy the time-independent Schrödinger equation

$$\hat{H}_S \Phi_n^{\text{exc}} = E_n^{\text{exc}} \Phi_n^{\text{exc}}. \quad (1.1.9)$$

Quasiparticles of the system Hamiltonian are referred to as excitons^{84,9}, and they are system's excitations delocalized over many molecules simultaneously⁵⁰.

The vibrational normal modes of molecules and their surrounding medium will be treated as a collection of quantum harmonic oscillators (QHO). Each molecule is assigned its own collection of oscillators, to which we will refer as local baths. The bath Hamiltonian is then given by

$$\hat{H}_B = \sum_{k,q} \omega_{kq}^g \hat{b}_{kq}^\dagger \hat{b}_{kq}, \quad (1.1.10)$$

where we have set the reduced Planck's constant to $\hbar = 1$. Here ω_{kq}^g is the frequency of the q -th oscillator in a k -th local bath, \hat{b}_{kq}^\dagger and \hat{b}_{kq} are bosonic QHO creation and annihilation operators, respectively. Note that we do not include QHO zero-point energy in Eq. (1.1.10), as it would only shift the absolute vibrational energy scale without affecting the dynamics of the SB model.

During an electronic transition from the ground to excited states of a system, the potential energy surfaces (PES) of vibrational modes may change. To account for these changes, we use the displaced oscillator model⁸⁷, which as-

sumes that the potentials of vibrational modes become displaced along their coordinate axes when the system transitions into an excited state. Displaced oscillators leads to the linear SB coupling Hamiltonian

$$\hat{H}_{S-B} = - \sum_n \hat{a}_n^\dagger \hat{a}_n \sum_q \omega_{nq}^e g_{nq} \left(\hat{b}_{nq}^\dagger + \hat{b}_{nq} \right), \quad (1.1.11)$$

which couples the excited electronic states of molecules to vibrational states of local baths' oscillators. Here g_{nq} is the dimensionless coupling strength of the q -th oscillators coupled to the n -th molecule. In addition to the term in Eq. (1.1.11), the displaced oscillator model introduces a static energy shift, known as the reorganization energy, given by

$$\Lambda_n = \sum_q \omega_{nq}^e g_{nq}^2. \quad (1.1.12)$$

We assume that all excited electronic states have the same coupling strengths g_{nq} , which causes all excited state energies to change by the same amount. Therefore, for simplicity in our equations, we absorb the reorganization energy shift into the definition of the ground-to-excited transition energy ε_n .

The linear SB coupling term \hat{H}_{S-B} effectively modulate excitation energies ε_n by coordinates of oscillators

$$\hat{x}_{kq} = \frac{1}{\sqrt{2}} \left(\hat{b}_{nq}^\dagger + \hat{b}_{nq} \right). \quad (1.1.13)$$

Molecular environment fluctuations are characterized by the spectral density function¹⁶ given by

$$C_n''(\omega) = \pi \sum_q g_{nq}^2 (\omega_{nq}^e)^2 \left(\delta(\omega - \omega_{nq}) - \delta(\omega + \omega_{nq}) \right). \quad (1.1.14)$$

In the SB model, fluctuations are modelled as the motion of bath oscillators with the overall strength given by the reorganization energy in Eq. (1.1.12). The function $C_n''(\omega)$ is generally obtained from experiments and is assumed to be known.

In the ground state, both the \hat{H}_S and \hat{H}_{S-B} terms vanish; therefore, the ground state Hamiltonian is simply equivalent to the bath Hamiltonian

$$\hat{H}_G = \hat{H}_B. \quad (1.1.15)$$

1.1.1 Non-linear displaced oscillator model

The higher order SB couplings are derived from the displaced oscillator model if the potential energy surfaces of QHOs in the molecular excited states are not only shifted with respect to those in the molecular ground state, but also differ by their frequencies and/or shape^{60,88–93}. In Section (2.4), we will investigate effects of QHO frequency shifts during the ground-to-excited state transition. This assumption leads to the quadratic SB coupling Hamiltonian term

$$\hat{H}_{\text{S-B}^2} = \frac{1}{4} \sum_n \hat{a}_n^\dagger \hat{a}_n \sum_q (\omega_{nq}^e - \omega_{nq}^g) (\hat{b}_{nq}^\dagger + \hat{b}_{nq})^2, \quad (1.1.16)$$

which must be included along the linear SB coupling term in Eq. (1.1.11). It contributes only if the QHO frequencies in the electronic ground state ω_{nq}^g are different from those in the excited state ω_{nq}^e .

The equations for computing time evolution of the SB model in Section (1.3) will include terms, which result due to the quadratic SB coupling. However, unless explicitly stated otherwise in the text, it will be assumed that oscillator frequencies in both electronic manifolds are the same

$$\omega_{nq}^e = \omega_{nq}^g = \omega_{nq}, \quad (1.1.17)$$

and the quadratic term does not contribute.

1.2 Time-dependent variational principle

Equations describing dynamics of the model are derived by applying the time-dependent variational principle^{94,95}. The principal idea of variational approach is to vary a parametrized trial wavefunction $|\Psi(\boldsymbol{\xi}(t))\rangle$, such that the action functional

$$S(t) = \int_{t_i}^{t_f} dt \mathcal{L}[\Psi(\boldsymbol{\xi}(t))], \quad (1.2.1)$$

is stationary and maintained at an extremum

$$\delta S(t) = \delta \int_{t_i}^{t_f} dt \mathcal{L}[\Psi(\boldsymbol{\xi}(t))] = 0, \quad (1.2.2)$$

where \mathcal{L} is a Lagrangian, and $\delta S(t)$ is a variation of action functional in terms of wavefunction, obtained by varying parameters $\boldsymbol{\xi}(t)$. To achieve this, the

parameters of the time-dependent wavefunction

$$\boldsymbol{\xi}(t) = (\xi_1(t), \xi_2(t), \dots, \xi_N), \quad (1.2.3)$$

are propagated in time according to the Euler-Lagrange equations

$$\frac{d}{dt} \left(\frac{\partial \mathcal{L}(t)}{\partial (\partial_t \xi_i^*)} \right) - \frac{\partial \mathcal{L}(t)}{\partial \xi_i^*} = 0, \quad (1.2.4)$$

where $\partial_t \xi_i$ is the time derivative of ξ_i , and the Lagrangian of the model is given by

$$\mathcal{L}(t) = \frac{i}{2} (\langle \Psi(t) | \partial_t \Psi(t) \rangle - \langle \partial_t \Psi(t) | \Psi(t) \rangle) - \langle \Psi(t) | \hat{H} | \Psi(t) \rangle. \quad (1.2.5)$$

This procedure results in a system of time-dependent equations for parametrization parameters $\boldsymbol{\xi}(t)$, which attempts to minimize the deviation of the ansatz from the solution of the corresponding Schrödinger's equation.

Time-dependent variational methods are intricately linked to the geometric interpretation of quantum states within a Hilbert space. The family of states spanned by the $\Psi(\boldsymbol{\xi}(t))$ can be viewed as a manifold \mathcal{M} within a Hilbert space. Then the time evolution of $\boldsymbol{\xi}(t)$ is determined by projecting the variation of the state $\delta\Psi(\boldsymbol{\xi}(t))$ onto the tangent space of \mathcal{M} . A comprehensive review of this geometric view can be found in the Refs.^{96,97}.

1.3 Davydov's ansätze

In this chapter, we will present four ansätze from the Davydov's family. The first three are the most common and will be presented in an order of increasing complexity and, presumably, accuracy, while the last ansatz is of an intermediate complexity. In Section (1.3.1) we will describe the simplest variant, and the backbone of the family, the Davydov D_2 ansatz^{41,42}. In Section (1.3.2) we will define the squeezed-Davydov D_2 ansatz by maintaining the same D_2 ansatz structure, but including an additional degree of freedom (DOF) to the states basis set. In Section (1.3.3) we will formulate the numerically exact ansatz of multiple-Davydov D_2 by considering a superposition of D_2 ansätze. For each ansatz, we will derive the corresponding EOMs for the SB model presented in Section (1.1). These are the principal Davydov ansätze, while many more can be found in the literature, each tailored to the specific needs of the model at hand and the physical processes that it is trying to capture.

With that in mind, in Section (1.3.4) we will propose a modification of the multiple-Davydov D_2 for simulation of molecular internal conversion, termed the superposition-Davydov D_2 .

1.3.1 Davydov D_2 ansatz

The Davydov D_2 ansatz is defined as

$$|\Psi_{D_2}^E\rangle = \sum_n^N \alpha_n(t) |n\rangle \otimes |\boldsymbol{\lambda}(t)\rangle. \quad (1.3.1)$$

For the system states, it considers a superposition of excited molecular states $|n\rangle$ with complex time-dependent amplitudes $\alpha_n(t)$. Meanwhile, bath QHO states are represented by the time-dependent multi-dimensional coherent state (CS)^{47,98,99}

$$|\boldsymbol{\lambda}(t)\rangle = \otimes_{k,q}^{K,Q} |\lambda_{kq}(t)\rangle. \quad (1.3.2)$$

A single-dimensional CS $|\lambda_{kq}(t)\rangle$ is an eigenstate of QHO annihilation operator

$$\hat{b}_{kq} |\lambda_{kq}(t)\rangle = \lambda_{kq}(t) |\lambda_{kq}(t)\rangle, \quad (1.3.3)$$

with complex eigenvalue $\lambda_{kq}(t)$. It is generated by applying the translation operator

$$\hat{D}(\lambda_{kq}(t)) = \exp\left(\lambda_{kq}(t) \hat{b}_{kq}^\dagger - \lambda_{kq}^*(t) \hat{b}_{kq}\right), \quad (1.3.4)$$

to the vacuum, zero quanta, state of QHO

$$\hat{D}(\lambda_{kq}(t)) |0\rangle_{kq} = |\lambda_{kq}(t)\rangle. \quad (1.3.5)$$

Therefore, we will regard $\lambda_{kq}(t)$ as a CS displacement parameter. By expressing it in the polar coordinate system

$$\lambda_{kq}(t) = |\lambda_{kq}(t)| e^{i\varphi_{kq}} \quad (1.3.6)$$

CS can be interpreted as being a Gaussian wavepacket displaced from the minima of the QHO energy potential by $|\lambda_{kq}(t)|$ and rotated counterclockwise by an angle φ in the coordinate-momentum phase space of QHO.

By applying the TDVP to the Davydov D_2 ansatz with the SB Hamiltonian,

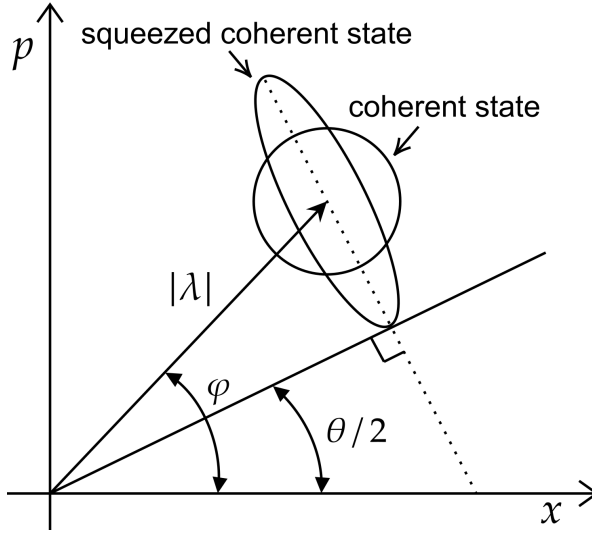


Figure 1.3.1: Diagram plot of a CS and a squeezed CS wavepackets in coordinate-momentum (x, p) phase space.

given by Eq. (1.1.1), we derive EOM for the free parameters of the ansatz:

$$\begin{aligned}
 \partial_t \alpha_n(t) = & -i\alpha_n \left(\varepsilon_n + \frac{1}{4} \sum_q \Delta\omega_{nq} \right) - i \sum_m^{n \neq m} \alpha_m J_{nm} \\
 & + i\alpha_n \sum_q \left(2\omega_{nq}^e g_{nq} \text{Re}\lambda_{nq} - \frac{1}{\rho} \sum_m |\alpha_m|^2 \omega_{mq}^e g_{mq} \text{Re}\lambda_{mq} \right) \\
 & - i\alpha_n \sum_q \left(\Delta\omega_{nq} (\text{Re}\lambda_{nq})^2 - \frac{1}{\rho} \sum_m |\alpha_m|^2 \Delta\omega_{mq} (\text{Re}\lambda_{mq})^2 \right) \quad (1.3.7)
 \end{aligned}$$

for each index $n = 1, 2, \dots, N$, and

$$\partial_t \lambda_{kq}(t) = -i\omega_{kq}^g \lambda_{kq} + \frac{i}{\rho} |\alpha_k|^2 \omega_{kq}^e g_{kq} - \frac{i}{\rho} |\alpha_k|^2 \Delta\omega_{kq} \text{Re}\lambda_{kq} \quad (1.3.8)$$

for all index combinations (k, q) , where $k = 1, 2, \dots, K$ and $q = 1, 2, \dots, Q$. We define the total wavefunction probability as $\rho = \sum_n^N |\alpha_n|^2$.

Equations (1.3.7), (1.3.8) constitute a system of explicitly coupled differential equations of size $N + KQ$. The terms on the right-hand side (RHS) of Eq. (1.3.7) in the first line describe dynamics of an isolated system, while terms on the second and third lines are due to the bath's influence on the system resulting from linear and quadratic SB couplings, respectively. Similarly, the first term

on the RHS of Eq. (1.3.8) describes the dynamics of an isolated QHO, while the remaining terms are due to the SB couplings.

1.3.2 Squeezed-Davydov D_2 ansatz

To broaden the range of QHO states represented by the D_2 ansatz, additional degrees of freedom must be unlocked. One possibility is to apply the squeeze operator

$$\hat{S}(\zeta_{kq}(t)) = \exp\left(\frac{1}{2}\left(\zeta_{kq}^*(t)\hat{b}_{kq}\hat{b}_{kq} - \zeta_{kq}(t)\hat{b}_{kq}^\dagger\hat{b}_{kq}^\dagger\right)\right), \quad (1.3.9)$$

with the complex squeeze parameter $\zeta_{kq}(t)$, in addition to the translation operator in Eq. (1.3.4). This operator contracts and expands the CS Gaussian wavepacket along its coordinate and momentum axes. By applying the displacement and squeeze operators to the QHO vacuum state

$$\hat{D}(\lambda_{kq}(t))\hat{S}(\zeta_{kq}(t))|0\rangle_{kq} = |\lambda_{kq}(t), \zeta_{kq}(t)\rangle, \quad (1.3.10)$$

the multi-dimensional time-dependent squeezed CS is generated, given by

$$|\boldsymbol{\lambda}(t), \boldsymbol{\zeta}(t)\rangle = \otimes_{k,q}^{K,Q} |\lambda_{kq}(t), \zeta_{kq}(t)\rangle. \quad (1.3.11)$$

The complex squeeze parameter $\zeta_{kq}(t)$ can be expressed in the polar form as

$$\zeta_{kq}(t) = r_{kq}(t)e^{i\theta_{kq}(t)}, \quad (1.3.12)$$

where the real-valued squeeze amplitude is given by

$$r_{kq}(t) = |\zeta_{kq}(t)|, \quad (1.3.13)$$

and the squeeze angle is denoted as $\theta_{kq}(t)$. The squeeze amplitude and angle together describe how much, and along which direction, the wavepacket become elongated, see Fig. (1.3.1)

The squeezed-Davydov D_2 ansatz (sqD₂) is defined as

$$|\Psi_{\text{sqD}_2}^E(t)\rangle = \sum_n^N \alpha_n(t) |n\rangle \otimes |\boldsymbol{\lambda}(t), \boldsymbol{\zeta}(t)\rangle. \quad (1.3.14)$$

Applying the TDVP leads to a system of explicitly coupled differential equa-

tions for the free parameters of the sqD₂ ansatz:

$$\begin{aligned}
\partial_t \alpha_n(t) = & -i\alpha_n \left(\varepsilon_n + \frac{1}{4} \sum_q \Delta\omega_{nq} \right) - i \sum_{m \neq n} \alpha_m J_{nm} \\
& + i\alpha_n \sum_q \left(2\omega_{nq}^e g_{nq} \text{Re}\lambda_{nq} - \frac{1}{\rho} \sum_m |\alpha_m|^2 \omega_{mq}^e g_{mq} \text{Re}\lambda_{mq} \right) \\
& - i\alpha_n \sum_q \left(\Delta\omega_{nq} (\text{Re}\lambda_{nq})^2 - \frac{1}{\rho} \sum_m |\alpha_m|^2 \Delta\omega_{mq} (\text{Re}\lambda_{mq})^2 \right) \\
& - \frac{i}{4} \alpha_n \sum_q \Delta\omega_{nq} (\cosh(2r_{nq}) - \sinh(2r_{nq}) \cos(\theta_{nq})) \\
& + \frac{i}{2\rho} \alpha_n \sum_{k,q} |\alpha_k|^2 \Delta\omega_{kq} \sinh^2(r_{kq}) (1 - \coth(2r_{kq}) \cos(\theta_{kq})) \quad (1.3.15)
\end{aligned}$$

for each index $n = 1, 2, \dots, N$, and

$$\partial_t \lambda_{kq} = -i\omega_{kq}^g \lambda_{kq} + \frac{i}{\rho} |\alpha_k|^2 \omega_{kq}^e g_{kq} - \frac{i}{\rho} |\alpha_k|^2 \Delta\omega_{kq} \text{Re}\lambda_{kq}, \quad (1.3.16)$$

$$\partial_t r_{kq} = \frac{1}{2\rho} |\alpha_k|^2 \Delta\omega_{kq} \sin(\theta_{kq}), \quad (1.3.17)$$

$$\partial_t \theta_{kq} = -2\omega_{kq}^g - \frac{1}{\rho} |\alpha_k|^2 \Delta\omega_{kq} (1 - \coth(2r_{kq}) \cos(\theta_{kq})) \quad (1.3.18)$$

for all index combinations (k, q) , where $k = 1, 2, \dots, K$ and $q = 1, 2, \dots, Q$. The number of equations is $N + 3KQ$.

It has been postulated that sqD₂ ansatz better represents QHO states with non-Gaussian wavepackets, which can be induced by the non-linear SB coupling terms, e.g., the quadratic SB coupling of Eq. (1.1.16). Upon inspecting differential equations of squeeze operator parameters r_{kq} and θ_{kq} , we find that if the frequency shift $\Delta\omega_{kq}$ is equal to zero, differential Eqs. (1.3.17), (1.3.18) simplify and have solutions:

$$\partial_t r_{kq} = 0 \quad \rightarrow \quad r_{kq}(t) = r_{kq}(0), \quad (1.3.19)$$

$$\partial_t \theta_{kq} = -2\omega_{kq}^g \quad \rightarrow \quad \theta_{kq}(t) = -2\omega_{kq}^g t + \theta_{kq}(0). \quad (1.3.20)$$

Indeed, without quadratic SB coupling, squeeze amplitudes become time-independent, while the squeeze angle changes at a constant rate. If the initial CS is not squeezed ($r_{kq}(0) = 0$), the Gaussian wavepacket is symmetric with respect to the rotation angle θ_{kq} . Therefore, the non-squeezed CS will remain non-squeezed indefinitely, i.e., it is the quadratic SB coupling that generates squeezing of CS.

1.3.3 Multiple-Davydov D_2 ansatz

The most general ansatz considered in this work is the multiple-Davydov D_2 ansatz (mD₂), which is given by⁶³

$$|\Psi_{\text{mD}_2}^E(t)\rangle = \sum_i^M \sum_n^N \alpha_{i,n}(t) |n\rangle \otimes |\lambda_i(t)\rangle, \quad (1.3.21)$$

where the free parameters of i -th superposition terms (multiples) are complex amplitudes $\alpha_{i,n}(t)$ and multi-dimensional CS

$$|\lambda_i(t)\rangle = \otimes_{k,q}^{K,Q} |\lambda_{i,kq}(t)\rangle, \quad (1.3.22)$$

with displacements $\lambda_{i,kq}(t)$. Each i -th multiple corresponds to an excited state associated with oscillator states.

By considering the mD₂ ansatz with depth M – the number of superposition terms, the complexity and accuracy of the mD₂ ansatz increase. The mD₂ ansatz reduces to the regular D_2 ansatz when depth is $M = 1$.

To illustrate principal idea of the mD₂ ansatz, in Fig. (1.3.2) we show an example of vibrational mode coordinate probability density $P(x)$, computed using the D_2 ansatz and the mD₂ ansatz with depth $M = 4$. The wavepacket of the D_2 ansatz always remains Gaussian, while the mD₂ ansatz represents the wavepacket using a superposition of four Gaussians, resulting in a non-Gaussian wavepacket. The importance of the circle to the overall representation of the ansatz is indicated by the color intensity of the circle.

Applying the TDVP to the mD₂ ansatz yields a system of implicitly coupled differential equations, given by:

$$\begin{aligned} & \sum_j (S_{ij} \partial_t \alpha_{j,n} + \alpha_{j,n} S_{ij} K_{ij}) = \\ & -i \sum_{j,m} \alpha_{j,m} S_{ij} J_{nm} - i \sum_j \alpha_{j,n} S_{ij} (A_{ij} + B_{ij,n} + C_{ij,n}), \end{aligned} \quad (1.3.23)$$

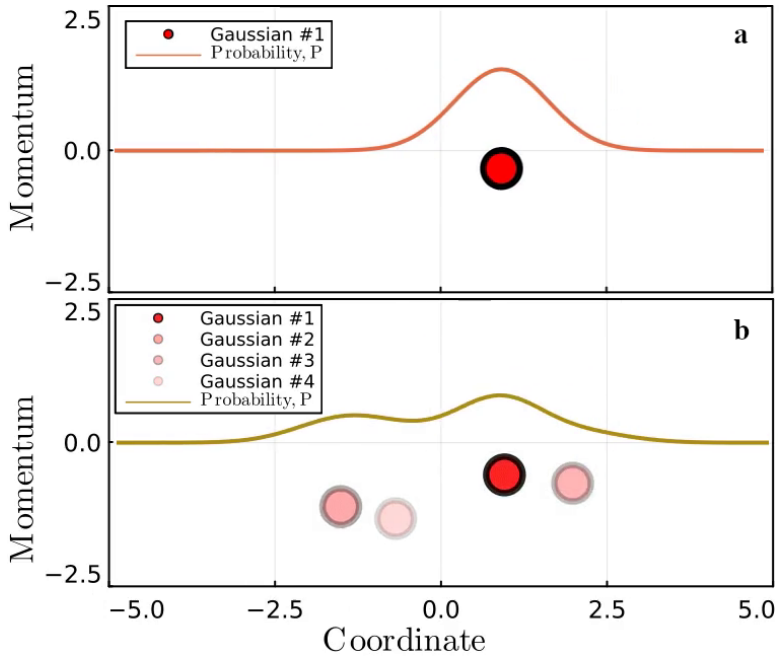


Figure 1.3.2: An example of the vibrational mode coordinate probability density $P(x)$ for (a) the D_2 ansatz, and (b) the mD_2 ansatz with depth of $M = 4$. Circles represent CSs of i -th multiples' projection to a vibrational mode coordinate-momentum phase space (x, p) . Color intensities of circles are proportional to the multiples' contribution to the mD_2 wavefunction norm.

for each pair of indices (i, n) , and

$$\begin{aligned}
& \sum_{j,n} (\alpha_{i,n}^* S_{ij} \lambda_{j,kq} \partial_t \alpha_{j,n} + G_{ij,nn} \partial_t \lambda_{j,kq}) = \\
& -i \sum_{j,n,m} G_{ij,nm} \lambda_{j,kq} J_{nm} - i \sum_{j,n} G_{ij,nn} \lambda_{j,kq} (A_{ij} + B_{ij,n} + C_{ij,n}) \\
& -i \sum_{j,n} G_{ij,nn} \omega_{kq}^g \lambda_{j,kq} + i \sum_j P_{ij,k} g_{kq} \omega_{kq}^e - 2i \sum_j G_{ij,kk} \Delta \omega_{kq} (\lambda_{i,kq}^* + \lambda_{j,kq}),
\end{aligned} \tag{1.3.24}$$

for all combinations of (i, k, q) indices. We additionally defined the function

$$K_{ij} = \sum_{k,h} \left(\left(\lambda_{i,kq}^* - \frac{1}{2} \lambda_{j,kq}^* \right) \partial_t \lambda_{j,kq} - \frac{1}{2} \lambda_{j,kq} \partial_t \lambda_{j,kq}^* \right), \tag{1.3.25}$$

which contains time derivatives of CS displacements. Other definitions are

$$G_{ij,nm} = \alpha_{i,n}^* \alpha_{j,m} S_{ij}, \tag{1.3.26}$$

$$A_{ij} = \sum_{k,q} \omega_{kh}^g \lambda_{i,kh}^* \lambda_{j,kh}, \tag{1.3.27}$$

$$B_{ij,n} = - \sum_q g_{nq} \omega_{nq}^e (\lambda_{i,nq}^* + \lambda_{j,nq}), \tag{1.3.28}$$

$$C_{ij,n} = \sum_q \Delta \omega_{nq} \left(1 + (\lambda_{i,nq}^* + \lambda_{j,nq})^2 \right), \tag{1.3.29}$$

and the overlap of two CS is

$$S_{ij} = \langle \boldsymbol{\lambda}_i | \boldsymbol{\lambda}_j \rangle = \exp \sum_{k,q}^{N,Q} \left(\lambda_{i,kq}^* \lambda_{j,kq} - \frac{1}{2} \left(|\lambda_{i,kq}|^2 + |\lambda_{j,kq}|^2 \right) \right) \tag{1.3.30}$$

1.3.4 Superposition-Davydov D_2 ansatz

While the D_2 ansatz is the simplest and the mD_2 ansatz is the most sophisticated, we have proposed an ansatz with intermediate complexity termed the superposition-Davydov D_2 (sD_2) ansatz

$$|\Psi_{sD_2}^E(t)\rangle = \underbrace{\sum_n^N \int_{\mathbf{x}^{\min}}^{\mathbf{x}^{\max}} d\mathbf{x} \Phi_n(\mathbf{x}, t) |n, \mathbf{x}\rangle}_{\text{system}} \otimes \underbrace{\sum_{\alpha}^M \theta_{\alpha}(t) |\boldsymbol{\lambda}_{\alpha}(t)\rangle}_{\text{bath}}, \tag{1.3.31}$$

where $\int_{\mathbf{x}_{\min}}^{\mathbf{x}_{\max}}$ is a multi-dimensional integral over the coordinate space of intramolecular vibrational modes. The sD₂ ansatz is constructed as a product of the system and the bath wavefunctions. The key conceptual difference from the mD₂ ansatz is that instead of considering amplitudes $\alpha_{i,n}(t)$ of the combined electron-vibrational states, the sD₂ ansatz splits them into separate amplitudes for each sub-part: amplitudes for electron-vibrational states $\Phi_n(\mathbf{x}, t)$ and amplitudes for bath vibrational states $\theta_\alpha(t)$, i.e., the sD₂ ansatz applies the Born-Oppenheimer approximation to the mD₂ ansatz.

The electronic states of the system and the intramolecular vibrational DOFs are treated numerically exactly using the coordinate basis set representation

$$\hat{x}_p|x_p\rangle = x_p|x_p\rangle, \quad (1.3.32)$$

where \hat{x}_p is the p -th intramolecular vibrational mode coordinate operator. These form system's electron-vibrational states

$$|n, \mathbf{x}\rangle = |n\rangle \otimes |x_1\rangle \otimes |x_2\rangle \otimes \dots \otimes |x_P\rangle, \quad (1.3.33)$$

with complex time-dependent amplitudes $\Phi_n(\mathbf{x}, t)$. The eigenstates of the bath QHOs are expanded in the superposition of multi-dimensional CSs

$$|\lambda_\alpha(t)\rangle = \otimes_{k,q}^{K,Q} |\lambda_{\alpha,q}(t)\rangle, \quad (1.3.34)$$

with complex time-dependent amplitudes $\theta_\alpha(t)$.

This approach enables us to gradually improve the accuracy of the bath wavefunction by adjusting the superposition depth M and to gauge bath representation precision influence on the system dynamics, while keeping the system wavefunction representation numerically exact and unchanged.

Because bath wavefunction is represented by a superposition of CSs, the resulting EOMs of the sD₂ ansatz again constitute a system of implicitly coupled differential equations, which require two-step numerical approach. The resulting EOMs can be found in the supplementary information of Article [A2].

1.4 Solving implicit EOM of the mD₂ ansatz

Equations of the D₂ and sqD₂ ansätze can be straightforwardly solved using most numerical libraries intended for finding solutions of explicit differential equations¹⁰⁰. The Runge-Kutta method with appropriate accuracy parameters

to ensure conservation of energy and the wavefunction norm, is a good choice. It requires to know the initial state vector, made up of the free parameters of the respective ansatz, defined as

$$\mathbf{x}_0 = \{\alpha_n(0), \lambda_{kq}(0), \dots, \theta_{kq}(0), r_{kq}(0)\}, \quad (1.4.1)$$

and the time derivative of the state vector

$$\partial_t \mathbf{x}(t) = \{\partial_t \alpha_n(t), \partial_t \lambda_{kq}(t), \dots, \partial_t \theta_{kq}(t), \partial_t r_{kq}(t)\}, \quad (1.4.2)$$

which is constructed from the EOMs of ansätze. This is sufficient to propagate the state vector $\mathbf{x}(t)$ in time.

For the implicit equations of the mD₂ ansatz, the vector $\partial_t \mathbf{x}(t)$ is not straightforwardly accessible and require an additional step to find it. We solved EOMs of the mD₂ ansatz in terms of the real and imaginary parts of variables $\alpha_{i,n}(t)$, $\lambda_{i,kq}(t)$, which were ordered in the column state vector

$$\mathbf{x}(t) = \{\alpha_{i,n}^R(t), \alpha_{i,n}^I(t), \lambda_{i,kq}^R(t), \lambda_{i,kq}^I(t)\}. \quad (1.4.3)$$

Consideration of the real and imaginary parts, instead of the complex variable form, removes consistency problems of having to treat derivatives of the complex CS displacements $\partial_t \lambda_{i,kq}(t)$ and their conjugates $\partial_t \lambda_{i,kq}^*(t)$ as two separate variables.

The time derivative of the state vector is found by writing Eqs. (1.3.23), (1.3.24) in a matrix form

$$\mathbf{M}(t) \partial_t \mathbf{x}(t) = \mathbf{f}(t), \quad (1.4.4)$$

where $\mathbf{M}(t)$ is a coefficient matrix of the time derivative terms, appropriately formed from the left-hand sides (LHS) of Eqs. (1.3.23), (1.3.24), while the column vector, $\mathbf{f}(t)$, is constructed from the RHSs.

We solved for $\partial_t \mathbf{x}(t)$ using the Generalized Minimal Residual Method (GMRES) with the Lower–Upper decomposition as a lower preconditioner. Suggestions to solve for $\partial_t \mathbf{x}(t)$ using the numerically less costly methods of the Moore–Penrose pseudo-inverse or the Lower–Upper decomposition, in conjunction with a small random noise applied to free variables, has been made. However, we found GMRES method to have a better numerical stability and, although each solve of GMRES is numerically more expensive, the resulting solution is more accurate, which, in turn, allows the numerical solver to take

larger time steps, reducing the overall numerical cost.

Now that the $\partial_t \mathbf{x}(t)$ vector is known, a variety of ordinary differential equation solvers can be used to propagate $\mathbf{x}(t)$. We found that the adaptive-order adaptive-time Adams-Moulton method¹⁰¹ provide just as accurate solution as a typical Runge–Kutta fourth-order method, but with less computational effort when used along the GMRES method. It evaluates the numerically expensive step of finding $\partial_t \mathbf{x}(t)$ fewer times than Runge-Kutta methods, thus, is well-suited for simulations of large SB models.

Another numerical aspect to consider when solving EOMs of the mD₂ ansatz is the fact that CSs of different multiples are never orthogonal

$$\langle \boldsymbol{\lambda}_i(t) | \boldsymbol{\lambda}_j(t) \rangle \neq 0, \quad (1.4.5)$$

they constitute an overcomplete set of states. This can lead to a situation, where two or more CSs approach each other during time evolution of the mD₂ ansatz and become highly overlapped. This results in an ill-conditioned coefficient matrix $M(t)$ with two or more equations becoming approximately linearly dependent, and, therefore, Eq. (1.4.4) no longer have a consistent solution for $\partial_t \mathbf{x}(t)$.

To address this issue, we use the programmed removal of overlapping multiples⁶⁷, which effectively connects two, or more, overlapping CS by imposing condition

$$\boldsymbol{\lambda}_i(t) = \boldsymbol{\lambda}_j(t) + \mathbf{C}, \quad (1.4.6)$$

for $t \geq t_0$, where $\mathbf{C} = \boldsymbol{\lambda}_i(t_0) - \boldsymbol{\lambda}_j(t_0)$ and t_0 is the time when the distance $d_{i,j}$ between CSs become less than d_0 , see Eq. (1.6.11). We found the critical distance of $d_0 = 0.05$ to be ideal for avoiding both: the numerical instabilities when $d_{i,j}$ is too small, and the unnecessary removal of multiples when $d_{i,j}$ is too large.

While the CS displacements remain connected for the remaining time of propagation $t \geq t_0$, the amplitudes of corresponding multiples $\alpha_{i,n}(t)$, $\alpha_{j,n}(t)$ are still independent, therefore, the overall dynamics are impacted minimally by the connection of $\boldsymbol{\lambda}_i(t)$ and $\boldsymbol{\lambda}_j(t)$. The value of the critical distance d_0 also give hints for the appropriate placement of the initially unpopulated CSs during the ground-to-excited state transition, as discussed in Section (1.6.1).

All numerical simulations presented in this dissertation were performed using a custom numerical package written during the project using the Julia programming language. The package has been made public and is available on-

line⁸³.

1.5 Modelling thermal effects

Temperature of molecular aggregate is included by averaging over dynamical trajectories with different initial conditions. Prior to excitation of molecular aggregate via an external field, the aggregate is in its electronic ground state $|0\rangle$, while vibrational modes are thermally excited. Thermal properties of QHOs in the ground state are straightforward. All oscillators are uncoupled from the system and each other, therefore, QHOs obey statistics of canonical ensemble. In representation of CSs, QHO canonical ensemble is described by a diagonal density operator given by the Glauber-Sudarshan distribution⁴⁵

$$\mathcal{P}(\lambda_{kq}) = \mathcal{Z}_{kq}^{-1} \exp\left(-|\lambda_{kq}|^2 \left[e^{\frac{\omega_{kq}}{k_B T}} - 1\right]\right), \quad (1.5.1)$$

where \mathcal{Z}_{kq} is the partition function, k_B is the Boltzmann constant and T is the temperature. It is a Gaussian function with mean equal to 0 and variance $(\exp[\omega_{kq}/k_B T] - 1)^{-1}/2$.

The ground state Hamiltonian of the SB model is equivalent to that of QHO, as shown in Eq. (1.1.15). Therefore, it is adequate to use the D_2 ansatz to describe states of the SB model. We define the ground state variants of the D_2 ansatz as

$$|\Psi_{D_2}^G(t)\rangle = \theta_0(t) |0\rangle \otimes |\boldsymbol{\lambda}(t)\rangle, \quad (1.5.2)$$

where $\theta_0(t)$ is the ground state complex amplitude.

If the ground state of a system is obtained by considering the downward electronic transitions, the resulting state may not necessarily be Gaussian, and then representation may require a more accurate ansatz. Therefore, we define the ground states of the sqD₂ and mD₂ ansätze as follows:

$$|\Psi_{\text{sqD}_2}^G(t)\rangle = \theta_0(t) |0\rangle \otimes |\boldsymbol{\lambda}(t), \boldsymbol{\zeta}(t)\rangle, \quad (1.5.3)$$

$$|\Psi_{\text{mD}_2}^G(t)\rangle = \sum_i^M \theta_{i,0}(t) |0\rangle \otimes |\boldsymbol{\lambda}_i(t)\rangle. \quad (1.5.4)$$

The approach to include temperature is the same for all considered ansätze. The only difference lies in how the thermal initial condition, sampled from Eq. (1.5.1), is represented by each ansatz.

For the $\Psi_{D_2}^G$ ansatz, we draw an independent sample for each QHO from the $\mathcal{P}(\lambda_{kq})$ distribution and set it as an initial CS displacement $\lambda_{kq}(0)$, which unambiguously characterizes thermal state of the model before electronic excitation. The ground state amplitude is set to $\theta_0(0) = 1$ for the wavefunction to be normalized. For the $\Psi_{sqD_2}^G$ ansatz, we also sample the $\mathcal{P}(\lambda_{kq})$ to deduce initial displacements $\lambda_{kq}(0)$. Squeeze amplitudes and angles for all QHOs are set to $r_{kq} = 1, \theta_{kq} = 0$, which correspond to non-squeezed Gaussian wavepackets. The ground state amplitude is again set to $\theta_0(0) = 1$.

1.5.1 Observable of an operator

The observable $X(t)$ of an operator \hat{X} is obtained by taking the average of the ensemble of wavefunction trajectories

$$X(t) = \frac{1}{\Gamma} \sum_{\gamma=1}^{\Gamma} \langle \Psi(t) |_{\gamma} \hat{X} | \Psi(t) \rangle_{\gamma} = \left\langle \langle \Psi(t) | \hat{X} | \Psi(t) \rangle \right\rangle, \quad (1.5.5)$$

where each γ -th trajectory has an initial thermal condition $\Psi(0)$ deduced in the manner as described in Section (1.5). Γ is the number of trajectories in an ensemble, which must be increased until the observable in Eq. (1.5.5) converge. To explicitly indicate that the observable of an operators \hat{X} is ensemble-averaged, we may surround the observable with brackets, $\langle X(t) \rangle$.

1.6 Simulating absorption and fluorescence spectra

1.6.1 Transitions between electronic manifolds

Molecular aggregates undergo transitions between their ground and excited states due to interactions with the external electric field $\mathbf{E}(t)$. Within the molecular dipole and the Frank-Condon approximations, molecules interact with the electric field via their purely electronic transition dipole vectors $\boldsymbol{\mu}_n$. Then the system-field coupling Hamiltonian is given by

$$\hat{H}_{S-F}(t) = \hat{\boldsymbol{\mu}} \cdot \mathbf{E}(t). \quad (1.6.1)$$

$\hat{\boldsymbol{\mu}} = \hat{\boldsymbol{\mu}}_+ + \hat{\boldsymbol{\mu}}_-$ is the vector transition dipole operator, and

$$\hat{\boldsymbol{\mu}}_+ = \sum_n^N \boldsymbol{\mu}_n \hat{a}_n^\dagger, \quad (1.6.2)$$

$$\hat{\boldsymbol{\mu}}_- = \sum_n^N \boldsymbol{\mu}_n \hat{a}_n, \quad (1.6.3)$$

are the vector transition operators that increase $\hat{\boldsymbol{\mu}}_+$ and decrease $\hat{\boldsymbol{\mu}}_-$ the number of excitation quanta in the aggregate. In this work, we consider the electric field in an impulsive limit

$$E(t) \rightarrow E_0 \delta(t - \tau), \quad (1.6.4)$$

with the rotating wave approximation¹⁰², where τ is the time at which system-field interaction occur. As a result, transitions between the aggregate's electronic manifolds occur instantaneously.

In general, state of the aggregate is a superposition of the ground state wavefunction Ψ^G and the excited state wavefunction Ψ^E . However, in the current perturbative treatment of interaction with the optical field, the electronic state of the aggregate will always adhere to either the ground or excited state manifold. Therefore, it is sufficient to consider the evolution of these wavefunctions independently.

Molecular aggregate's transitions between its ground and excited state manifolds are manifested via the action of the scalar transition operators

$$\hat{\mu}_\pm = \mathbf{e} \cdot \hat{\boldsymbol{\mu}}_\pm, \quad (1.6.5)$$

on wavefunctions of the aggregate, such as

$$\hat{\mu}_+ |\Psi_{D_2}^G(t)\rangle = |\Psi_{mD_2}^E(t)\rangle, \quad (1.6.6)$$

$$\hat{\mu}_- |\Psi_{mD_2}^E(t)\rangle = |\Psi_{D_2}^G(t)\rangle. \quad (1.6.7)$$

\mathbf{e} is the electric field polarization vector.

Free parameters of the initial state of the ansatz are known, whereas parameters of the final state of the ansatz must be computed and/or set appropriately. We will present description for the transitions using the mD_2 ansatz, however, the same conceptual ideas apply to the D_2 , sqD_2 , sD_2 ansätze.

For the ground-to-excited state transition in Eq. (1.6.6), as already mentioned in Section (1.5), it is sufficient to represent the initial ground state of

the model by the D_2 ansatz. Meanwhile, for the excited state the $\Psi_{mD_2}^E$ ansatz must be used. It can be equivalently represented by a single multiple out of the $i = 1, 2, \dots, M$ multiples of the mD_2 ansatz. For this reason, we choose to populate the first ($i = 1$) multiple and label rest of the multiples ($j \neq i$) as the initially unpopulated. Then the newly created state $\Psi_{mD_2}^E$, given by Eq. (1.3.21), has amplitudes:

$$\alpha_{1,n}(t) = (\mathbf{e} \cdot \boldsymbol{\mu}_n) \vartheta_0(t), \quad (1.6.8)$$

$$\alpha_{2\dots M,n}(t) = 0, \quad (1.6.9)$$

and CS displacements of the populated multiple are equivalent to displacement in the ground state

$$\lambda_{1,kq}(t) = \lambda_{kq}(t). \quad (1.6.10)$$

The unpopulated CS variables $\lambda_{2\dots M,kq}(t)$ do not initially contribute to the model dynamics. Their values are, in principle, arbitrary, however, during the following evolution of $\Psi_{mD_2}^E(t)$, the unpopulated multiples can become populated and begin to influence model dynamics. It is known that the initial distance

$$d_{i,j} = \sqrt{\sum_{kq} |\lambda_{i,kq}(t) - \lambda_{j,kq}(t)|^2}, \quad (1.6.11)$$

between the populated and the unpopulated CSs should not be too large. Otherwise, they will not participate in the excited state dynamics, even at long propagation times CSs will remain separated⁹³. On the other hand, setting all CS in a close proximity to each other $\lambda_{j \neq 1,kq}(t) \approx \lambda_{1,kq}(t)$ lead to a highly singular EOMs of the mD_2 ansatz, which are difficult to solve^{46,67} and were already discussed in Section (1.4).

Therefore, although the exact arrangement of the unpopulated CSs is not critical, we chose to set them in a layered hexagonal pattern around the populated CS⁹³, given by

$$\lambda_{j=2,\dots,M,kq}(t) = \lambda_{1,kq}(t) + \frac{\Delta}{2} (1 + \lfloor \beta(j) \rfloor) e^{i2\pi(\beta(j) + \frac{1}{12} \lfloor \beta(j) \rfloor)}, \quad (1.6.12)$$

where Δ is the distance parameter, $\beta(j) = (j - 2) / 6$ is the coordination function and $\lfloor x \rfloor$ is the floor function of x . The distance parameter Δ should be chosen to be sufficiently large to prevent significant overlap among the distribution of CSs, yet not so large as to eliminate overlap entirely. We have found $\Delta = 0.5$ to be reasonable value that gives numerically stable, consistent, and

convergent results.

For the excited-to-ground state transition in Eq. (1.6.7), the resulting ground state wavefunction is represented by the mD₂ ansatz to preserve phase relations between multiples of excited state wavefunction. The newly created state $\Psi_{\text{mD}_2}^{\text{G}}$ has amplitudes

$$\vartheta_{i,0}(t) = \sum_n (\mathbf{e} \cdot \boldsymbol{\mu}_n) \alpha_{i,n}(t), \quad (1.6.13)$$

and CS displacements $\lambda_{i,kq}(t)$ remain the same for all multiples.

1.6.2 Absorption and fluorescence response functions

Absorption and fluorescence spectra of a quantum system, in general, can be written as a Fourier transforms

$$F_{\text{fl}}(\omega) = \text{Re} \int_0^\infty dt e^{i\omega t} S_{\text{fl}}(t), \quad (1.6.14)$$

$$F_{\text{abs}}(\omega) = \text{Re} \int_0^\infty dt e^{i\omega t} S_{\text{abs}}(t), \quad (1.6.15)$$

of a time-domain absorption $S_{\text{abs}}(t)$ and fluorescence $S_{\text{fl}}(t)$ response functions¹⁰².

The absorption response function can be written as

$$S_{\text{abs}}(t) = \left\langle \langle \Psi^{\text{G}}(0) | \hat{\mu}_- \hat{\mathcal{V}}_{\text{E}}^\dagger(t) \hat{\mu}_+ \hat{\mathcal{V}}_{\text{G}}(t) | \Psi^{\text{G}}(0) \rangle \right\rangle, \quad (1.6.16)$$

where $\hat{\mathcal{V}}_{\text{E}}$ and $\hat{\mathcal{V}}_{\text{G}}$ are the excited and the ground state propagators, respectively, with the following properties:

$$\hat{\mathcal{V}}_{\text{A}}(t_1) |\Psi^{\text{A}}(t_2)\rangle = |\Psi^{\text{A}}(t_1 + t_2)\rangle, \quad (1.6.17)$$

$$\left(\hat{\mathcal{V}}_{\text{A}}(t_1) |\Psi^{\text{A}}(t_2)\rangle \right)^\dagger = \langle \Psi^{\text{A}}(t_2) | \hat{\mathcal{V}}_{\text{A}}^\dagger(t_1). \quad (1.6.18)$$

The fluorescence response function is a special case of the time-resolved fluorescence (TRF) response function^{102,103}

$$S_{\text{TRF}}(\tau_{\text{eq}}, t) = \langle \Psi^{\text{G}}(0) | \hat{\mu}_- \hat{\mathcal{V}}_{\text{E}}^\dagger(\tau_{\text{eq}} + t) \hat{\mu}_+ \hat{\mathcal{V}}_{\text{G}}(t) \hat{\mu}_- \hat{\mathcal{V}}_{\text{E}}(\tau_{\text{eq}}) \hat{\mu}_+ | \Psi^{\text{G}}(0) \rangle \quad (1.6.19)$$

It is a function of two times. During the equilibration time τ_{eq} , the system evolves in its excited state and relaxes due to its interaction with the environment until it reaches a steady state. After equilibration, during the coherence

time t , spontaneous emission occurs. We take the equilibration time τ_{eq} to be a model parameter, sufficiently long for the system to fully relax. Then we define the fluorescence response function as

$$S_{\text{fl}}(t) = \left\langle \left\langle \Psi^{\text{E}}(\tau_{\text{eq}}) \left| \hat{\mathcal{V}}_{\text{E}}^{\dagger}(t) \hat{\mu}_{+} \hat{\mathcal{V}}_{\text{G}}(t) \hat{\mu}_{-} \right| \Psi^{\text{E}}(\tau_{\text{eq}}) \right\rangle \right\rangle. \quad (1.6.20)$$

For convenience, once the equilibrated state

$$|\Psi^{\text{E}}(\tau_{\text{eq}})\rangle = \hat{\mathcal{V}}_{\text{E}}(\tau_{\text{eq}}) \hat{\mu}_{+} |\Psi^{\text{G}}(0)\rangle, \quad (1.6.21)$$

is obtained, we shift the time axis, such that the equilibrated state become the starting point,

$$\Psi^{\text{E}}(\tau_{\text{eq}}) \rightarrow \Psi^{\text{E}}(0), \quad (1.6.22)$$

as it represent the initial state from which emission takes place, therefore, we rewrite Eq. (1.6.20) as

$$S_{\text{fl}}(t) = \left\langle \left\langle \Psi^{\text{E}}(0) \left| \hat{\mathcal{V}}_{\text{E}}^{\dagger}(t) \hat{\mu}_{+} \hat{\mathcal{V}}_{\text{G}}(t) \hat{\mu}_{-} \right| \Psi^{\text{E}}(0) \right\rangle \right\rangle. \quad (1.6.23)$$

2 EXCITATION RELAXATION USING DAVYDOV'S ANSATZE

One of the goals of both experimental and theoretical investigations is to understand electronic and vibrational energy relaxation in molecules and their aggregates. The revealed excitation pathways might be harnessed for interpretation of experimental measurements and their functional applications.

In this chapter, we will utilize the ansätze of the Davydov's family to simulate excitation relaxation dynamics, as well as absorption and fluorescence spectra of SB models. Section (2.1) presents findings of the Article [A1], which explores the connection between sets of vibrational modes in different electronic states of β -carotene using the D_2 ansatz.

Then, in Section (2.2) the results of the Article [A2] are discussed, which investigate intramolecular energy relaxation dynamics induced by the internal conversion process using the proposed sD_2 ansatz. Section (2.3) covers the essential results of the Article [A3], which is concerned with the application and convergence of the mD_2 ansatz for simulation of the absorption spectra of H and J-type molecular aggregates. Lastly, in Section (2.4), the Article [A4] is introduced, which compares the simulated absorption and fluorescence spectra of molecular aggregates using the D_2 , sqD_2 and mD_2 ansätze.

2.1 Absorption spectrum of β -carotene with fully resolved vibrational modes

Carotenoids form a unique class of pigments with a conjugated polyene chain, responsible for light absorption in green-blue color region, over 700 carotenoid molecules are found in Nature. In photosynthesis carotenoids are essential in solar energy harvesting and in photoprotection from oxygen damage. Carotenoids demonstrate a complex structure of electronic excited states^{104,105} with at least three electronic states necessary to fully capture excitation long-time dynamics. Direct optical excitation induces electronic $S_0 \rightarrow S_2$ transition, where S_0 is the electronic ground state and S_2 is the first optically accessible bright electronic state, and the optically dark electronic state S_1 lies between

S_0 and S_2 in energy.

Experimental absorption spectra of carotenoids exhibit a high intensity¹⁰⁶ shoulder on a to a higher energy side, which is attributed to strong electronic-vibrational coupling. This feature is often associated with two vibrational modes: C-C symmetric and asymmetric stretching vibrations, which are known to be active in Raman spectra and their frequencies scale linearly with the conjugation length in carotenoids¹⁰⁵. To explain empirical data, the effective 2-mode model has proposed^{107,108,3,109,110,4}. It attempts to fit the absorption spectra with two QHOs, however, the resulting model does not capture the tail of the high energy vibrational wing and it is not clear whether two modes are sufficient to describe the more complex ultrafast internal conversion and energy transfer processes.

We explore the approach of simulating $S_0 \rightarrow S_2$ transition absorption spectra of β -carotene using all 282 vibrational normal modes of the molecule. The absorption spectra are simulate using the D_2 ansatz. The parameters of normal vibrational modes in the ground and excited states were obtained using the Density functional theory with hybrid functional B3LYP with 6-311G(d,p) basis set. The GAMESS¹¹¹ and Gaussian-16 codes¹¹² were used. The resulting sets of normal modes are different and not orthogonal, they are related by the Duschinsky transformation, which relates two sets of normal modes of different electronic states^{113–115}.

2.1.1 Mixing of vibrational modes upon electronic excitation

The coordinates $Q_k^{S_2}$ of normal modes in the excited electronic state S_2 are expressed in terms of normal mode coordinates $Q_j^{S_0}$ in the electronic ground state S_0 as

$$Q_k^{S_2} = a_{kj} Q_j^{S_0} - d_k. \quad (2.1.1)$$

The expansion coefficient of the k -th mode in terms of the j -th normal modes is a_{kj} , and d_k is the QHO potential displacement in S_2 with respect to its position in the ground state S_0 .

To understand the extent of normal mode mixing during the $S_0 \rightarrow S_2$ transition, we plot absolute values of expansion coefficients $|a_{kj}|$ in Fig. (2.1.1). The largest amplitude expansion coefficients lay close the main diagonal, implying that the majority of normal modes are mixed with similar frequency modes. However, certain regions indicate mixing between modes with vastly different frequencies. E.g., modes in a frequency region of 2500 cm^{-1} are highly

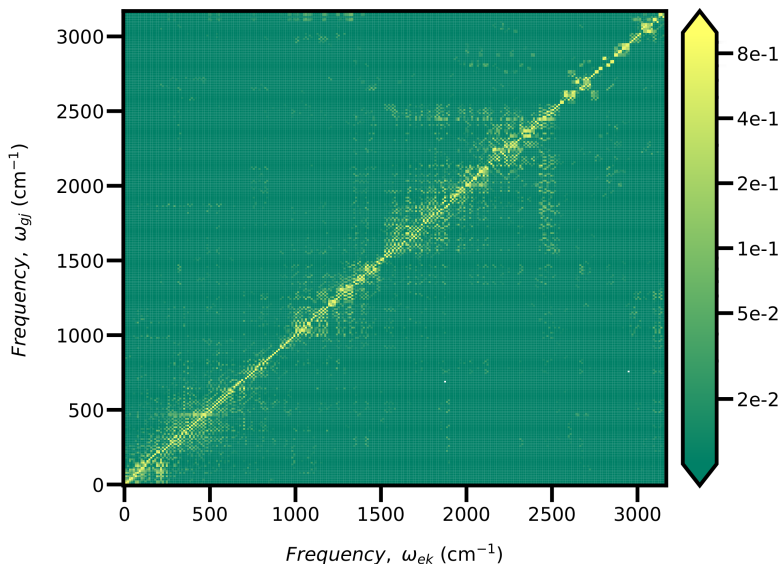


Figure 2.1.1: Absolute value of expansion coefficients $|a_{kj}|$ of the β -carotene normal modes. The k -th mode in the S_2 state is expanded in terms of the mode j -th in the state S_0 .

mixed with numerous modes in a frequency range of $1500 - 2500 \text{ cm}^{-1}$. The strong mixing can also be clearly seen between modes in frequency regions of $0 - 250 \text{ cm}^{-1}$, $400 - 750 \text{ cm}^{-1}$, $1000 - 1500 \text{ cm}^{-1}$. In addition, expansion coefficients along the diagonal axis of Fig. (2.1.1) are not symmetric, not even when their absolute values are compared $|a_{kj}| \neq |a_{jk}|$. This demonstrates that there is no one-to-one correspondence between normal modes of β -carotene in its electronic ground S_0 and excited S_2 state.

2.1.2 Absorption spectra of the β -carotene

The simulated absorption spectrum of β -carotene model with 282 normal modes at different temperatures is shown in Fig. (2.1.2) along the experimental β -carotene spectrum, measured in diethylamine at room temperature¹¹⁰. The absorption spectra have been normalized to their maximum value, as well as aligned on the 0-0 transition band for easier comparison. We find the 282-mode model spectrum to qualitatively reproduce position and amplitudes of the first two absorption peaks, however, it greatly overestimates the amplitude of vibrational peak progression at 300 K temperature.

The absorption of the high frequency modes displays non-trivial dependence on the temperature, which is an effect of normal mode mixing. For major-

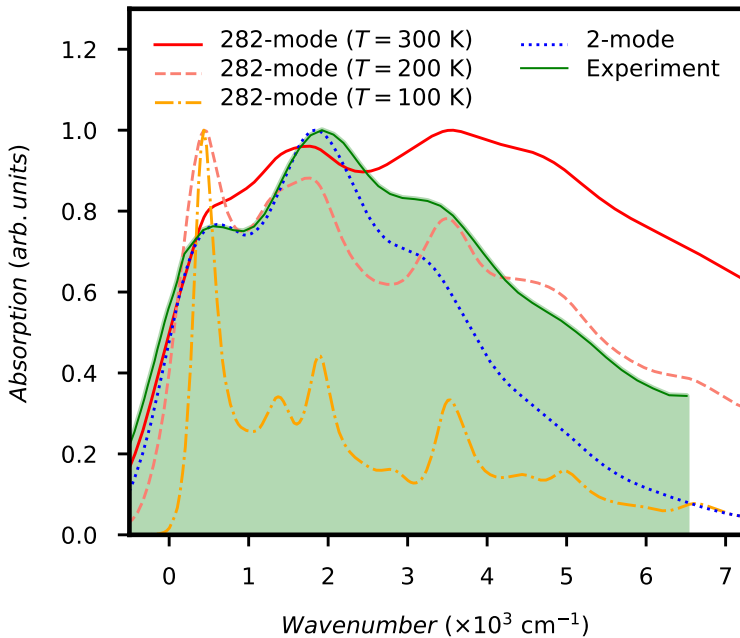


Figure 2.1.2: Absorption spectra of the β -carotene model at different temperatures. Experimental spectrum of β -carotene measured in diethylamine, as well as the simulated spectrum of 2-mode model at room temperature are also shown. All spectra are normalized to their maximum value and aligned on their 0-0 vibrational transition band.

ity of modes the average thermal energy is much smaller than the energy gap between the vibrational mode energy levels $k_B T \ll \omega$, thus, for non-mixed modes, dependence of absorption spectrum on temperature would be negligible. However, in Fig. (2.1.2) we observe strong dependence of absorption on temperature. Thermally excited low frequency vibrational modes translate to the excitation of the high frequency modes via normal mode mixing, which results in a high intensity absorption shoulder at high energies.

For comparison, we also simulated absorption spectrum of the empirical 2-mode β -carotene model at 300 K temperature. It includes only the C=C and C-C stretching vibrational modes with no mixing between them with frequencies 1522 cm^{-1} , 1157 cm^{-1} and displacements $d_{\text{C=C}} = 1.3$, $d_{\text{C-C}} = 0.9$, respectively¹⁰⁷. As shown in Fig. (2.1.2), the 2-mode model fits first two peaks well, but underestimates absorption intensities at higher frequencies.

To further compare the 282-mode and the 2-mode models, we look at their stick absorption spectrum in Fig. (2.1.3) simulated at 0 K temperature. The

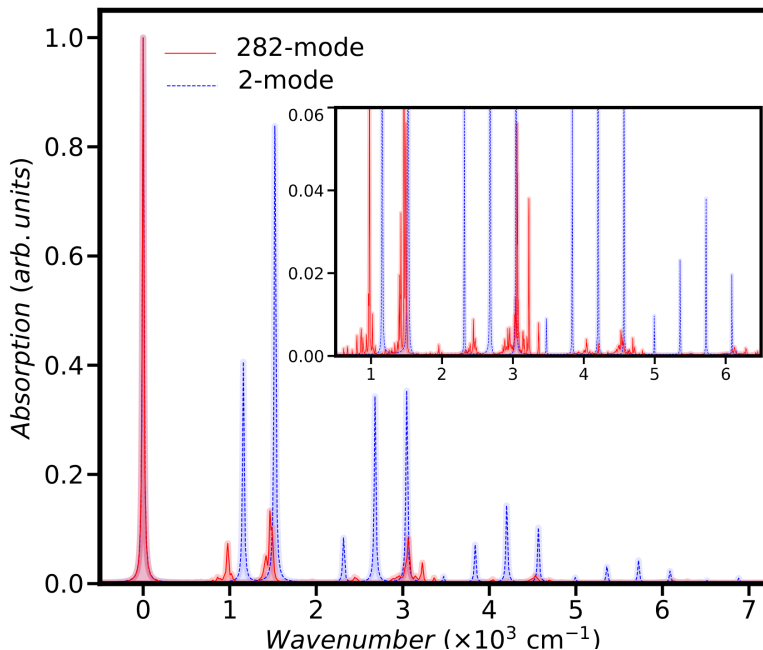


Figure 2.1.3: Stick absorption spectra at 0 K temperature of the 282-mode and the 2-mode models. Purely electronic transition energies are set to 0 cm^{-1} . To have finite width sticks, each spectrum have been convoluted with the Gaussian function of $\tau = 1 \text{ ps}$ variance. The inset more closely shows low amplitude sticks, they have been convoluted with $\tau = 5 \text{ ps}$ variance Gaussian.

inset more closely shows low amplitude sticks. The 2-mode model stick spectrum has a straightforward peak progression, the spectrum is a sum of each of the two mode peak progressions. The 282-mode model spectrum has a more complex structure. Even though each of the 282 modes have a small absorption peak, the combined spectrum produces frequency regions with noticeable absorption intensity. These regions show clear overlap with the absorption peaks of the 2-mode model at 1522 cm^{-1} and 1157 cm^{-1} , only this time, they are due to the absorption of a large number of mixed normal modes.

Looking at smaller intensity peaks at higher energies in the inset of Fig. (2.1.3), we find that the 282-mode model has absorption in the 3000 cm^{-1} , 4500 cm^{-1} , 6000 cm^{-1} frequency regions as well, and they account for the high frequency absorption tail seen in experiments. The 2-mode model has stick peaks at these frequencies as well, and they visually look more intense than the 282-mode model peaks. And yet, due to the normal mode mixing when nonzero temperature is included, the absorption peaks in Fig. (2.1.2) at

high frequencies become more intense. The strong absorption is produced by the summation of a large number of weak intensity absorption peaks. Two harmonic modes simply cannot account for absorption over a such a wide range of frequencies.

2.1.3 Main outcomes of the Article [A1]

We simulated and analysed the absorption spectra a β -carotene molecule, explicitly considering all its 282 vibrational modes. To compute the vibrational frequencies and amplitudes of normal modes in both the ground S_0 and excited S_2 states, we employed the Density functional theory with the hybrid functional B3LYP and the 6-311G(d,p) basis set. Subsequently, we used the D_2 ansatz to simulate the absorption spectra at various temperatures.

We found that there is no one-to-one correspondence between the ground and excited state vibrational modes. The normal modes of different electronic states are non-trivially mixed and should not be treated as being the same. Furthermore, we observed an strong dependence of the absorption intensity at higher energies on model's temperature, which can be explained by the mixing of normal modes.

Lastly, we observed that at 0 K temperature the strong absorption peaks of the empirical 2-mode model qualitatively matches frequencies of the 282-mode model. However, in the case of the 282-mode model, these peaks are the result of numerous weak transitions that accumulate to form a strong absorption feature. While the presented 282-mode model qualitatively matches the experimental data, it overestimate the high frequency region. Nevertheless, it provides substance ground for the origin of the empirical 2-mode model.

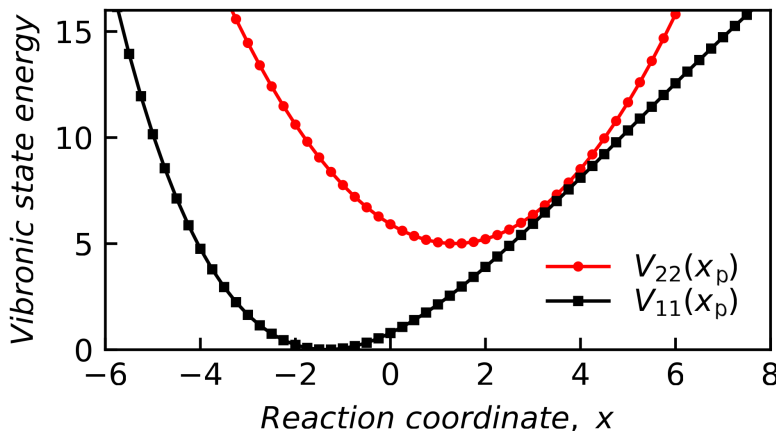


Figure 2.2.1: PESs of internal conversion model. Electron-vibrational states $|1, x\rangle$ are coupled to the Morse potential $V_{11}(x) = 40 \left(1 - \exp\left(-\frac{(x+1.35)}{4\sqrt{5}}\right)\right)^2$, while $|2, x\rangle$ states are coupled to harmonic potential $V_{22}(x) = \frac{1}{2}(x - 1.35)^2$. The coordinate space is discretized with equidistant step-size of $\delta x = 0.25$ in the interval $x \in [-10, 12]$. Circular and square markers denote the coordinate states $|x\rangle$ of the intramolecular vibration mode. The chosen width of coordinate space is sufficient to include all significant electron-vibrational wavepacket amplitudes during excitation relaxation dynamics. Periodic boundary conditions for PESs are used.

2.2 Molecular internal conversion

We examine the molecular internal conversion process, specifically the relaxation of excitation from the high lying excited electronic state to the lower energy excited electronic state of a single molecule. During the internal conversion, the majority of the energy from the relaxed excited electronic state is converted into the energy of intramolecular vibrational modes. This energy should then redistribute among all vibrational DOFs within the model, including both the intramolecular and the intermolecular modes of the immediate molecular surrounding. To thoroughly capture the entire excitation relaxation process, from start to finish, it is important to sufficiently accurately model all the necessary DOFs. In our approach, mixing of molecular electronic and intramolecular vibrational states are responsible for the internal conversion dynamics, while the intermolecular vibrational modes of the environment primarily serve to absorb the generated thermal energy from intramolecular modes.

2.2.1 Setup of the model

We consider a SB model, where each electronic state $|n\rangle$ is coupled to P intramolecular vibrational modes. The vibrational modes $p = 1, 2, \dots, P$ are described by their generalized P -dimensional PES $V(\mathbf{x})$, where $\mathbf{x} = (x_1, x_2, \dots, x_P)$ is a point in the P -dimensional coordinate space of intramolecular vibrational modes. PESs can be different for each electronic state. The surface associated with the state $|n\rangle$ will be labelled as an diagonal term $V_{nn}(\mathbf{x})$, while the non-diagonal terms $V_{nm}(\mathbf{x})$ represent the nonadiabatic coupling between two electronic states $|n\rangle$ and $|m\rangle$. It is well established that the PESs $V_{nn}(\mathbf{x})$ of different molecular electronic states can get close to each other in their energies (the avoided crossing region) or even cross each other (the conical intersection)¹¹⁶, which permits non-radiative excitation relaxation between different electronic states. Each intermolecular vibrational mode is modelled as a QHO.

Internal conversion dynamics between two electron-vibrational states $|1, x\rangle$, $|2, x\rangle$ with one-dimensional PES, as shown in Fig. (2.2.1) are investigated. PESs of different electronic states are coupled by the linear nonadiabatic electron-vibrational coupling $V_{12}(x) = \frac{1}{10}x$. To facilitate vibrational energy transfer from the intramolecular vibrational mode to the intermolecular modes, we include the vibrational coupling Hamiltonian term

$$\hat{H}_{V-V^2} = \sum_n \hat{a}_n^\dagger \hat{a}_n \sum_{p,q} k_{npq} \hat{x}_p \hat{x}_q^2, \quad (2.2.1)$$

where k_{npq} is a coupling strength parameter in units of energy. It couples coordinates \hat{x}_p of intramolecular vibrational mode to coordinates \hat{x}_q^2 of intermolecular modes. It is the lowest order coupling term for energy transfer, since the bi-linear vibrational coupling term $\propto \hat{x}_p \hat{x}_q$ would only redistribute oscillation strengths, which could be equivalently represented by a new set of uncoupled normal modes.

The model states will be represented by the sD₂ ansatz, which we formulated in Section (1.3.4). The excitation of the system is assumed to occur vertically, i.e., the electron-vibrational system wavepacket is transferred from the ground state potential surface into the excited state potential without undergoing any changes. The initial excited electron-vibrational state amplitudes are then equal to $\Phi_2(x, 0) = \frac{1}{\sqrt{2\pi}} e^{-\frac{x^2}{2}}$, $\Phi_1(x, 0) = 0$. The bath is assumed to be at 0 K temperature, therefore, the bath amplitudes are $\theta_1(0) = 1$, $\theta_{2\dots M}(0) = 0$, and

CS displacements are set to $\lambda_{i,kq}(0) = 0$.

2.2.2 Excitation energy relaxation dynamics

In order to track the processes of internal conversion and vibrational energy redistribution, we analyze dynamics of the total energy of electronic states $\varepsilon_{\text{el}}(t)$, the total energy of intramolecular vibrational modes $\varepsilon_{\text{vibr}}(t)$ and the energy of intermolecular modes of the bath $\varepsilon_{\text{bath}}(t)$, which are shown in Fig. (2.2.2).

In the case of an isolated system, we observe sporadic reversible mixing of electronic and intramolecular vibrational energy, resulting solely from the free evolution and mixing of electron-vibrational wavepackets on the potential energy surfaces $V_{11}(x)$ and V_{22} . By including the bath and using the simplest CS representation ($M = 1$), the energy mixing becomes harmonic, yet no energy is transferred from the system to bath. The slight increase in the bath energy is due to QHO reorganization in the excited states. When more superposition terms are considered ($M > 1$), the internal conversion becomes irreversible, i.e., the generated intramolecular vibrational mode energy is transferred to bath QHOs without it being converted back into electronic energy. The dynamics become converged when $M = 5$ terms are included.

When only a single CS is considered ($M = 1$), the total lack of energy exchange between the intramolecular and bath QHOs indicates that the necessary eigenstates of QHOs are not able to be represented by the sD_2 ansatz. We want to highlight the fact that the energy of CS is not limited in any way and is simply proportional to the displacement $\propto |\lambda|^2$. Therefore, the lack of energy transfer is imposed strictly by the insufficient representation of the necessary eigenstates. When the eigenstates become present, by considering state representation by the superposition of several CS, energy absorption by the bath is observed.

2.2.3 Wavepacket evolution

To investigate how representation of QHO states changes as the ansatz depth increases, in Fig. (2.2.3) we display dynamics of a single QHO coordinate and momentum variances, as well as their arithmetic average. In the case of $M = 1$, both variances are expectedly equal to 0.5 and remain constant in time, since the wavepacket is strictly Gaussian. For $M > 1$, we observe asymmetric oscillations between the coordinate and momentum variances, and the average variance surpasses that of the Gaussian. This suggests that the wavepacket

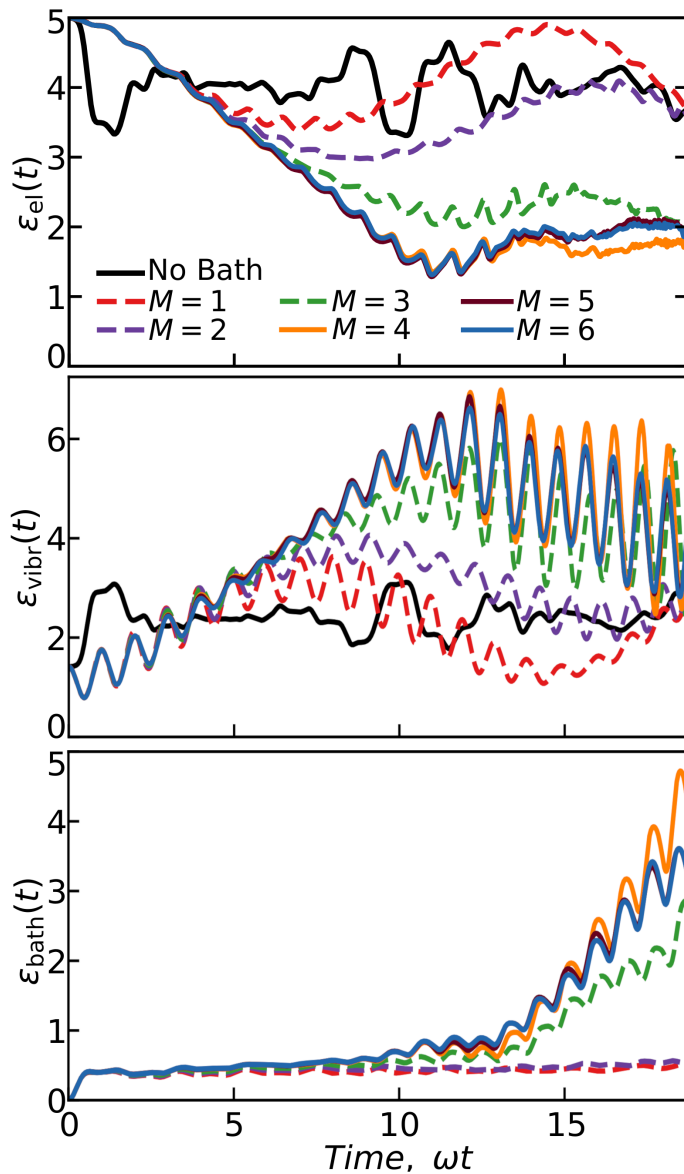


Figure 2.2.2: Time dependence of the system electronic energy ε_{el} , intramolecular vibrational mode energy $\varepsilon_{\text{vibr}}$, and the total energy of the bath $\varepsilon_{\text{bath}}$. The nonadiabatic coupling $V_{nm}(x)$ energy is included in the definition of $\varepsilon_{\text{vibr}}(t)$. Zero-point energy of bath QHO are excluded. The black line represents dynamics of an isolated system, computed by excluding bath modes from the model. M is the number of superposition terms considered in the definition of the sD_2 ansatz.

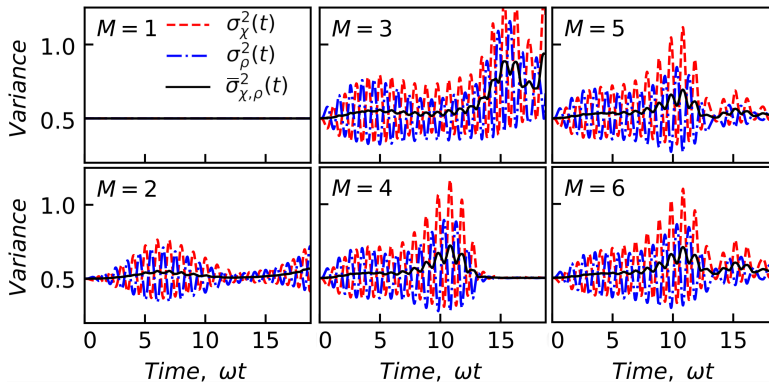


Figure 2.2.3: Time dependence of frequency $\omega = 0.5$ QHO'S coordinate $\sigma_x^2(t)$ momentum $\sigma_\rho^2(t)$ variances and their arithmetic average $\bar{\sigma}_{x,\rho}^2(t)$, computed with the sD₂ ansatz of depth M .

broadens and is slightly squeezed along the momentum axis.

2.2.4 Main outcomes of the Article [A2]

We employed the sD₂ ansatz to simulate the molecular internal conversion process. Specifically, we focused on the relaxation of excitation from the high lying excited electronic state to the lower energy excited electronic state. In our model, the internal conversion dynamics are induced by the mixing of molecular electronic states and intramolecular vibrations, while the intermolecular vibrational modes of the environment primarily serve to absorb thermal energy from intramolecular modes.

By examining the time evolution of the electronic, intramolecular and intermolecular vibrational energies, we found that the proposed model captures internal conversion relaxation process. The energy exchange, induced by the non-linear coupling term Eq. (2.2.1), between vibrational modes occur if the eigenstates of the intermolecular modes are represented in terms of CS superposition. The resulting wavepacket of intermolecular modes becomes broader and asymmetrically squeezed compared to a Gaussian wavepacket.

The observed wavepacket features are impossible to represent using a single CS, therefore, the most basic representation using the D₂ ansatz is not sufficient, a more sophisticated ansatz, such as the proposed sD₂ ansatz, is required, otherwise, direct energy transfer from intramolecular to intermolecular vibrational modes is suppressed.

2.3 Excitation relaxation in molecular aggregates

Absorption spectrum and excitation relaxation dynamics of a linear molecular aggregate are key quantities that may serve for establishing relation between parameters of theoretical models and experiments. Molecular aggregate electronic properties significantly depend on the transition dipoles, whether the dipoles are in the head-to-tail configuration, which are called J-type aggregates, or in the side-to-side configuration, termed H-type aggregate^{117–121,17}. In a J aggregate, excitation by an external electric field excites the lowest energy excitonic state, therefore, energy relaxation dynamics are minimal and the absorption spectrum is dominated by the exchange narrowing effect^{122–124}. It effectively reduces electron-vibrational coupling strength and the shape of the spectrum become similar to that of a single molecule. Meanwhile, in an H aggregate, external fields excite the highest energy excitonic state, thus, various available electron-vibrational energy relaxation pathways make H aggregate spectra more complicated than that of the J aggregate with non-trivial spectral line shape^{122,124}.

To simulate absorption spectra of H and J-type molecular aggregates, we use the mD₂ ansatz presented in Section (1.3.3). The ability of ansatz to represent complicated electron-vibrational eigenstates of molecular aggregates depends on its depth M . When $M = 1$, the mD₂ ansatz reduces to the D₂ ansatz, which has EOM that are considerably easier to solve. Therefore, it is crucial to determine if the D₂ ansatz is sufficient to simulate molecular aggregates and in what regimes of model parameters. If not, then it is necessary to understand the appropriate minimal depth of the mD₂ ansatz.

2.3.1 Absorption spectra convergence using the mD₂ ansatz

We consider an aggregate composed of $N = 10$ identical molecules. The nearest neighbour coupling between them is $J_{n,n+1} = J = \pm 500 \text{ cm}^{-1}$, and the aggregate is in an open chain configuration with boundary conditions $J_{N,1} = J_{1,N} = 0 \text{ cm}^{-1}$. A positive sign of J coupling result in an H-type aggregate, while a negative sign yields an J-type aggregate.

Each molecule is coupled to one intramolecular vibrational mode with a frequency $\omega_{kq} = \omega = 500 \text{ cm}^{-1}$ and Huang-Rhys (HR) factor $S = g_{1,1}^2 = 1$, which defines the electron-vibrational coupling strength. The electronic transition dipole moment vectors of molecules are identical and set to $\boldsymbol{\mu}_n = (1, 0, 0)$. The initial thermal energy of vibrational modes is $k_B T = \omega_{kq}/2$, which corre-

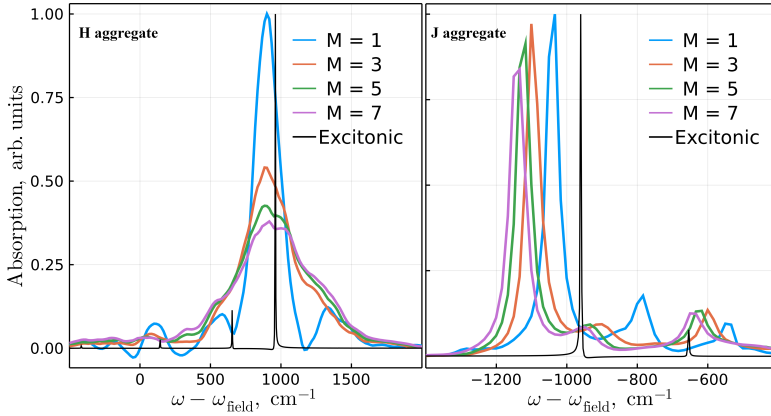


Figure 2.3.1: Absorption spectra of the H and J-type model aggregate simulated using the mD_2 ansatz with depth $M = 1 \dots 7$. Purely excitonic spectra are obtained by excluding the bath. The spectra consists of a main absorption peak at an energy $\approx 2J$ and $N - 1$ additional peaks with lower amplitudes, which are result of the aggregate being in an open chain configuration.

sponds to a temperature of $T = 360$ K.

The simulated absorption spectra for the H and J-type aggregates, including their excitonic spectra, are presented in Fig. (2.3.1). We observe that absorption spectra of both aggregate types converge with a depth of $M = 7$ when using the mD_2 ansatz. Spectra obtained with a higher depth, up to $M = 11$, yielded quantitatively identical results. The vibrational side-peaks on the higher energy side of excitonic peaks arise from the combined electron-vibrational transitions from vibrational states of QHOs with 0 quanta to states with $n > 0$ quanta. On the lower energy side of excitonic peaks, absorption intensities due to transition from the n to $m < n$ quanta are present, which are populated due to the nonzero temperature of the model. The absorption peak widths result from dephasing between electron-vibrational states induced by the coupling to the bath fluctuations.

For the H-type aggregate, the spectrum of the $M = 1$ depth has absorption peaks at frequencies similar to the converged spectrum ($M = 5$), however, peak intensities are incorrect, and some are even negative. By increasing the depth, already at $M = 3$, absorption peak intensities become strictly positive, and the overall absorption line shape qualitatively matches that of the converged spectrum. For the J-type aggregate, by increasing the depth, the whole absorption spectrum shifts to the lower energy side, while qualitatively retaining the main peak shape and intensity. Changes of absorption peaks due

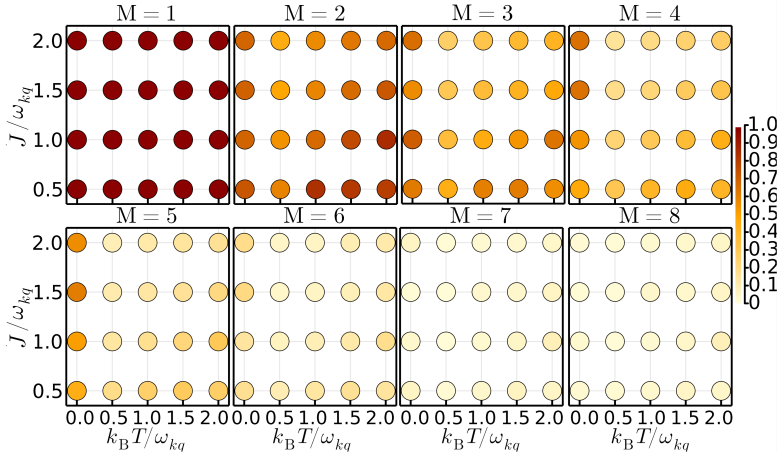


Figure 2.3.2: The discrepancy metric $\mathcal{D}(M)$ as a function of the mD₂ ansatz depth M of the H-type molecular aggregate model for a range of dimensionless parameters J/ω , $k_B T/\omega$.

to transitions to the higher energy excitonic are more pronounced. In addition, unlike for the H-type aggregate spectrum, all absorption peaks are positive, even when $M = 1$.

2.3.2 The mD₂ ansatz depth dependence on model parameters

Next we want to answer the question of whether the required depth of the mD₂ ansatz, to obtain convergent absorption spectra, is dependent on the parameters of the model. Although the absorption line shape is affected by all model parameters, we focus on investigating the influence of the nearest neighbour coupling J , the thermal energy $k_B T$, and the vibrational mode frequency ω . To do so, we considered the dimensionless frequency-normalized coupling J/ω and the thermal energy $k_B T/\omega$. We did not account for the influence of the HR factor of vibrational modes, but we keep it set to a high value of $S = 1$, to have a challenging molecular aggregate model.

In order to quantify the convergence of absorption spectra, we use the discrepancy metric, defined as

$$\mathcal{D}(M) = \frac{1}{\mathcal{N}} \int d\omega \sqrt{(A(\omega, M) - \bar{A}(\omega))^2}, \quad (2.3.1)$$

where $A(\omega, M)$ is the absorption spectrum obtained using the mD₂ ansatz with depth M and $\bar{A}(\omega) = A(\omega, M = 11)$ is the converged reference spectrum. \mathcal{N}

is the normalization factor, which ensures that $0 \leq \mathcal{D} \leq 1$.

We focus on the convergence of absorption spectra of the H-type molecular aggregate because its peak frequencies remain mostly unchanged, allowing the discrepancy metric to accurately capture intensity variations. Fig. (2.3.2) displays $\mathcal{D}(M)$ for a range of depths. We find that the discrepancy significantly depends on the model parameters for a given depth. When $M = 1$, the discrepancy is always high regardless of the model parameters. When $M = 2 \dots 5$, high-discrepancy regions are observed at low temperatures, irrespective of the coupling strength, as well as at high temperatures with weak coupling.

The high discrepancy at high temperatures can be attributed to the fact that more CS are needed to represent QHO eigenstates with $n > 0$ vibrational quanta, which are excited by thermal energy. In the case of low temperatures, equilibrium coordinates of vibrational modes become significantly displaced in the excited state. The high displacement causes the wavepacket of an excited aggregate to relax via a complicated energy surfaces of electron-vibrational states. This results in changes to the wavepacket and/or splitting between electron-vibrational surfaces, which require many CS to be represented accurately. It is difficult to pinpoint a single reason for the increased discrepancy in any specific case of model parameter because many aspects of eigenstate representation are intertwined.

2.3.3 Main outcomes of the Article [A3]

We used the numerically exact mD_2 ansatz to simulate absorption spectra of H and J-type molecular aggregate made up of 10 identical monomers in order to examine convergence of the ansatz over a wide range of temperatures and the nearest neighbour coupling strengths.

We found that it is necessary to use the mD_2 ansatz with at least 7 superposition terms. The D_2 ansatz, which reduces from the mD_2 ansatz with 1 superposition term, but has less complex EOMs, is insufficient across all considered model parameter regimes. Specifically, for H-type aggregates, it is necessary to use the multiple-type ansatz to achieve a positive absorption line shape and accurate peak intensities. For J-type aggregates, increasing the depth of the mD_2 ansatz predominantly results in a redshift of the absorption spectrum, while the overall line shape remains qualitatively unchanged.

It is difficult to pinpoint a single reason for the necessity to use the mD_2 ansatz, however, it can be attributed to having to represent QHO eigenstates with high quantum number at high temperatures, as well as to allow for decou-

pled time evolution of excitation wavepacket on different electron-vibrational states.

2.4 Vibrational frequency shift

The standard SB model, introduced in Section (1.1), assumes that frequencies of vibrational modes in the aggregate's excited state are identical to those in the ground state. However, experimental studies, as well as theoretical modelling, suggest that these frequencies differ. In this section, we will explore effects and modelling of the quadratic SB coupling term of Eq. (1.1.16), which emerges as a result of assuming that QHO frequencies in the excited state ω_{kq}^e become shifted with respect to frequencies ω_{kq}^g in the the ground state.

We will examine the impact of frequency shift on both absorption and fluorescence spectra of molecular aggregates. While we have described the fluorescence response function for simulating fluorescence spectra in Eq. (1.6.23), the initial state of the excited molecular aggregate $\Psi^E(0)$ from which emission takes place, has not yet been defined. Therefore, in the next Section (2.4.1), we propose an approach to generate thermal equilibrium states by solving a numerical optimization problem. The results of this approach will be analysed in Section (2.4.2).

2.4.1 Numerical optimization approach for simulating fluorescence spectra

The energy of the SB model in a state $\Psi^E(0)$ is given by

$$E^E(0) = \langle \Psi^E(0) | \hat{H} | \Psi^E(0) \rangle. \quad (2.4.1)$$

In the case of temperature $T = 0$ K, vibrational mode thermal fluctuations are absent. Therefore, fluorescence occurs from the lowest energy equilibrium state of the aggregate

$$\Psi_{E_0}^E = \Psi^E(0) |_{T=0\text{K}}, \quad (2.4.2)$$

energy of which we denote as

$$E_0 = E^E(0) |_{T=0\text{K}}. \quad (2.4.3)$$

Then, following from Eq. (1.6.23), the fluorescence response function at $T = 0$ K can be rewritten as

$$S_{\text{fl}}(t) |_{T=0\text{K}} = \langle \Psi_{E_0}^E | \hat{\mathcal{V}}_E^\dagger(t) \hat{\mu}_+ \hat{\mathcal{V}}_G(t) \hat{\mu}_- | \Psi_{E_0}^E \rangle. \quad (2.4.4)$$

Notice that Eq. (2.4.4) no longer averages over the ensemble of wavefunction trajectories. This is because the $\Psi_{E_0}^E$ state is exclusively a function of the model Hamiltonian and the free parameters of the ansatz, without any dependence on statistical sampling of initial thermal state parameters.

The lowest energy state $\Psi_{E_0}^E$ is deduced by solving the numerical problem of minimizing the energy, given by Eq. (2.4.1), of the excited aggregate in terms of the chosen ansatz free parameters. We found the heuristic adaptive particle swarm optimization algorithm^{125,126} to be well-suited for the problem.

In the case of a nonzero temperature ($T > 0$ K), thermal fluctuations of vibrational modes must be accounted for. Thus, by allowing molecular aggregate to relax during the equilibration time τ_{eq} , see Eq. (1.6.19), the model will eventually relax into one γ -th of many available equilibrium thermal states

$$\Psi_{E_T, \gamma}^E = \Psi_{\gamma}^E(0) |_{T>0 \text{ K}}, \quad (2.4.5)$$

with energies

$$E_{T, \gamma} = E_{\gamma}^E(0) |_{T>0 \text{ K}}. \quad (2.4.6)$$

The average energy $\langle E_T \rangle$ of the ensemble of equilibrium thermal states $E_{T, \gamma}$ is larger than E_0 because of thermal fluctuation energy.

The fluorescence response function at a nonzero temperature ($T > 0$ K), following from Eq. (2.4.4), can be expressed as

$$S_{\text{fl}}(t) |_{T>0 \text{ K}} = \left\langle \langle \Psi_{E_T}^E | \hat{\mathcal{V}}_E^\dagger(t) \hat{\mu}_+ \hat{\mathcal{V}}_G(t) \hat{\mu}_- | \Psi_{E_T}^E \rangle \right\rangle, \quad (2.4.7)$$

and is obtained by averaging over an ensemble of equilibrium thermal states of Eq. (2.4.5).

In order to generate $\Psi_{E_T, \gamma}^E$ states, we impose energy fluctuations of vibrational modes to the equilibrium state $\Psi_{E_0}^E$. Energy fluctuations are introduced by applying perturbations $\delta\lambda_{kq}$ to CS displacements of the $\Psi_{E_0}^E$ state, while keeping all other ansatz parameters fixed. Our objective is to find states $\Psi_{E_T, \gamma}^E$, which have energies equal to

$$E_{T, \gamma} \simeq E_0 + \delta E_{\gamma}, \quad (2.4.8)$$

where the perturbation energy in terms of CS displacements is

$$\delta E_{\gamma} = \sum_{k, q} \omega_{kq} |\delta\lambda_{kq}|^2. \quad (2.4.9)$$

Necessary CS displacements are obtained by repeatedly sampling the Glauber-Sudarshan distribution of Eq. (1.5.1) until the energy equality of Eq. (2.4.8) is satisfied within precision of 0.1 cm^{-1} . If the QHO frequency shift is assumed, as discussed in Section (1.1.1), the frequencies in Eq. (2.4.9) should be substituted with frequencies in the excited state $\omega_{kq} \rightarrow \omega_{kq}^e$.

2.4.2 Absorption and fluorescence spectra with frequency shifts

In this section we will investigate the ability of three ansätze with increasing sophistication, namely the D_2 , sqD_2 and mD_2 , to account for the effects of vibrational mode frequency shift upon excitation of a molecular aggregate.

Consider a single molecule (monomer) with an intramolecular vibrational mode of frequency $\omega^g = 1000 \text{ cm}^{-1}$ in the ground state. In the excited state, frequency becomes $\omega^e = \omega^g + \Delta\omega$ and HR factor $S = 1$. In Figs. (2.4.1a, b) we present the simulated absorption spectra using the D_2 , sqD_2 and mD_2 ansätze with frequency shifts $\Delta\omega$ equal to -250 cm^{-1} and 0 cm^{-1} .

When $\Delta\omega = 0$, all three ansätze produce identical spectra. However, when $\Delta\omega = -250 \text{ cm}^{-1}$, spectra simulated using the D_2 , sqD_2 ansätze have negative intensities at frequencies of $\approx 2250 \text{ cm}^{-1}$, indicating their inability to fully capture the effects induced by the frequency shift. In contrast, the mD_2 ansatz produce a strictly positive spectrum. By examining the absorption peak progression intensities in Fig. (2.4.1a), we find that frequency shift changes absorption peak frequencies (direction of change are indicated by arrows), which effectively decreases the vibrational mode HR factor when $\Delta\omega < 0$ and increases it when $\Delta\omega > 0$ (not shown).

In Figs. (2.4.1c, d) we plot absorption spectra of a dimer consisting of two monomers with an electronic coupling $J_{12} = -500 \text{ cm}^{-1}$ between them. When the frequency shift is $\Delta\omega = 0$, we find a mismatch between spectra simulated using the D_2 , sqD_2 ansätze and the mD_2 ansatz. This indicates that the former two ansätze are unable to accurately represent electron-vibrational states induced solely by the electronic coupling. The mD_2 spectrum has an absorption line shape dominated by the exchange narrowing effect¹²¹, which reduces HR factor compared to the monomer in Fig. (2.4.1b). The D_2 , sqD_2 ansätze spectra reproduce the exchange narrowing effect, but have additional secondary peaks not present in the mD_2 spectrum. Similar observations can be drawn by examining spectra with $\Delta\omega = -250 \text{ cm}^{-1}$. However, in this case, the D_2 and sqD_2 ansätze produce spectra without negative intensities.

Now, in Figs. (2.4.1e, f) we present fluorescence spectra of the dimer. When

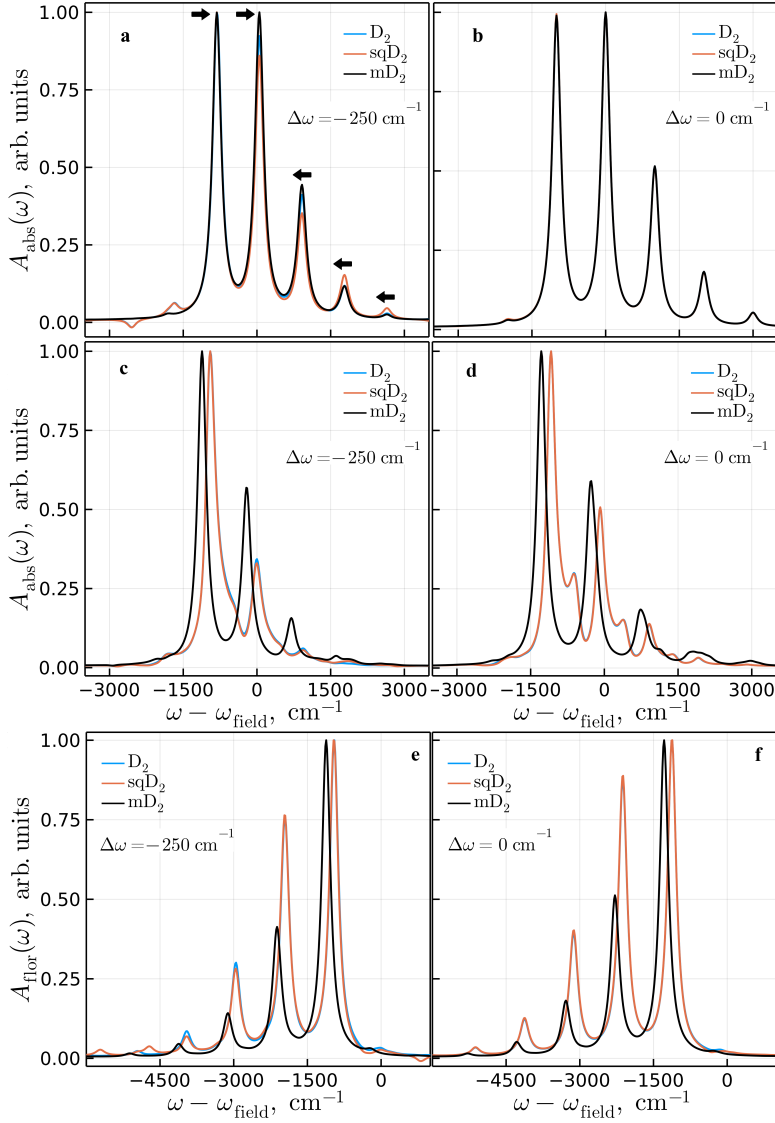


Figure 2.4.1: Absorption spectra of (a, b) a monomer, as well as (c, d) absorption and (e, f) fluorescence spectra of the dimer with frequency shifts $\Delta\omega$ simulated using the D_2 , $\text{sq}D_2$ and mD_2 ansätze. For the mD_2 ansatz, the depth is $M = 5$. Arrows indicate the direction of the peak frequency shift compared to the case where $\Delta\omega = 0$.

Table 2.1: Energy E_0 of the equilibrium state $\Psi_{E_0}^E$ of the dimer model deduced using the numerical minimization approach with the D_2 , $\text{sq}D_2$ and $\text{m}D_2$ ansätze. The depth of the $\text{m}D_2$ is $M = 5$. The values are in units of cm^{-1} .

$\Delta\omega$	D_2	$\text{sq}D_2$	$\text{m}D_2$
-250	-956.3	-959.9	-1119.2
0	-1125.0	-1125.0	-1284.7

$\Delta\omega = 0$, the D_2 and $\text{sq}D_2$ ansätze yield identical spectra, but differ from the spectrum obtained with the $\text{m}D_2$ ansatz in both the fluorescence peak intensities and frequencies. We have already seen that the D_2 and $\text{sq}D_2$ ansätze are unable to reproduce spectral features of absorption spectra of both the electronic coupling and the quadratic electron-vibrational coupling. Additional discrepancies are revealed by examining the lowest energy equilibrium state energy, E_0 , given in Table (2.1), as described in Section (2.4.1).

When frequency shifts are absent ($\Delta\omega = 0$), the D_2 and $\text{sq}D_2$ ansätze can represent the equilibrium state with an energy of -1125.0 cm^{-1} , while the $\text{m}D_2$ ansatz represent a state with energy equal to -1284.7 cm^{-1} . This equilibrium state energy difference explains the observed shift in energies between peaks simulated using the three ansätze in both the absorption and fluorescence spectra. When $\Delta\omega = -250 \text{ cm}^{-1}$, the $\text{sq}D_2$ ansatz manages to represent a slightly lower energy equilibrium state, compared to the D_2 ansatz, showing that additional DOFs provided by squeezing of CSs can capture some aspects of the quadratic electron-vibrational coupling. However, it still is unable to adequately account for the electronic coupling between molecules.

2.4.3 Fluorescence spectra temperature dependence

In the previous section, we examined the effects of frequency shift on high frequency intramolecular modes. In this section, we investigate its effects on an overdamped phonon mode bath, which is described by the Drude spectral density function, $C_n''(\omega) = \omega^3 / (\omega^2 + \gamma^2)$ with the damping constant $\gamma = 100 \text{ cm}^{-1}$. The electronic molecular coupling is $J_{12} = -50 \text{ cm}^{-1}$. Each local bath QHO frequencies ω_{nq}^g span from the 0.1 cm^{-1} to 490.1 cm^{-1} with a step-size of 10 cm^{-1} . Reorganization energies are $\Lambda_n = 100 \text{ cm}^{-1}$. We will compare the simulated absorption and fluorescence spectra in two cases: when the QHO frequencies in the molecular excited state remain unchanged ($\omega_{nq}^e = \omega_{nq}^g$) and when frequencies are reduced by 5% ($\omega_{nq}^e = 0.95 \cdot \omega_{nq}^g$).

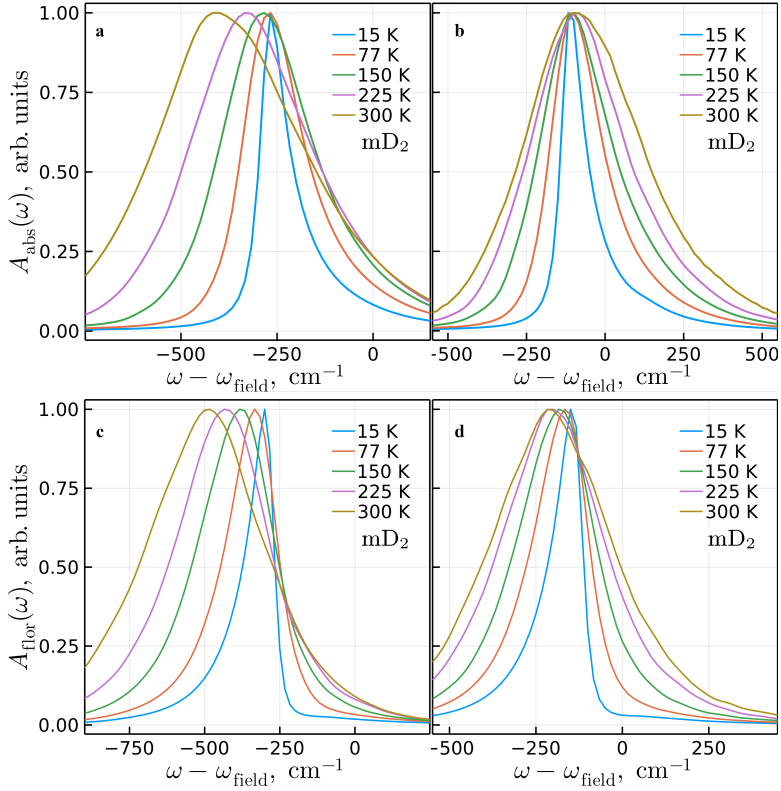


Figure 2.4.2: The simulated absorption and fluorescence spectra of a J-type dimer coupled to the overdamped phonon bath with frequencies of vibrational modes in molecular excited states, ω_{nq}^e , being equal to (a, c) $0.95 \cdot \omega_{nq}^g$ and (b, d) ω_{nq}^g . Spectra with various bath temperatures are shown. The mD_2 ansatz is used with depth of $M = 5$.

As shown in the Article [A4], the simulated spectra of this model are qualitatively equivalent regardless of the ansatz used. This holds true for both the absorption and fluorescence spectra. Therefore, we examine the absorption and fluorescence spectra simulated only using the mD₂ ansatz shown in Fig. (2.4.2). Spectra are simulated for both frequency shift cases and at various temperatures. We observe effects of spectral broadening with increasing temperature, as well as two types of spectral shifts when $\omega_{nq}^e = 0.95 \cdot \omega_{nq}^g$: a static shift which affects the whole spectrum by shifting it to lower energies, and a temperature-dependent fluorescence peak shift. In addition to these, the fluorescence peak also drifts to lower energies with increasing temperature, even when the frequency shift is excluded ($\omega_{nq}^e = \omega_{nq}^g$).

2.4.4 Main outcomes of the Article [A4]

We proposed a numerical optimization-based approach to determine equilibrium states of excited molecular systems, which are necessary for simulating fluorescence spectra. Using the D₂, sqD₂ and the mD₂ ansätze, we simulated the absorption and fluorescence spectra of a J-type molecular dimer.

We found that neither the D₂ ansatz nor the sqD₂ ansatz can accurately reproduce the absorption and fluorescence spectra of the dimer with high frequency intramolecular vibrational modes, not even when vibrational frequencies are the same in the ground and excited states. For a J-type dimer coupled to an overdamped phonon bath, the simulated absorption and fluorescence spectra are qualitatively equivalent regardless of the ansatz used.

The energy gap observed between the peaks in the spectra simulated using the D₂, sqD₂ and the mD₂ can be explained by the ability of the mD₂ ansatz to represent the lowest energy equilibrium state of the model. While the sqD₂ ansatz captures some changes in the equilibrium state induced by the quadratic electron-vibrational coupling, both the sqD₂ and D₂ fail to account for changes due to the electronic coupling between molecules.

3 THERMALIZATION OF SYSTEM-BATH MODEL

An important aspect of modelling a constant temperature thermostat as a collection of QHOs is its heat capacity. Ideally, the energy required to significantly raise the temperature of the bath QHOs, which are in resonant with the system states, should be much greater than the energy of the electronic and thermal excitations in the system. Otherwise, the in-resonant QHOs can become highly excited¹²⁷, which changes its temperature⁷⁴. This, in turn, can result in artificially broadened spectra, changes to excitation relaxation rates and other associated effects. This is particularly important for simulations at low temperature because it takes relatively small amount of energy to rapidly increase temperature of QHOs⁷⁴. In Nature, the thermal energy from hot vibrational modes redistributes among all DOFs of the physical system. However, in majority of SB models, QHOs of the bath are considered as independent normal modes. Consequently, no direct energy exchange between vibrational modes of the bath is possible. In most cases, the bath heating effects are undesirable as the bath is supposed to represent a constant temperature thermostat.

Therefore, in this chapter we propose a numerical thermalization algorithm, which address this shortcomings in Section (3.1), we formulate a thermalization algorithm for the D_2 ansatz. Then in Section (3.1.1) we examine its ability to dynamically control the temperature of a single QHO, while in Section (3.1.2) we apply it to a molecular trimer model and investigate thermalization effects on excitonic relaxation dynamics. The thermalization algorithm for the D_2 ansatz is not straightforwardly applicable to the more accurate mD_2 , therefore, in Section (3.2) we extend the thermalization algorithm to be used with the mD_2 ansatz. Thermalization effects on excitonic relaxation dynamics using the mD_2 ansatz is examined in Section (3.2.1). Lastly, in Section (3.2.2) we demonstrate how the presented thermalization algorithms can be used to generate the equilibrium states of excited molecular aggregates, which are necessary for simulation of fluorescence spectra.

3.1 Thermalization algorithm for the D_2 ansatz

To thermalize the bath, we extend the standard SB model by introducing a secondary bath. We will refer to local baths as being primary baths. The secondary bath is treated implicitly, meaning that its effective heat capacity is infinite, therefore it maintains a constant temperature T_∞ , which can be different from the initial temperature of the primary bath. The primary baths interact with the secondary bath through stochastic scattering events, or quantum jumps^{128,129}, which changes kinetic energies of vibrational modes of the primary baths.

The scattering statistics follows a Poisson distribution

$$P_{kq}(\theta, \tau_{\text{sc}}) = \frac{1}{\theta!} (\tau_{\text{sc}} \nu_{kq})^\theta e^{-\tau_{\text{sc}} \nu_{kq}}, \quad (3.1.1)$$

which describe the probability of observing θ scattering events per time interval τ_{sc} with the individual scattering rate ν_{mq} . Numerically, Poisson statistics are realised by simulating Bernoulli processes^{130,131} in the limit of $\tau_{\text{sc}} \rightarrow 0$, while maintaining condition that $\nu_{mq} \tau_{\text{sc}} \ll 1$. To simulate the scattering events, we divide wavefunction propagation into equal time length τ_{sc} intervals

$$t_i = (i\tau_{\text{sc}}, (i+1)\tau_{\text{sc}}], \quad i = 0, 1, \dots \quad (3.1.2)$$

At the end of each interval, for every mode in the primary bath, we flip a biased coin with the probability $\nu_{mq} \tau$ of landing heads. If the coin lands heads, we change the momentum of the vibrational mode. Otherwise, no changes are made.

The CS displacement can be defined in terms of the QHO's average coordinate x_{kq} and momentum p_{kq} as

$$\lambda_{kq}(t) = \frac{1}{\sqrt{2}} (x_{kq}(t) + ip_{kq}(t)). \quad (3.1.3)$$

Therefore, if the coin lands heads, we change momentum of the scattered mode in Eq. (3.1.3) with

$$p_{kq}(t) = \langle \lambda_{kq}^{\mathcal{P}} | \hat{p}_{kq} | \lambda_{kq}^{\mathcal{P}} \rangle = \sqrt{2} \text{Im} (\lambda_{kq}^{\mathcal{P}}(t)), \quad (3.1.4)$$

where $|\lambda_{kq}^{\mathcal{P}}\rangle$ is a CS sampled from the Glauber-Sudarshan distribution of Eq. (1.5.1), and

$$\hat{p}_{kq} = \frac{i}{\sqrt{2}} (\hat{b}_{kq}^\dagger - \hat{b}_{kq}), \quad (3.1.5)$$

is the momentum operator. Sampling the Glauber-Sudarshan distribution for a vibrational mode state in the excited electronic state is an approximation since the vibrational modes in the excited state are not independent. The actual thermal equilibrium distribution should also take into account the coupling between the system and the bath.

The converged thermalization statistics are obtained by applying the thermalization algorithm to every trajectory of the thermal ensemble. To prepare for the simulation, a list of scattering times, at which the numerical simulation must be paused to perform scatterings, can be precomputed prior to starting the simulation by drawing probabilities for all time intervals t_i .

3.1.1 Time evolution of the thermalized primary bath

To understand how the proposed thermalization algorithm changes the temperature of the primary bath over time, we will first apply thermalization to a monomer coupled to the bath. This will allow us to study dynamics of the primary bath without complications resulting from excitation relaxation, which will be examined in the next Section (3.1.2).

The primary bath consists of $Q = 750$ vibrational modes with frequencies, $\omega_{kq} = 0.01 + (q - 1) \Delta\omega$, where step-size $\Delta\omega = 1 \text{ cm}^{-1}$. The initial primary bath temperature is $T(0) = 300 \text{ K}$ and, for demonstration purposes, we set the constant temperature of the secondary bath below the temperature of the primary bath, at $T_\infty = 200 \text{ K}$. To characterize the bath fluctuations, the super-Ohmic spectral density function $C''(\omega) = \omega^2/\omega_c \exp(-\omega/\omega_c)$ with $\omega_c = 100 \text{ cm}^{-1}$ is used. The reorganization energy is $\Lambda_k = 100 \text{ cm}^{-1}$. We consider scattering rates of all modes to be equal $\nu_{mq} \rightarrow \nu$ and set the scattering step-size to $\tau_{sc} = 0.01 \text{ ps}^{-1}$.

The transient temperature of the primary bath can be estimated⁷⁴ by computing the average kinetic energy of QHOs, given by

$$\langle K_{kq}(t, \epsilon) \rangle = \frac{1}{\epsilon} \int_0^\epsilon ds \frac{\omega_{kq}}{2} \langle \langle \Psi(t+s) | \hat{p}_{kq}^2 | \Psi(t+s) \rangle \rangle, \quad (3.1.6)$$

over some time resolution interval, ϵ , where \hat{p}_{kq} is the momentum operator of Eq. (3.1.5). The transient temperature of the primary bath is then equal to

$$T_k(t) = \frac{1}{k_B Q} \sum_q^Q \omega_{kq} \ln^{-1} \left(1 + \frac{\omega_{kq}}{2 \langle K_{kq}(t, \epsilon) \rangle} \right). \quad (3.1.7)$$

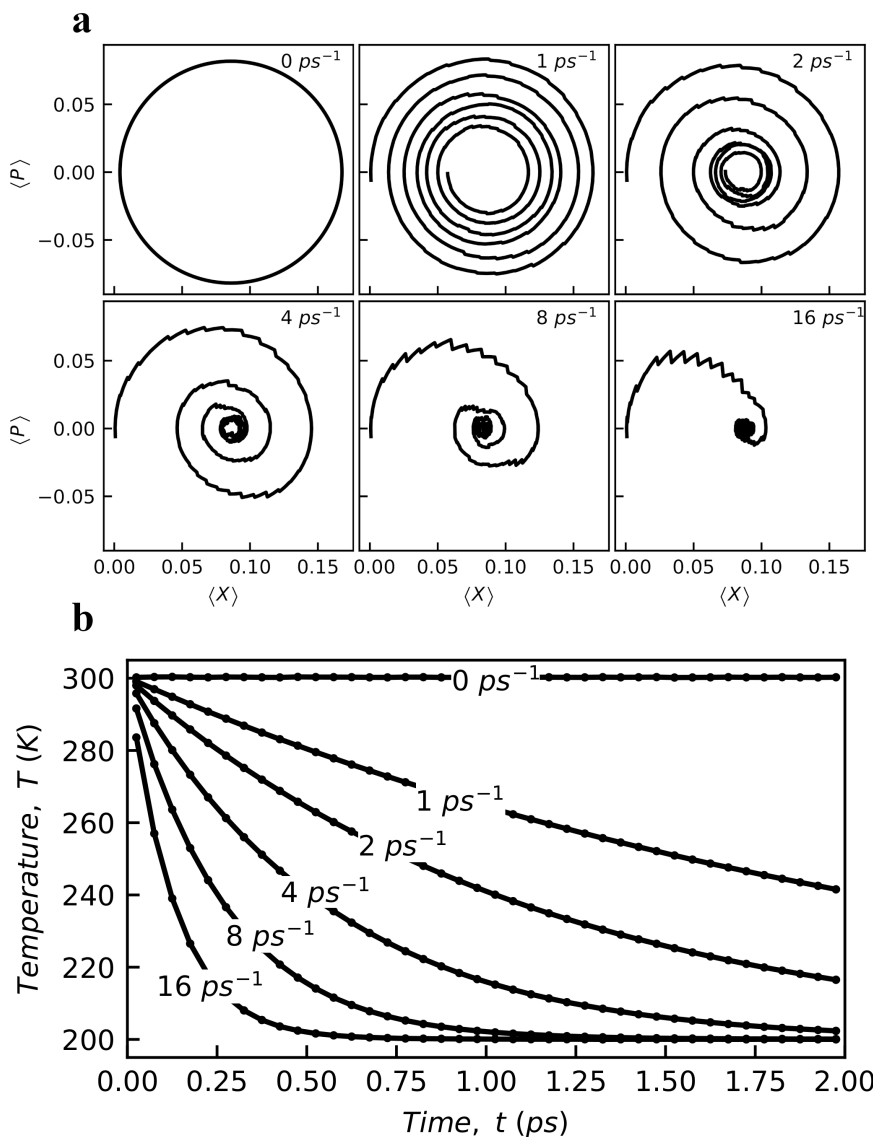


Figure 3.1.1: (a) The average trajectory in the coordinate-momentum phase space of QHO with a frequency of $\omega = 100 \text{ cm}^{-1}$ and (b) the primary bath temperature $T(t)$ with various scattering rates ν . The scattering step-size is $\tau_{\text{sc}} = 0.01 \text{ ps}$, the transient temperature resolution is $\epsilon = 50 \text{ fs}$. The thermal ensemble consisted of 5000 trajectories.

In Fig. (3.1.1), we show the time evolution of the average trajectory of the QHO with frequency $\omega = 100 \text{ cm}^{-1}$ in its coordinate-momentum phase space, given by

$$(x(t), p(t)) = \sqrt{2} (\langle \text{Re} \lambda(t) \rangle, \langle \text{Im} \lambda(t) \rangle), \quad (3.1.8)$$

as well as the average temperature of the entire primary bath $T(t)$. These bath properties were simulated with various scattering rates, ν . We find that in the absence of thermalization, the QHO evolves along a closed trajectory around the shifted potential minimum point, $x^{\text{min}} \approx 0.09$, and the temperature of the primary bath remains unchanged. Once the thermalization algorithm is applied, we find that the trajectory of QHO tends towards the stationary point in the coordinate-momentum space. The average coordinate evolves towards the potential minimum point, while the average momentum approaches zero. The rate of relaxation can be adjusted by changing the scattering rate. The loss of QHO's kinetic energy is reflected in the decay of the primary bath temperature. It gradually tends towards the temperature of the secondary bath $T_{\infty} = 200 \text{ K}$.

3.1.2 Thermalized excitation relaxation using the \mathbf{D}_2 ansatz

Let us now examine the impact of the thermalization on electronic excitation relaxation dynamics. We will consider the linear trimer model, which consists of three coupled molecules with excited state energies $\varepsilon_{1\dots 3}$ equal to 0, 250 and 500 cm^{-1} and the nearest neighbour couplings set to $J_{1,2} = J_{2,3} = 100 \text{ cm}^{-1}$ with the boundary condition $J_{3,1} = 0$. This setup results in an energy funnel configuration of excited electronic states. The molecular electronic dipole moment vectors in the Cartesian coordinate system are $\boldsymbol{\mu}_n = (1, 0, 0)$, which classifies the trimer as an H-type molecular aggregate¹²¹.

Each molecule interact with its own primary bath, described by the same parameters as previous in the Section (3.1.1); the only difference is the bath discretization step size $\Delta\omega$. We consider three bath models: the dense bath model, where the spectral density function $C''(\omega)$ is discretized into $Q = 75$ oscillators per primary bath with step size of $\Delta\omega = 10 \text{ cm}^{-1}$; the sparse bath model, where the number of modes is reduced to just $Q = 15$ per bath with $\Delta\omega = 50 \text{ cm}^{-1}$; and the sparse bath with thermalization model, where the $C''(\omega)$ is discretized according to the sparse bath model, and thermalization is used. The initial temperature of the primary baths now is $T_k(0) = 77 \text{ K}$.

In the absence of the bath, the system has three single-excitation stationary excitonic states with energies: $\varepsilon_1^{\text{exc}} \approx -37.23 \text{ cm}^{-1}$, $\varepsilon_2^{\text{exc}} = 250 \text{ cm}^{-1}$,

$\varepsilon_3^{\text{exc}} \approx 537.23 \text{ cm}^{-1}$. We denote the probability of finding aggregate in its n -th excitonic state as $\rho_n^{\text{exc}}(t)$, also known as the population. In terms of the D_2 ansatz free parameters, the excitonic state populations are given by

$$\rho_n^{\text{exc}}(t) = \sum_{k,l} (\Phi_k^{\text{exc}})_n^* \langle \alpha_k^*(t) \alpha_l(t) \rangle (\Phi_l^{\text{exc}})_n, \quad (3.1.9)$$

where Φ_k^{exc} are the excitonic eigenstates, see Eq. (1.1.9). The initial excitonic state populations correspond to the optically excited highest energy state: $\rho_3^{\text{exc}}(0) = 1, \rho_{1,2}^{\text{exc}}(0) = 0$.

Fig. (3.1.2) shows population dynamics of excitonic state and temperatures of primary baths in the trimer considered with the three different bath models. The fluctuations of QHOs in the primary baths induces dephasing between excitonic states, which causes population relaxation to be irreversible^{102,84}. Consequently, exciton populations sequentially relax to lower energy exciton states until reaching the lowest energy state^{132–134}. Most of the excitation energy is transferred to vibrational modes of primary baths.

In the case of the dense bath model, the excitation almost entirely relaxes into the lowest energy excitonic state. Whereas, in the case of the sparse bath model, the final population distribution is significantly different from that of the dense bath model. The origin of this discrepancy is two-fold. Firstly, the bath recursion time¹³⁵ $t_{\text{rec}} = 2\pi/\Delta\omega$ for the sparse bath model is shorter than the considered propagation time $t_{\text{rec}} < 2 \text{ ps}$. At the time of t_{rec} QHOs of the primary bath artificially synchronize into the initial state of the bath, which negatively affect system dynamics. Secondly, the temperature of the primary baths in the sparse bath model increases significantly more because heat capacity of the sparse bath is lower. The initial rapid rise in temperature can be attributed to QHOs' reorganization in the excited states of the trimer, while the subsequent slow rise is caused by the energy transfer from the system to the primary baths. Both of these problems are addressed in the model of the sparse bath with thermalization of scattering rate $\nu_{kq} = 1 \text{ ps}^{-1}$.

By looking at Fig. (3.1.2E), we find that population dynamics of the excitonic states and the population distribution of the equilibrium state at long times become quantitatively comparable to the population distribution of the dense bath model. Due to the stochastic nature of the QHOs dynamics when thermalization is applied, the bath recursion time effectively becomes infinite if the scattering rate is sufficiently high. Furthermore, the initial rise in bath temperatures is now lower and continuously reduces.

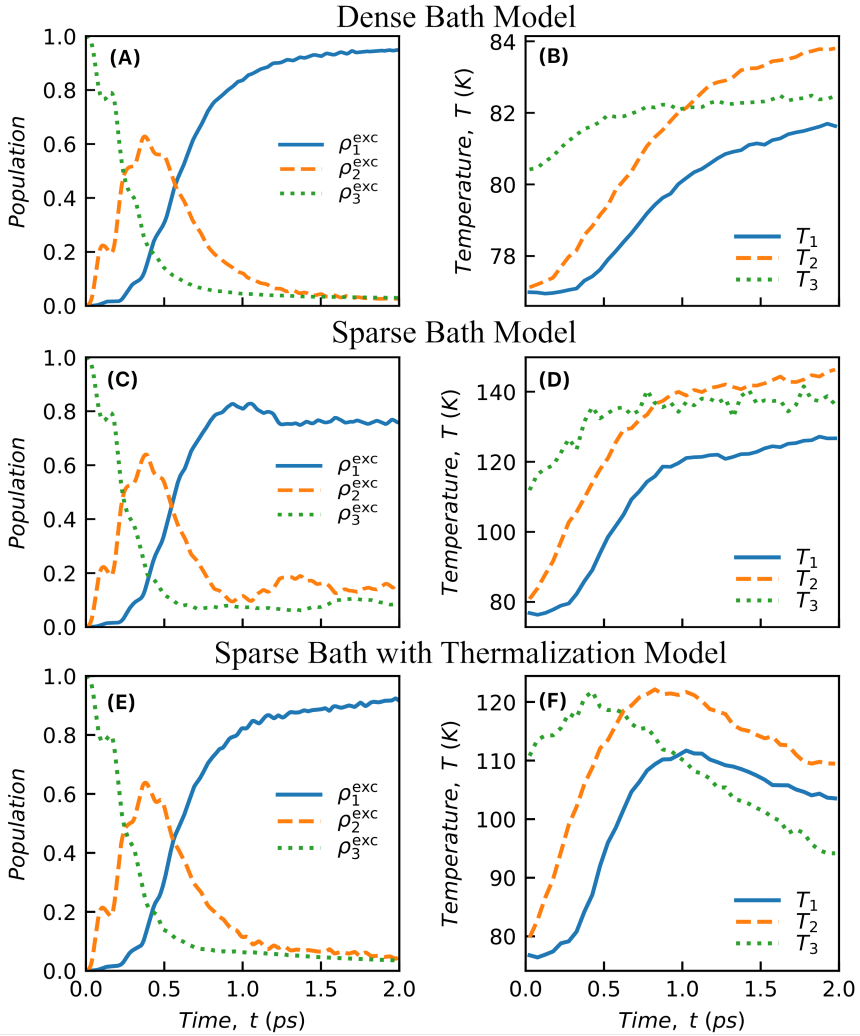


Figure 3.1.2: The trimer model exciton state populations $\rho_n^{\text{exc}}(t)$ and temperatures $T_k(t)$ of the primary baths of (a, b) the dense bath model, (c, d) the sparse bath model and of (e, f) the sparse bath model with thermalization.

3.1.3 Main outcomes of the Article [A5]

We proposed a thermalization algorithm to be used in conjunction with the D_2 ansatz. It performs stochastic scattering events during the time evolution of the ansatz, which changes its free parameters. This approach enables us to control the temperature of the model by dynamically steering vibrational modes towards their canonical thermal equilibrium of the desired temperature.

We applied thermalization to the simulation of the excitation relaxation dynamics of the molecular trimer and demonstrated that we are able to significantly reduce the required number of vibrational modes in the bath and resolve the associated problems stemming from the usage of low number of vibrational modes.

3.2 Thermalization algorithm for the mD₂ ansatz

In our thermalization approach, we sample the new state of a scattered mode from the Glauber-Sudarshan distribution in Eq. (1.5.1). The sampled states have Gaussian wavepackets and can be exactly represented by a single CS. The fact that the D₂ ansatz is only able to represent Gaussian wavepackets makes changing states of QHOs straightforward.

Meanwhile, wavepackets of the mD₂ ansatz are not limited to Gaussians. Therefore, it becomes almost impossible to represent the newly sampled Gaussian state of the scattered mode without simultaneously altering the properties of all the non-scattered modes. This is because any property of vibrational mode is a complex function of all free parameters of the mD₂ ansatz, e.g., see Eqs. (3.2.5), (3.2.6) for the average coordinate and momentum of a QHO. To adapt the thermalization algorithm of the D₂ ansatz for the mD₂ ansatz, several modifications are required.

Whenever a scatterings event occurs, we project the mD₂ ansatz into the D₂ ansatz form and only then modify the states of the scattered modes. This follows the concept of decoherence¹³⁶, where the macroscopic environment interacts with the quantum system and causes the wavefunction to collapse into a set of preferred states. In our case, the preferred states are defined by the D₂ ansatz. Afterwards, the wavefunction is projected back into the mD₂ ansatz form, and the time evolution of the model is continued.

The projection operation is defined as follows. Let us assume that the state of the SB model at the time of a scattering event is given by the mD₂ ansatz with amplitudes $\alpha_{i,n}(t)$ and CS $|\lambda_i(t)\rangle$. The target projected D₂ ansatz is defined as

$$|\psi(t)\rangle = \sum_n^N \beta_n(t) |n\rangle \otimes |\tilde{\lambda}(t)\rangle, \quad (3.2.1)$$

where β_n are the projected complex amplitudes and $|\tilde{\lambda}(t)\rangle$ is the projected multi-dimensional CS.

The projected complex amplitudes are equal to

$$\beta_n(t) = \sum_i^M \alpha_{i,n}(t) \langle \tilde{\lambda}(t) | \lambda_i(t) \rangle, \quad (3.2.2)$$

and the projected multi-dimensional CS is defined as

$$|\tilde{\lambda}(t)\rangle = \exp \sum_{k,q}^{N,Q} \left(\tilde{\lambda}_{kq}(t) \hat{b}_{kq}^\dagger - \tilde{\lambda}_{kq}^*(t) \hat{b}_{kq} \right) |0\rangle_{\text{vib}}. \quad (3.2.3)$$

It is expressed in terms of complex CS displacements

$$\tilde{\lambda}_{kq}(t) = \frac{1}{\sqrt{2}} (x_{kq}(t) + ip_{kq}(t)), \quad (3.2.4)$$

where $x_{kq}(t)$ and $p_{kq}(t)$ are the coordinate and momentum averages of QHO:

$$x_{kq} = \frac{1}{\sqrt{2}} \sum_{i,j,n}^{M,M,N} \alpha_{i,n}^* \alpha_{j,n} \langle \lambda_i | \lambda_j \rangle \sum_{k,q}^{N,Q} (\lambda_{i,kq}^* + \lambda_{j,kq}), \quad (3.2.5)$$

$$p_{kq} = \frac{i}{\sqrt{2}} \sum_{i,j,n}^{M,M,N} \alpha_{i,n}^* \alpha_{j,n} \langle \lambda_i | \lambda_j \rangle \sum_{k,q}^{N,Q} (\lambda_{i,kq}^* - \lambda_{j,kq}). \quad (3.2.6)$$

$\langle \lambda_i | \lambda_j \rangle$ is the overlap of two CS and is given by Eq. (1.3.30).

Once the projected state $\psi(t)$ is determined, we modify the scattered QHOs by setting their momenta in Eq. (3.2.4) to

$$p_{kq}(t) = \sqrt{2} \text{Im} \left(\tilde{\lambda}_{kq}^{\mathcal{P}} \right), \quad (3.2.7)$$

where $|\tilde{\lambda}_{kq}^{\mathcal{P}}\rangle$ is a CS sampled from the Glauber-Sudarshan distribution of Eq. (1.5.1). The coordinates x_{kq} of both the scattered and non-scattered modes remain unchanged.

Now, we project the D_2 ansatz back into the mD_2 ansatz form, given by Eq. (1.3.21). We do it by setting amplitudes and CS displacements of the first ($i = 1$) populated multiple as:

$$\alpha_{1,n}(t) = \beta_n(t), \quad (3.2.8)$$

$$\lambda_{1,kq}(t) = \tilde{\lambda}_{kq}(t), \quad (3.2.9)$$

while amplitudes of the unpopulated multiples are set to

$$\alpha_{j=2,\dots,M,n}(t) = 0. \quad (3.2.10)$$

The CS displacements of the unpopulated multiples ($j = 2, \dots, M$) are positioned in a layered hexagonal pattern around the CS displacements of the pop-

ulated multiple, given by Eq. (1.6.12). Once the mD_2 ansatz is computed, the scattering event is concluded, and the time evolution of the ansatz is continued until the next scattering event.

A few comments are in order. The projection operation should not occur too frequently because it takes time for the mD_2 ansatz, after the scattering event, to become once again correlated between its many multiples. If the projection is performed too frequently, the initially unpopulated multiples ($j = 2, \dots, M$) will not have enough time to contribute to the dynamics of the model. In such case, the mD_2 ansatz would essentially behave like the D_2 ansatz, just with a more complex definition. The average interval between projection operations depends on the scattering rate, see Eq. (3.1.1).

To reduce the rate of projections in the thermalization algorithm of the mD_2 ansatz, we adopt a coarse scattering approximation. Instead of considering the scattering probabilities of individual oscillators ν_{kq} as was the case for the D_2 ansatz, we now consider events where all QHOs of certain local baths are scattered simultaneously. In other words, the scattering events become vibrational mode independent, and the scattering rates now are $\nu_{kq} \rightarrow \nu_k$. This coarser approach requires a single projection operation to scatter multiple oscillators at once, enabling us to consider lower scattering rates and increase the time to the next scattering even of the model. As we will see, this approximation allows the mD_2 ansatz to continue utilizing all its multiples to maintain the superior accuracy over the D_2 ansatz, while simultaneously to benefit from the thermalization process.

While the projection from the mD_2 ansatz into the D_2 ansatz may be considered crude, resulting in an oversimplified wavefunction, it is important to note that this projection exactly preserves the values of average coordinates and momenta of the QHOs, while affecting only the variance and higher-order moments of canonical variables. However, the majority of SB models rely primarily on the linear coupling between the system and the average coordinates of QHOs, which are maintained exactly during the projection. As a result, the expected discrepancy introduced by the infrequent projection on the dynamics of the model should be minimal. The higher-order couplings become necessary when anharmonic vibrational modes or changes to their frequencies upon excitation^{60,62}.

3.2.1 Thermalized excitation relaxation using the mD₂ ansatz

In this section, we will repeat examination of the thermalization algorithm effects on the excitation dynamics of the trimer model presented in Section (3.1.2). This time the mD₂ ansatz with a depth of $M = 5$ will be used.

In Fig. (3.2.1), we present the exciton state populations $\rho_n^{\text{exc}}(t)$ of the trimer model along the average temperatures $T_k(t)$ of the primary baths simulated for all three bath models. The exciton state populations are expressed in terms of the mD₂ ansatz free parameters as

$$\rho_n^{\text{exc}}(t) = \sum_{k,l,i,j} (\Phi_k^{\text{exc}})_n^* \langle \alpha_{i,k}^*(t) \alpha_{j,l}(t) S_{i,j}(t) \rangle_{\text{th}} (\Phi_l^{\text{exc}})_n, \quad (3.2.11)$$

where Φ_k^{exc} are the excitonic eigenstates, see Eq. (1.1.9). The population dynamics of the dense bath model exhibit sequential relaxation, starting from the highest energy excitonic state and progressing towards the the lowest energy state via the intermediate energy state. Eventually, the population dynamics reach an equilibrium state.

When comparing the population dynamics obtained using the D₂ ansatz (shown in Fig. (3.1.2)), we find that the more precise mD₂ ansatz yields faster excitation relaxation. By examining the population and temperature dynamics of the sparse bath model, we again find the same insufficiencies as we did with the D₂ ansatz when compared to the dynamics of the dense bath model. Specifically, the population equilibrium at long propagation times become skewed, and the temperatures of the primary baths increases noticeably more. Note, that these shortcomings of the sparse bath model were not expected to be improved by using the mD₂ ansatz because the mentioned problems are induced by the insufficiently dense discretization of the bath spectral density function.

When the thermalization algorithm is applied to the simulation of the sparse bath model with the scattering rate of $\nu_k = 1.25 \text{ ps}^{-1}$, the population dynamics are restored and qualitatively match those of the dense model. Although the initial rise in temperatures of the primary baths surpasses those of the dense bath model, the thermalization algorithm gradually steers temperatures towards the initial values.

Simulating dynamics using the sparse bath model with thermalization offers a significant speed advantage when compared to the dense bath model. On average, it took 166 minutes to simulate population dynamics using the dense bath model, whereas only 1.3 minutes were required using the sparse bath model,

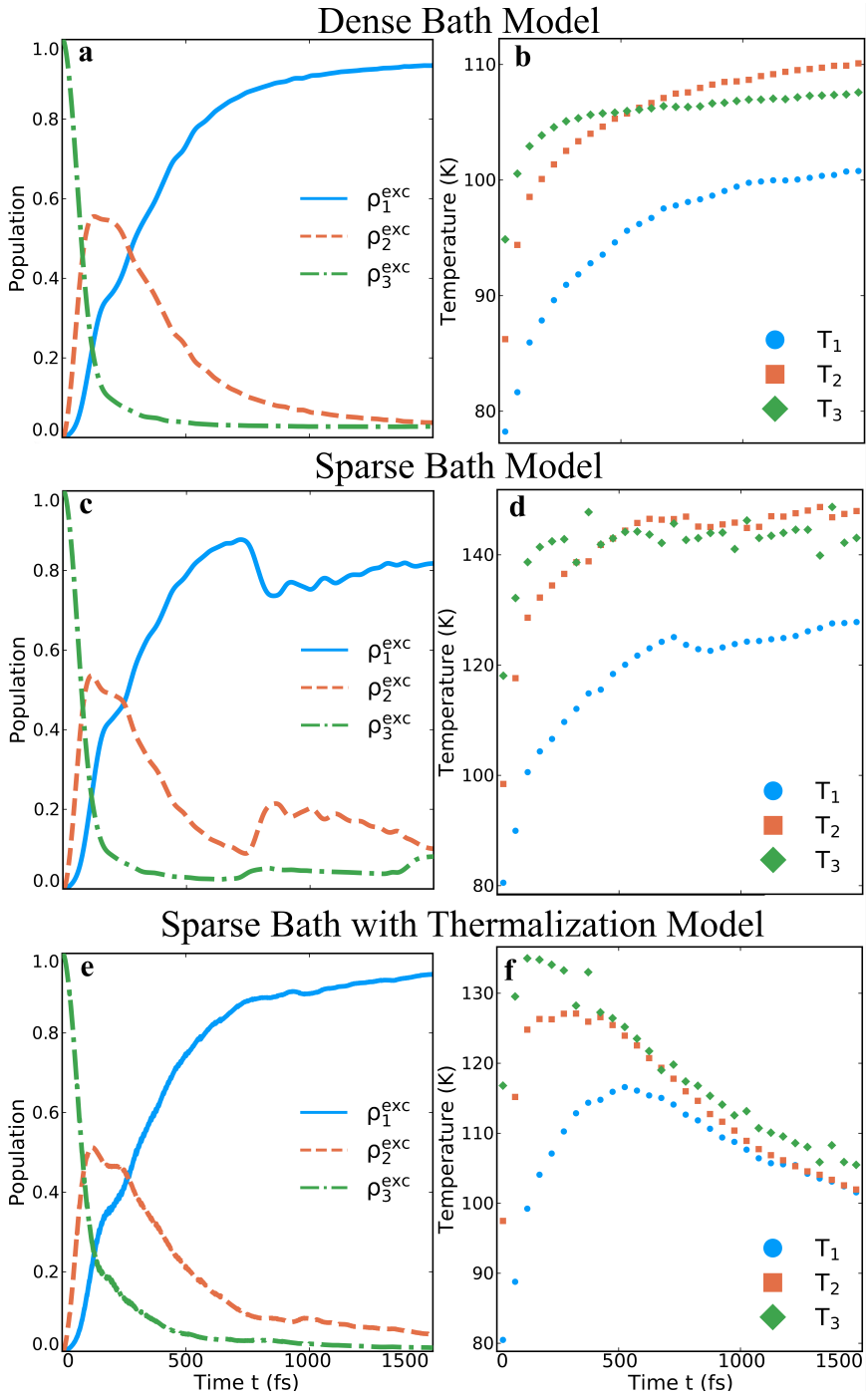


Figure 3.2.1: The exciton state populations $\rho_n^{\text{exc}}(t)$ and the average temperatures $T_k(t)$ of local baths of the trimer with (a, b) the dense bath model, (c, d) the sparse bath model and (e, f) the sparse bath model with thermalization.

and 2 minutes using the sparse bath model with thermalization. Although we see that there is a computational overhead associated with using thermalization algorithm, it is small compared to the overall reduction in simulation time when switching from the dense bath to the sparse bath model.

These significant simulation speed gains are the result of the sparse bath model taking into account 5 times fewer QHOs in each primary bath compared to the dense bath model. The reduction in the number of simulated QHOs is even more critical for the mD₂ ansatz due to the rapid scaling of the numerical cost with the increasing number of QHOs. This is because EOMs of the mD₂ ansatz constitute an implicit system of differential equations that require a more involved and expensive two-step numerical approach to find a solution^{66,67}, as discussed in Section (1.4).

3.2.2 Thermalized fluorescence spectra

In this section we will use the thermalization algorithm to find the initial thermal states $\Psi^E(0)$ of the excited SB model, which are required to simulate the fluorescence spectrum. Additionally, we will compare the obtained fluorescence spectra with those simulated using the numerical optimization approach, presented in Section (2.4.1).

As a reminder, the fluorescence response function $S_{\text{fl}}(t)$ is a special case of a more general time-resolved fluorescence response function $S_{\text{TRF}}(\tau_{\text{eq}}, t)$. It is a function of two times: the equilibration time τ_{eq} and the coherence time t . During the equilibration time, the system evolves in its excited state and, due to the SB interaction, relaxes to an equilibrium state. Afterward, during the coherence time, spontaneous emission occurs.

We will apply the thermalization during the equilibration time to encourage excitation relaxation into the lowest energy equilibrium state by removing the excess thermal energy from primary baths. We use $\hat{\mathcal{G}}_{E,\gamma}$ to denote the excited state propagator with thermalization, while $\hat{\mathcal{V}}_E$ is still the propagator without thermalization, seen in Section (1.6.2). Following from the definition of the TRF response function in Eq. (1.6.19), we define the thermalized TRF (TTRF) response function as

$$\begin{aligned} \tilde{S}_{\text{TRF}}(\tau_{\text{eq}}, t) &= \frac{1}{\Gamma} \sum_{\gamma=1}^{\Gamma} \langle \Psi_G(0) |_{\gamma} \hat{\mu}_- \hat{\mathcal{G}}_{E,\gamma}^{\dagger}(\tau_{\text{eq}}) \hat{\mathcal{V}}_G^{\dagger}(t) \hat{\mu}_+ \\ &\quad \times \hat{\mathcal{V}}_G(t) \hat{\mu}_- \hat{\mathcal{G}}_{E,\gamma}(\tau_{\text{eq}}) \hat{\mu}_+ | \Psi_G(0) \rangle_{\gamma}. \end{aligned} \quad (3.2.12)$$

By assuming that the equilibration time τ_{eq} is sufficiently long to reach the equilibrium state of the SB model, we define the fluorescence response function as

$$S_{\text{fl}}(t) = \lim_{\tau_{\text{eq}} \rightarrow \infty} S_{\text{TRF}}(\tau_{\text{eq}}, t), \quad (3.2.13)$$

and the thermalized fluorescence (TF) response function as

$$\tilde{S}_{\text{fl}}(t) = \lim_{\tau_{\text{eq}} \rightarrow \infty} \tilde{S}_{\text{TRF}}(\tau_{\text{eq}}, t). \quad (3.2.14)$$

Note that this formulation of fluorescence and TF response functions is applicable to both the thermalization algorithms of the D_2 and mD_2 ansätze, as it does not differentiate between the actual implementation of the thermalization. To determine the necessary equilibration time interval for numerical simulations, we incrementally increase τ_{eq} until the resulting fluorescence spectrum converge.

In Fig. (3.2.2) we compare the TRF and TTRF spectra with increasing equilibration times τ_{eq} and scattering rate $\nu_k = 0.1 \text{ ps}^{-1}$. When $\tau_{\text{eq}} = 0$, both the TRF and TTRF spectra are equivalent and exactly match the absorption spectrum, which consists of three peaks due to transition involving the combined excitonic-vibrational states and cannot be regarded as purely excitonic. For reference, the vertical dotted lines indicate energies E^{exc} of excitonic states. These do not match the three peak energies exactly due to the system being coupled to the environment.

By allowing equilibration to occur ($\tau_{\text{eq}} > 0$), both the TRF and TTRF spectra exhibit a shift in peak intensity towards lower energies as the excitation relaxes towards the equilibrium state. After equilibrating for $\tau_{\text{eq}} = 2 \text{ ps}$, we find that both spectra have converged and do not meaningfully change by considering longer τ_{eq} . Therefore, the TRF and TTRF spectra with $\tau_{\text{eq}} = 2 \text{ ps}$ can be considered as the fluorescence and TF spectra of the trimer model, as defined in Eqs. (3.2.13) and (3.2.14).

Both spectra exhibit the highest fluorescence intensities at the energies of the lowest excitonic-vibrational states. However, the fluorescence spectrum also shows significant intensities at energies corresponding to the intermediate and highest excitonic-vibrational states. Surprisingly, the higher energy peak is more intense than the intermediate peak, which indicates presence of excitation trapping effects. Meanwhile, the TF spectrum intensities at these energies are negligible, suggesting that thermalization allows the trimer to reach a lower energy equilibrium state, which is no longer hindered by the excess thermal

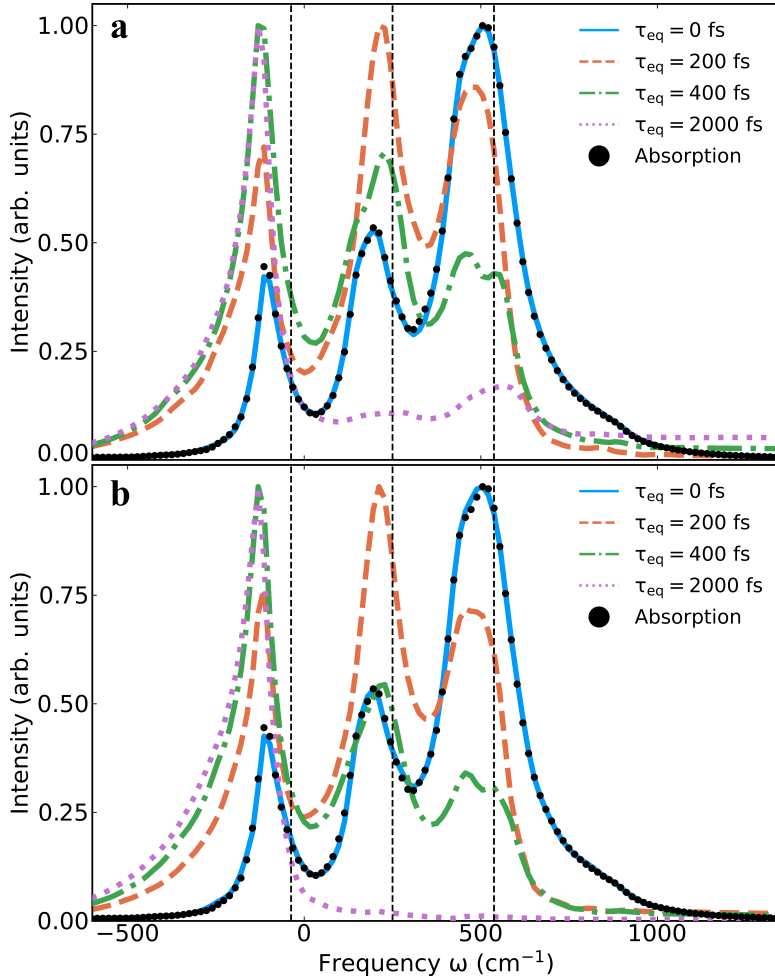


Figure 3.2.2: (a) The TRF and (b) TTRF spectra of the trimer with the dense bath model, simulated with an increasing equilibration time τ_{eq} . The absorption spectrum is also shown. Vertical dashed lines show energies E^{exc} of the excitonic states.

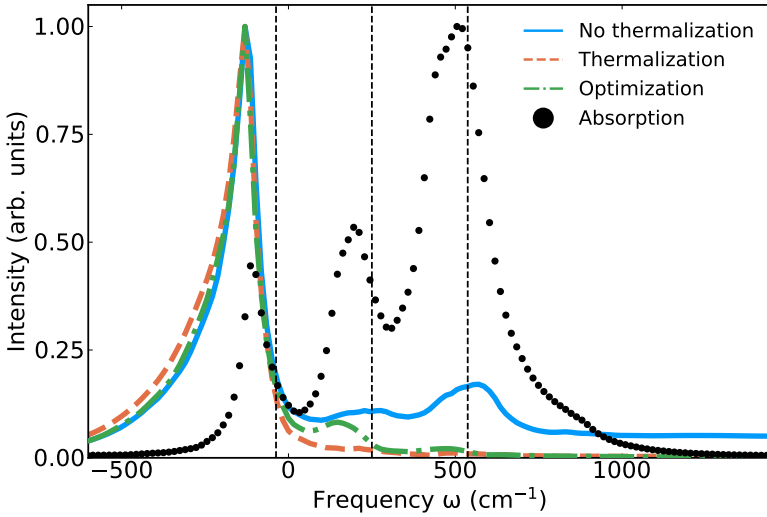


Figure 3.2.3: The fluorescence spectra comparison of the trimer with the dense bath model obtained with and without thermalization, and using the optimization approach. The absorption spectrum is also shown. Vertical dashed lines show energies E^{exc} of the excitonic states.

energy accumulation in the QHOs of primary baths.

In Fig. (3.2.3) we compare the fluorescence and TF spectra with the fluorescence spectrum simulated using a previously proposed numerical optimization approach, described in Section (2.4.1). We find that all three methods produce a similar lowest energy excitonic-vibrational peak. However, the TF spectrum has a higher intensity tail towards the low energy side, with almost no intensities present at energies of the intermediate and the highest excitonic-vibrational states. Meanwhile, the fluorescence spectrum simulated using the optimization approach show a small intensity at the energy of the intermediate excitonic-vibrational states. The spectrum with the optimization approach more closely resembles that of the TF rather than the fluorescence spectrum.

Regarding numerical efficiency of the approaches. It took an average of 79 minutes to compute a single trajectory of the TTRF response function in Eq. (3.2.12) with an equilibration time of $\tau_{\text{eq}} = 2$ ps. The numerical optimization method does not require explicit propagation of the model wavefunction during equilibration time and the optimization must be performed only once. However, it took 193 minutes to perform. Besides the fluorescence spectra differences, we found that computation of TTRF is more reliable and numerically stable. The optimization approach struggles to consistently find the lowest en-

ergy excitonic state of the model due to its heuristic nature. It requires many attempts at finding the solution and eventually having to choose the one with the lowest energy. Numerical optimization becomes particularly difficult when a wide range of QHO frequencies are considered.

For SB models without Hamiltonian parameter disorder, the optimization approach can serve as a useful starting point for fluorescence spectra simulation. However, a more accurate spectra most likely will always be obtained using the TTRF approach. On the other hand, for models with Hamiltonian disorder, such as excitation energy disorder^{137–139}, the optimization approach would require finding the lowest energy excitonic state of the model for each realization of the Hamiltonian. This would negate any advantage provided by the numerical optimization approach.

3.2.3 Main outcomes of the Article [A6]

We extended the thermalization algorithm, originally developed for the D_2 ansatz, to be used with the mD_2 ansatz. The improved algorithm relies on the preferred state and the coarse scattering approximations. They allow the mD_2 ansatz to maintain its superior accuracy over the D_2 ansatz, while benefiting from the thermalization process. The numerical cost of the mD_2 ansatz rapidly scales with the number of vibrational modes.

Therefore, we used thermalization to simulate the excitation relaxation dynamics of the molecular trimer model. We demonstrated that thermalization permits to reduce the required number of vibrational modes, which significantly lowers numerical cost of the simulation. This development opens possibilities to investigate larger SB models than was previously feasible using the mD_2 ansatz.

Furthermore, we demonstrated how the thermalization algorithm can be applied to generate equilibrium states of excited SB models, which are necessary for simulating fluorescence spectra. Compared to the numerical optimization approach, thermalization approach offers lower computation cost, improved numerical stability and accuracy.

SANTRAUKA

Įvadas

Daugelio biologinių molekulinų sistemų veikimas yra glaudžiai susijęs su energijos vyksmais jų elektroninėse ir (arba) virpesinėse būsenose. Svarbu suprasti išorinės spinduliuotės indukuotos energijos relaksacijos spartas ir kelius įvairiose molekulių dydžių skalėse – nuo pačių mažiausių, susidedančių iš vienos molekulės energetinių lygmenų¹⁻⁴, iki vidutinio dydžio molekulinų agregatų, sudarytų iš kelių sąveikaujančių molekulių⁵⁻⁸ ir didžiausių gamtoje randamų fotosintezės kompleksų⁹⁻¹³, kuriuose be energijos relaksacijos, taip pat vyksta erdvinė krūvio ir energijos pernaša, ir jie gali būti sudaryti iš dešimčių ar net šimtų molekulių.

Teoriniai modeliai, išskyrus pačių primityviausių molekulinų sistemų, neturi analitinių sprendinių. Net sąlyginai mažoms molekulinėms sistemoms, dėl didelio sąveikaujančių laisvės laipsnių skaičiaus, primityvūs skaitmeniniai metodai nėra pajėgūs išspręsti energijos relaksacijos uždavinio. Standartinis teorinis būdas spręsti šią problemą yra traktuoti molekulinę sistemą kaip atvirą kvantinę sistemą^{14,15}. Šiame aprašyme tik tie molekulių elektroniniai ir virpesiniai laisvės laipsniai, kurie dalyvauja dominančiame relaksavimo procese, sudaro stebimą sistemą, o mažiau svarbūs laisvės laipsniai yra laikomi, didesnio nei sistema, termostato dalimi – aplinka. Aplinkos fliuktuacijų intensyvumą nusako tolydi spektrinio tankio funkcija^{16,17}. Dažniausiai toks laisvės laipsnių išskyrimas į sistemą ir aplinką yra tik formalus, kadangi šios dvi dalys sąveikauja tarpusavyje.

Jei sąveikos stipris tarp sistemos ir aplinkos yra mažas, lyginant su sąveika pačioje sistemoje, tuomet galima naudoti palyginti nesudėtingus, trikdžių teorija besiremiančius, Redfildo metodus¹⁸⁻²¹. Esant atvirkščiai situacijai, kai sistemos ir aplinkos sąveika yra stipri, galima taikyti Försterio²²⁻²⁴ trikdžių teorijos metodus. Šie metodai sprendžia jungtines sistemos ir aplinkos judėjimo lygtis, galiausiai siekiant suvidurkinti aplinkos fliuktuacijų poveikį sistemai. Taip gaunamos redukuotos, tik mus dominančios sistemos, dinaminės lygtys. Šių metodų patikimumas priklauso nuo aiškios sąveikos stiprių atskirties. Jei minėtieji sąveikos stipriai yra panašaus dydžio, sistemos ir

aplinkos laikinė evoliucija nebegali būti skaičiuojama trikdžių teorijos metodais, nes energijos relaksacijos sistemoje ir energijos mainų su aplinka procesų laiko skalės tampa tapačios. Nors šį sąveikos režimą modeliuoti yra sudėtinga, buvo sukurta formaliai tikslų, tačiau skaitmeniškai brangių, metodų, pvz., taikant hierarchines judėjimo lygtis²⁵, tankio matricos renormalizavimo grupes²⁶, grandininį aplinkos vaizdavimą^{27–29}, trajektorijų integralo formulutes³⁰.

Šie metodai naudoja redukuoto tankio operatoriaus aprašymą, tačiau tam pačiam tikslui galima tiesiogiai naudoti ir pačią banginę funkciją, pvz., taikant kelių konfigūracijų nuo laiko priklausomą Hartree^{31,32}, paviršių šuoliavimo³³, kvantinių šuolių³⁴, stochastinių Schrödingerio lygčių³⁵, grynujų būsenų hierarchijų³⁶, termolauko dinamikos^{37,38} ir kt. metodus. Pagrindinė daugelio banginė funkcija besiremiančių metodų idėja yra išskleisti sistemos ir aplinkos modelio būsenas pasirinktoje būsenų bazėje. Tokie metodai puikiai tinka sąveikų stiprių režimams, kai nebegalioja trikdžių teorija, kadangi banginė funkcija išreikštai ir lygiaverčiai aprašo tiek sistemos, tiek aplinkos laisvės laipsnių būsenas. Šiuo atveju, metodo tikslumas priklauso nuo to, kaip tiksliai pasirinkta būsenų bazė gali atvaizduoti tikrines sistemos ir aplinkos modelio būsenas, arba bent jau tas būsenas, kurios labiausiai dalyvauja mus dominančiame fizikiniame procese.

Šiame darbe nagrinėjama bandomųjų banginių funkcijų (anzacų) šeima, pavadinta Aleksandro Davydovo garbei. Ji remiasi 1973 m. Davydovo pasiūlytu aprašymu^{39,40} virpesinės energijos pernašai ir lokalizacijai α spiralės baltymuose, kuriame energiją pernešanti kvazidalelė pavadinta Davydovo solitonu^{41,42}. Davydovo anzacų^{43,44} idėja yra išskleisti sistemos ir aplinkos virpesinių laisvės laipsnių tikrines būsenas nuo laiko priklausančiomis koherentinėmis būsenomis^{45–47}, kurios fazinėje erdvėje turi Gauso paketo formą. Taikant judėjimo lygtis, gautas pasinaudojus nuo laiko priklausančiu variaciniu principu, koherentinės būsenos nuolatos keičia savo poziciją fazinėje erdvėje, siekdamos, jog kuo tiksliau atvaizduotų tuo momentu svarbias tikrines modelio būsenas. Taip siekiama sumažinti neatitikimą tarp banginės funkcijos ir Schrödingerio lygties sprendinio.

Paprasčiausias ir pagrindinis Davydovo šeimos anzacas yra D_2 banginė funkcija^{48–53}. Ji kiekvieną modelio virpesinį laisvės laipsnį vaizduoja viena koherentine būsena, nepriklausomai nuo sistemos elektroninės būsenos. Siekiant pagerinti D_2 anzaco tikslumą, buvo pasiūlyti įvairūs pakeitimai^{49,54}. Pvz., D_1 anzacas^{55–57} kiekvienam virpesiniam laisvės laipsniui kiekvienoje

elektroninėje būsenoje priskiria nuosavą koherentinę būseną, o tai išplečia galimų atvaizduoti virpesinių būsenų spektrą, dalinai atsiejant banginių paketų judėjimą skirtingose elektroninėse būsenose. $D_{1.5}$ anzacas, kurio struktūra yra tarpinis variantas tarp ankščiau minėtųjų, buvo pasiūlytas specifiniam sistemos ir aplinkos modelio pradinių sąlygų atvejui⁵⁴. Kaip alternatyva, vietoje bandymo naudoti vis daugiau koherentinių būsenų, buvo sugalvota modifikuoti pačias koherentes būsenas. Taikant suspaudimo operatorius⁴⁷, yra siekiama pagerinti ne Gauso tikrinių būsenų vaizdavimą. Suspaudimo operatorius viena kryptimi suspaudžia Gauso bangų paketą fazinėje erdvyje, tuo pačiu metu išplečiant jį statmena kryptimi. Tokios banginės funkcijos vadinamos suspaustais Davydovo D_2 ir D_1 anzacais^{58–62}. Nors šie pakeitimai išplečia galimų vaizduoti būsenų diapazoną, jie taip pat padidina skaitmeninio skaičiavimo kaštus ir gali sukelti skaitmeninius nestabilumus.

Šie anzacai buvo sėkmingai naudojami skaičiuojant sužadinių relaksacijos dinamikas ir spektroskopinius molekulių ir jų agregatų signalus trikdžių teorijos režimuose, tačiau jie nėra pakankami už jų ribų^{63,64}, ypač esant žemai temperatūrai. Idėja, kuri paskatino tolesnę šio metodo pažangą, buvo užrašyti bandomąją banginę funkciją kaip D_2 anzacų superpozicija, vadinama multiplanetiniu Davydovo D_2 anzacu^{63–65}. Teoriškai, įtraukus begalinį superpozicijos narių skaičių, multiplanetinis Davydovo D_2 anzacas yra tikslus bet kurio sistemos ir aplinkos modelio tikrinių būsenų vaizdinys. Tačiau praktikoje, dėl sudėtingos judėjimo lygčių struktūros, narių skaičių riboja spartus skaitinių kaštų augimas, įtraukiant didelį virpesių laisvės laipsnių skaičių^{66,67}. Nepaisant to, dėl laike kintančių koherentinių būsenų bazės, multiplanetinis Davydovo D_2 anzacas gali atkartoti kitų skaitmeniškai tikslių metodų rezultatus, pvz., hierarchinių judėjimo lygčių^{63,64,70}, kvazidiabatinių trajektorijų integralų⁷¹ ir nuo kelių konfigūracijų priklausomo Hartree^{72,73}, net kai įtraukiamas didelis skaičius virpesinių laisvės laipsnių.

Tankio operatoriumi besiremiantys metodai gali atsižvelgti į begalinio dydžio termostato įtaką sistemai, išbraukdami virpesinių laisvės laipsnių kintamuosius iš judėjimo lygčių, variacinis metodas to padaryti negali, todėl reikia apsiriboti baigtinio dydžio aplinka. Dažniausiai tolydi aplinkos spektrinio tankio funkcija yra tiesiškai arba logaritmiškai⁷⁰ diskretizuojama dažnių ašyje, siekiant pakankamai tiksliai imituoti tolydinės funkcijos poveikį. Baigtinis skaičius diskretizuotų dažnių ir jas atitinkančių svyravimų amplitudės yra priskiriami kvantiniams harmoniniams osciliatoriams, kurie yra išreikštai modeliuojami kartu su elektroninėmis būsenomis.

Kadangi banginių funkcijų metodai apima ribotą skaičių elektroninių ir virpesinių būsenų, techniškai tai sudaro uždara kvantinė sistema, o ne atvira. Kad būtų išlaikytas lygiavertiškumas tarp redukuoto tankio operatoriaus atviroms kvantinėms sistemoms ir banginėmis funkcijomis pagrįstų uždarų kvantinių sistemų, diskretizuota aplinka turi funkcionuoti kaip tikras termostatas – turėti didesnę šiluminę talpą nei sistema. Tačiau įtraukti pakankamai daug kvantinių harmoninių osciliatorių, kad aplinka turėtų pakankamai didelę šiluminę tamplą, reikalauja didelių skaitmeninių kaštų.

Vykstant sužadavimo relaksacijai, energija iš sistemos pirmiausia yra sugeriama kelių aplinkos osciliatorių, esančių rezonanse su sistemos būsenomis. Šie osciliatoriai stipriai nukrypsta nuo pusiausvyros, o to pasekoje, temperatūra, kurioje vyksta sistemos ir aplinkos modelio dinamika, nebeatitinka pradinės temperatūros, šis procesas vadinamas lokaliu aplinkos kaitimu⁷⁴. Kadangi aplinka dažniausiai modeliuojama kaip nepriklausomų harmoninių osciliatorių rinkinys, nevyksta tiesioginiai energijos mainai tarp osciliatorių. Tai lemia, jog vienintelis kelias įkaitusiai aplinkai atsikratyti pertekline šilumine energija yra gražinti ją atgal į sistemą, o tai paneigia pastovios temperatūros termostato prielaidą ir turi nepageidaujamą grįžtamąjį ryšį sistemos dinamikai.

Ši teorinė aplinkos šilimo problema primena procesą gamtoje, vadinamą molekulinio lokaliu kaitimu^{75,76}, kuomet, molekulei staiga išsklaidžius didelį kiekį šiluminės energijos į aplinką, pvz., eksitonų anihilacijos proceso metu^{77–79} arba vykstant itin sparčiai molekulinei vidinei konversijai^{4,80}, pakyla molekulės aplinkos temperatūra. Natūralu, jog toliau vykstant artimiausios aplinkos vėsimui^{81,82} – termalizacijai, šiluminės energijos perteklius yra išsklaidomas iš artimiausios molekulės aplinkos į tolimesnius aplinkos sluoksnius.

Teorinės aplinkos šilimo problemos yra aktualios visiems Davydovo šeimos anzacams. Naudojant ne multiplanetinius anzacus, galima išreikštai modeliuoti šimtus ar net tūkstančius aplinkos osciliatorių, kad kiekvienas osciliatorius iš sistemos sugertų tik po nedidelį kiekį energijos, taip minimaliai pakeičiant jo pradinę temperatūrą. Tačiau šis tiesmukas metodas, dėl reikalingų didelių skaitmeninių resursų, nėra pritaikomas multiplanetiniams anzacams, kurie naudojami siekiant didžiausio tikslumo. Reikalingas naujas pažangus šios problemos sprendimas.

Disertacijos tikslai ir užduotys

Šio tiriamojo darbo tikslai yra (1) išsiaiškinti, kurie Davydovo anzacai yra taikytini įvairiems sistemos ir aplinkos modeliams, ir (2) plėtoti teorinius ir skaitmeninius metodus našesniems ir tikslesniems sužadavimo relaksacijos ir spektroskopijos signalų skaičiavimams, taikant Davydovo anzacus.

Norint įgyvendinti pirmąjį (1) tikslą, buvo iškeltos šios užduotys:

- Sukurti skaitmeninių skaičiavimų paketą, kuris leistų skaičiuoti sistemos ir aplinkos modelių laikinę evoliuciją ir spektroskopijos signalus, naudojant nuo laiko priklausantį variacinį metodą su Davydovo anzacais.
- Teoriškai aprašyti ir ištirti D_2 anzaco taikymą, skaičiuojant sistemos ir aplinkos modelių laikinę dinamiką su normaliųjų virpesinių modų maišymusi skirtingose elektroninėse būsenose.
- Ištirti sužadintų kvantinių harmoninių osciliatorių būsenų vaizdavimą, naudojant koherentinių būsenų superpoziciją.
- Išnagrinėti multiplanetinio D_2 anzaco taikymą ir konvergavimą H ir J tipo molekulinį agregatų sugerties spektrų skaičiavimams.
- Palyginti įprasto, suspausto ir multiplanetinio D_2 anzacų tikslumą, modeliuojant sistemos ir aplinkos modelio sugerties ir fluorescencijos spektrus, kai sistemos sužadavimo metu pasikeičia virpesinių modų dažniai.

Norint įgyvendinti antrąjį (2) tikslą, užduotys buvo šios:

- Sukurti teorinį aprašymą ir skaitmeninį metodą, leidžiantį nustatyti sužadinto sistemos ir aplinkos modelio šiluminių pusiausvyros būsenų ansamblį.
- Sukurti ir ištirti D_2 anzaco termalizacijos algoritmo poveikį kvantiniams harmoniniams osciliatoriams bei sistemos sužadavimo relaksacijai.
- Išplėsti D_2 anzaco termalizacijos algoritmo aprašymą multiplanetiniam D_2 anzacui.
- Išplėtoti skaitmeninius algoritmus spektroskopijos signalų skaičiavimam.

Ginamieji teiginiai

1. Multiplanetinis D_2 anzacas leidžia tiksliai skaičiuoti molekulinų agregatų sužadavimo relaksacijos dinamiką ir spektroskopijos signalus, tuo tarpu mažiau sofistikuoti nemultiplanetiniai anzacai atkuria tik specifinius agregatų modelio aspektus.
2. Norint modeliuoti netiesinio koordinačių sąveikos nario $\propto x_p x_q^2$ sukeltus energijos mainus tarp kvantinių harmoninių osciliatorių, naudojant Davydovo anzacus, jų tikrinės būsenos turėtų būti vaizduojamos koherentinių būsenų superpozicija.
3. Skaitmeninis termalizacijos algoritmas įprastam ir multiplanetiniam D_2 anzacui leidžia sumažinti reikalingą aplinkos kvantinių harmoninių osciliatorių skaičių, ko pasekoje, sumažėja skaičiavimų kaštai.
4. Sužadintos sistemos ir aplinkos modelio nuostoviųjų būsenų šilumą ansamblį galima rasti, naudojant tiek skaitmeninio optimizavimo, tiek termalizacijos metodus. Termalizacijos metodas yra labiau tinkamas modeliams su daug virpesinių laisvės laipsnių.

Pagrindinių rezultatų apžvalga

Straipsnio [A1] rezultatai

Modeliuoti ir lyginti β -karoteno suskaičiuoti ir eksperimentiniai spektrai, į teorinį aprašymą įtraukus visas 282 normaliąsias virpesines modas. Normalių modų dažniai ir amplitudės tiek pagrindinėje S_0 , tiek sužadintoje S_2 elektroninėje būsenoje buvo skaičiuoti, naudojant tankio funkcionalo teoriją su B3LYP hibridiniu funkcionalu ir 6-311G(d,p) bazinių funkcijų rinkiniu. Vaizduojant β -karoteno būsenas D_2 anzacu ir remiantis nustatytais normaliųjų modų parametrais, buvo suskaičiuoti sugerties spektrai esant įvairioms aplinkos temperatūroms.

Nustatyta, jog virpesinės normalinės modos elektroninėje pagrindinėje S_0 ir sužadintoje S_2 būsenoje nėra tapačios. Priklausomybė tarp virpesinių modų skirtingose elektroninėse būsenose yra netriviali, todėl jos neturėtų būti traktuojamos, kaip vienodos modos. Toks modų maišymasis paaiškina ir pastebėtą stiprią sugerties spektro intensyvumo aukštose energijose priklausomybę nuo temperatūros, kuri nėra paaiškinta empirinio 2 modų modelio.

Taip pat pademonstruota, jog esant 0 K temperatūrai, 2 modų modelio didelio intensyvumo sugerties smailės kokybiškai atitinka 282 modų modelio dažnius. Tačiau, 282 modų modelio atveju, šios smailės atsiranda dėl daugybės silpnų $S_0 \rightarrow S_2$ sugerties šuolių, kurių intensyvumai sumuojasi ir sudaro stiprią sugerties smailę. Pateiktas 282 modų modelis kokybiškai atitinka eksperimentinius duomenis ir paaiškinimą empirinio 2 modų modelio smailių prigimtį, tačiau pervertina aukšto dažnio sugerties intensyvumą.

Straipsnio [A2] rezultatai

Taikant pasiūlytą sD_2 anzacą, skaičiuota vidinės konversijos molekulėje proceso dinamika. Dėmesys skirtas sužadavimo relaksavimo procesui iš aukštos energijos sužadintos elektroninės būsenos į mažesnės energijos sužadintą elektroninę būseną.

Modelyje vidinės konversija sukelia molekulinę elektroninę būsenų ir vidinių virpesių būsenų maišymą. Virpesinės modos aplinkoje pirmiausia yra skirtos sugerti šiluminę energiją iš molekulės virpesinių modų, jau įvykus vidinei konversijai.

Nagrinėtos molekulės elektroninės ir virpesinės energijos, bei aplinkos virpesinės energijos, laikinės priklausomybės. Nustatyta, jog pateiktas teorinis aprašymas leidžia vykdyti vidinei konversijai. Energijos mainai tarp molekulės ir aplinkos virpesinių modų, kuriuos sukelia netiesinis sąveikos narys lygtyje (2.2.1), vyksta, jei aplinkos osciliatorių būsenos yra vaizduojamos koherentių būsenų superpozicija. Šių modų banginės funkcijos paketas yra platesnis ir asimetriškai suspaustas, lyginant su su Gausiniu bangų paketu.

Šių banginės funkcijos sąvybių neįmanoma atvaizduoti naudojant vieną koherentinę būseną, todėl nepakanka taikyti vaizdavimo D_2 anzacu, o reikalingas sudėtingesnis vaizdavimas, pvz., siūlomu sD_2 anzacu. Kitu atveju, tiesioginis energijos perdavimas iš molekulės į aplinkos virpesines modas yra draudžiamas.

Straipsnio [A3] rezultatai

Taikytas formaliai tikslus mD_2 anzacą skaičiuojant H ir J tipo molekulinę agregatų, sudarytų iš 10 identiškų molekulių, sugerties spektrus. Siekta nustatyti, kaip priklauso mD_2 anzaco konvergavimas nuo modelio temperatūros ir tarp-molekulinės sąveikos stiprio.

Nustatyta, jog šiems molekuliniais agregatams pakanka naudoti mD_2 anzacą sudarytą iš 7 superpozicijos narių. D_2 anzacas, kuris atitinka mD_2 anzacą su 1 superpozicijos nariu, bet kurio laikinė evoliucija yra paprastesnėmis judėjimo lygtimis, yra netinkamas visuose nagrinėtuose modelio parametru režimuose. Konkrečiai, H tipo agregatams reikia naudoti multipletinį anzacą, kad būtų užtikrintas sugerties spektro teigiamumas ir tikslūs sugerties smailių intensyvumai. mD_2 anzaco naudojimas J tipo agregatams sukelia sugerties spektro poslinkį į žemesnių energijų pusę, o bendra sugerties linijos forma išlieka kokybiškai nepakitusi.

Reikalingumas molekulinų agregatų modelio būsenas vaizduoti mD_2 anzacu yra siejamas su tuo, jog aukštoje temperatūroje dalyvauja sužadintos kvantinių harmoninių osciliatorių tikrinės būsenos. mD_2 anzacas taip pat leidžia atsieti banginių paketų laikinę evoliuciją skirtinguose elektroninių ir virpesinių būsenų energetiniuose paviršiuose.

Straipsnio [A4] rezultatai

Pasiūlytas skaitmeninis optimizavimo metodas, skirtas rasti sužadintų molekulinų sistemų terminės nuostoviosioms būsenoms, kurios yra reikalingos fluorescencijos spektrams skaičiuoti. Šis metodas taikytas D_2 , sqD_2 ir mD_2 anzacams, skaičiuojant J tipo molekulinio dimero sugerties ir fluorescencijos spektrus, atsižvelgiant į molekulinų virpesių dažnių pokyčius sužadintoje būsenoje.

Nustatyta, kad nei D_2 , nei sqD_2 anzacas negali tiksliai atkurti dimero, su aukšto dažnio virpesinėmis modomis, sugerties ir fluorescencijos spektrų, net jei virpesiniai dažniai pagrindinėje ir sužadintoje būsenoje yra vienodi. Tačiau J tipo dimerui, sąveikaujančiam su žemo dažnio fononais, suskaičiuoti sugerties ir fluorescencijos spektrai su D_2 , sqD_2 ir mD_2 anzacais yra kokybiškai lygiaverčiai.

Stebėti energijos skirtumai tarp smailių spektruose, taikant skirtingus anzacus, gali būti paaiškinti mD_2 anzaco gebėjimo atvaizduoti mažiausios energijos terminės nuostoviąsias būsenas. Nors sqD_2 anzacas sugeba atvaizduoti kai kuriuos nuostoviųjų būsenų pokyčius, atsiradusius dėl kvadratinės sąveikos nario tarp elektroninių ir virpesinių laisvės laipsnių, tiek sqD_2 , tiek D_2 anzacas neatkuria spektrinių pokyčių dėl tarpmolekulinės sąveikos.

Straipsnio [A5] rezultatai

Pasiūlytas skaitmeninis termalizacijos algoritmas, skirtą naudoti kartu su D_2 anzacu. Jis postuluoja antrinio termostato egzistavimą, kuris nėra modeliuojamas išreikštai, o atsižvelgiama tik į jo termodinamines savybes. Antrinis termostatas sąveikauja su sistemos ir aplinkos modelių stochastiniais sklaidos įvykiais, kurie modeliuojami diskretaus laiko Bernulio procesais su sklaidos tikimybėmis aprašytomis Puasono skirstiniu. Sklaidos metu stochastiškai pasikeičia aplinkos osciliatorių judėsio kiekio momentai, kurių skirstinį nusako Glauberio ir Sudaršano funkcija, žr. (1.5.1) lygtį.

Šis termalizacijos metodas leidžia valdyti aplinkos temperatūrą, kvantinius harmoninius osciliatorius dinamiškai vedant į siekiamos temperatūros šiluminės pusiausvyros būsenas. Galimybė kontroliuoti aplinkos temperatūrą leidžia užkirsti kelią nepageidaujamam aplinkos kaitimo efektui. Skaičiuojant molekulinio trimero sužadavimo relaksacijos dinamiką su D_2 anzacu, parodyta, kad didelio skaičiaus aplinkos osciliatorių poveikį sistemai galima lygiaverčiai modeliuoti mažesniu osciliatorių skaičiumi, kartu taikant termalizacijos algoritmą.

Straipsnio [A6] rezultatai

Išplėstas D_2 anzacui skirtas termalizacijos algoritmas, jį pritaikant mD_2 anzacui, pasinaudojant pageidaujamų būsenų ir grubios sklaidos aproksimacijas. Tai leidžia mD_2 anzacui išlaikyti geresnį tikslumą, lyginant su D_2 anzacu, ir tuo pačiu naudotis termalizacijos suteikiamais privalumais.

Skaičiuojant molekulinio trimero sužadavimo relaksacijos dinamiką su mD_2 anzacu, parodyta, jog išplėstas termalizacijos algoritmas leidžia sumažinti reikiamą aplinkos osciliatorių skaičių, kokybiškai nepakeičiant dinamikos savybių. Tai ženkliai sumažina skaičiavimo kaštus. mD_2 anzacui skirtas termalizacijos algoritmas atveria galimybes skaitmeniškai tirti didelių sistemos ir aplinkos modelių dinamiką ir spektrus.

Taip pat pademonstruota, kaip termalizacija gali būti pritaikyta ieškant sužadintos sistemos ir aplinkos modelio terminų nuostoviųjų būsenų. Lyginant su ankščiau pasiūlytu skaitmeninio optimizavimo metodu, termalizacijos metodas reikalauja mažesnių skaičiavimo kaštų, turi geresnį skaitmeninį stabilumą ir tikslumą, ypač modeliams su daug laisvės laipsnių.

BIBLIOGRAPHY

1. H.-D. Meyer, Wiley Interdiscip. Rev. Comput. Mol. Sci. **2**, 351 (2012).
2. P. M. Shenai, S. Fernandez-Alberti, W. P. Bricker, S. Tretiak, and Y. Zhao, J. Phys. Chem. B **120**, 49 (2016).
3. V. Balevičius, D. Abramavicius, T. Polívka, A. Galestian Pour, and J. Hauer, J. Phys. Chem. Lett. **7**, 3347 (2016).
4. V. Balevičius, T. Wei, D. Di Tommaso, D. Abramavicius, J. Hauer, T. Polívka, C. D. P. Duffy, V. Balevičius Jr, T. Wei, D. Di Tommaso, D. Abramavicius, J. Hauer, T. Polívka, and C. D. P. Duffy, Chem. Sci. **10**, 4792 (2019).
5. F.-J. Schmitt, I. Trostmann, C. Theiss, J. Pieper, T. Renger, J. Fuesers, E. H. Hubrich, H. Paulsen, H. J. Eichler, and G. Renger, J. Phys. Chem. B **112**, 13951 (2008).
6. E. Meneghin, A. Volpato, L. Cupellini, L. Bolzonello, S. Jurinovich, V. Mascoli, D. Carbonera, B. Mennucci, and E. Collini, Nat. Commun. **9**, 3160 (2018).
7. H. Staleva-Musto, R. West, M. Trathnigg, D. Bína, R. Litvín, and T. Polívka, Faraday Discuss. **216**, 460 (2019).
8. K. F. Fox, V. Balevičius, J. Chmeliov, L. Valkunas, A. V. Ruban, and C. D. Duffy, Phys. Chem. Chem. Phys. **19**, 22957 (2017).
9. H. van Amerongen, R. van Grondelle, and L. Valkunas, *Photosynthetic Excitons* (World Scientific, 2000).
10. A. Chenu and G. D. Scholes, Annu. Rev. Phys. Chem. **66**, 69 (2015).
11. P. Malý, J. M. Gruber, R. J. Cogdell, T. Mančal, and R. van Grondelle, Proc. Natl. Acad. Sci. **113**, 2934 (2016).
12. S. J. Jang and B. Mennucci, Rev. Mod. Phys. **90**, 35003 (2018).
13. E. Thyraug, C. N. Lincoln, F. Branchi, G. Cerullo, V. Perlík, F. Šanda, H. Lokstein, and J. Hauer, Photosynth. Res. **135**, 45 (2018).
14. H.-P. Breuer and F. Petruccione, *The Theory of Open Quantum Systems* (Oxford University PressOxford, 2007).

15. U. Weiss, *Quantum Dissipative Systems* (WORLD SCIENTIFIC, 2012).
16. A. Kell, X. Feng, M. Reppert, and R. Jankowiak, *J. Phys. Chem. B* **117**, 7317 (2013).
17. M. Schröter, S. Ivanov, J. Schulze, S. Polyutov, Y. Yan, T. Pullerits, and O. Kühn, *Phys. Rep.* **567**, 1 (2015).
18. A. G. Redfield, *IBM J. Res. Dev.* **1**, 19 (1957).
19. A. G. Redfield, *Adv. Magn. Opt. Reson.* **1**, 1 (1965).
20. A. Köhl and W. Domcke, *J. Chem. Phys.* **116**, 263 (2002).
21. A. Montoya-Castillo, T. C. Berkelbach, and D. R. Reichman, *J. Chem. Phys.* **143**, 194108 (2015).
22. T. Förster, *Ann. Phys.* **437**, 55 (1948).
23. D. Beljonne, C. Curutchet, G. D. Scholes, and R. J. Silbey, *J. Phys. Chem. B* **113**, 6583 (2009).
24. J. Seibt and T. Mančal, *J. Chem. Phys.* **146**, 174109 (2017).
25. Y. Tanimura, *J. Chem. Phys.* **153**, 020901 (2020).
26. U. Schollwöck, *Rev. Mod. Phys.* **77**, 259 (2005).
27. J. Prior, A. W. Chin, S. F. Huelga, and M. B. Plenio, *Phys. Rev. Lett.* **105**, 050404 (2010).
28. I. de Vega and M.-C. Bañuls, *Phys. Rev. A* **92**, 052116 (2015).
29. M. Sánchez-Barquilla and J. Feist, *Nanomaterials* **11**, 2104 (2021).
30. L. Mühlbacher and E. Rabani, *Phys. Rev. Lett.* **100**, 176403 (2008).
31. M. Beck, *Phys. Rep.* **324**, 1 (2000).
32. I. Burghardt, K. Giri, and G. A. Worth, *J. Chem. Phys.* **129**, 174104 (2008).
33. L. Wang, A. Akimov, and O. V. Prezhdo, *J. Phys. Chem. Lett.* **7**, 2100 (2016).

34. J. Piilo, S. Maniscalco, K. Härkönen, and K. A. Suominen, *Phys. Rev. Lett.* **100**, 180402 (2008).
35. L. Diósi and W. T. Strunz, *Phys. Lett. A* **235**, 569 (1997).
36. D. Suess, A. Eisfeld, and W. T. Strunz, *Phys. Rev. Lett.* **113**, 150403 (2014).
37. R. Borrelli and M. F. Gelin, *J. Chem. Phys.* **145**, 224101 (2016).
38. L. Chen and Y. Zhao, *J. Chem. Phys.* **147**, 214102 (2017).
39. A. Davydov, *J. Theor. Biol.* **38**, 559 (1973).
40. A. S. Davydov and N. I. Kislukha, *Phys. Status Solidi* **59**, 465 (1973).
41. A. S. Davydov, *Phys. Scr.* **20**, 387 (1979).
42. A. C. Scott, *Phys. D Nonlinear Phenom.* **51**, 333 (1991).
43. Y. Zhao, K. Sun, L. Chen, and M. Gelin, *WIREs Comput. Mol. Sci.* **12**, e1589 (2022).
44. Y. Zhao, *J. Chem. Phys.* **158**, 80901 (2023).
45. R. J. Glauber, *Phys. Rev.* **131**, 2766 (1963).
46. V. Bargmann, P. Butera, L. Girardello, and J. R. Klauder, *Reports Math. Phys.* **2**, 221 (1971).
47. L. Rodney, *The Quantum Theory of Light* (OUP Oxford, 2000).
48. B. Luo, J. Ye, C. Guan, and Y. Zhao, *Phys. Chem. Chem. Phys.* **12**, 15073 (2010).
49. J. Sun, B. Luo, and Y. Zhao, *Phys. Rev. B* **82**, 014305 (2010).
50. V. Chorošajev, O. Rancova, and D. Abramavicius, *Phys. Chem. Chem. Phys.* **18**, 7966 (2016).
51. M. Jakučionis, V. Chorošajev, and D. Abramavičius, *Chem. Phys.* **515**, 193 (2018).
52. K.-W. Sun, M. F. Gelin, V. Y. Chernyak, and Y. Zhao, *J. Chem. Phys.* **142**, 212448 (2015).

53. M. Jakucionis, I. Gaiziunas, J. Sulskus, and D. Abramavicius, *J. Phys. Chem. A* **126**, 180 (2022).
54. M. Werther and F. Grossmann, *Phys. Scr.* **93**, 074001 (2018).
55. A. W. Chin, J. Prior, S. F. Huelga, and M. B. Plenio, *Phys. Rev. Lett.* **107**, 160601 (2011).
56. V. Chorošajev, A. Gelzinis, L. Valkunas, and D. Abramavicius, *J. Chem. Phys.* **140**, 244108 (2014).
57. A. D. Somoza, K.-W. Sun, R. A. Molina, and Y. Zhao, *Phys. Chem. Chem. Phys.* **19**, 25996 (2017).
58. Y. Tsue and Y. Fujiwara, *Prog. Theor. Phys.* **86**, 443 (1991).
59. F. Grossmann, M. Werther, L. Chen, and Y. Zhao, *Chem. Phys.* **481**, 99 (2016).
60. V. Chorošajev, T. Marčiulionis, and D. Abramavicius, *J. Chem. Phys.* **147**, 074114 (2017).
61. D. Abramavičius and T. Marčiulionis, *Lith. J. Phys.* **58**, 307 (2018).
62. M. Jakučionis, A. Žukas, and D. Abramavičius, *Phys. Chem. Chem. Phys.* **25**, 1705 (2023).
63. N. Zhou, L. Chen, Z. Huang, K. Sun, Y. Tanimura, and Y. Zhao, *J. Phys. Chem. A* **120**, 1562 (2016).
64. L. Chen, M. Gelin, and Y. Zhao, *Chem. Phys.* **515**, 108 (2018).
65. N. Zhou, Z. Huang, J. Zhu, V. Chernyak, and Y. Zhao, *J. Chem. Phys.* **143**, 014113 (2015).
66. M. Jakučionis, A. Žukas, and D. Abramavičius, *Phys. Chem. Chem. Phys.* **24**, 17665 (2022).
67. M. Werther and F. Großmann, *Phys. Rev. B* **101**, 174315 (2020).
68. Y. Fujihashi, L. Wang, and Y. Zhao, *J. Chem. Phys.* **147**, 234107 (2017).
69. E. W. Fischer, M. Werther, F. Bouakline, F. Grossmann, and P. Saalfrank, *J. Chem. Phys.* **156**, 214702 (2022).

70. L. Wang, L. Chen, N. Zhou, and Y. Zhao, *J. Chem. Phys.* **144**, 024101 (2016).
71. L. Wang, Y. Fujihashi, L. Chen, and Y. Zhao, *J. Chem. Phys.* **146**, 124127 (2017).
72. L. Chen, M. F. Gelin, and W. Domcke, *J. Chem. Phys.* **150**, 24101 (2019).
73. J. Zeng and Y. Yao, *J. Chem. Theory Comput.* **18**, 1255 (2022).
74. D. Abramavicius, V. Chorošajev, and L. Valkunas, *Phys. Chem. Chem. Phys.* **20**, 21225 (2018).
75. Z. Chen and R. S. Sorbello, *Phys. Rev. B* **47**, 13527 (1993).
76. M. Ichikawa, H. Ichikawa, K. Yoshikawa, and Y. Kimura, *Phys. Rev. Lett.* **99**, 148104 (2007).
77. V. Gulbinas, L. Valkunas, D. Kuciauskas, E. Katilius, V. Liulia, W. Zhou, and R. E. Blankenship, *J. Phys. Chem.* **100**, 17950 (1996).
78. L. Valkunas and V. Gulbinas, *Photochem. Photobiol.* **66**, 628 (1997).
79. V. Gulbinas, R. Karpicz, G. Garab, and L. Valkunas, *Biochemistry* **45**, 9559 (2006).
80. V. Balevičius, C. N. Lincoln, D. Viola, G. Cerullo, J. Hauer, and D. Abramavicius, *Photosynth. Res.* **135**, 55 (2018).
81. J. Choi, H. Zhou, S. Choi, R. Landig, W. W. Ho, J. Isoya, F. Jelezko, S. Onoda, H. Sumiya, D. A. Abanin, and M. D. Lukin, *Phys. Rev. Lett.* **122**, 043603 (2019).
82. V. Scarani, M. Ziman, P. Štelmachovič, N. Gisin, and V. Bužek, *Phys. Rev. Lett.* **88**, 097905 (2002).
83. M. Jakucionis, (2023), 10.5281/zenodo.7985830.
84. L. Valkunas, D. Abramavicius, and T. Mančal, *Molecular Excitation Dynamics and Relaxation* (Wiley-VCH Verlag GmbH & Co. KGaA, Weinheim, Germany, 2013).
85. C. J. Bardeen, *Annu. Rev. Phys. Chem.* **65**, 127 (2014).

86. J. Frenkel, Phys. Rev. **37**, 17 (1931).
87. V. May and O. Kühn, *Charge and Energy Transfer Dynamics in Molecular Systems* (Wiley-VCH Verlag GmbH & Co. KGaA, Weinheim, Germany, 2011).
88. T. Steffen and Y. Tanimura, J. Phys. Soc. Japan **69**, 3115 (2000).
89. Y. Tanimura and T. Steffen, J. Phys. Soc. Japan **69**, 4095 (2000).
90. J. Zhang, R. Borrelli, and Y. Tanimura, J. Chem. Phys. **152**, 214114 (2020).
91. B. L. Hu, J. P. Paz, and Y. Zhang, Phys. Rev. D **47**, 1576 (1993).
92. R.-X. Xu, Y. Liu, H.-D. Zhang, and Y. Yan, J. Chem. Phys. **148**, 114103 (2018).
93. M. Jakučionis, T. Mancal, and D. Abramavičius, Phys. Chem. Chem. Phys. **22**, 8952 (2020).
94. Y. Shen and L. Hao, J. Phys. Conf. Ser. **99**, 012009 (2008).
95. C. Lubich, *From Quantum to Classical Molecular Dynamics: Reduced Models and Numerical Analysis* (EMS Press, 2008).
96. L. Hackl, T. Guaita, T. Shi, J. Haegeman, E. Demler, and I. Cirac, SciPost Phys. **9**, 048 (2020).
97. R. Martinazzo and I. Burghardt, Phys. Rev. Lett. **124**, 150601 (2020).
98. W.-M. Zhang, D. H. Feng, and R. Gilmore, Rev. Mod. Phys. **62**, 867 (1990).
99. S. Kais and R. D. Levine, Phys. Rev. A **41**, 2301 (1990).
100. Q. Rackauckas, Christopher and Nie, J. Open Res. Softw. **5**, 15 (2017).
101. Ernst Hairer, Gerhard Wanner, and Syvert P. Nørsett, *Solving Ordinary Differ. Equations I*, Springer Series in Computational Mathematics (Springer Berlin Heidelberg, 1993).
102. S. Mukamel, *Principles of nonlinear optical spectroscopy* (Oxford University Press, 1995).

103. V. Balevičius, L. Valkunas, and D. Abramavicius, *J. Chem. Phys.* **143**, 074101 (2015).
104. T. Polívka and V. Sundström, *Chem. Rev.* **104**, 2021 (2004).
105. M. J. Llansola-Portoles, A. A. Pascal, and B. Robert, *J. R. Soc. Interface* **14**, 20170504 (2017).
106. M. M. Mendes-Pinto, E. Sansiaume, H. Hashimoto, A. A. Pascal, A. Gall, and B. Robert, *J. Phys. Chem. B* **117**, 11015 (2013).
107. T. Polívka, D. Zigmantas, H. A. Frank, J. A. Bautista, J. L. Herek, Y. Koyama, R. Fujii, and V. Sundström, *J. Phys. Chem. B* **105**, 1072 (2001).
108. N. Christensson, F. Milota, A. Nemeth, J. Sperling, H. F. Kauffmann, T. Pullerits, and J. Hauer, *J. Phys. Chem. B* **113**, 16409 (2009).
109. K. F. Fox, V. Balevičius, J. Chmeliov, L. Valkunas, A. V. Ruban, and C. D. Duffy, *Phys. Chem. Chem. Phys.* **19**, 22957 (2017).
110. N. Gong, H. Fu, S. Wang, X. Cao, Z. Li, C. Sun, and Z. Men, *J. Mol. Liq.* **251**, 417 (2018).
111. M. W. Schmidt, K. K. Baldridge, J. A. Boatz, S. T. Elbert, M. S. Gordon, J. H. Jensen, S. Koseki, N. Matsunaga, K. A. Nguyen, S. Su, T. L. Windus, M. Dupuis, and J. A. Montgomery, *J. Comput. Chem.* **14**, 1347 (1993).
112. J. A. M. J. Frisch and G. W. Trucks and H. B. Schlegel and G. E. Scuseria and M. A. Robb and J. R. Cheeseman and G. Scalmani and V. Barone and G. A. Petersson and H. Nakatsuji and X. Li and M. Caricato and A. V. Marenich and J. Bloino and B. G. Janesko and R. G. J. E. Peralta, F. Ogliaro, M. J. Bearpark, J. J. Heyd, E. N. Brothers, K. N. Kudin, V. N. Staroverov, T. A. Keith, R. Kobayashi, J. Normand, K. Raghavachari, A. P. Rendell, J. C. Burant, S. S. Iyengar, and J., “Gaussian 16 {R}evision {C}.01,” (2016).
113. F. Duschinsky, *Acta Physicochim. U.R.S.S.* **7**, 551 (1937).
114. G. M. Sando, K. G. Spears, J. T. Hupp, and P. T. Ruhoff, *J. Phys. Chem. A* **105**, 5317 (2001).
115. P. Meier and G. Rauhut, *Mol. Phys.* **113**, 3859 (2015).

116. W. Domcke, D. R. Yarkony, and H. Köppel, *Conical Intersections: Electronic Structure, Dynamics & Spectroscopy* (WORLD SCIENTIFIC, 2004).
117. E. G. McRae and M. Kasha, *J. Chem. Phys.* **28**, 721 (1958).
118. M. Kasha, *Radiat. Res.* **20**, 55 (1963).
119. M. Kasha, H. R. Rawls, and M. A. El-Bayoumi, *Pure Appl. Chem.* **11**, 371 (1965).
120. F. C. Spano, *Acc. Chem. Res.* **43**, 429 (2009).
121. N. J. Hestand and F. C. Spano, *Chem. Rev.* **118**, 7069 (2018).
122. A. Eisfeld and J. S. Briggs, *Chem. Phys.* **324**, 376 (2006).
123. P. B. Walczak, A. Eisfeld, and J. S. Briggs, *J. Chem. Phys.* **128**, 044505 (2008).
124. J. Roden, A. Eisfeld, and J. S. Briggs, *Chem. Phys.* **352**, 258 (2008).
125. Z. H. Zhan, J. Zhang, Y. Li, and H. S. Chung, *IEEE Trans. Syst. Man. Cybern. B. Cybern.* **39**, 1362 (2009).
126. P. K. Mogensen and A. N. Riseth, *J. Open Source Softw.* **3**, 615 (2018).
127. A. W. Chin, J. Prior, R. Rosenbach, F. Caycedo-Soler, S. F. Huelga, and M. B. Plenio, *Nat. Phys.* **9**, 113 (2013).
128. M. B. Plenio and P. L. Knight, *Rev. Mod. Phys.* **70**, 101 (1998).
129. K. Luoma, W. T. Strunz, and J. Piilo, *Phys. Rev. Lett.* **125**, 150403 (2020).
130. V. N. Kampen, *Stochastic Processes in Physics and Chemistry* (Elsevier, 2007).
131. D. Bertsekas and J. Tsitsiklis, *Introduction to probability* (IOP Publishing Ltd, 2008).
132. J. M. Moix, Y. Zhao, and J. Cao, *Phys. Rev. B* **85**, 115412 (2012).
133. Y. Subaşı, C. H. Fleming, J. M. Taylor, and B. L. Hu, *Phys. Rev. E* **86**, 061132 (2012).

134. A. Gelzinis and L. Valkunas, *J. Chem. Phys.* **152**, 051103 (2020).
135. F. Leyvraz and F. Calogero, *J. Stat. Mech. Theory Exp.* **2009**, P02022 (2009).
136. M. Schlosshauer, *Decoherence and the Quantum-To-Classical Transition*, Frontiers Collection (Springer Berlin Heidelberg, Berlin, Heidelberg, 2007).
137. D. Abramavicius and L. Valkunas, *Phys. Rev. B* **68**, 245203 (2003).
138. A. Eisfeld, S. M. Vlaming, V. A. Malyshev, and J. Knoester, *Phys. Rev. Lett.* **105**, 137402 (2010).
139. O. Rancova, M. Jakučionis, L. Valkunas, and D. Abramavicius, *Chem. Phys. Lett.* **674**, 120 (2017).

CURRICULUM VITAE

Name: Mantas
Surname: Jakučionis
Date of birth: 1994-05-04
Place of birth: Vilnius, Lithuania

Education:

2017 - 2019 Vilnius University, Faculty of Physics
Master's degree (Magna Cum Laude)
2013 - 2017 Vilnius University, Faculty of Physics
Bachelor's degree
2001 - 2013 Vilnius Simonas Daukantas gymnasium

Conferences and workshops:

2023 Quantum Effects In Biological Systems Workshop, United Kingdom
2022 Hanseatic Workshop on Exciton Dynamics and Spectroscopy, Lithuania
2022 14th European Conference on Atoms Molecules and Photons, Lithuania
2022 12th International Workshop on Quantum Effects in Biological Systems, Greece
2022 Open Readings 2022, virtual
2021 Computational methods in photosynthesis: From atoms to the mesoscale, from theory to experiment, virtual
2020 Open Readings 2020, Lithuania
2019 43rd Lithuanian National Physics Conference, Lithuania
2019 Prague May Meeting, Germany
2018 Humboldt Kolleg. Controlling quantum matter: From ultracold atoms to solids, Lithuania

- 2018 10th Workshop on Quantum Effects in Biological Systems,
Lithuania
- 2015 41st Lithuanian National Physics Conference, Lithuania
- 2015 Optical probes of conjugated polymers and organic
nanostructures: the 11th international conference, Hong Kong
- 2015 Open Readings 2015, Lithuania

Work experience:

- 2016 - 2023 Laboratory assistant at Vilnius University
Institute of Chemical Physics

COPIES OF ARTICLES

A1

Simulation of Ab Initio Optical Absorption Spectrum of β -Carotene with
Fully Resolved S0 and S2 Vibrational Normal Modes

M. Jakučionis, I. Gaižiūnas, J. Šulskus, D. Abramavičius

The Journal of Physical Chemistry A, **126**, 180–189 (2022)

Reproduced with permission from J. Phys. Chem. A 2022, 126, 2, 180–189.
Copyright 2023 American Chemical Society.

Simulation of Ab Initio Optical Absorption Spectrum of β -Carotene with Fully Resolved S_0 and S_2 Vibrational Normal Modes

Mantas Jakučionis, Ignas Gaiziūnas, Juozas Šulskus, and Darius Abramavičius*

Cite This: <https://doi.org/10.1021/acs.jpca.1c06115>

Read Online

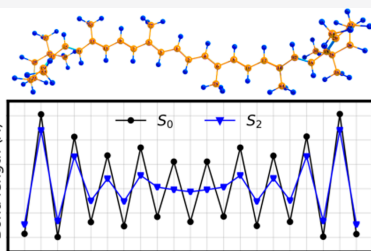
ACCESS |

Metrics & More

Article Recommendations

Supporting Information

ABSTRACT: The electronic absorption spectrum of β -carotene (β -Car) is studied using quantum chemistry and quantum dynamics simulations. Vibrational normal modes were computed in optimized geometries of the electronic ground state S_0 and the optically bright excited S_2 state using the time-dependent density functional theory. By expressing the S_2 -state normal modes in terms of the ground-state modes, we find that no one-to-one correspondence between the ground- and excited-state vibrational modes exists. Using the ab initio results, we simulated the β -Car absorption spectrum with all 282 vibrational modes in a model solvent at 300 K using the time-dependent Dirac–Frenkel variational principle and are able to qualitatively reproduce the full absorption line shape. By comparing the 282-mode model with the prominent 2-mode model, widely used to interpret carotenoid experiments, we find that the full 282-mode model better describes the high-frequency progression of carotenoid absorption spectra; hence, vibrational modes become highly mixed during the $S_0 \rightarrow S_2$ optical excitation. The obtained results suggest that electronic energy dissipation is mediated by numerous vibrational modes.



INTRODUCTION

Pigment molecules in nature form the basis of life on earth by enabling organisms to utilize the solar energy. Carotenoids form a unique class of pigments with a conjugated polyene chain, responsible for light absorption in a green-blue color region. Over 700 carotenoid molecules are found in nature. They primarily play a role as coloring materials, which underlie a vital and complex signaling process.^{1,2} In photosynthesis, carotenoids are essential in solar energy harvesting and in photoprotection from oxygen damage. The latter emerge on the microscopic level, when light illumination is high, by the formation of energy trapping states.^{3,4} This trapping has been related to quenching of the chlorophyll excited states by the carotenoid singlet state^{5,6} or by the excitonic interaction between chlorophyll and the carotenoid, which is controlled by carotenoid conformations.^{7,8} Carotenoids become thus responsible for the regulation of excitation energy fluxes in photosynthesis in volatile conditions of daylight irradiation. One of the possible mechanisms of such behavior involves a limited conformational rearrangement of the protein scaffold that could act as a molecular switch to activate or deactivate the quenching mechanism.⁹ A strong correlation between carotenoid and local environment deformations is necessary for such mechanism to exist.

However, the primary deformations leading to carotenoid flexibility are the molecular vibrations. They are usually induced during photon absorption (and emission) and following excitation relaxation processes. Probing excitation

and vibration-mediated relaxation processes in carotenoids, necessary for understanding the fundamental physical processes involved in their functioning, is possible by performing time-resolved optical spectroscopy experiments. It is well established that carotenoids demonstrate a complex structure of electronic excited states^{10,11} with at least three electronic states necessary to fully capture the excitation longtime dynamics. Direct optical excitation induces electronic $S_0 \rightarrow S_2$ transition, where S_0 is the electronic ground state and S_2 is the first optically accessible (bright) electronic state, and the optically dark electronic state S_1 lies between S_0 and S_2 . Additional intramolecular charge-transfer (CT) states have been proposed in peridinin in agreement with the experimental results.^{12,13} Quantum chemical calculations using the time-dependent density functional theory with the Tamm–Dancoff approximation^{14–16} demonstrate the presence of the CT state in the same energy range. The energy of the CT state has been shown to decrease dramatically in solvents of increasing polarity, while the energy of the dark S_1 state remains comparatively constant.¹⁷ Several other types of electronic

Received: July 9, 2021

Revised: October 11, 2021

excited states have been suggested; however, their existence and involvement in the relaxation process are still debatable.¹⁸ Specific spectral features have been assigned to S_1 and CT states, and these may play an important role in de-excitation processes.^{9,13,19}

Vibrational heating and cooling are involved in the relaxation process via electronic-vibrational (vibronic) coupling.²⁰ Indeed, strong vibronic coupling is rooted in broad electronic absorption spectra, more specifically, in a strong vibronic shoulder for a range of different carotenoids as observed experimentally.²¹ This feature is often associated with two vibrational modes: C–C symmetric and asymmetric stretching vibrations with the cumulative Huang–Rhys factor larger than 1. These modes are known to be active in Raman spectra, and their frequencies scale linearly with the conjugation length in carotenoids.¹¹ While molecular vibrations affect the symmetry properties of the molecules, they do not affect the oscillator strength of the dark state.²² Such empirical effective 2-mode model has been extensively used for spectroscopy simulations.^{20,23–27} However, the two vibrational modes do not capture the high-energy vibrational wing, and it is not clear whether the two modes are sufficient to accurately describe the more complex ultrafast internal conversion and energy-transfer processes.

In this paper, we present quantum chemistry and quantum dynamics description of vibrational manifold of β -Car in its electronic states S_0 and S_2 . We find that numerous vibrational modes become highly mixed during the $S_0 \rightarrow S_2$ optical excitation, resulting in a complex S_2 state wave packet. We are able to reveal the full absorption spectrum, including the high-energy vibrational shoulder. Simulations thus suggest that pathways responsible for the ultrafast electronic excitation relaxation and internal conversion are mediated by numerous vibrational modes, resulting in a rapid and efficient electronic energy dissipation.

THEORETICAL METHODS

Quantum chemical analysis starts from the complete molecular Hamiltonian including both electronic and vibrational degrees of freedom (DOFs).^{28,29} Using the Born–Oppenheimer approximation, the full Schrödinger equation is split into separate equations for electronic and nuclear DOFs. The stationary Schrödinger equation for electrons then parametrically depends on the nuclear coordinates

$$\hat{H}_{\text{el}}(\mathbf{R})\Phi_m(\mathbf{R}) = E_m(\mathbf{R})\Phi_m(\mathbf{R}) \quad (1)$$

where \hat{H}_{el} includes the electron kinetic energy, electronic interaction with nuclei, electron–electron interactions, and internuclear interaction energy, $\mathbf{R} \equiv R_1, R_2, \dots$ labels nuclei coordinates. The eigenvalues $E_m(\mathbf{R})$ and the corresponding eigenstates $\Phi_m(\mathbf{R})$, which parametrically depend on nuclei configuration, characterize the electronic system.

Electronic energy minimum of the electronic ground state denotes the reference point—the equilibrium molecular structure. If the nuclear configuration deviates from the minimum, the electronic energy is increased; hence, the electronic energy can be treated as the potential energy for nuclei DOFs. For small deviations from the energy minimum, we use the harmonic approximation, where the potential energy operator is expanded up to quadratic terms. Therefore, the potential energy for nuclei displacements in the electronic

state n can be written as (using Einstein summation convention for repeating indices)

$$U_n(u) \approx \frac{1}{2} \mathcal{H}_{ij}^{(n)} u_i u_j \quad (2)$$

where we introduce mass-weighted Cartesian coordinates $u_i = \sqrt{M_i}(R_i - R_{i0}^{(n)})$, as the shifts of nuclei from their equilibrium positions, and

$$\mathcal{H}_{ij}^{(n)} = \frac{1}{\sqrt{M_i M_j}} \left. \frac{\partial^2 E_n(\mathbf{R})}{\partial R_i \partial R_j} \right|_{\text{min}} \quad (3)$$

is the Hessian matrix with derivatives taken at the global minimum of the state n . The Schrödinger equation for the nuclear wave functions with respect to the specific electronic state n is

$$(\hat{T} + \hat{U}_n(u)) \chi_{\alpha n}(u) = \epsilon_{\alpha n} \chi_{\alpha n}(u) \quad (4)$$

where α is the vibrational quantum-state index with energy $\epsilon_{\alpha n}$ and wave function $\chi_{\alpha n}$. The vibrational Schrödinger equation splits into an independent set of equations in the normal coordinate representation; we denote these coordinates by Q_k . Normal modes are obtained by diagonalizing the Hessian matrix for each electronic state n . Solving the eigenstate equation

$$\mathcal{H}_{ij}^{(n)} L_{jk}^{(n)} = \omega_{nk}^2 L_{ik}^{(n)} \quad (5)$$

yields normal mode frequencies ω_{nk} , where k labels normal modes. The Hessian eigenvectors $L_{jk}^{(n)}$ relate the normal modes k and nuclei displacements u_i . Placing eigenvectors in columns, we form the matrix $L^{(n)}$, whose rank is $M = 3N - 6$ (six of the modes are physically irrelevant as three of them correspond to the uniform translation of the whole molecule along the Cartesian axes, while the other three are uniform rotations about these axes, they are excluded), and it is used to transform mass-weighted Cartesian internal coordinates u_i into normal coordinates $Q_k^{(n)} = (L^{(n)})_{ki}^{-1} u_i$.

Complete description of the *vibronic* molecular states, when the electronic and vibrational states are known, is given by the state vectors $|\mathbf{n}\alpha_n\rangle$, where $\alpha_n \equiv (\alpha_{n1}, \alpha_{n2}, \dots, \alpha_{nk})$ is the M -dimensional vector denoting the vibrational states of all vibrational modes in the electronic state n . As the normal modes are harmonic, the vibrational Hamiltonian in the electronic state n is given by

$$\hat{H}^{(n)} = \frac{1}{2} \sum_k ((\hat{P}_k^{(n)})^2 + \omega_{nk}^2 (\hat{Q}_k^{(n)})^2) |\mathbf{n}\rangle \langle \mathbf{n}| \quad (6)$$

The absorption spectrum of a vibronic system involves all possible optical transitions from the vibronic ground state $|\mathbf{g}\mathbf{g}\rangle$ to the excited states $|\mathbf{n}\alpha\rangle$. Starting from the linear response theory, the absorption spectrum is given by the Fourier transform of the linear response function

$$S(\omega) = \frac{\omega}{nc} \text{Re} \int_0^\infty dt e^{i\omega t} F(t) \quad (7)$$

where n is the refraction index and c is the speed of light,^{28,30} and

$$F(t) = \langle \mathbf{g}\alpha | e^{i\hat{H}_{\text{el}} t} \hat{\mathbf{P}} e^{-i\hat{H}_{\text{el}} t} | \mathbf{g}\alpha \rangle \quad (8)$$

is the dipole operator correlation function. In the Born approximation, the polarization operator $\hat{\mathbf{P}}$ acts only on

electronic DOFs; hence, $\hat{P} = \mu_{\text{eg}}^{(e)}(|e\rangle\langle g| + |g\rangle\langle e|)$ and $\mu_{\text{eg}}^{(e)}$ is the electronic transition dipole. The matrix elements of the polarization operator are given by

$$\langle e|\hat{P}|g\rangle = \mu_{\text{eg}}^{(e)} \int d^N \mathbf{u} \prod_{j,k} \chi_{\text{eti}_j}^*(\mathbf{u}) \chi_{\text{gfk}_k}(\mathbf{u}) \quad (9)$$

The multi-dimensional integral corresponds to the vibrational overlaps between the vibrational wave function in different electronic states. The integral computation is not trivial because the sets of normal modes in different electronic states are not orthogonal, and transformation of one set of normal modes into another is necessary.^{31–33}

Differences of the set of normal modes in different electronic states are characterized as follows. In the electronic state n , the deviation of atomic Cartesian coordinates R_i from the equilibrium position $R_{i0}^{(n)}$ may be expressed via the normal modes via the relation

$$\sqrt{M_i}(R_i - R_{i0}^{(n)}) = L_{ij}^{(n)} Q_j^{(n)} \quad (10)$$

and allows us to relate the relative mass-weighted atom shifts $D_i^{(mn)} \equiv \sqrt{M_i}(R_{i0}^{(m)} - R_{i0}^{(n)})$ between the equilibrium positions in electronic states m and n as

$$D_i^{(mn)} = L_{ij}^{(n)} Q_j^{(n)} - L_{ij}^{(m)} Q_j^{(m)} \quad (11)$$

then the normal mode coordinates in state m can be expressed in terms of state n normal mode coordinates as

$$Q_i^{(m)} = a_{ij}^{(mn)} Q_j^{(n)} - d_i^{(mn)} \quad (12)$$

where the expansion coefficient of the i th normal mode in the m th state in terms of j th mode in the n th state is

$$a_{ij}^{(mn)} \equiv (L^{(m)})_{ik}^{-1} L_{kj}^{(n)} \quad (13)$$

and the i th normal mode potential displacement in the m th state, with respect to the position in the n th state, is

$$d_i^{(mn)} \equiv (L^{(m)})_{ik}^{-1} D_k^{(mn)} \quad (14)$$

These are the two quantities that relate the normal modes in different electronic states. Likewise, the normal mode momentum is also expanded in terms of the $a_{ij}^{(sg)}$ coefficients (and zero displacement)

$$P_i^{(m)} \equiv a_{ij}^{(mn)} P_j^{(n)} \quad (15)$$

Further on, we consider two electronic states: the ground state $|g\rangle$ and the electronic excited state $|e\rangle$. Instead of evaluating propagators in eq 8 by computing the multi-dimensional vibrational overlaps in eq 9, we choose to specify a vibronic state basis using the coherent-state representation and propagate it following the time-dependent Dirac–Frenkel variational principle.

We begin with writing dimensionless Hamiltonian by introducing the dimensionless momentum $\hat{p}_k^{(n)} \equiv \sqrt{\omega_{nk}}^{-1} \hat{p}_k^{(n)}$ and coordinate $\hat{q}_k^{(n)} \equiv \sqrt{\omega_{nk}} \hat{Q}_k^{(n)}$ operators for states $n = g, e$. After inserting them in eq 6, the electronic ground-state Hamiltonian is

$$\hat{H}^{(g)} = \sum_k \frac{\omega_{gk}}{2} ((\hat{p}_k^{(g)})^2 + (\hat{q}_k^{(g)})^2) |g\rangle\langle g| \quad (16)$$

and the electronic excited-state $|e\rangle$ Hamiltonian is

$$\hat{H}^{(e)} = \left(\varepsilon_e + \Lambda_e^{\text{vib}} + \sum_k \frac{\omega_{ek}}{2} ((\hat{p}_k^{(e)})^2 + (\hat{q}_k^{(e)})^2) \right) |e\rangle - \sum_k \omega_{ek} \bar{d}_k^{(eg)} \hat{q}_k^{(eg)} \hat{q}_k^{(e)} |e\rangle \langle e| \quad (17)$$

where $\bar{d}_k^{(eg)} \equiv \sqrt{\omega_{ek}} d_k^{(eg)}$ is the dimensionless displacement and $\Lambda_e^{\text{vib}} \equiv \frac{1}{2} \sum_k \omega_{ek} (\bar{d}_k^{(eg)})^2$ is the total vibrational reorganization energy. The resulting operators in eqs 16 and 17 read

$$\hat{q}_k^{(n)} \equiv \beta_{nk,j}^{-1} a_{kj}^{(ng)} \hat{q}_j^{(g)} \quad (18)$$

$$\hat{p}_k^{(n)} \equiv \beta_{nk,j}^{-1} a_{kj}^{(ng)} \hat{p}_j^{(g)} \quad (19)$$

where $\beta_{nk,j} \equiv \sqrt{\omega_{nk}/\omega_{gj}}$. Equations 18 and 19 describe the dimensionless coordinate and momentum of the k th normal mode about its equilibrium point in the n th electronic state. Terms $\beta_{nk,j}$ appear due to the normal mode mixing and different vibrational frequencies in states g and e . We also add ε_e as the purely electronic excitation energy and set $\varepsilon_g = 0$ cm⁻¹. The total system Hamiltonian is the sum over all electronic state terms $\hat{H}_S = \hat{H}^{(g)} + \hat{H}^{(e)}$.

Solvent effects will be simulated by considering energy fluctuations of the molecular environment. Thermal fluctuations are induced by a set of quantum harmonic oscillators of a given temperature, and we will refer to this subsystem as the phonon bath. The phonon bath Hamiltonian is

$$\hat{H}_B = \sum_p \frac{w_p}{2} (\hat{p}_p^2 + \hat{q}_p^2) \quad (20)$$

where w_p is the frequency of the p th phonon mode, while \hat{p}_p and \hat{q}_p are the momentum and the coordinate operators, respectively. The interaction between the system electronic states and the phonon bath is included using the displaced oscillator model,²⁹ with the system–bath interaction Hamiltonian

$$\hat{H}_{S-B} = - \sum_p w_p f_{ep} \hat{q}_p |e\rangle\langle e| \quad (21)$$

where f_{ep} is the electron–phonon coupling strength of the p th phonon mode to the electronic state e . The electronic ground state is taken as the reference point, so it is not affected by bath fluctuations $f_{gp} = 0$. Notice that the system–bath coupling has the same form as the last term in eq 17. The electronic state energy modulation by the intramolecular and intermolecular vibrations is treated equivalently. Likewise, we get additional contribution to the reorganization energy $\Lambda_e^{\text{ph}} = \frac{1}{2} \sum_p w_p f_{ep}^2$. Usually, all excited electronic states are described as having the same coupling strength to the bath, thus changing all states' energies by the same amount. For simplicity, we absorb Λ_e^{ph} into the definition of the excited-state energy ε_e ; however, Λ_e^{ph} is still used to define the electron–phonon coupling strengths f_{ep} . The full model Hamiltonian is the sum of terms

$$\hat{H} = \hat{H}_S + \hat{H}_B + \hat{H}_{S-B} \quad (22)$$

The fluctuation characteristics of the phonon bath can be represented by the spectral density function

$$C_c''(\omega) = \frac{\pi}{2} \sum_p \int_{-\infty}^{\infty} f_{cp}^2 w_p^2 [\delta(\omega - w_p) - \delta(\omega + w_p)] \quad (23)$$

where $\delta(\omega)$ is the Dirac delta function. Integration of eq 23 over the complete frequency range defines the phonon bath reorganization energy in the n th electronic state

$$\Lambda_c^{\text{ph}} = \frac{1}{\pi} \int_0^{\infty} \frac{C_c''(\omega)}{\omega} d\omega = \frac{1}{2} \sum_p w_{pf_{cp}}^2 \quad (24)$$

Many theories have been proposed to evaluate the linear response function and the necessary polarization operator matrix elements (eqs 8 and 9), notably, the foundational theory by Yan and Mukamel,³⁴ Franck–Condon approaches,^{35–37} and the theories that include non-Condon effects.^{38–41}

We chose to compute the linear response function by propagating the Davydov D_2 trial wave function originating from the molecular chain soliton theory.^{42,43} For N electronic states, we can write an arbitrary state of the system as a superposition—the Davydov D_2 wave function is

$$|\Psi(t)\rangle = \sum_n \alpha_n(t) |n\rangle \times \underbrace{|\tilde{\lambda}_1(t), \tilde{\lambda}_2(t), \dots, \tilde{\lambda}_K(t)\rangle}_{\text{molecule state}} \times \underbrace{|\lambda_1(t), \lambda_2(t), \dots, \lambda_p(t)\rangle}_{\text{solvent phonon state}} \quad (25)$$

It utilizes the coherent-state representation for all vibrational modes. For the shifted harmonic oscillator model, the coherent states result in an exact dynamics.⁴⁴ $\alpha_n(t)$ is the amplitude of electronic state $|n\rangle$, in our case $n = g, e$. Vibrational and phonon bath modes are represented using coherent states $|\lambda(t)\rangle = \exp(\lambda(t)\hat{b}^\dagger - \lambda^*(t)\hat{b})|0\rangle$, defined with respect to the electronic ground-state vibrational modes, where $\lambda(t)$ is the coherent-state parameter and $|0\rangle$ is the vacuum state of a quantum harmonic oscillator. \hat{b}_i^\dagger and \hat{b}_i are the corresponding bosonic creation and annihilation operators. Only the electronic ground-state normal modes are represented by the coherent states, and modes of the excited state are expanded in terms of the ground-state coherent states. Davydov-type wave functions have been extensively used to model a single molecule, as well as their aggregate dynamics,^{45–49} linear and nonlinear spectra.^{50–54}

Time evolution of the Davydov D_2 wave function is obtained by applying the Euler–Lagrange equation

$$\frac{d}{dt} \left(\frac{\partial \mathcal{L}(t)}{\partial \dot{\eta}_i^*(t)} \right) - \frac{\partial \mathcal{L}(t)}{\partial \eta_i^*(t)} = 0 \quad (26)$$

to each of the time-dependent parameter $\eta_i = \alpha_n \tilde{\lambda}_i \lambda_{ip}$, where

$$\mathcal{L}(t) = \frac{i}{2} \left(\langle \Psi | \frac{d}{dt} \Psi \rangle - \langle \frac{d}{dt} \Psi | \Psi \rangle \right) - \langle \Psi | \hat{H} | \Psi \rangle \quad (27)$$

is the Lagrangian of the model given in terms of the Hamiltonian \hat{H} . For convenience, we omit explicitly writing time dependence. The Euler–Lagrange equation yields a system of coupled differential equations for the α_n , $\tilde{\lambda}_i$, and λ_p parameters of the Davydov D_2 wave function, see the Supporting Information for the full derivation. Equations describing model dynamics while the system is in the excited state $|e\rangle$ are

$$\frac{d}{dt} \alpha_e = -i \alpha_e \left(\epsilon_e + \Lambda_e^{\text{vib}} + \sum_{k,j} \frac{\omega_k^2 + \omega_j^2}{4\omega_{kj}} (a_{kj}^{\text{(eg)}})^2 \right) + i \alpha_e \left(\sum_k \frac{\omega_k}{2} d_k^{\text{(eg)}} x_k^{(e)} + \sum_q w_q \frac{f_{eq}}{\sqrt{2}} \text{Re } \lambda_q \right) \quad (28)$$

$$\frac{d}{dt} \tilde{\lambda}_k = -i \sum_j \frac{\omega_j}{\sqrt{2}} \beta_{j,k} a_{jk}^{\text{(eg)}} (x_j^{(e)} - d_j^{\text{(eg)}} + i p_j^{(e)}) \quad (29)$$

$$\frac{d}{dt} \lambda_q = -i w_q \left(\lambda_q - \frac{f_{eq}}{\sqrt{2}} \right) \quad (30)$$

where $x_k^{(e)} = \beta_{k,j} a_{kj}^{\text{(eg)}} \sqrt{2} \text{Re } \tilde{\lambda}_j$ and $p_k^{(e)} = \beta_{k,j}^{-1} a_{kj}^{\text{(eg)}} \sqrt{2} \text{Im } \tilde{\lambda}_j$ are the expectation values of operators in eqs 18 and 19. The resulting system of equations for the ground state $|g\rangle$ dynamics can be solved analytically: $\alpha_g(t) = \alpha_g(0) \exp\left(-\frac{i}{2} \sum_k \omega_{gk} t\right)$, $\tilde{\lambda}_k(t) = \tilde{\lambda}_k(0) \exp(-i\omega_{gk} t)$, $\lambda_q(t) = \lambda_q(0) \exp(-i w_q t)$. Separation of equations into the ground- and excited-state manifold is convenient for the computation of the optical observables using the response function theory. Terms due to the mixing of normal modes remain present in eqs 28 and 29. In the latter, evolution of the k th mode is influenced by the motion of all other j th modes. Equations 28–30 were solved numerically using the adaptive step size Runge–Kutta algorithm.

The temperature of the normal vibrational modes, as well as the phonon modes, is included by performing the Monte Carlo simulation to generate the thermal ensemble of the Davydov D_2 wave function trajectories. At the zero time, before optical excitation, in each trajectory, the initial coherent-state displacements $\tilde{\lambda}_q(0)$ and $\lambda_p(0)$ are sampled from the Glauber–Sudarshan distribution⁵⁵

$$\mathcal{P}(\lambda) = \mathcal{Z}^{-1} \exp(-|\lambda|^2 (e^{\omega/k_B T} - 1)) \quad (31)$$

where \mathcal{Z} is the partition function of a single coherent state $|\lambda\rangle$ with the corresponding frequency ω , k_B is the Boltzmann constant, and T is the model temperature. Observables averaged over the thermal ensemble will be denoted as $\langle \dots \rangle$. We found 500 trajectories to be sufficient to obtain the converged ensemble for the model of β -Car as described in the next section.

■ SIMULATION RESULTS

Normal Modes of β -Car in S_0 and S_2 Electronic States.

We consider a model of β -Car in thermal equilibrium with a solvent at 300 K. For the photon absorption process, β -Car is described by the electronic ground state $|S_0\rangle \equiv |g\rangle$ and the excited state $|S_2\rangle \equiv |e\rangle$. The optically dark excited state $|S_1\rangle$ does not directly participate in the electronic absorption process and is excluded.

The electronic Schrödinger equation of the β -Car molecule was solved using the density functional theory (DFT) method for the ground electronic state S_0 and the time-dependent DFT (TD-DFT) method for the electronic excited state S_2 , from which atom equilibrium positions R_0^a , R_0^b are acquired. The GAMESS⁵⁶ and Gaussian-16 codes⁵⁷ were used.

The calculation methods were based on the experience from previous calculations of resonance RAMAN spectra of carotenoids, investigation of dependence between the position of the $S_0 \rightarrow S_2$ transition and the frequency of the $\nu 1$ Raman

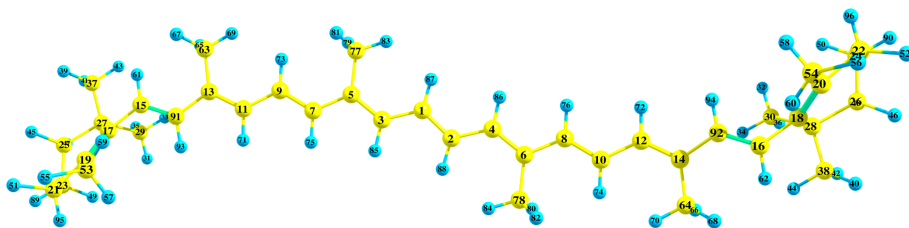


Figure 1. Structure and atom numeration of the C_{2v} symmetry carotene.

band.^{58,59} The most RAMAN intense band, ν_1 , located at around 1500 cm^{-1} , arises from the stretching of the C=C bonds. Previous calculations of the ν_1 Raman bands in the ground electronic state S_0 were performed for another carotenoid, lycopene, using the DFT method with B3LYP/6-31G, B3LYP/TZVP, B3LYP/6-31G(2df,p), BP86/6-31G(d), BPW91/6-31G(d), B3P86/6-31G(d), B3PW91/6-31G(d), and SVWN/6-31G(d) potentials.⁶⁰ It was shown that all methods based on DFT are able to perform calculation of vibrational frequencies with an overall root-mean-square error of $34\text{--}48\text{ cm}^{-1}$.⁶¹ Also, it was shown that the dependence of the Raman peak frequency shift, compared between that computed under vacuum and experimental, is linear over the whole spectra,⁵⁸ using the B3LYP/6-31G(d,p) method, and a scaling factor of 0.9613 has to be used.^{58,61} On the other hand, the energy of β -Car corresponding to the first optically allowed transition in the gas phase was reported to be between 2.85 and 2.93 eV.⁵⁹ This value is 0.62 eV higher than the excitation energy calculated using TD-DFT at the B3LYP/6-311G(d,p) level (2.224 eV).⁵⁸ Other methods give similar results: Tamm–Dancoff approximation (TDA) blyp/6-31G(d)—2.15 eV, TD b3lyp/cc-pvdz—2.19 eV, and TD b3lyp/cc-pvtz—2.21 eV.

Equilibrium structures of excited states, optimized using the TDA⁶² and TD-DFT^{63,64} with the BLYP functional, and the DZP basis set, in contrast to B3LYP, yields correct energetic order of the two lowest β -Car excited states, and it has been shown to reach an accuracy of 0.2 eV for the S_1 excitation energy in carotenoids.⁶⁵ However, later this has been explained by a fortuitous cancellation of errors caused by the neglect of double excitations in the ground and excited states.⁶⁶

We performed geometry optimization using various methods with TD-SCF, TDA-SCF basis sets and b3lyp/6-311G(d,p), blyp/6-31G(d), b3lyp/cc-pvdz, and b3lyp/cc-pvtz potentials. The Car molecule equilibrium structure and enumeration of atoms are shown in Figure 1, and the changes of the C–C bond lengths along the Car polyene chain in both electronic states calculated using the TD-SCF B3LYP/6-311G(d,p) method are shown in Figure 2. All the tested methods give similar alternation of the C–C bond lengths in the S_0 state, close to that shown in Figure 2. For the S_2 state, the situation is different—methods using the TDA-SCF basis set give alternation similar to the S_0 state case. The largest alternation of the S_2 state polyene bond lengths was achieved using the TDA blyp/6-31G(d) method. All TD-SCF calculations provide almost 10 times smaller alternation of C–C bond lengths in the middle of the polyene chain, as compared to the TDA-DFT calculations, again, similar to the results shown in Figure 2.

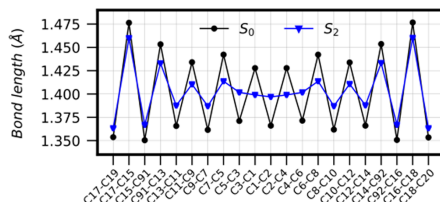


Figure 2. Polyene chain C–C bond lengths in the electronic ground state S_0 and the excited state S_2 calculated using the TD-SCF B3LYP/6-311G(d,p) method.

In order to evaluate the influence of the chosen method to the vibrational mode frequencies and their bands, we performed the calculation of vibrational spectra using TD-SCF and TDA-SCF methods with different basis sets and potentials (b3lyp/6-311G(d,p), blyp/6-31G(d), b3lyp/cc-pvdz, and b3lyp/cc-pvtz). In the S_0 state, the valence vibrational frequencies of the C–C bonds of the polyene chain scale equally and agree to within the range of 20 cm^{-1} . The same vibrational frequencies in the S_2 state also scale equally, with the exception of the TDA blyp/6-31G(d) method, as shown in Figure 3. All the tested methods agree

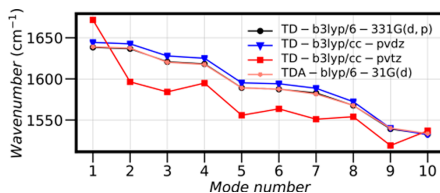


Figure 3. Polyene backbone C–C valence vibrational mode frequencies in the excited state S_2 calculated using various quantum chemistry methods.

on the C–C bond vibrational frequencies in the S_2 state within a range of 46 cm^{-1} . Previous ν_1 Raman band evaluation and correlation with $S_0 \rightarrow S_2$ excitation in the gas phase were performed under vacuum using the TD-SCF B3LYP/6-311G(d,p) method, and the results are in agreement with the experimental observations.^{58,59} Based on this knowledge, all further presented quantum chemistry calculations were performed under vacuum using the B3LYP/6-311G(d,p) method as in ref 59 and the scaling factor was not applied.

The changes in polyene chain geometry during $S_0 \rightarrow S_2$ electronic excitation causes changes in molecular electronic structure, normal mode frequencies, and vibrational mode coordinates. The C–H valence bond vibrations in all β -Car parts are in the region of 2970–3170 cm^{-1} for the ground state and in the region of 2960–3168 cm^{-1} for the excited state. The lower frequency region is characterized by the change of C=C bond lengths in polyene chain. Here, the S_0 normal mode frequencies lay in the region of 1558–1674 cm^{-1} and the corresponding region for the S_2 state is 1533–1636 cm^{-1} . Transition $S_0 \rightarrow S_2$ mainly induces differences in the polyene chain bond lengths between carbon atoms in both electronic states. As a consequence, the vibrational frequencies in the S_2 state become lower by 40–50 cm^{-1} .

Expressing normal mode coordinates in the electronic state S_2 by the normal coordinates of the ground electronic state S_0 , according to eq 12, allows us to investigate normal mode mixing upon $S_0 \rightarrow S_2$ electronic transition. In Figure 4, we plot

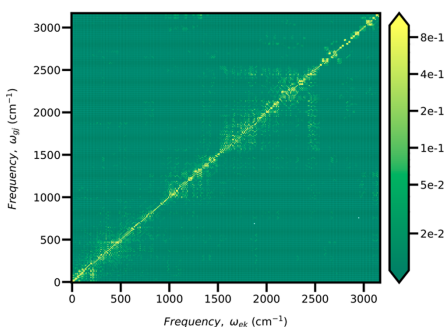


Figure 4. Expansion coefficient absolute value $|a_{kj}^{(g)}|$ of the β -Car normal modes. The k th mode in the S_2 state is expanded in terms of the mode j th in the state S_0 calculated using the TD-SCF B3LYP/6-311G(d,p) method.

the expansion coefficient absolute value $|a_{kj}^{(g)}|$, that is, the k th mode in the S_2 state is expanded in terms of the mode j th in the state S_0 . The largest expansion coefficients lay close to the main diagonal, implying that the majority of normal modes are non-negligibly mixed with similar frequency modes. However, certain modes show mixing with modes that has vastly different frequencies; for example, modes in a frequency region of $\approx 2500 \text{ cm}^{-1}$ are highly mixed with modes in a frequency range of 1500–2500 cm^{-1} . Strong mixing can also be clearly seen between modes in frequency regions of 0–250 cm^{-1} , 400–750 cm^{-1} , and 1000–1500 cm^{-1} . Such a broad frequency mixing range signifies a wide range of available vibrational relaxation pathways. At a first glance, expansion coefficients along the $\omega_{gi} = \omega_{gj}$ diagonal may look symmetric; however, they are not, even when absolute values are considered $|a_{ij}^{(g)}| \neq |a_{ji}^{(g)}|$. This demonstrates that there is no one-to-one correspondence between the β -Car normal modes in the electronic S_0 and S_2 states.

Additionally, we found that during transitions between S_0 and S_2 electronic states, the transition dipole weakly depends on the nuclear configuration. For transition $S_0 \rightarrow S_2$, the transition moment components are $\mu_{02} = (8.35, 0.71, 0.0)$ in a.u.

(21.28 Debye), while for the $S_2 \rightarrow S_0$ it is equal to $\mu_{20} = (9.45, 0.57, 0.0)$ in a.u. (24.06 Debye). The difference between the two transitions is minimal; thus, the non-Condon effects can be reasonably excluded from the calculations. The transition dipole moment is oriented with the z component being perpendicular to the plane of the polyene chain, while the x component is directed along the polyene chain.

Absorption Spectrum of the β -Carotene Model. The quantum chemistry results of the β -Car are now used to compute the absorption spectrum given by eq 7. Fourier transformation is performed on the linear response function averaged over the thermal ensemble, $\langle F(t) \rangle$, and the single trajectory of the ensemble linear response is defined in eq 8 and is equal to

$$F(t) = |\mu_{eg}^{(d)}|^2 e^{i/2 \sum_k \omega_{gk} \alpha_k^*(0) \alpha_k(t)} \times \exp \sum_k \left(e^{i\omega_{gk} t} \tilde{\lambda}_k^*(0) \tilde{\lambda}_k(t) - \frac{1}{2} (\tilde{\lambda}_k(0))^2 + \tilde{\lambda}_k(t)^2 \right) \times \exp \sum_p \left(e^{i\omega_{gp} t} \tilde{\lambda}_p^*(0) \tilde{\lambda}_p(t) - \frac{1}{2} (\tilde{\lambda}_p(0))^2 + \tilde{\lambda}_p(t)^2 \right) \quad (32)$$

It is expressed in terms of the dynamical parameters $\alpha_k(t)$, $\tilde{\lambda}_k(t)$, and $\tilde{\lambda}_p(t)$; therefore, it is enough to propagate the excited-state dynamics.

For the solvent, the phonon bath modes are defined by uniformly discretizing the spectral density function $C_w^g(\omega)$ in the frequency domain in the range $[w_{\min} = 0.1, w_{\max} = 1250] \text{ cm}^{-1}$ with discretization step size $\Delta_w = 10 \text{ cm}^{-1}$. Then, the frequency of the p th bath mode is given by $w_p = w_{\min} + (p - 1)\Delta_w$. Form of the spectral density function was chosen to be the overdamped Brownian oscillator function $C_w^g(\omega) = 2\Lambda_k^{\text{th}} \omega \gamma / (\omega^2 + \gamma^2)$. The damping parameter $\gamma = 200 \text{ cm}^{-1}$ (167 fs) has been chosen based on the previous modeling of the β -Car²⁷ spectra. The amplitude of the spectral density function is set by normalizing the f_{ep} values according to the reorganization energy definition by eq 24. The bath reorganization energy of $\Lambda_k^{\text{th}} = 100 \text{ cm}^{-1}$ has been chosen to qualitatively match the line widths of the experimental data.

The simulated absorption spectrum of the β -Car model with 282 normal modes at different temperatures is shown in Figure 5 along the experimental β -Car spectrum in diethylamine solvent at room temperature.²⁷ The absorption spectra have been normalized to their maximum value, as well as aligned on the 0–0 transition band for easier comparison. We find the 282-mode model spectrum to qualitatively reproduce the position and amplitudes of the first two absorption peaks; however, it greatly overestimates the amplitude of vibrational peak progression at 300 K temperature. Also, absorption of the high-frequency modes displays non-trivial dependence on the temperature. For majority of modes, the average thermal energy is much smaller than the energy gap between the vibrational mode energy levels, $k_B T \ll \omega$; thus, for non-mixed modes, dependence of absorption spectrum on temperature would be negligible. However, in Figure 5, we observe strong dependence of absorption on temperature due to the mode mixing; that is, thermally excited low-frequency vibrational modes contribute to the excitation of the high-frequency modes, which result in a wide high-frequency absorption shoulder.

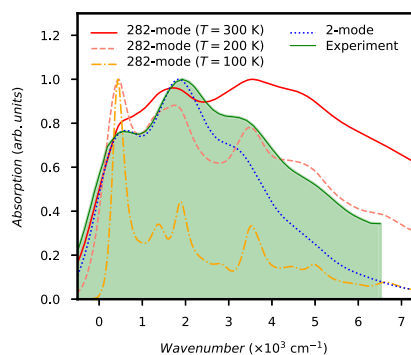


Figure 5. Absorption spectra of the β -Car model, based on the B3LYP/6-311G(d,p) method, at different temperatures along the experimental β -Car spectrum in diethylamine solvent at room temperature (shown as contoured green). The widely used two-mode model at 300 K temperature is also shown for comparison, and the model parameters are taken from ref 23. All spectra are normalized to their maximum value and aligned on their 0–0 transition band.

For comparison, we also computed the absorption spectrum of a widely used empirical two-mode β -Car model at 300 K temperature, which includes only the C=C and C–C stretching vibrational modes with no mixing between them. Typical model frequencies $\omega_{e,C=C} = 1522 \text{ cm}^{-1}$ and $\omega_{e,C-C} = 1157 \text{ cm}^{-1}$ and displacements $d_{e,C=C}^{(0)}$ = 1.3 and $d_{e,C-C}^{(0)}$ = 0.9 are taken from ref 23. To have correct line widths, the bath reorganization energy is now set to a much larger $\Lambda_b^{\text{ph}} = 800 \text{ cm}^{-1}$ to account for the lack of the rest β -Car modes. As shown in Figure 5, the two-mode model fits the first two peaks well but underestimates the amplitude of the higher frequency progression.

To further compare the 282-mode and the 2-mode models, we look at their stick absorption spectrum in Figure 6. The purely electronic transition energy is set to 0 cm^{-1} for both spectra. For visibility, the spectra have been convoluted with the $\tau = 1 \text{ ps}$ variance Gaussian function, and $\tau = 5 \text{ ps}$ is used for the spectra in the inset. The 2-mode model stick spectrum has a straightforward peak progression; that is, the spectrum is a sum of each of the two-mode peak progressions. The 282-mode model spectrum has a more complex structure. Even though each of the 282 modes has a small absorption peak, the combined spectrum produces frequency regions with non-negligible absorption intensity. These regions show a clear overlap with the absorption peaks of the two-mode model. The two-mode spectrum has peaks at 1522 and 1157 cm^{-1} frequencies, produced by the C=C and C–C stretching vibrational modes. The 282-mode spectrum has similar frequency regions, only this time, they are due to the absorption of a large number of mixed normal modes. These modes are responsible for the first two peaks seen in the Figure 5 spectra.

Looking further on in Figure 6, the 282-mode model has absorption in the 3000, 4500, and 6000 cm^{-1} frequency regions. These account for the high-frequency absorption tail seen in experiments. Due to the C=C and C–C mode

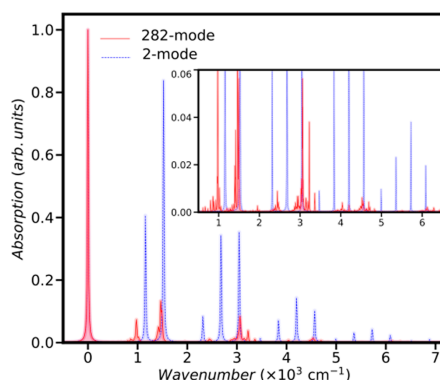


Figure 6. Stick absorption spectrum of the 282-mode model, computed using the B3LYP/6-311G(d,p) method, and the empirical 2-mode model. Purely electronic transition energy is set to 0 cm^{-1} for both spectra. For visibility, each spectrum has been convoluted with the $\tau = 1 \text{ ps}$ variance Gaussian function. The inset more closely shows low-amplitude sticks, and these have been convoluted with the $\tau = 5 \text{ ps}$ variance Gaussian function.

progression, the two-mode model has a peak at these frequencies as well; however, even though visually they look more intense than the 282-mode model peaks, Figure 5 simulations show it being the opposite. Again, the strong absorption is produced by the summation of a large number of weak intensity absorption peaks. Two harmonic modes simply cannot accurately describe absorption over such a wide range of frequencies; therefore, the high-frequency absorption of the two-mode model is lacking.

DISCUSSION

The vibrational modes of carotenoids have been extensively studied by Raman spectroscopy.^{68,69} The frequency of the most Raman-active vibration in the S_0 state is 1642.3 cm^{-1} , which changes to a weak Raman vibration of frequency 1584.08 cm^{-1} in the S_2 state. The C–C valence bond frequencies in the S_0 state lay in the region of $1018\text{--}1353 \text{ cm}^{-1}$, while it is in the region of $1156\text{--}1370 \text{ cm}^{-1}$ for the S_2 state. These frequencies are strongly mixed with the polyene chain C–H bond in-plane vibrations and the C–C valence vibrations of peripheral rings. The strongest Raman-active vibration in this region, for the S_0 state, is 1187.22 cm^{-1} , while the mode with the most similar vibrational form in the S_2 state has a frequency of 1219 cm^{-1} . The vibrations of lower frequencies are associated with the C–H vibrations outside of the polyene chain, deformations of the peripheral rings, changes of the polyene chain valence angles, dihedral angles, and the deformations of the whole molecule by twisting and waving. The frequencies of these vibrations change by no more than 10 cm^{-1} after the $S_0 \rightarrow S_2$ transition. The differences in the vibrational forms are not as strong for these modes as were in the case of the polyene chain C–C and C=C valence bond vibrations.

Recently, Balevičius Jr. and co-workers²⁰ have presented an in-depth excitation energy relaxation model in carotenoids by considering four relaxation processes. Simply put, the event of

photoexcitation instantaneously promotes the carotenoid molecules to a non-equilibrium state and launches the internal vibrational redistribution (IVR) cascade within the high-frequency optically active modes, resulting into a transient thermally "hot" state. Generally, it is assumed that the thermally hot carotenoid subsequently transfers the vibrational energy to the solvent molecules; that is, vibrational cooling (VC) takes place. The authors demonstrated how modeling the IVR and VC concurrently, and not subsequently, naturally explains the presence of the highly discussed transient absorption S^* signal⁷⁰ in terms of the vibrationally hot ground-state S_0 . The two-mode model was used; that is, only the C–C and C=C intramolecular modes were coupled to the thermal bath—their coupling strength remains speculative. Both the IVC and VC relaxation were modeled implicitly by prescribing process timescales. We have shown that the two-mode (not mixed) model is not sufficient in describing the photon absorption spectrum. In fact, upon photoexcitation, many vibrational modes become excited. No two distinctive modes could be isolated in the relevant frequency region. We observe grouping of vibrational modes in the 1000 and 1500 cm^{-1} frequency regions, as shown in Figure 6. The two-mode model yields progression of peaks with few strong features at 2700 and 4000–6000 cm^{-1} frequencies. Meanwhile, the 282-mode model has a large number of weak absorption features at these frequencies; however, it is the cumulative effect that combines them into the observed "progression". This entropic factor actually simplifies the overall electronic excitation relaxation picture since each mode is weakly coupled to the electronic transition; therefore, the weak coupling regime could be used in the theoretical models of relaxation dynamics. Consequently, the two- or multiple-quanta vibrational excitations become improbable. Hence, only the entropic factor as a cumulative effect of all modes would have decisive impact on both the IVR and VC process timescales.

In nature, carotenoids participate in the energy conversion process together with other types of pigments. Carotenoids play an important role in light-harvesting complexes by transferring their excitation to chlorophylls on a femtosecond timescale. It is especially evident in the peridinin–chlorophyll–protein, in which the dominant energy transfer occurs from the peridinin S_2 to chlorophyll Q_y state via an ultrafast coherent mechanism. The coherent superposition of the two states functions in a way as to drive the population to the final acceptor state,⁷¹ providing an important piece of evidence in the quest of connecting coherent phenomena and biological functions.⁷² This process is highly sensitive to structural perturbations of the peridinin polyene backbone, which has a profound effect on the overall lifetime of the complex.⁷³ We have found that β -Car also undergoes polyene backbone changes, mainly in its C–C bond lengths.

Also, it has been suggested that the ultrafast population transfer from the carotenoid state S_2 to the bacteriochlorophyll (BChl) state Q_x occurs due to the vibronic coupling of the carotenoid electron-vibrational DOFs to the BChl.⁷⁴ The energy flow pathway opened up by the resonance of the energy gap between the carotenoid vibrational levels, and the BChl $|g\rangle_{\text{BChl}} \rightarrow |Q_x\rangle$ transition is the primary reason for its ultrafast nature. We, hence, suggest that by going beyond the two-mode model and taking into account more carotenoid vibrational modes, in turn, more vibrational levels, the probability of resonance between the carotenoid and BChl would greatly increase, changing the overall population-transfer rate.

In conclusion, we have presented a β -Car model with a fully explicit treatment of all its 282 vibrational normal modes, which were computed using the quantum chemical methods. Additionally, we described how to treat the β -Car excited-state dynamics when in contact with solvent at finite temperature. We found β -Car to change the bond lengths between the polyene chain atoms during the $S_0 \rightarrow S_2$ electronic transition and that there is no one-to-one correspondence between the ground- and excited-state vibrational modes; that is, modes on different electronic states are highly mixed and should not be treated as being the same. The model absorption spectrum qualitatively matches the experimental data, and it better describes the high-frequency progression of the carotenoid spectrum than the typical two-mode carotenoid model.

■ ASSOCIATED CONTENT

Supporting Information

The Supporting Information is available free of charge at <https://pubs.acs.org/doi/10.1021/acs.jpca.1c06115>.

Derivation of the Davydov D_2 ansatz equations of motion for the β -carotene model using the Dirac–Frenkel variational method (PDF)

■ AUTHOR INFORMATION

Corresponding Author

Darius Abramavičius – Institute of Chemical Physics, Vilnius University, LT-10222 Vilnius, Lithuania; orcid.org/0000-0003-0087-9791; Email: darius.abramavicius@ff.vu.lt

Authors

Mantas Jakučionis – Institute of Chemical Physics, Vilnius University, LT-10222 Vilnius, Lithuania; orcid.org/0000-0001-6387-7131

Ignas Gažiūnas – Institute of Chemical Physics, Vilnius University, LT-10222 Vilnius, Lithuania

Juozas Šulskus – Institute of Chemical Physics, Vilnius University, LT-10222 Vilnius, Lithuania

Complete contact information is available at: <https://pubs.acs.org/doi/10.1021/acs.jpca.1c06115>

Notes

The authors declare no competing financial interest.

■ ACKNOWLEDGMENTS

We thank the Research Council of Lithuania for financial support (grant no. S-MIP-20-47). Computations were performed on resources at the High Performance Computing Center, "HPC Sauletekis" in Vilnius University Faculty of Physics.

■ REFERENCES

- (1) Tian, L. Recent advances in understanding carotenoid-derived signaling molecules in regulating plant growth and development. *Front. Plant Sci.* **2015**, *6*, 790.
- (2) Weaver, R. J.; Santos, E. S. A.; Tucker, A. M.; Wilson, A. E.; Hill, G. E. Carotenoid metabolism strengthens the link between feather coloration and individual quality. *Nat. Commun.* **2018**, *9*, 73.
- (3) Murchie, E. H.; Harbinson, J. Non-Photochemical Fluorescence Quenching Across Scales: From Chloroplasts to Plants to Communities. *Non-Photochemical Fluorescence Quenching Across Scales: From Chloroplasts to Plants to Communities*; Springer: Dordrecht, 2014, pp 553–582.

- (4) Ruban, A. V. Nonphotochemical chlorophyll fluorescence quenching: Mechanism and effectiveness in protecting plants from photodamage. *Plant Physiol.* **2016**, *170*, 1903–1916.
- (5) Ruban, A. V.; Berera, R.; Illoia, C.; Van Stokkum, I. H. M.; Kennis, J. T. M.; Pascal, A. A.; Van Amerongen, H.; Robert, B.; Horton, P.; Van Grondelle, R. Identification of a mechanism of photoprotective energy dissipation in higher plants. *Nature* **2007**, *450*, 575–578.
- (6) Holt, N. E.; Zigmantas, D.; Valkunas, L.; Li, X.-P.; Niyogi, K. K.; Fleming, G. R. Carotenoid cation formation and the regulation of photosynthetic light harvesting. *Science* **2005**, *307*, 433–436.
- (7) Llansola-Portoles, M. J.; Sobotka, R.; Kish, E.; Shukla, M. K.; Pascal, A. A.; Polivka, T.; Robert, B. Twisting a β -Carotene, an Adaptive Trick from Nature for Dissipating Energy during Photo-protection. *J. Biol. Chem.* **2017**, *292*, 1396–1403.
- (8) Bode, S.; Quentmeier, C. C.; Liao, P.-N.; Hafi, N.; Barros, T.; Wilk, L.; Bittner, F.; Walla, P. J. On the regulation of photosynthesis by excitonic interactions between carotenoids and chlorophylls. *Proc. Natl. Acad. Sci. U.S.A.* **2009**, *106*, 12311–12316.
- (9) Cupellini, L.; Calvani, D.; Jacquemin, D.; Mennucci, B. Charge transfer from the carotenoid can quench chlorophyll excitation in antenna complexes of plants. *Nat. Commun.* **2020**, *11*, 662.
- (10) Polivka, T.; Sundström, V. Ultrafast Dynamics of Carotenoid Excited States—From Solution to Natural and Artificial Systems. *Chem. Rev.* **2004**, *104*, 2021–2072.
- (11) Llansola-Portoles, M. J.; Pascal, A. A.; Robert, B. Electronic and vibrational properties of carotenoids: from in vitro to in vivo. *J. R. Soc. Interface* **2017**, *14*, 20170504.
- (12) Bautista, J. A.; Connors, R. E.; Raju, B. B.; Hiller, R. G.; Sharples, F. P.; Gosztola, D.; Wasielewski, M. R.; Frank, H. A. Excited State Properties of Peridinin: Observation of a Solvent Dependence of the Lowest Excited Singlet State Lifetime and Spectral Behavior Unique among Carotenoids. *J. Phys. Chem. B* **1999**, *103*, 8751–8758.
- (13) Frank, H. A.; Bautista, J. A.; Josue, J.; Pendon, Z.; Hiller, R. G.; Sharples, F. P.; Gosztola, D.; Wasielewski, M. R. Effect of the Solvent Environment on the Spectroscopic Properties and Dynamics of the Lowest Excited States of Carotenoids. *J. Phys. Chem. B* **2000**, *104*, 4569–4577.
- (14) Tamm, I. Relativistic Interaction of Elementary Particles. *Sel. Pap.* **1991**, *9*, 157–174.
- (15) Dancoff, S. M. Non-adiabatic meson theory of nuclear forces. *Phys. Rev.* **1950**, *78*, 382–385.
- (16) Andreussi, O.; Knecht, S.; Marian, C. M.; Kongsted, J.; Mennucci, B. Carotenoids and light-harvesting: From DFT/MRCI to the Tamm-Dancoff approximation. *J. Chem. Theory Comput.* **2015**, *11*, 655–666.
- (17) Vaswani, H. M.; Hsu, C.-P.; Head-Gordon, M.; Fleming, G. R. Quantum Chemical Evidence for an Intramolecular Charge-Transfer State in the Carotenoid Peridinin—Chlorophyll—Protein. *J. Phys. Chem. B* **2003**, *107*, 7940–7946.
- (18) Hashimoto, H.; Uragami, C.; Yukihira, N.; Gardiner, A. T.; Cogdell, R. J. Understanding/unravelling carotenoid excited singlet states. *J. R. Soc. Interface* **2018**, *15*, 20180026.
- (19) Premvardhan, L.; Papagiannakis, E.; Hiller, R. G.; Van Grondelle, R. The charge-transfer character of the S₀ → S₂ transition in the carotenoid peridinin is revealed by stark spectroscopy. *J. Phys. Chem. B* **2005**, *109*, 15589–15597.
- (20) Balevičius, V.; Wei, T.; Di Tommaso, D.; Abramavicius, D.; Hauer, J.; Polivka, T.; Duffy, C. D. The full dynamics of energy relaxation in large organic molecules: From photo-excitation to solvent heating. *Chem. Sci.* **2019**, *10*, 4792–4804.
- (21) Mendes-Pinto, M. M.; Sansiaume, E.; Hashimoto, H.; Pascal, A. A.; Gall, A.; Robert, B. Electronic absorption and ground state structure of carotenoid molecules. *J. Phys. Chem. B* **2013**, *117*, 11015–11021.
- (22) Wei, T.; Balevičius, V.; Polivka, T.; Ruban, A. V.; Duffy, C. D. P. How carotenoid distortions may determine optical properties: Lessons from the orange carotenoid protein. *Phys. Chem. Chem. Phys.* **2019**, *21*, 23187–23197.
- (23) Polivka, T.; Zigmantas, D.; Frank, H. A.; Bautista, J. A.; Herek, J. L.; Koyama, Y.; Fujii, R.; Sundström, V. Near-infrared time-resolved study of the S₁ state dynamics of the carotenoid spheroidene. *J. Phys. Chem. B* **2001**, *105*, 1072–1080.
- (24) Christensson, N.; Milota, F.; Nemeth, A.; Sperling, J.; Kauffmann, H. F.; Pullerits, T.; Hauer, J. Two-dimensional electronic spectroscopy of β -carotene. *J. Phys. Chem. B* **2009**, *113*, 16409–16419.
- (25) Balevičius, V.; Abramavicius, D.; Polivka, T.; Galesian Pour, A.; Hauer, J. A Unified Picture of S* in Carotenoids. *J. Phys. Chem. Lett.* **2016**, *7*, 3347–3352.
- (26) Fox, K. F.; Balevičius, V.; Chmeliov, J.; Valkunas, L.; Ruban, A. V.; Duffy, C. D. P. The carotenoid pathway: What is important for excitation quenching in plant antenna complexes? *Phys. Chem. Chem. Phys.* **2017**, *19*, 22957–22968.
- (27) Gong, N.; Fu, H.; Wang, S.; Cao, X.; Li, Z.; Sun, C.; Men, Z. All-trans- β -carotene absorption shift and electron-phonon coupling modulated by solvent polarizability. *J. Mol. Liq.* **2018**, *251*, 417–422.
- (28) Valkunas, L.; Abramavicius, D.; Mancal, T. *Molecular Excitation Dynamics and Relaxation*; John Wiley & Sons, Ltd, 2013.
- (29) May, V.; Kühn, O. *Charge and Energy Transfer Dynamics in Molecular Systems*. 3rd Ed.; Wiley-VCH Verlag GmbH & Co. KGaA: Weinheim, Germany, 2011.
- (30) Letokhov, V. S. Principles of nonlinear optical spectroscopy. *Uspekhi Fiz. Nauk*; Oxford University Press, 1998; Vol. 168, p 591.
- (31) Duschinsky, F. On the Interpretation of Electronic Spectra of Polyatomic Molecules. *Acta Physicochim. URSS* **1937**, *7*, 551–566.
- (32) Sando, G. M.; Spears, K. G.; Hupp, J. T.; Ruhoff, P. T. Large electron transfer rate effects from the Duschinsky mixing of vibrations. *J. Phys. Chem. A* **2001**, *105*, 5317–5325.
- (33) Meier, P.; Rauhut, G. Comparison of methods for calculating Franck-Condon factors beyond the harmonic approximation: How important are Duschinsky rotations? *Mol. Phys.* **2015**, *113*, 3859–3873.
- (34) Yan, Y. J.; Mukamel, S. Eigenstate-free, Green function, calculation of molecular absorption and fluorescence line shapes. *J. Chem. Phys.* **1986**, *85*, 5908–5923.
- (35) Borrelli, R.; Peluso, A. Dynamics of radiationless transitions in large molecular systems: A Franck-Condon-based method accounting for displacements and rotations of all the normal coordinates. *J. Chem. Phys.* **2003**, *119*, 8437–8448.
- (36) Ianconescu, R.; Pollak, E. Photoinduced cooling of polyatomic molecules in an electronically excited state in the presence of duschinskii rotations. *J. Phys. Chem. A* **2004**, *108*, 7778–7784.
- (37) Borrelli, R.; Capobianco, A.; Peluso, A. Franck-Condon factors—Computational approaches and recent developments. *Can. J. Chem.* **2013**, *91*, 495–504.
- (38) Niu, Y.; Peng, Q.; Deng, C.; Gao, X.; Shuai, Z. Theory of excited state decays and optical spectra: Application to polyatomic molecules. *J. Phys. Chem. A* **2010**, *114*, 7817–7831.
- (39) Borrelli, R.; Capobianco, A.; Peluso, A. Generating function approach to the calculation of spectral band shapes of free-base chlorin including Duschinsky and Herzberg-Teller effects. *J. Phys. Chem. A* **2012**, *116*, 9934–9940.
- (40) Baiardi, A.; Bloino, J.; Barone, V. General time dependent approach to vibronic spectroscopy including franck-condon, herzberg-teller, and duschinsky effects. *J. Chem. Theory Comput.* **2013**, *9*, 4097–4115.
- (41) Toutounji, M. Spectroscopy of Vibronically Coupled and Duschinskally Rotated Polyatomic Molecules. *J. Chem. Theory Comput.* **2020**, *16*, 1690–1698.
- (42) Davydov, A. S. Solitons in molecular systems. *Phys. Scr.* **1979**, *20*, 387–394.
- (43) Scott, A. C. Davydov's soliton revisited. *Phys. D* **1991**, *51*, 333–342.
- (44) Choi, J. R. Coherent states of general time-dependent harmonic oscillator. *Pramana - J. Phys.* **2004**, *62*, 13–29.

- (45) Sun, J.; Luo, B.; Zhao, Y. Dynamics of a one-dimensional Holstein polaron with the Davydov ansätze. *Phys. Rev. B: Condens. Matter Mater. Phys.* **2010**, *82*, 014305.
- (46) Chorošajev, V.; Rancova, O.; Abramavičius, D. Polaronic effects at finite temperatures in the B850 ring of the LH2 complex. *Phys. Chem. Chem. Phys.* **2016**, *18*, 7966–7977.
- (47) Wang, L.; Chen, L.; Zhou, N.; Zhao, Y. Variational dynamics of the sub-Ohmic spin-boson model on the basis of multiple Davydov D1 states. *J. Chem. Phys.* **2016**, *144*, 024101.
- (48) Jakučionis, M.; Chorošajev, V.; Abramavičius, D. Vibrational damping effects on electronic energy relaxation in molecular aggregates. *Chem. Phys.* **2018**, *515*, 193–202.
- (49) Jakučionis, M.; Mančal, T.; Abramavičius, D. Modeling irreversible molecular internal conversion using the time-dependent variational approach with sD2 ansatz. *Phys. Chem. Chem. Phys.* **2020**, *22*, 8952–8962.
- (50) Sun, K.-W.; Gelin, M. F.; Chernyak, V. Y.; Zhao, Y. Davydov Ansatz as an efficient tool for the simulation of nonlinear optical response of molecular aggregates. *J. Chem. Phys.* **2015**, *142*, 212448.
- (51) Zhou, N.; Chen, L.; Huang, Z.; Sun, K.; Tanimura, Y.; Zhao, Y. Fast, Accurate Simulation of Polaron Dynamics and Multidimensional Spectroscopy by Multiple Davydov Trial States. *J. Phys. Chem. A* **2016**, *120*, 1562–1576.
- (52) Chorošajev, V.; Marčulionis, T.; Abramavičius, D. Temporal dynamics of excitonic states with nonlinear electron-vibrational coupling. *J. Chem. Phys.* **2017**, *147*, 74114.
- (53) Somoza, A. D.; Sun, K.-W.; Molina, R. A.; Zhao, Y. Dynamics of coherence, localization and excitation transfer in disordered nanorings. *Phys. Chem. Chem. Phys.* **2017**, *19*, 25996–26013.
- (54) Chen, L.; Gelin, M. F.; Domcke, W. Multimode quantum dynamics with multiple Davydov D2 trial states: Application to a 24-dimensional conical intersection model. *J. Chem. Phys.* **2019**, *150*, 024101.
- (55) Glauber, R. J. Coherent and incoherent states of the radiation field. *Phys. Rev.* **1963**, *131*, 2766–2788.
- (56) Schmidt, M. W.; Baldrige, K. K.; Boatz, J. A.; Elbert, S. T.; Gordon, M. S.; Jensen, J. H.; Koseki, S.; Matsunaga, N.; Nguyen, K. A.; Su, S.; et al. General atomic and molecular electronic structure system. *J. Comput. Chem.* **1993**, *14*, 1347–1363.
- (57) Frisch, M. J.; Trucks, G. W.; Schlegel, H. B.; Scuseria, G. E.; Robb, M. A.; Cheeseman, J. R.; Scalmani, G.; Barone, V.; Petersson, G. A.; Nakatsuji, H.; et al. *Gaussian 16*, Revision C.01.; Gaussian Inc.: Wallingford CT, 2016.
- (58) Macernis, M.; Sulskus, J.; Malickaja, S.; Robert, B.; Valkunas, L. Resonance raman spectra and electronic transitions in carotenoids: A density functional theory study. *J. Phys. Chem. A* **2014**, *118*, 1817–1825.
- (59) Macernis, M.; Galzerano, D.; Sulskus, J.; Kish, E.; Kim, Y.-H.; Koo, S.; Valkunas, L.; Robert, B. Resonance Raman spectra of carotenoid molecules: Influence of methyl substitutions. *J. Phys. Chem. A* **2015**, *119*, 56–66.
- (60) Liu, W.; Wang, D.-M.; Zheng, Z.-R.; Li, A.; Su, W.-H. Solvent effects on the S0 S2 absorption spectra of β -carotene. *Chin. Phys. B* **2010**, *19*, 013102–013106.
- (61) Wong, M. W. Vibrational frequency prediction using density functional theory. *Chem. Phys. Lett.* **1996**, *256*, 391–399.
- (62) Hirata, S.; Head-Gordon, M. Time-dependent density functional theory within the Tamm-Dancoff approximation. *Chem. Phys. Lett.* **1999**, *314*, 291–299.
- (63) Casida, M. E. *Time-Dependent Density Functional Response Theory for Molecules*; Université de Montréal, 1995, pp 155–192.
- (64) Dreuw, A.; Head-Gordon, M. Single-reference ab initio methods for the calculation of excited states of large molecules. *Chem. Rev.* **2005**, *105*, 4009–4037.
- (65) Dreuw, A. Influence of geometry relaxation on the energies of the S1 and S2 states of violaxanthin, zeaxanthin, and lutein. *J. Phys. Chem. A* **2006**, *110*, 4592–4599.
- (66) Starcke, J. H.; Wormit, M.; Schirmer, J.; Dreuw, A. How much double excitation character do the lowest excited states of linear polyenes have? *Chem. Phys.* **2006**, *329*, 39–49.
- (67) Balevičius, V.; Pour, A. G.; Savolainen, J.; Lincoln, C. N.; Lukeš, V.; Riedle, E.; Valkunas, L.; Abramavičius, D.; Hauer, J. Vibronic energy relaxation approach highlighting deactivation pathways in carotenoids. *Phys. Chem. Chem. Phys.* **2015**, *17*, 19491–19499.
- (68) de Oliveira, V. E.; Castro, H. V.; Edwards, H. G.; de Oliveiraa, L. F. C. Carotenes and carotenoids in natural biological samples: A Raman spectroscopic analysis. *J. Raman Spectrosc.* **2010**, *41*, 642–650.
- (69) Tschirner, N.; Schenderlein, M.; Brose, K.; Schlodder, E.; Mroginski, M. A.; Thomsen, C.; Hildebrandt, P. Resonance Raman spectra of β -carotene in solution and in photosystems revisited: an experimental and theoretical study. *Phys. Chem. Chem. Phys.* **2009**, *11*, 11471–11478.
- (70) Polívka, T.; Sundström, V. Dark excited states of carotenoids: Consensus and controversy. *Chem. Phys. Lett.* **2009**, *477*, 1–11.
- (71) Roscioli, J. D.; Ghosh, S.; LaFountain, A. M.; Frank, H. A.; Beck, W. F. Quantum Coherent Excitation Energy Transfer by Carotenoids in Photosynthetic Light Harvesting. *J. Phys. Chem. Lett.* **2017**, *8*, 5141–5147.
- (72) Meneghin, E.; Volpato, A.; Cupellini, L.; Bolzonello, L.; Jurinovich, S.; Mascoli, V.; Carbonera, D.; Mennucci, B.; Collini, E. Coherence in carotenoid-to-chlorophyll energy transfer. *Nat. Commun.* **2018**, *9*, 3160.
- (73) Ghosh, S.; Bishop, M. M.; Roscioli, J. D.; LaFountain, A. M.; Frank, H. A.; Beck, W. F. Excitation Energy Transfer by Coherent and Incoherent Mechanisms in the Peridinin-Chlorophyll a Protein. *J. Phys. Chem. Lett.* **2017**, *8*, 463–469.
- (74) Perlik, V.; Seibt, J.; Cranston, L. J.; Cogdell, R. J.; Lincoln, C. N.; Savolainen, J.; Sanda, F.; Mančal, T.; Hauer, J. Vibronic coupling explains the ultrafast carotenoid-to-bacteriochlorophyll energy transfer in natural and artificial light harvesters. *J. Chem. Phys.* **2015**, *142*, 212434.

**HAZARD AWARENESS
REDUCES LAB INCIDENTS**

**ACS Essentials of
Lab Safety for
General Chemistry**

A new course from the
American Chemical Society

ACS Institute
Learn. Develop. Excel.

EXPLORE
ORGANIZATIONAL
SALES
solutions.acs.org/essentialsoflabsafety

REGISTER FOR
INDIVIDUAL ACCESS
institute.acs.org/courses/essentials-lab-safety.html

A2

Modelling irreversible molecular internal conversion using the
time-dependent variational approach with sD2 ansatz

M. Jakučionis, T. Mancal, D. Abramavičius

Physical Chemistry Chemical Physics, **22**, 8952-8962 (2020)

Reproduced with permission from the Royal Society of Chemistry.

Cite this: *Phys. Chem. Chem. Phys.*,
2020, 22, 8952

Modeling irreversible molecular internal conversion using the time-dependent variational approach with sD_2 ansatz†

Mantas Jakučionis,^a Tomas Mancal^b and Darius Abramavičius^{b,*†}

Effects of non-linear coupling between the system and the bath vibrational modes on the system internal conversion dynamics are investigated using the Dirac–Frenkel variational approach with a newly defined sD_2 ansatz. It explicitly accounts for the entangled system electron–vibrational states, while the bath quantum harmonic oscillator states are expanded in a superposition of quantum coherent states. Using a non-adiabatically coupled three-level model, we show that efficient irreversible internal conversion due to quadratic vibrational–bath coupling occurs when the initially populated system vibrational levels are in resonance with the vibrational levels of a lower energy electronic state, also, a non-Gaussian bath wavepacket representation is required. The quadratic system–bath couplings result in broadened and asymmetrically squeezed bath quantum harmonic oscillator wavepackets in the coordinate–momentum phase space.

Received 26th February 2020,
Accepted 26th March 2020

DOI: 10.1039/d0cp01092h

rsc.li/pccp

1. Introduction

Function of many biological molecular systems is tightly connected to the process of energy relaxation in their electronic or vibrational (or both) manifolds. The problem of unraveling photo-excitation energy relaxation pathways is relevant on a wide range of molecular spatial scales: from the smallest molecular aggregates, consisting of just a couple of molecules,^{1–4} to photosynthetic complexes involving tens or hundreds of pigments.^{5–7} Generally, due to a high number of degrees of freedom (DOF) involved, brute-force numerical simulations of non-equilibrium dynamics in even the smallest systems are challenging. The standard approach to overcome this challenge is to apply the reduced (density operator) description within the theory of open quantum systems.^{8–10} In this description the most relevant electronic and vibrational DOFs of the problem constitute the observable system, while all the rest of the DOFs are treated as a part of the fluctuating thermal reservoir – the bath. When such a distinction is associated with a small parameter characterizing the interaction strength between the system and the bath, relatively simple perturbative approaches are sufficient to describe energy relaxation phenomena. In a more general case, division into the system and its bath is only formal, as electronic states may be strongly coupled to both the vibrational states of the system and those of the bath. As a result, excitation energy exchange

mechanisms between different states have to be modeled non-perturbatively since the system and the bath become essentially inseparable.

Dynamics of open quantum systems can be obtained using a broad range of techniques. In recent years, a formally exact, but relatively expensive, approach of the Hierarchical equations of motion^{11–14} has gained popularity. Among the perturbative methods, various forms of the Redfield theory^{15,16} of the weak system–bath coupling, and the Förster type of methods^{17–20} for the weak resonance coupling limit, still play an essential role in understanding biologically relevant energy transfer and relaxation processes. Among the phenomenological approaches, the Lindblad equations^{10,21} with their convenient formal properties provide the basis for cheap and reliable modelling. All the above-mentioned techniques are based on the density operator description, however, for the same purposes one can also directly treat the wavefunction itself, *i.e.*, to expand electronic and vibrational states of the model in a chosen electron–vibrational state basis. One family of formally exact wavefunction approaches is based on the multi-configuration time-dependent Hartree method (MCTDH)^{22,23} and include its multi-layer,^{24,25} Gaussian-based^{26,27} extensions. Additionally, methods of coupled coherent states,^{28,29} its generalization to non-adiabatic dynamics – multiconfigurational Ehrenfest,^{30,31} variational multiconfigurational Gaussians,^{32,33} and iterative real-time path integral^{34,35} are also available.

A wavefunction technique utilizing the time-dependent Dirac–Frenkel variational principle with a trial wavefunction (ansatz) based on the Davydov D_2 ansatz for the molecular chain soliton theory^{36,37} is also being developed. It models dynamics of both the system and the bath vibrational DOFs approximately by

^a Institute of Chemical Physics, Vilnius University, Sauletekio Ave. 9–III, LT-10222 Vilnius, Lithuania. E-mail: darius.abramavicius@ff.vu.lt

^b Faculty of Mathematics and Physics, Charles University, Ke Karlovu 5, 121 16 Prague, Czech Republic

† Electronic supplementary information (ESI) available. See DOI: 10.1039/d0cp01092h

representing vibrational states using coherent states (CSs). Accuracy of the technique has been shown to improve by considering variants of the Davydov ansätze, *i.e.*, the D_1 ansatz^{38,39} or by using the intermediately complex $D_{1.5}$ ansatz.⁴⁰ Still, the greatest improvement came by considering a trial wavefunction made of a linear superposition of the Davydov D_2 ansatz (multi- D_2) and its more complex multi- D_1 variant,^{41–43} where electronic and vibrational DOFs become mixed beyond Born–Oppenheimer approximation (BOA). Simulations of exciton and polaron dynamics and the non-linear optical spectra of molecular aggregates,^{38,44} light harvesting complexes,⁴⁵ also, dynamics of a simplified pyrazine excitation relaxation through conical intersection,⁴⁶ have proven the technique to be a potent and flexible tool for simulating open quantum system excitation energy relaxation dynamics and both the linear and non-linear spectra. However, laborious numerical calculations are required since the approaches result in a huge number of coupled nonlinear differential equations.

In the present work, we extend this approach by considering non-linear system-bath coupling terms to allow for vibrational energy exchange between the system and the bath vibrational DOFs within the normal mode description, using the modified multi- D_2 ansatz *within* BOA. Entangled system electron-vibrational states were included formally exactly using a coordinate representation, while the bath vibrational states were represented by a superposition of coherent states. We show that efficient irreversible internal conversion can be achieved within BOA and suggest resonance conditions between the electronic state energy gap and system vibrational mode frequency, in addition to the highly non-Gaussian bath wavepacket representation.

The rest of the paper is organized as follows: in Section II we specify a general interacting system-bath model and give a brief overview of the Dirac–Frenkel variational principle, while the derivations of the model equations of motion are presented in ESL† In Section III we present dynamics of a simulated excitation relaxation between a non-adiabatically coupled three-level model with anharmonic potential energy surfaces (PESs) and non-linear vibrational-bath coupling. Results, relevance and a general applicability of our approach are also discussed. Conclusions are provided in Section IV. In Appendix A we present investigation of the initially non-degenerate CS representation on dynamics convergence.

II. Theory

We consider a simple quantum system consisting of electronic and vibrational DOFs. Electronic states and specific internal vibrational DOFs (*e.g.* anharmonic molecular vibrations) constitute the observable system (a molecule). This vibronic system is coupled to a fluctuating bath, composed of many external vibrational DOFs of a molecular environment, *e.g.* vibrations of a polymeric matrix, proteins, solvent molecules, *etc.* Here, and throughout the paper, for the internal and external vibrational manifold we will use dimensionless coordinates x, χ and momenta p, ρ , respectively, and set the reduced Planck constant equal to one ($\hbar = 1$).

The Hamiltonian operator \hat{H} of the described quantum system as usual can be written as a sum of the system operator

\hat{H}_S , the bath operator \hat{H}_B , electronic-bath interaction operator \hat{H}_{E-B} and internal vibrational-bath interaction operator \hat{H}_{V-B}

$$\hat{H} = \hat{H}_S + \hat{H}_B + \hat{H}_{E-B} + \hat{H}_{V-B}. \quad (1)$$

The system consists of N electronic states $|n\rangle$ ($n = 0, 1, \dots, N$), with ϵ_n representing the ground-excited state transition ($|0\rangle \rightarrow |n\rangle$) energies. Each electronic state $|n\rangle$ is attached to Q internal vibrational modes. Vibrational modes $q = 1, 2, \dots, Q$ are characterized by the generalized Q -dimensional PES $V(\mathbf{x})$, where $\mathbf{x} = (x_1, x_2, \dots, x_Q)$ is a Q -dimensional space point. PESs attached to different electronic states may differ, thus, the surface associated with the state $|n\rangle$ will be labelled as a diagonal term $V_{nn}(\mathbf{x})$.

To represent quantum states of a system vibrational mode q , we use the coordinate representation for which the action of coordinate operator \hat{x}_q on coordinate state $|x_q\rangle$ has the eigenvalue x_q : $\hat{x}_q|x_q\rangle = x_q|x_q\rangle$. For each mode q we consider coordinate states with eigenvalues from the interval $x_q \in [x_q^{\min}, x_q^{\max}]$ with equidistant spacing δx_q between the states. States $|x_q\rangle$ form a Q -dimensional space states $|\mathbf{x}\rangle \equiv |x_1\rangle |x_2\rangle \dots |x_Q\rangle$ with orthonormality condition $\langle x_q|x_{q'}\rangle = \delta_{q,q'}\delta(x_q - x_{q'})$, where $\delta_{a,b}$ and $\delta(\epsilon)$ are Kronecker and Dirac delta functions, respectively. We will refer to the generalized system electronic-vibrational states

$$|n, \mathbf{x}\rangle \equiv |n\rangle |x_1\rangle |x_2\rangle \dots |x_Q\rangle, \quad (2)$$

as vibronic states.

It is well established that the PESs $V_{nn}(\mathbf{x})$ of different molecular electronic states can get close to each other in their energies (the avoided crossing region) or even cross each other (the conical intersection),⁴⁷ allowing for non-radiative excitation relaxation between different electronic states. Such a transition is called the internal conversion. During the internal conversion, the molecule traverses to the lower energy electronic state $|n\rangle \rightarrow |m < n\rangle$ with the excess energy $\epsilon_n - \epsilon_m > 0$ being converted into the molecular vibrational energy (reverse transition is also possible). Such a process is facilitated by the non-adiabatic interaction between PESs of electronic state $|n\rangle$ and $|m\rangle$, *i.e.*, by Q -dimensional off-diagonal PES term $V_{nm}(\mathbf{x}) = V_{mn}(\mathbf{x})$.

Therefore, the complete Hamiltonian of the system is defined as

$$\hat{H}_S = \sum_n \epsilon_n |n\rangle \langle n| + \sum_q \frac{\omega_q}{2} \hat{p}_q^2 + \sum_{n,m} \hat{V}_{nm}(\mathbf{x}) |n\rangle \langle m|, \quad (3)$$

where $\hat{p}_q = -i \frac{\partial}{\partial x_q}$ is the system-related momentum operator.

The Hamiltonian operator of the bath is simply that of quantum harmonic oscillators (QHOs). In the unit-mass representation we can write

$$\hat{H}_B = \sum_p \frac{w_p}{2} \left(\hat{\rho}_p^2 + \hat{\chi}_p^2 \right). \quad (4)$$

We assume that before an external excitation, the system is in its electronic ground state $|0\rangle$ and both the system and bath vibrational DOFs are in a state of thermodynamic equilibrium. All system-bath coupling terms will be defined with respect to this pre-excitation equilibrium state, therefore, the system in its

ground state is stationary (*i.e.* it is effectively not influenced by the bath DOFs in any way).

System-bath interactions will be modelled *via* two mechanisms. First, the excited electronic state energies are to be modulated by the bath fluctuations. This will be modeled using the shifted PES model,¹⁸ *i.e.*, surfaces $V_m(\mathbf{x})$ are shifted along the bath oscillator reaction coordinates χ_p by s_{np} , relative to the minimum of the $V_{00}(\mathbf{x})$. For convenience, we choose displacements to be directed in the positive χ_p axis. In the regime of linear electronic-bath interaction, the coupling is described by the Hamiltonian operator

$$\hat{H}_{E-B} = \sum_{n,p} w_p \left(\frac{1}{2} s_{np}^2 - s_{np} \hat{\chi}_p \right) |n\rangle \langle n|, \quad (5)$$

where the first term represents a shift of the electronic state $|n\rangle$ excitation energy, while the second term induces dynamical electronic state $|n\rangle$ energy modulation *via* fluctuating bath coordinate χ_p . This additional excitation energy shift of the $|n\rangle$ state is usually termed the bath reorganization energy A_n^{bath} , and it is often merged with the \hat{v}_n . We keep them separate in this work. Second, to allow vibrational energy relaxation in the system (vibrational energy exchange between the system and the bath), we include interaction terms between vibrational system coordinates and the bath modes up to a second order. Then the corresponding vibrational-bath interaction Hamiltonian reads as

$$\hat{H}_{V-B} = \sum_{n,q,p} \left(k_{np}^{(1,1)} \hat{\chi}_q \hat{\chi}_p + k_{np}^{(1,2)} \hat{\chi}_q \hat{\chi}_p^2 + k_{np}^{(2,1)} \hat{\chi}_q^2 \hat{\chi}_p \right) |n\rangle \langle n|, \quad (6)$$

where matrices $k_{np}^{(1,1)}$, $k_{np}^{(1,2)}$, $k_{np}^{(2,1)}$ define interaction strengths between vibrational mode q and p when the system is in the electronic state $|n\rangle$ for different order coupling terms, indicated by the superscript. The first term includes a single-quantum dissipative transitions, while the last two terms allows the double-quanta emission events.

Statistical properties of the bath can be defined for a single specific system-bath coupling term. For example, according to eqn (5), the excited electronic state $|n\rangle$ energy modulation by the bath fluctuations can be characterized by the spectral density function $C_n''(w)$,^{8–10} which can be defined in terms of $V_m(\mathbf{x})$ displacements s_{np} as

$$C_n''(v) = \frac{\pi}{2} \sum_p s_{np}^2 w_p^2 (\delta(v - w_p) - \delta(v + w_p)). \quad (7)$$

Here v is the parameter of the spectral density function $-\infty < v < \infty$, while $w_p > 0$ denotes the frequency of the bath oscillators. Note that this form leads to $C_n''(v) = -C_n''(-v)$. The corresponding bath reorganization energy is then given by

$$A_n^{\text{bath}} = \int_0^\infty \frac{dv C_n''(v)}{\pi v} \equiv \frac{1}{2} \sum_p s_{np}^2 w_p. \quad (8)$$

The constant π comes from normalization of the involved Fourier transform. Combining eqn (7) and (8), the bath oscillator displacement absolute values $|s_{np}|$ can be expressed as

$$|s_{np}| = \frac{1}{w_p} \sqrt{\frac{2C_n''(w_p) dv}{\pi}}, \quad (9)$$

where dv is the discretization step size.

To define other system-bath coupling matrices, we further assume for simplicity that both electronic and vibrational DOFs of the system interact with the same DOFs of the bath (the same external vibrational modes), and the interaction strength matrix $k_{np}^{(\beta)}$ elements, with $\beta = \{1,1\}, \{1,2\}, \{2,1\}$, will then be expressed in terms of displacements s_{np} (see ref. 48)

$$k_{np}^{(\beta)} = \gamma^{(\beta)} \frac{w_p |s_{np}|}{\sqrt{2}}, \quad (10)$$

for all q , where $\gamma^{(\beta)}$ is a dimensionless vibrational-bath interaction strength scaling factor. This implies that all intramolecular vibrational modes will have the same capacity for relaxation.

Equations of the model dynamics are obtained by applying the time-dependent Dirac-Frenkel variational method.⁴⁹ The main idea behind Dirac-Frenkel variational method is that a parametrized trial wavefunction $|\Psi(\xi(t))\rangle$ is varied so that the model Lagrangian $\mathcal{L}(t)$ is maintained at an extremum. For this purpose, the time evolution of every free parameter $\xi_i(t)$ is deduced using the Euler-Lagrange equation⁵⁰

$$\frac{d}{dt} \left(\frac{\partial \mathcal{L}(t)}{\partial \dot{\xi}_i(t)} \right) - \frac{\partial \mathcal{L}(t)}{\partial \xi_i(t)} = 0, \quad (11)$$

where $\dot{\xi}_i$ is the time derivative of ξ_i and the Lagrangian $\mathcal{L}(t)$ of the model is given by

$$\begin{aligned} \mathcal{L}(t) = & \frac{i}{2} (\langle \Psi(\xi(t)) | \dot{\Psi}(\xi(t)) \rangle - \langle \Psi(\xi(t)) | \Psi(\xi(t)) \rangle) \\ & - \langle \Psi(\xi(t)) | \hat{H} | \Psi(\xi(t)) \rangle. \end{aligned} \quad (12)$$

The procedure results in a system of time-dependent equations for parameters $\xi(t)$, which minimize the deviation of $|\Psi(\xi(t))\rangle$ from the solution of the corresponding Schrödinger equation.

For this work, we define a Davydov D_2 ansatz superposition (sD₂) wavefunction

$$|\Psi_{\text{sD}_2}(t)\rangle = \sum_n^N \int_{x^{\text{min}}}^{x^{\text{max}}} dx \Phi_n(x, t) |n, x\rangle \times \sum_z^M \theta_z(t) \prod_p^P |\lambda_{zp}(t)\rangle. \quad (13)$$

The first product term of sD₂ defines all possible vibronic states of the system with complex amplitudes $\Phi_n(x, t)$. The sum over index n represents a superposition of electronic states, while the Q -dimensional integral represents the coordinate basis states of internal vibrational modes. Representation of the internal vibronic states spans the whole space of the system states, and it can be used to calculate dynamics of the system to an arbitrary precision. The second product term defines possible states of the bath QHO modes. Each mode p of the bath is represented by a superposition of M coherent states $|\lambda_{zp}(t)\rangle$ ($\alpha = 1, 2, \dots, M$) with CS displacements $\lambda_{zp}(t)$, while each superposition term z is parameterized by a complex amplitude $\theta_z(t)$. In general, a single CS is an eigenstate of QHO annihilation operator $\hat{a}|\lambda(t)\rangle = \lambda(t)|\lambda(t)\rangle$, whose displacement $\lambda(t)$ uniquely defines the properties of the oscillator wavepacket.⁵¹ Interpretation of CS displacement is especially straightforward in the coordinate and momentum

(z, ρ) phase space with respective operator expectation values being equal to

$$\bar{z}(t) = \sqrt{2} \operatorname{Re} \lambda(t), \quad (14)$$

$$\bar{\rho}(t) = \sqrt{2} \operatorname{Im} \lambda(t). \quad (15)$$

Per definition, the single CS wavepacket has the Gaussian shape and is centred in the $(\bar{z}(t), \bar{\rho}(t))$ phase space point at time t , thus, it follows trajectory defined solely by $\lambda(t)$. By considering the superposition of CSs, we allow for the wavepacket of each mode p to be composed of M interfering Gaussian wavepackets. As such, the superposition can represent non-Gaussian wavefunctions of the excited QHO states. For the superposition length of $M = 1$, representation of the bath vibrational mode states by the sD_2 wavefunction is reduced to the standard D_2 ansatz – single CS wavepacket representation. The sD_2 parameter M allows to incrementally increase the accuracy of the bath modeling. Alternatively, combining the amplitudes of the system and the bath into a single amplitude, $\Phi_n(\mathbf{x}, t) \times \theta_n(t) \rightarrow Y_{n\alpha}(\mathbf{x}, t)$ would remove BOA, giving the most general and, presumably, the most accurate ansatz at a cost of significantly increased computational effort.^{41–43}

With the superposition given by the sD_2 wavefunction (13), normalization of the wavefunction $\langle \Psi_{sD_2}(t) | \Psi_{sD_2}(t) \rangle = 1$ imposes

$$\sum_n \int d\mathbf{x} \Phi_n^*(\mathbf{x}, t) \Phi_n(\mathbf{x}, t) = 1, \quad (16)$$

$$\sum_{\alpha, \beta} \theta_{2\alpha}^*(t) \theta_{2\beta}(t) S_{\alpha\beta}(t) = 1, \quad (17)$$

conditions, where $S_{\alpha\beta}(t) = \prod_k \langle \lambda_{2k}(t) | \lambda_{\beta k}(t) \rangle$ is an overlap of α and β CS product superposition terms.

Applying the Dirac–Frenkel variational method to sD_2 wavefunction (13) with the Hamiltonian operator (1), we derived model equations of motion in the form of a system of implicit differential equations, see the ESI† for details.

III. Results and discussion

In this section, the approach described above is used to investigate excitation energy relaxation dynamics between two excited electronic states $|1\rangle$, $|2\rangle$ attached to the PES with an avoided crossing along a vibrational coordinate. The electronic ground state $|0\rangle$ is included solely to account for the system before an external excitation. The electronic states are attached to a single internal vibrational mode $Q = 1$ (therefore, we drop index q) with Morse PES $V_{11}(x)$ for $|1\rangle$ and harmonic PESs $V_{00}(x)$ and $V_{22}(x)$ for $|0\rangle$ and $|2\rangle$ states, respectively

$$V_{00}(x) = \frac{\omega}{2} x^2, \quad (18)$$

$$V_{11}(x) = D_0 \left(1 - c \frac{(x-d_1)}{\sqrt{2D_0}} \right)^2, \quad (19)$$

$$V_{22}(x) = \frac{\omega}{2} (x - d_2)^2, \quad (20)$$

with dissociation energy D_0 and frequency ω . The PES equilibrium points are displaced by $d_1 = -1.35$ and $d_2 = 1.35$. Excited state PESs are coupled by a linear non-adiabatic coupling $V_{12}(x) = \frac{\omega}{10} x$, often referred to as a vibronic coupling. Throughout the paper we will use dimensionless energy units by normalizing energies to ω . On this scale, we set electronic state energies to $\varepsilon_1 = 0$, $\varepsilon_2 = 5$, PES $V_{00}(x)$ and $V_{22}(x)$ frequencies to $\omega = 1$, and dissociation energy to $D_0 = 40$. In the limit of $D_0 \rightarrow \infty$, $V_{11}(x)$ approaches harmonic PES shape with frequency $\omega = 1$. The coordinate x space was discretized in the interval from $x^{\min} = -10$ to $x^{\max} = 12$ with an equidistant step size of $\delta x = 0.25$. The selected width of x space is large enough to include all significant electron-vibrational wavepacket amplitudes during its time evolution.

We base these parameters on the typical energy scales found in organic pigments present in Nature. Setting internal mode frequency to an approximate frequency of carbon C=C bond vibration $\omega = 1500 \text{ cm}^{-1}$, the $|2\rangle \rightarrow |1\rangle$ internal conversion transition energy gap is then $\Delta\varepsilon_{21} = \varepsilon_2 - \varepsilon_1 = 5\omega$, which corresponds to an optical gap. The internal conversion energy gap varies widely between molecular pigments, e.g., the chlorophyll-*a* Q_x - Q_y energy gap is 1.3ω ,⁵² while the S_2 - S_1 energy gap in carotenoids ranges from 1ω to 5ω depending on the carotenoid length.⁵³ The rest of the model parameters are kept quite arbitrary, since concrete parametrization of both the chlorophyll and the carotenoid PESs is lacking. Note that the ground electronic state does not couple to excited state manifold via vibronic coupling and, thus, will be left out of the analysis. The resulting PES avoided crossing is shown in Fig. 1.

The statistical properties of the bath fluctuations are represented by the Ohmic spectral density function

$$C_n''(w) = \frac{w^s}{w_c^{s-1}} \exp(-w/w_c), \quad (21)$$

with parameter $s = 3$, cut-off frequency $w_c = 0.1$ and the bath reorganization energy $A_n^{\text{bath}} = 0.2$ for each n . The frequency range of the bath vibrational modes $w \in [0.05, 2]$ was uniformly covered by

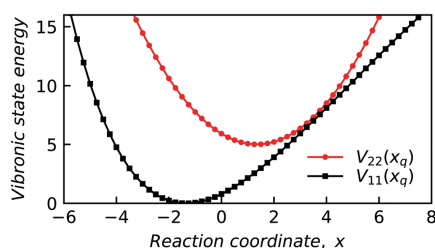


Fig. 1 Avoided crossing of the first and second excited electronic states $|1\rangle$, $|2\rangle$ attached to Morse $V_{11}(x)$ and harmonic $V_{22}(x)$ potential energy surfaces, respectively. The ground state potential surface is not shown, it is centred at zero. Circle and square markers indicate considered coordinate states $|x\rangle$ of the intramolecular vibrations. Optical excitation from the ground state $|0\rangle$ to electronic state $|2\rangle$ results in a Gaussian vibrational wavepacket centred at $x = 0$.

40 modes with a discretization step size of $d\omega = 0.05$. This setup is sufficiently dense to produce the convergent dynamics and the interval of frequencies is wide enough to cover all relevant resonances of the system-bath interactions.

The system and the bath interact *via* electronic-bath coupling (eqn (5)) and one vibrational-bath coupling term $k_{\text{vib}}^{1,2} \hat{x}_p \hat{p}_p^2$ (see eqn (6)), *i.e.*, for simplicity we set scaling factors to $\gamma^{(1,2)} = 1$ and $\gamma^{(1,1)} = \gamma^{(2,1)} = 0$. Condition $\gamma^{(1,1)} = 0$ guarantees that the bath vibrational modes are retained as the normal modes, while $\gamma^{(2,1)} = 0$ implies that the double vibrational quanta absorption by the system is not included.

The initial conditions of the system and the bath are taken to correspond to the lowest energy states. Assuming that transition $|0\rangle \rightarrow |1\rangle$ is either optically forbidden or is off-resonant, the optical excitation by an external field is modeled using the Franck-Condon ground $|0\rangle$ to excited $|2\rangle$ state electronic transition. This corresponds to the projection of the system ground state wavepacket into the 2nd excited state potential surface, thus, setting $\Phi_2(x, 0) = \frac{1}{\sqrt{2\pi}} e^{-\frac{x^2}{2}}$ and $\Phi_1(x, 0) = 0$. Wavepackets of the bath are Gaussian and they can be exactly represented by a single CS. Correspondingly, we choose to set initial amplitudes to $\theta_1(0) = 1$, $\theta_{2\dots M}(0) = 0$ and CS displacements to $\lambda_{\alpha p}(0) = 0$ for every combination of α and p indices. At $t = 0$ there are M degenerate CSs, while only the first $\alpha = 1$ CS amplitude is non-zero, and all QHO wavepackets are centred in their respective coordinate-momentum phase space ($\lambda_p = 0, p_p = 0$). Note that when $M > 1$, the lowest energy bath state preparation in terms of CS amplitudes and displacements is not unique, see Appendix A.

A Following excitation energy and its dissipation

To track excitation energy relaxation within the system itself and energy exchange between the system and the bath, we look at dynamics of electronic, vibrational energies $\varepsilon_{\text{el}}(t)$, $\varepsilon_{\text{vibr}}(t)$, and of the bath vibrational energy $\varepsilon_{\text{bath}}(t)$, defined as

$$\varepsilon_{\text{el}}(t) = \sum_n \varepsilon_n P_n(t), \quad (22)$$

$$\begin{aligned} \varepsilon_{\text{vibr}}(t) = & \sum_n \int dx \Phi_n^*(x, t) \left(V_{nn}(x) - \frac{\omega}{2} \frac{\partial^2}{\partial x^2} \right) \Phi_n(x, t) \\ & + \sum_{n \neq m} \int dx \Phi_n^*(x, t) V_{nm}(x) \Phi_m(x, t) \end{aligned} \quad (23)$$

$$\varepsilon_{\text{bath}}(t) = \sum_{\alpha, \beta, p} \theta_\alpha^*(t) \theta_\beta(t) \lambda_{\alpha p}^*(t) \lambda_{\beta p}(t) S_{\alpha\beta}(t), \quad (24)$$

with $P_n(t) = \int dx |\Phi_n(x, t)|^2$ being the n th electronic state population. For consistency with the system Hamiltonian (eqn (3)), we include non-adiabatic coupling $V_{nm}(x)$ energy in the definition of $\varepsilon_{\text{vibr}}(t)$, also, for simplicity, we exclude QHO zero-point energy from the bath energy $\varepsilon_{\text{bath}}(t)$.

In Fig. 2 we present the time dependence of the system, bath energies and initially occupied electronic state $|2\rangle$ population P_2 calculated with ansatz superposition length $M = 1, \dots, 6$. For reference we also plot a system energy dynamics of an

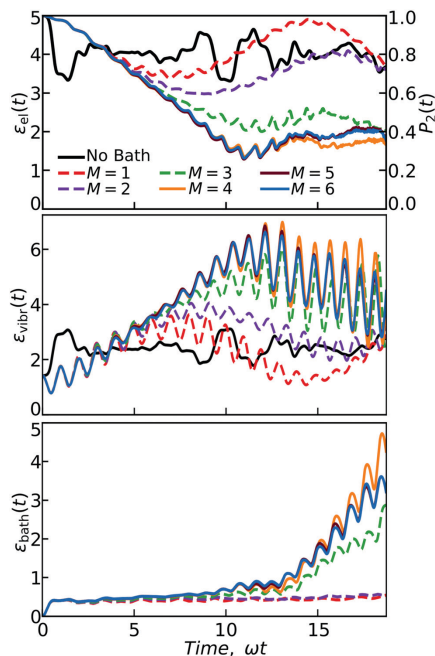


Fig. 2 Time dependence of system electronic energy ε_{el} and electronic state $|2\rangle$ population P_2 , system vibrational energy $\varepsilon_{\text{vibr}}$ and bath vibrational energy $\varepsilon_{\text{bath}}$, calculated with no bath and ansatz superposition length $M = 1, \dots, 6$.

isolated system. Note that, because excitation energy of the state $|1\rangle$ is $\varepsilon_1 = 0$, the total electronic energy is a function of just $|2\rangle$ electronic state population, $\varepsilon_{\text{el}}(t) = \varepsilon_2 P_2(t)$.

In the case of an isolated system, nontrivial oscillations between the system electronic and vibrational energy are observed (internal conversion due to non-adiabatic PES coupling $V_{12}(x)$), however, only about 25% of the electronic state $|2\rangle$ population transfers to the $|1\rangle$ state and a large amount of the transferred population from the state $|1\rangle$ is then repeatedly transferred back to the $|2\rangle$ state, *i.e.*, internal conversion is reversible.

Now let us also include the bath and couple it to the system. In the case of the bath wavefunction representation by $M = 1$ superposition terms, the character of the system energy oscillations changes. It now displays harmonic, reversible behaviour with a period of $\tau_{\text{IC}} \approx 15$ (in the units of ωt). Additionally, ε_{el} and $\varepsilon_{\text{vibr}}$ are also modulated with a period of $\tau_{\text{IV}} \approx 1$, yet, with a smaller modulation amplitude. However, no appreciable vibrational energy exchange between the system and bath modes is observed. The slight increase in the bath energy is solely due to the electron-bath coupling induced bath reorganization. By increasing superposition

length to $M=2$, system electronic and vibrational energies no longer simply oscillate, but some of the electronic energy is now irreversibly converted into the system vibrational energy. Still, no significant energy dissipation to the bath occurs. Taking $M=3$, non-negligible energy exchange between the system and the bath vibrational modes finally takes place. Considering even more superposition terms, irreversible internal conversion and dissipation effects become further pronounced and converge at $M=5$. The convergent irreversible internal conversion occurs on a time scale of τ_{IC} with 60% of the initially occupied $|2\rangle$ state population relaxed to the $|1\rangle$ state, which is followed by the system vibrational energy dissipation to the bath.

The drastic change in the behaviour of the ϵ_{el} and ϵ_{vibr} energies, when the system becomes coupled to the bath, is induced by the bath vibrational mode action on the evolution of the system electron-vibrational wavepacket due to the vibrational-bath coupling term $\propto k_{vib}^{1,2} \hat{x}_q \hat{p}_p^2$. For an isolated system, internal conversion dynamics are decided solely by the free evolution and mixing of the electron-vibration wavepackets on $V_{11}(x)$ and $V_{22}(x)$ PES. By coupling the system to the bath, electron-vibrational wavepacket evolution becomes influenced by the motion of the bath vibrational modes. By looking at the visualization of the electron-vibrational wavepacket evolution, presented in the ESI,[†] we found that vibrational-bath coupling effectively reduces the oscillation amplitude of the electron-vibrational wavepacket on $V_{22}(x)$, making it harder to reach the avoided crossing area ($x \approx 4$) between the $V_{11}(x)$ and $V_{22}(x)$, however, on each oscillation of the $V_{22}(x)$ PES electron-vibrational wavepacket with a period of τ_{IV} , a small amount of wavepacket is still transferred to $V_{11}(x)$. In the case of $M=1$, for the first $\frac{\tau_{IC}}{2}$ after excitation, we observe a gradual population transfer from the $|2\rangle$ state to the $|1\rangle$ state with the reversed process occurring for the following $\frac{\tau_{IC}}{2}$ time interval.

In the convergent case of $M=5$, for roughly the full period of τ_{IC} , we observe analogous population transfer from the $|2\rangle$ state to $|1\rangle$, however, now the generated system vibrational energy is irreversibly dissipated to the bath, instead of being converted back into the electronic $|2\rangle$ state energy.

The total lack of vibrational energy exchange between the system and the bath vibrational modes at $M=1$ suggests that the simple D_2 ansatz is incapable of representing any QHO states necessary to absorb vibrational energy due to the quadratic vibrational-bath coupling term $\propto k_{vib}^{1,2} \hat{x}_q \hat{p}_p^2$. Meanwhile, superposition of CSs allows for the formation of QHO non-zero vibrational energy state wavepackets and for absorbing vibrational energy from the system.

B Characteristics of the bath QHO wavepackets

To evaluate the characteristics of the bath wavepackets, we have computed the coordinate, momentum variances and their arithmetic average for a selected set of bath vibrational modes

$$\sigma_{x_p}^2(t) = \overline{\chi_p^2(t)} - \overline{\chi_p(t)}^2, \quad (25)$$

$$\sigma_{p_p}^2(t) = \overline{\rho_p^2(t)} - \overline{\rho_p(t)}^2, \quad (26)$$

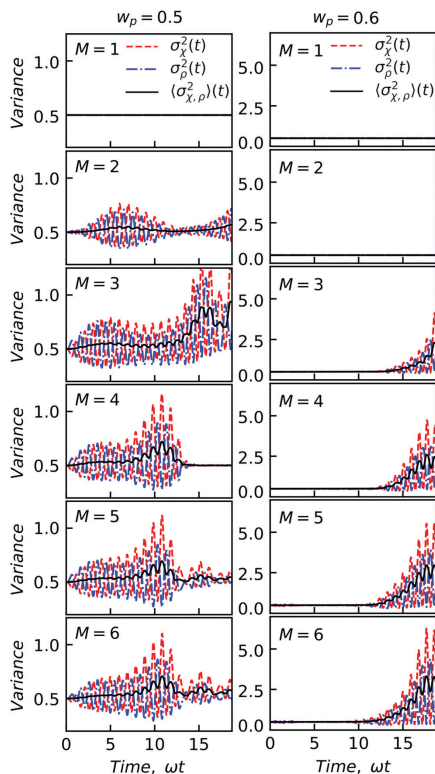


Fig. 3 Time dependence of a frequency $\omega_p = 0.5$ (left column) and $\omega_p = 0.6$ (right column) bath vibrational mode coordinate $\sigma_x^2(t)$, momentum $\sigma_p^2(t)$ variances and their arithmetic average $\sigma_{x,p}^2(t)$ calculated with ansatz superposition length $M = 1, \dots, 6$.

$$\langle \sigma_{x_p, p_p}^2 \rangle(t) = \frac{1}{2} (\sigma_{x_p}^2(t) + \sigma_{p_p}^2(t)), \quad (27)$$

where $\overline{O_p(t)} = \langle \Psi_{SD_2}(x, t) | \hat{O}_p | \Psi_{SD_2}(x, t) \rangle$ is an expectation value of operator \hat{O}_p . We have chosen to look at two modes with frequencies close to half of the electronic energy gap, $\omega_p \approx \frac{\omega}{2}$, as it is the frequency of the expected resonance band created by the quadratic vibrational-bath coupling. Time dependence of frequency $\omega_p = 0.5$ and $\omega_p = 0.6$ bath vibrational mode variances calculated with $M = 1, \dots, 6$ are shown in Fig. 3.

In the case of $M=1$, both coordinate and momentum variances are equal to 0.5 and, as expected, they do not change in time, because the wavepacket of each mode remains strictly Gaussian. Taking $M=2$, the coordinate and momentum variances

of the mode with $w_p = 0.5$ oscillate almost harmonically, indicating that the wavepacket remains almost Gaussian, but it is successively squeezed along x_p and p_p axes (behaviour characteristics of the squeezed coherent states), no significant variance change for $w_p = 0.6$ is observed. Considering $M = 3$, variance oscillations of the mode with $w_p = 0.5$ are no longer harmonic, *i.e.*, oscillation amplitude maximum of $\sigma_{x_p}^2$ exceeds that of $\sigma_{p_p}^2$, implying that the Gaussian wavepacket is asymmetrically squeezed. Variance oscillations of the mode with $w_p = 0.6$ are now also observed. By including more superposition terms, the pattern of the variance oscillations continues to change, and, in accordance with energy dynamics, superposition of $M = 5$ provides convergent dynamics with both modes displaying anharmonic variance oscillations.

Variance oscillation amplitudes of the $w_p = 0.6$ mode are about 5 times greater than that of the $w_p = 0.5$ mode, suggesting that the former mode must lie in an effective resonance band for considered vibrational-bath coupling and it is responsible for absorbing the major part of vibrational energy dissipated from the system to the bath. The latter mode is off-resonant and contributes less to the vibrational energy absorption, rest of the bath modes are also off-resonant. Also, the variance oscillation pattern of the $w_p = 0.6$ mode closely resembles that of $v_{\text{bath}}(t)$ in Fig. 2, further providing evidence that this mode is the main absorber of the system vibrational energy.

Additionally, the variance averages $\langle \sigma_{x,p}^2 \rangle$ of both modes are not static and exceed variance average of the initially prepared Gaussian wavepacket, implying that wavepackets broaden. This is in accordance with the analytical solution of the uncoupled QHO variance, which states that $\langle \sigma_{x,p}^2 \rangle = \frac{1+2k}{2}$ is linearly proportional to QHO eigenstate occupation number k . In our case, bath QHO high occupation number states are accessed by absorbing vibrational energy from the system.

C Resonance conditions for the quadratic coupling induced internal conversion

In the previous section we have investigated the internal conversion dynamics of PESs in an avoided crossing region. To gain more insight into the underlying excitation energy relaxation pathway, now we will look at dynamics in the crossing PESs and large-gap PES avoided crossings. Keeping the same model parameters as in the previous Section IIIA, and setting ansatz superposition length to $M = 5$, now we vary $|2\rangle \rightarrow |1\rangle$ transition energy gap $\Delta\varepsilon_{21}$ by changing electronic state $|2\rangle$ excitation energy ε_2 .

In Fig. 4 we present the time dependence of the electronic state $|2\rangle$ population P_2 calculated with various transition energy gaps. Gaps of $\Delta\varepsilon_{21} < 5$ represent crossing PESs (on the left), while $\Delta\varepsilon_{21} > 5$ produce a large-gap PES avoided crossings (on the right). First looking at the crossing PESs, a clear distinction can be made between two types of population dynamics: some of the dynamics display an internal conversion with an oscillatory behaviour dependent on the energy gap, while other dynamics display only the small amplitude population oscillations about an initial population value. Dynamics of the large-gap PES avoided crossings display a similar tendency, however, internal

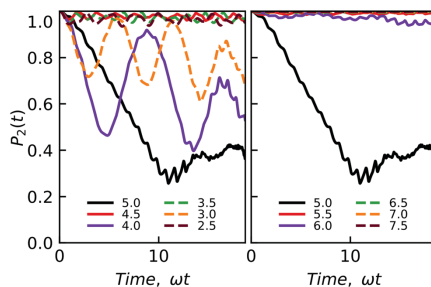


Fig. 4 Time dependence of the electronic state $|2\rangle$ population P_2 calculated with different $|2\rangle \rightarrow |1\rangle$ transition energy gaps $\Delta\varepsilon_{21}$. Dynamics of the crossing PESs and a large-gap PES avoided crossings are shown on the left and right, respectively. The rest of the model parameters are kept the same as in Section IIIA, the ansatz superposition length of $M = 5$ is used.

conversion now occurs on a much longer time scale as compared to crossing PESs.

We conclude that the internal conversion is induced when the initially populated ground vibrational level (with zero vibrational quanta) energy of $V_{22}(x)$ PES is in resonance with vibrational level energies of the $V_{11}(x)$ PES. In the case of our model, with PESs of the same fundamental frequency ω , we expect the internal conversion to occur when the transition energy gap $\Delta\varepsilon_{21}$ is equal to the integer multiple of the lower PES (in our case $V_{11}(x)$) fundamental frequency ω , *i.e.*, $\Delta\varepsilon_{21} = k\omega$ with k being a positive integer number. Note that the prescribed resonance conditions ought to have uncertainties as PES anharmonicities displace PES vibrational level energies and the electronic-bath coupling (eqn (5)) redistributes vibrational level populations.

To examine such a condition validity, in Fig. 5 we present time dependence of the electronic state $|2\rangle$ population P_2 calculated with a slight variation in the electronic state $|2\rangle$ excitation energy about the resonance conditions $\varepsilon_2 = k\omega + \delta\varepsilon_2$ for $k = 3, 4, 5$ and $|\delta\varepsilon_2| \ll \omega$. Looking at the $k = 5$ case first, we find $\varepsilon_2 = 5\omega$ to be the optimal energy gap for internal conversion and even a slight shift in the excitation energy $|\delta\varepsilon_2| < 0.2\omega$ breaks the resonance condition and, in turn, the internal conversion. Meanwhile, in the cases of $k = 4$ and $k = 3$, the energy gaps of $\varepsilon_2 = 4\omega - 0.08\omega$ and $\varepsilon_2 = 3\omega - 0.2\omega$, respectively, are optimal. Again, a slight variation in the optimal energy gaps $|\delta\varepsilon_2| < 0.2\omega$ breaks the resonance condition. This shows that the resonance condition $\Delta\varepsilon_{21} \approx k\omega$, $k = 1, 2, \dots$ between the transition energy gap $\Delta\varepsilon_{21}$ and the fundamental vibrational frequency ω allows qualitatively predicting the onset of the internal conversion due to the quadratic vibrational-bath coupling term.

D Discussion

To model vibrational energy exchange between the system (q) and the bath (p) vibrational modes, we have included quadratic vibrational-bath coupling term $\hat{H}_{V-B} \propto \hat{x}_q \hat{x}_p^2$. It is the simplest coupling term that still maintains vibrational modes as normal

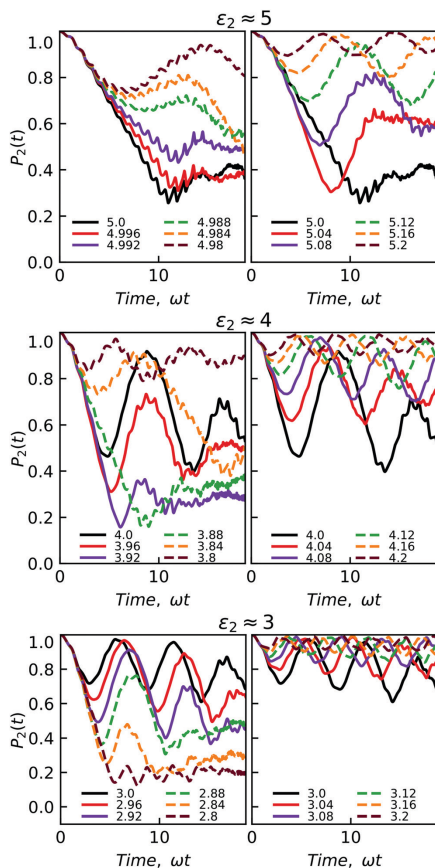


Fig. 5 Time dependence of the electronic state $|2\rangle$ population P_2 calculated with a slight variation in the electronic state $|2\rangle$ excitation energy about the resonance conditions $\nu_2 = k\omega + \delta\nu_2$ for $k = 3, 4, 5$ and $|\delta\nu_2| \ll \omega$, the rest of the parameters are kept the same as in Section IIIA, ansatz superposition length of $M = 5$ is used.

modes. Bilinear coupling term $\hat{H}_{V-B} \propto \hat{x}_q \hat{p}_p$ would only redistribute oscillation amplitudes among vibrational modes. Performing a unitary transformation, we would again obtain uncoupled normal modes. The linear term is still included in deriving the equations of motion and could be used, however, the non-linear coupling term leads to irreversible dynamics.

Effects of quadratic electronic-phonon coupling term $\hat{H}_{E-B} \propto \hat{p}_p^2$ on time-resolved fluorescence of a single absorber have been investigated by Chorošajev *et al.*⁵⁴ They represented bath QHO states by a single squeezed coherent state (SCS) and

were able to account for spectral signatures of absorption from the hot ground state, and the breaking of the absorption and relaxed fluorescence mirror symmetry, *i.e.*, the effects lacking in CS representation. The SCS approach was also applied to model Morse vibrational modes and was shown to lead to wavepacket reorganization due to PES anharmonicity.⁵⁵ The ability of a single SCS to represent QHO wavepackets is greater than a single CS, as it allows modelling symmetric σ_x^2 and σ_p^2 variance oscillations, yet, it is still limited to just Gaussian-like wavepackets. Our more general approach revealed that quadratic vibrational-bath coupling not only induces asymmetric QHO variance oscillations, but also broadens wavepacket in the (χ_{pp}, p_p) phase space. Correct representation of both effects using a single SCS is inherently impossible. We believe that these effects would also be present in models with a quadratic electronic-phonon coupling term. Interestingly, superposition of $M = 2$ terms produced rather symmetric σ_x^2 and σ_p^2 variance oscillations and could perhaps be an alternative to using SCS for other applications. Additionally, we found that the solely linear electron-bath coupling model does not induce bath vibrational mode wavepacket variance changes, thus, the bath state representation by a single CS within BOA is then essentially sufficient (not shown).

Regarding the form of the wavefunction, the multi- D_2 ansatz does not use BOA and represents both system and bath vibrational mode states using CSs. By increasing the superposition length of multi- D_2 , representation accuracy (and numerical effort) of both the system and the bath vibrational states increases equally. Chen *et al.* have simulated pyrazine electron-vibrational wavepacket relaxation through conical intersection using the multi- D_2 ansatz⁴⁶ by considering a two-level system with 4 internal vibrational modes, 20 bath modes were linearly coupled to electronic states⁴⁶ and found that dynamics obtained by including more than 40 multi- D_2 superposition terms agreed well with those obtained using the state-of-the-art MCTDH method. It is well known that modeling of internal conversion requires non-BOA representation of the entangled system electron-vibrational wavepacket, for which multi- D_2 is well suited, however, question remains of whether one can apply BOA to separate system and bath wavefunctions, and have irreversible internal conversion, and whether representation of the separated bath wavefunction needs to be more complex than just of a single CS.

The newly defined sD_2 ansatz is of BOA structure, however, the most important DOFs for internal conversion, *i.e.*, entangled system electronic states and internal vibrational modes, are treated formally exactly. Using the sD_2 ansatz, we found that it is capable of modeling irreversible internal conversion with an avoided crossing along a vibrational coordinate and that internal conversion induced dynamics of the system electron-vibrational wavepacket is highly dependent on the complexity of the bath wavefunction representation. The simplest approach of the D_2 ansatz with CS ($M = 1$), or even SCS (similar to $M = 2$), is not sufficient, because of its limited ability in representing the complex QHO wavepackets. To obtain convergent dynamics we had to include the superposition of at least $M = 5$ CS terms. Irreversibility is induced by the system vibrational energy dissipation to the bath vibrational modes.

The full *ab initio* model of pyrazine⁵⁷ suggests an alternative excitation relaxation pathway *via* conical intersection between the optically dark $A_u(m^*)$ state and the pyrazine ground state, PESS of which require treatment of quadratic and higher order vibronic coupling in the form investigated in this paper. We looked at the effect of the quadratic vibronic coupling term, however, extension of the presented model to the higher order terms is straightforward by including them in the eqn (6) definition.

IV. Conclusion

In summary, the presented model allows investigating irreversible molecular internal conversion dynamics with simultaneous system thermal energy dissipation to a bath. We defined sD_2 ansatz, which represents the most essential states for internal conversion, *i.e.*, entangled electron-vibrational wavepacket states, formally exactly, while bath quantum harmonic oscillator states were expanded in a superposition of coherent states.

To have thermal energy dissipation to the bath, we included quadratic coupling term $\hat{H}_{V-B} \propto \hat{x}_{\nu,p}^2$ between the system and the bath vibrational modes. Using a non-adiabatically coupled three-site model, we showed that the irreversible internal conversion due to quadratic vibrational-bath coupling occurs when the initially populated system vibrational level is in resonance with an empty vibrational level of a lower energy electronic state. Hence, specific sharp resonances have to be met to observe fast and efficient internal energy conversion processes. Also, a highly non-Gaussian bath wavepacket representation is required. This results in broadened and asymmetrically squeezed bath vibrational mode wavepackets. We argue that these effects are, per definition, not possible with the simple Davydov D_2 ansatz, while squeezed coherent state representation is insufficient.

Also, we found that a linear coupling term in terms of bath vibrational mode coordinate $\hat{H} \propto \hat{x}_{\nu,p}$ does not induce wavepacket changes, thus, bath state representation by a single coherent state is sufficient. Additionally, we compared model dynamics and convergence with degenerate and non-degenerate initial coherent states and found that the degenerate case provided the same convergent results as the non-degenerate situation, however, required less computational effort. The presented approach is general in its formulation and could be used to model similar non-linear system-bath coupling effects.

Conflicts of interest

There are no conflicts of interest to declare.

Appendix A: lifting initial coherent state degeneracy

Although the considered CSs are dynamical, *i.e.*, CS displacements $\lambda_{xp}(0)$ evolve in time, choosing more appropriate CSs could perhaps better accommodate the QHO wavepacket at early times, leading to faster convergence and less computational effort.

In Section IIIA the initial bath state, corresponding to the lowest energy QHO state, was represented by degenerate CSs, *i.e.*, all vibrational mode p CS displacements were equivalent $\lambda_{xp}(t=0) = 0$. However, because we choose to set only the first superposition term amplitude to be non-zero $\theta_1(0) = 1$, $\theta_{2,\dots,M}(0) = 0$ initial displacement $\lambda_{x \geq 2,p}(0)$ values can be chosen arbitrarily without modifying the initial bath state. Therefore, now we investigate the effects of setting $\lambda_{x \geq 2,p}(0) \neq \lambda_{x=1,p}(0)$, which will lift initial CS degeneracy, on the model dynamics and convergence.

With our choice of the initial amplitudes $\theta_x(0)$, displacement $\lambda_{x=1,p}(0)$ defines the p th vibrational mode Gaussian wavepacket initial position in the coordinate-momentum phase space $(\lambda_{p,p}, \rho_p)$, see eqn (14) and (15), while displacements $\lambda_{x \geq 2,p}(0)$ define additional Gaussian wavepacket states of the p th vibrational mode, though, they carry zero amplitudes initially. Ideally, we would like to cover as much of phase space as possible with additional states, yet, keep them close enough to each other for their wavepackets to overlap, and centred around the initially populated state $x = 1$. Therefore, we chose to arrange initial CS displacements $\lambda_{xp}(0)$ in a cross-like pattern, see Fig. 6, while keeping $\lambda_{x=1,p}(0) = 0$ centred in phase space. The displacement pattern is reproduced by an expression

$$\lambda_{xp}(0) = \frac{\delta\lambda}{\sqrt{2}} \left(1 + \left\lfloor \frac{x-2}{4} \right\rfloor \right) \left((-1)^{\lfloor \frac{x}{2} \rfloor + x + 1} + i(-1)^x \right), \quad (\text{A1})$$

where $\lfloor \cdot \rfloor$ is a floor function of \cdot , and the parameter $\delta\lambda$ determines the separation between the nearest Gaussian wavepacket states x , allowing controlling their overlap. Separation of $\delta\lambda = 0$ reproduces the initial bath state basis used in Section IIIA.

In Fig. 7 we display the time dependence of the system electronic energy $\epsilon_{ei}(t)$ calculated with superposition length $M = 1, \dots, 6$ and separation $\delta\lambda = 0, \dots, 1$. In the case of $M = 2$, state separations in the range of $\delta\lambda = 0.25, \dots, 0.75$ provide identical and already semi-convergent results, as compared to the $M = 5$ case, while the degenerate state $\delta\lambda = 0$ case only slightly differs from the $M = 1$ case. Large separation of $\delta\lambda = 1$ performs the worst and does not differ from the $M = 1$ case at all, suggesting,

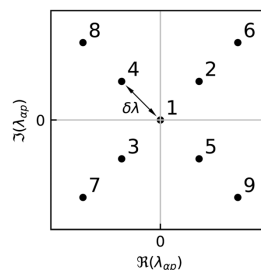


Fig. 6 Scheme of CS displacement $\lambda_{xp}(t=0)$ arrangement of $x = 1, \dots, 9$ states for all p . Free parameter $\delta\lambda$ determines separation between the nearest Gaussian wavepacket states x .

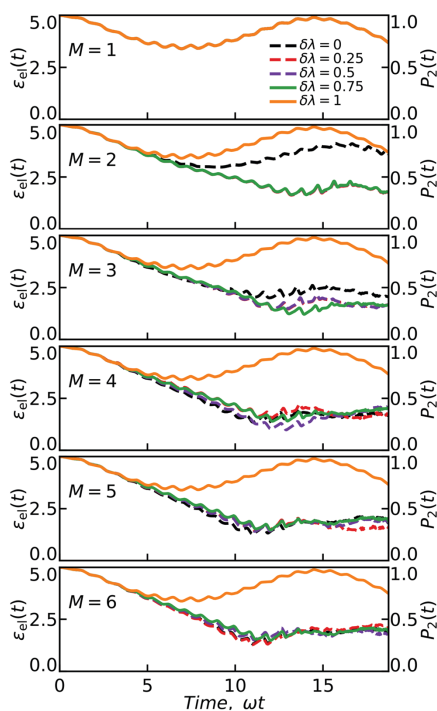


Fig. 7 Time dependence of the system electronic energy $\epsilon_{el}(t)$ calculated with superposition length $M = 1, \dots, 6$ and separation $\delta\lambda = 0, \dots, 1$ between the nearest coherent states.

that the CS wavepackets no longer sufficiently overlap to allow the formation of necessary QHO state wavepackets. By further increasing the number of superposition terms M , the dynamics calculated with $\delta\lambda = 0.25, \dots, 0.75$ separations M , the dynamics calculated with no $\delta\lambda = 0$ and small $\delta\lambda = 0.25, \dots, 0.75$ separations provide identical convergent results. On the other hand, if separation is too large $\delta\lambda = 1$, dynamics do not converge at all, independent of a number of M terms considered.

We found that the small and medium separations $\delta\lambda = 0, \dots, 0.75$ between the nearest states provided semi-converged dynamics at superposition of just $M = 2$ terms, however, $M = 5$ terms were required to obtain a fully convergent result, independent of the separation. Interestingly, if initial separation is too large $\delta\lambda = 1$. As for the computational effort, while keeping the same M , zero separation case $\delta\lambda = 0$ required the least computational effort and increasing separation only slowed

down calculations (not shown). In other words, the initially degenerate CSs used in Section III provide a convergent and efficient basis for computation.

Acknowledgements

M. J. and D. A. was supported by the European Social Fund under the No. 09.3.3-LMT-K-712 "Development of Competences of Scientists, other Researchers and Students through Practical Research Activities" measure. T. M. was supported by the Czech Science Foundation (GACR) grant no. 17-22160S. Computations were performed on resources at the High Performance Computing Center, "HPC Sauletekis" in Vilnius University Faculty of Physics.

References

- V. Balevičius, D. Abramavicius, T. Polivka, A. Galestian Pour and J. Hauer, *J. Phys. Chem. Lett.*, 2016, **7**, 3347–3352.
- V. Balevičius Jr, T. Wei, D. Di Tommaso, D. Abramavicius, J. Hauer, T. Polivka and C. D. P. Duffy, *Chem. Sci.*, 2019, **10**, 4792–4804.
- E. Meneghin, A. Volpato, L. Cupellini, L. Bolzonello, S. Jurinovich, V. Mascoli, D. Carbonera, B. Mennucci and E. Collini, *Nat. Commun.*, 2018, **9**, 3160.
- H. Staleva-Musto, R. West, M. Trathnigg, D. Bina, R. Litvin and T. Polivka, *Faraday Discuss.*, 2019, **216**, 460–475.
- E. Thyraug, C. N. Lincoln, F. Branchi, G. Cerullo, V. Perlik, F. Šanda, H. Lokstein and J. Hauer, *Photosynth. Res.*, 2018, **135**, 45–54.
- K. F. Fox, V. Balevičius, J. Chmeliov, L. Valkunas, A. V. Ruban and C. D. P. Duffy, *Phys. Chem. Chem. Phys.*, 2017, **19**, 22957–22968.
- P. Malý, J. M. Gruber, R. J. Cogdell, T. Mančal and R. van Grondelle, *Proc. Natl. Acad. Sci. U. S. A.*, 2016, **113**, 2934–2939.
- L. Valkunas, D. Abramavicius and T. Mančal, *Molecular Excitation Dynamics and Relaxation*, Wiley-VCH, 2013.
- U. Weiss, *Quantum Dissipative Systems*, World Scientific, 2012.
- H.-P. Breuer and F. F. Petruccione, *The Theory of Open Quantum Systems*, Oxford University Press, 2002, p. 625.
- Y. Tanimura and R. Kubo, *J. Phys. Soc. Jpn.*, 1989, **58**, 101–114.
- Y. Tanimura, *Phys. Rev. A: At., Mol., Opt. Phys.*, 1990, **41**, 6676–6687.
- C. Kreisbeck and T. Kramer, *J. Phys. Chem. Lett.*, 2012, **3**, 2828–2833.
- V. Balevičius, A. Gelzinis, D. Abramavicius and L. Valkunas, *J. Phys. Chem. B*, 2013, **117**, 11031–11041.
- A. G. Redfield, *IBM J. Res. Dev.*, 1957, **1**, 19–31.
- A. Redfield, *Advances in Magnetic and Optical Resonance*, Academic Press, 1965, vol. 1, pp. 1–32.
- T. Förster, *Ann. Phys.*, 1948, **437**, 55–75.
- V. May and O. Kühn, *Charge and Energy Transfer Dynamics in Molecular Systems: Third Edition*, Wiley-VCH, 2011.
- T.-C. Dinh and T. Renger, *J. Chem. Phys.*, 2016, **145**, 034105.
- J. Seibt and T. Mančal, *J. Chem. Phys.*, 2017, **146**, 174109.
- G. Lindblad, *Commun. Math. Phys.*, 1976, **48**, 119–130.

- 22 H.-D. Meyer, U. Manthe and L. Cederbaum, *Chem. Phys. Lett.*, 1990, **165**, 73–78.
- 23 M. Beck, A. Jäckle, G. Worth and H.-D. Meyer, *Phys. Rep.*, 2000, **324**, 1–105.
- 24 H. Wang and M. Thoss, *J. Chem. Phys.*, 2003, **119**, 1289–1299.
- 25 H. Wang and M. Thoss, *New J. Phys.*, 2008, **10**, 115005.
- 26 M. Ronto and D. V. Shalashilin, *J. Phys. Chem. A*, 2013, **117**, 6948–6959.
- 27 G. Richings, I. Polyak, K. Spinlove, G. Worth, I. Burghardt and B. Lasorne, *Int. Rev. Phys. Chem.*, 2015, **34**, 269–308.
- 28 D. V. Shalashilin and M. S. Child, *J. Chem. Phys.*, 2000, **113**, 10028–10036.
- 29 D. V. Shalashilin and M. S. Child, *J. Chem. Phys.*, 2004, **121**, 3563–3568.
- 30 D. V. Shalashilin, *J. Chem. Phys.*, 2010, **132**, 244111.
- 31 D. V. Makhov, C. Symonds, S. Fernandez-Alberti and D. V. Shalashilin, *Chem. Phys.*, 2017, **493**, 200–218.
- 32 G. A. Worth and I. Burghardt, *Chem. Phys. Lett.*, 2003, **368**, 502–508.
- 33 G. Worth, M. Robb and B. Lasorne, *Mol. Phys.*, 2008, **106**, 2077–2091.
- 34 S. Weiss, J. Eckel, M. Thorwart and R. Egger, *Phys. Rev. B: Condens. Matter Mater. Phys.*, 2008, **77**, 195316.
- 35 M. Thorwart, J. Eckel, J. Reina, P. Nalbach and S. Weiss, *Chem. Phys. Lett.*, 2009, **478**, 234–237.
- 36 A. S. Davydov, *Phys. Scr.*, 1979, **20**, 387–394.
- 37 A. C. Scott, *Phys. D*, 1991, **51**, 333–342.
- 38 V. Chorošajev, A. Gelzinis, L. Valkunas and D. Abramavičius, *J. Chem. Phys.*, 2014, **140**, 244108.
- 39 A. D. Somoza, K.-W. Sun, R. A. Molina and Y. Zhao, *Phys. Chem. Chem. Phys.*, 2017, **19**, 25996–26013.
- 40 M. Werther and F. Grossmann, *Phys. Scr.*, 2018, **93**, 074001.
- 41 N. Zhou, Z. Huang, J. Zhu, V. Chernyak and Y. Zhao, *J. Chem. Phys.*, 2015, **143**, 014113.
- 42 N. Zhou, L. Chen, Z. Huang, K. Sun, Y. Tanimura and Y. Zhao, *J. Phys. Chem. A*, 2016, **120**, 1562–1576.
- 43 L. Wang, L. Chen, N. Zhou and Y. Zhao, *J. Chem. Phys.*, 2016, **144**, 024101.
- 44 T. D. Huynh, K.-W. Sun, M. Gelin and Y. Zhao, *J. Chem. Phys.*, 2013, **139**, 104103.
- 45 L. Chen, M. F. Gelin, W. Domcke and Y. Zhao, *J. Chem. Phys.*, 2015, **142**, 164106.
- 46 L. Chen, M. F. Gelin and W. Domcke, *J. Chem. Phys.*, 2019, **150**, 024101.
- 47 W. Domcke, D. R. Yarkony and H. Köppel, *Conical Intersections: Electronic Structure, Dynamics & Spectroscopy*, World Scientific, 2004.
- 48 M. Jakučionis, V. Chorošajev and D. Abramavičius, *Chem. Phys.*, 2018, **515**, 193–202.
- 49 J. Frenkel, *Wave Mechanics: Elementary Theory*, Clarendon Press, Oxford, 1932.
- 50 D. P. Craig and T. Thirunamachandran, *Molecular Quantum Electrodynamics: An Introduction to Radiation Molecule Interactions*, Dover Publications, 1998.
- 51 L. Rodney, *The Quantum Theory of Light*, OUP, Oxford, 2000.
- 52 L. L. Shipman, T. M. Cotton, J. R. Norris and J. J. Katz, *J. Am. Chem. Soc.*, 1976, **98**, 8222–8230.
- 53 D. Kosumi, M. Fujiwara, R. Fujii, R. J. Cogdell, H. Hashimoto and M. Yoshizawa, *J. Chem. Phys.*, 2009, **130**, 214506.
- 54 V. Chorošajev, T. Marčiulionis and D. Abramavičius, *J. Chem. Phys.*, 2017, **147**, 074114.
- 55 D. Abramavičius and T. Marčiulionis, *Lith. J. Phys.*, 2018, **58**, 307–317.
- 56 G. A. Worth, H.-D. Meyer and L. S. Cederbaum, *J. Chem. Phys.*, 1998, **109**, 3518–3529.
- 57 M. Sala, S. Guérin and F. Gatti, *Phys. Chem. Chem. Phys.*, 2015, **17**, 29518–29530.

A3

Modelling Molecular J and H Aggregates using Multiple-Davydov D2 Ansatz

M. Jakučionis, A. Žukas, D. Abramavičius

Physical Chemistry Chemical Physics, **24**, 17665-17672 (2022)

Reproduced with permission from the Royal Society of Chemistry.



Cite this: *Phys. Chem. Chem. Phys.*,
2022, 24, 17665

Modeling molecular J and H aggregates using multiple-Davydov D₂ ansatz†

Mantas Jakučionis,  Agnius Žukas and Darius Abramavičius *

The linear absorption spectrum of J and H molecular aggregates is studied using the time-dependent Dirac–Frenkel variational principle (TDVP) with the multi-Davydov D₂ (mD₂) trial wavefunction (Ansatz). Both the electronic and vibrational molecular degrees of freedom (DOF) are considered. By inspecting and comparing the absorption spectrum of both open and closed chain aggregates over a range of electrostatic nearest neighbor coupling and temperature values, we find that the mD₂ Ansatz is necessary for obtaining an accurate aggregate absorption spectrum in all parameter regimes considered, while the regular Davydov D₂ Ansatz is not sufficient. Establishing a relationship between the model parameters and the depth of the mD₂ Ansatz is the main focus of this study. Molecular aggregate wavepacket dynamics, during excitation by an external field, is also studied. We find the wavepacket to exhibit an out-of-phase oscillatory behavior along the coordinate and momentum axes and an overall wavepacket broadening, implying the electron–vibrational (vibronic) eigenstates of an aggregate to reside on non-parabolic energy surfaces.

Received 18th February 2022,
Accepted 4th June 2022

DOI: 10.1039/d2cp00819j

rsc.li/pccp

1 Introduction

Molecular aggregate excitation dynamics can be computed using the wavefunction-based TDVP by postulating an Ansatz, which ought to be complex enough to represent the necessary vibronic states of the aggregate. The Davydov D₂ Ansatz, which was originally developed for the molecular chain soliton theory,^{1,2} represents quantum states of molecular vibrational modes using Gaussian wavepackets, also known as coherent states (CS). It has been widely applied to study excitation relaxation processes in both isolated molecules and molecular aggregates,^{3–6} as well as to compute their linear and nonlinear spectra.^{7–10}

While the TDVP method is based on propagating pure wavefunctions, its stochastic extension can be used to describe non-zero temperature by averaging over the initial equilibrium thermal state.¹¹ However, it still does not properly account for the energy dissipation effect in the vibronic system. This can be achieved using the thermalization approach, by implicitly modeling vibrational energy exchange with an extended environment.¹²

The D₂ Ansatz is not sufficient to allow for accurate modeling of molecular aggregates.¹³ Accuracy can be greatly improved by considering a superposition of multiple copies of the D₂ Ansatz,

termed the multi-Davydov D₂ Ansatz. The mD₂ Ansatz and, its more complex variant, mD₁ Ansatz¹⁴ have been applied to study polaron dynamics in Holstein molecular crystals,¹³ the spin-boson models¹⁵ and for nonadiabatic dynamics of single molecules,^{6,16} as well as to simulate nonlinear response function of molecular aggregates^{7,13} and others.^{17–20} A more in-depth overview of the various types of Davydov Ansatz and their applications can be found in a recent review article by Zhao *et al.*²¹

However, a well-defined strategy to determine the required number of multiples in mD₂ Ansatz (or the depth) needed to obtain the converged result is lacking. The absorption spectrum and excitation relaxation dynamics of a linear molecular aggregate are key quantities that may serve for establishing the relationship between model parameters and the parameters of the Ansatz. Optical electronic properties significantly depend on the transition dipoles, whether the dipoles are in the “head-to-tail” (J aggregate) or “side-to-side” (H aggregate) configurations.^{22–27} In a J aggregate, excitation by an external electric field produces an initially excited lowest energy excitonic state, therefore, the energy relaxation effect is minimal and the absorption spectrum is dominated by the exchange narrowing effect.^{28–30} It effectively reduces the electron–vibrational coupling strength and the shape of the spectrum is similar to that of a single molecule, rescaled due to exchange narrowing. Meanwhile, in an H aggregate, external fields excite the highest energy excitonic state, thus various available vibronic energy relaxation pathways make the H aggregate spectra more complicated than that of the J aggregate, with a non-trivial spectral lineshape.^{28,30}

*Institute of Chemical Physics, Vilnius University, Saulėtekio Ave. 9-III,
LT-10222 Vilnius, Lithuania*

† Electronic supplementary information (ESI) available. See DOI: <https://doi.org/10.1039/d2cp00819j>

The rest of the paper is organized in the following way. First, in Section 2 we describe the vibronic molecular aggregate model and the theory of linear absorption using the mD₂ Ansatz. Secondly, in Section 3 we analyze a range of J and H molecular aggregate absorption spectra and quantify their convergence in terms of mD₂ Ansatz depth. Lastly, in Section 4, we discuss our findings, relate the mD₂ Ansatz vibrational wavepacket evolution to the previously proposed sD₂ Ansatz and present the conclusions.

II Theory and its numerical implementation

We consider a vibronic molecular aggregate model, where both the electronic and the vibrational DOF are included. Each molecule (site) in the aggregate is modeled as a two electronic-level system, where ϵ_n is the n th site excited electronic state energy. Electrostatic interaction between excited electronic states of sites is given in terms of the resonant dipole-dipole interaction with strengths J_{nm} . Intramolecular vibrational modes of sites are modeled as harmonic vibrational modes. Mode q of the k th site is characterized by a frequency ω_{kq} and the electron-vibrational coupling strength f_{kq} .

Vibronic aggregate model Hamiltonian \hat{H} is given as a sum of the following Hamiltonians.^{31–34} The electronic site Hamiltonian

$$\hat{H}_S = \sum_n \epsilon_n \hat{a}_n^\dagger \hat{a}_n + \sum_{n,m}^{n \neq m} J_{nm} \hat{a}_n^\dagger \hat{a}_m, \quad (1)$$

describes an electronic excitation delocalized over the whole aggregate (exciton), where \hat{a}_n^\dagger (\hat{a}_n) are the n th site Paulionic excitation creation (annihilation) operators. The intramolecular vibrational mode Hamiltonian (with the reduced Planck's constant set to $\hbar = 1$) is that of quantum harmonic oscillators (QHO)

$$\hat{H}_V = \sum_{k,q} \omega_{kq} \hat{c}_{kq}^\dagger \hat{c}_{kq}, \quad (2)$$

with an excluded zero-quanta energy constant shift, where \hat{c}_{kq}^\dagger (\hat{c}_{kq}) are oscillator bosonic creation (annihilation) operators of the q th intramolecular mode, coupled to the k th site, which account for molecular vibrations. The electronic-vibrational interaction is included using the shifted oscillator model, *i.e.*, the vibrational mode potential becomes displaced along the coordinate axis in the excited electronic state. The electron-vibrational coupling Hamiltonian is then given by

$$\hat{H}_{S-V} = - \sum_n \hat{a}_n^\dagger \hat{a}_n \sum_q \omega_{nq} f_{nq} (\hat{c}_{nq}^\dagger + \hat{c}_{nq}). \quad (3)$$

Molecular aggregate sites also interact with an external electric field $\mathbf{E}(t) = \mathbf{e}E(t)\exp(-i\omega_{\text{field}}t)$, where \mathbf{e} is the optical polarization vector, $E(t)$ is the time-dependent field envelope and ω_{field} is the field frequency. In the dipole and Frank-Condon approximations, sites interact with the optical electric

field *via* their purely electronic transition dipole vectors μ_n , therefore, the site-field coupling Hamiltonian is given as $\hat{H}_{S-F}(t) = \hat{\mu} \cdot \mathbf{E}(t)$ with $\hat{\mu} = \hat{\mu}_+ + \hat{\mu}_-$ being the transition dipole operator and

$$\hat{\mu}_+ = \sum_n \hat{\mu}_n \hat{a}_n^\dagger, \quad (4)$$

$$\hat{\mu}_- = \sum_n \hat{\mu}_n \hat{a}_n, \quad (5)$$

are the transition operators that increase (decrease) the number of excitation quanta in the aggregate. We consider an electric field in an impulsive limit with rotating wave approximation,³⁵ $E(t) \rightarrow E_0 \delta(t - \tau)$, where τ is the interaction time, and therefore transitions between aggregate states with a different number of excitations occur instantaneously.

Using the Heitler-London approach,^{31,36} we construct the electronic states of the aggregate as products of molecular excitations: the molecular aggregate electronic ground state $|0\rangle = \otimes_n |0_n\rangle$ (global ground state of all sites) is taken as a reference state, thus, in the ground state, inter-site coupling and electron-vibrational coupling are absent, and we also have the electronic ground state energies equal to zero. Then the aggregate ground state Hamiltonian is purely vibrational $\hat{H}_G = \hat{H}_V$.

Time propagation of various states is computed using TDVP applied to the Davydov Ansatz.^{3,5,13} Since the ground electronic state (g) corresponds to independent molecular vibrations, it is sufficient to describe it by the simplest D₂ Ansatz

$$|\Psi_{D_2}^{(g)}(t)\rangle = \mathcal{G}(t)|0\rangle \otimes |\lambda(t)\rangle, \quad (6)$$

where $\mathcal{G}(t)$ is the ground state amplitude. The vibrational state is represented in terms of the multi-dimensional CS, $|\lambda(t)\rangle = \otimes_{k,q} |\lambda_{kq}(t)\rangle$. Single-dimensional CS $|\lambda_{kq}(t)\rangle$ is created by applying a translation operator

$$\hat{D}(\lambda_{kq}(t)) = \exp(\lambda_{kq}(t) \hat{c}_{kq}^\dagger - \lambda_{kq}^*(t) \hat{c}_{kq}), \quad (7)$$

with complex displacement parameter $\lambda_{kq}(t)$, to the QHO vacuum state: $\hat{D}(\lambda_{kq}(t))|0\rangle_{kq} = |\lambda_{kq}(t)\rangle$. For the time propagation of the aggregate's electronic excited state (e), mD₂ Ansatz will be used,¹³ given by

$$|\Psi_{mD_2}^{(e)}(t)\rangle = \sum_i \sum_n \alpha_{i,n}(t) |n\rangle \otimes |\lambda_i(t)\rangle, \quad (8)$$

where $|n\rangle = |1_n\rangle \otimes_{m \neq n} |0_m\rangle$ is an electronic state of amplitude $\alpha_{i,n}(t)$, which defines a singly excited n th site. The aggregate's vibrational state is now $|\lambda_i(t)\rangle = \otimes_{k,q} |\lambda_{i,kq}(t)\rangle$. Each multiple i corresponds to an excitonic state associated with an aggregate vibrational state. By considering more multiples, the complexity and, in principle, the accuracy of the $\Psi_{mD_2}^{(e)}$ is increased. The $\Psi_{mD_2}^{(e)}$ Ansatz with $M = 1$ reduces to the regular Davydov $\Psi_{D_2}^{(e)}$ Ansatz.

While, in general, the state of the aggregate is the superposition of the ground $\Psi_{D_2}^{(g)}$ and the excited $\Psi_{mD_2}^{(e)}$ state wavefunctions, in the perturbative treatment of the interaction with the optical field, the aggregate's electronic state will always

adhere to either $\Psi_{D_2}^{(g)}$ or $\Psi_{mD_2}^{(e)}$, therefore it is sufficient to consider evolution of these wavefunctions independently.

For the ground state, the TDVP procedure results in a system of explicit differential equations of motion (EOM) for variables $\vartheta(t)$, $\lambda_{kq}(t)$, which yield an analytical solution: $\vartheta(t) = \vartheta(0)$, $\lambda_{kq}(t) = \exp(-i\omega_{kq}t)$, while for the electronic excited state, the resulting EOM constitute a system of implicit differential equations for $\alpha_{i,n}(t)$, $\lambda_{i,kq}(t)$ variables, which can be solved numerically. Details on the mD_2 Ansatz EOM, their solution and numerical implementation, can be found in Appendix 5.

Using the response function theory,^{31,35} the linear absorption spectrum is given by a half-Fourier transform,

$$A(\omega) = \text{Re} \int_0^{\infty} dt e^{i\omega t - \gamma t} S^{(1)}(t), \quad (9)$$

of the linear response function $S^{(1)}(t)$, given by

$$S^{(1)}(t) = \langle \Psi_{D_2}^{(g)}(0) | \hat{\mu}_- e^{-iHt} \hat{\mu}_+ e^{iH_G t} | \Psi_{D_2}^{(g)}(0) \rangle, \quad (10)$$

where we defined a scalar dipole operator $\hat{\mu}_{\pm} = \mathbf{e} \cdot \hat{\mu}_{\pm}$. We also include a phenomenological dephasing rate of $\gamma = 100 \text{ cm}^{-1}$ to account for the decay of optical coherence due to the environmental fluctuations, explicitly unaccounted by our approach.

Numerical computation of $S^{(1)}(t)$ can be greatly streamlined by deriving expressions that relate variables of the ground state $\vartheta(t)$, $\lambda_{kq}(t)$ and the excited state $\alpha_{i,n}(t)$, $\lambda_{i,kq}(t)$, when upward transition operators $\hat{\mu}_+$ act on the ground state $\Psi_{D_2}^{(g)}$, such that we can define

$$\hat{\mu}_+ | \Psi_{D_2}^{(g)}(\tau) \rangle \equiv | \Psi_{mD_2}^{(e)}(\tau) \rangle, \quad (11)$$

and, from eqn (4) and (5), it also follows that

$$\langle \Psi_{D_2}^{(g)}(\tau) | \hat{\mu} \equiv \left(\hat{\mu}_+ | \Psi_{mD_2}^{(e)}(\tau) \rangle \right)^\dagger. \quad (12)$$

Notice that, in general, even though at the time of interaction τ , the initial state $\Psi_{D_2}^{(g)}$ is normalized, and the resulting excited state $\Psi_{mD_2}^{(e)}$ is not necessarily normalized. This does not introduce difficulties, since in the derivation of EOM, no assumptions of Ansatz normalization have been made. Alternatively, the resulting wavefunctions from eqn (11) and (12) can be manually normalized, however, this would require keeping track of excitation amplitudes separately.

During the ground to the excited state transition in eqn (11), the ground state wavefunction $\Psi_{D_2}^{(g)}$ can be equivalently represented by an arbitrary single CS out of the $i = 1, 2, \dots, M$ multiples of the $\Psi_{mD_2}^{(e)}$ Ansatz. For this reason, we choose to “populate” the $i = 1$ multiple after excitation, and call the rest of the multiples $j \neq i$ as initially “unpopulated”. Then the newly created state $\Psi_{mD_2}^{(e)}$, given by eqn (11), has amplitudes $\alpha_{i-1,n}(\tau) = \mu_n \vartheta(\tau)$, $\alpha_{j,n}(\tau) = 0$, where $\mu_n = \mathbf{e} \cdot \mathbf{m}_n$ and CS displacements $\lambda_{i-1,kq}(\tau) = \lambda_{kq}(\tau)$.

Unpopulated CS variables $\lambda_{j,kq}(\tau)$ initially do not contribute to the dynamics, therefore, their position, in principle, is arbitrary. However, during the following excited state evolution,

unpopulated multiples become populated and begin to influence model dynamics. It is known that the initial distance between the populated and unpopulated CS $\delta = |\lambda_{i-1,kq}(\tau) - \lambda_{j,kq}(\tau)|$ should not be too large, otherwise, they will not participate in the excited state dynamics (even at large propagation times CS will remain separated).⁶ On the other hand, setting all CS in close proximity to each other $\lambda_{j,kq}(\tau) \approx \lambda_{i-1,kq}(\tau)$, leads to a highly singular EOM.^{37,38} We chose to set unpopulated CS in a layered hexagonal pattern around the populated CS given by the equation

$$\lambda_{j,kq}(\tau) = \lambda_{i-1,kq}(\tau) + \Delta \sin\left(\frac{\pi}{m}\right) (1 + \lfloor \beta \rfloor) e^{i2\pi\left(\beta + \frac{1}{2m} \lfloor \beta \rfloor\right)} \quad (13)$$

where Δ is a distance parameter, $\beta(j, m) = (j - 2)/m$ is a coordination function with $m = 6$ being the number of CS in each layer and $\lfloor x \rfloor$ is the floor function of x . Δ should be large enough not to have significant overlap among the initial distribution of CS; we found $\Delta = 0.5$ to give numerically well behaved, consistent and convergent results.

After independently propagating *bra* (L) and *ket* (R) states of eqn (10), their overlap is given by

$$\begin{aligned} S^{(1)}(t) &= \langle \Psi_{mD_2}^{(e)}(t) |_{\text{L}} \cdot | \Psi_{mD_2}^{(e)}(t) \rangle_{\text{R}} \\ &= \sum_{i,j} \sum_n \alpha_{i,n}^{*(L)}(t) \alpha_{j,n}^{(R)}(t) \langle \lambda_{i,kq}(t) |_{\text{L}} \cdot | \lambda_{j,kq}(t) \rangle_{\text{R}}, \end{aligned} \quad (14)$$

where the CS overlap is given by

$$\begin{aligned} \langle \lambda_{i,kq}(t) |_{\text{L}} \cdot | \lambda_{j,kq}(t) \rangle_{\text{R}} &= \exp \sum_{k,q} \left(\lambda_{i,kq}^{*(L)}(t) \lambda_{j,kq}^{(R)}(t) \right) \\ &\times \exp \sum_{k,q} \left(-\frac{1}{2} \lambda_{i,kq}^{*(L)}(t) \right)^2 \\ &\times \exp \sum_{k,q} \left(-\frac{1}{2} \lambda_{j,kq}^{(R)}(t) \right)^2. \end{aligned} \quad (15)$$

The temperature of the molecular aggregate is included by implementing the Monte Carlo ensemble averaging scheme. Before excitation of the molecular aggregate *via* an external field, vibrational modes reside in the ground state and obey the canonical ensemble statistics with density operator in the P -representation given by the probability function^{4,11,39,40}

$$\mathcal{P}(\lambda_{kq}(0)) = \mathcal{Z}_{kq}^{-1} \exp \left(-|\lambda_{kq}(0)|^2 \left[\frac{\omega_{kq}}{e^{k_B T}} - 1 \right] \right), \quad (16)$$

where \mathcal{Z}_{kq} is the partition function, k_B is the Boltzmann constant and T is the temperature. By sampling vibrational mode initial conditions $\lambda_{kq}(0)$ from eqn (16), and averaging over the linear response functions $S^{(1)}(t)$, we obtain the thermally averaged linear response function $\langle S^{(1)}(t) \rangle_T$, which now depends on the temperature. We found 360 samples to result in the converged absorption spectrum presented in the next section.

III Results

We consider the absorption spectra of the H and J aggregates. The model aggregate consists of $N = 10$ sites, each of which can be resonantly excited by an external electric field, thus we set single site excitation energies to $\varepsilon_n = \omega_{\text{field}}$ with the nearest neighbor couplings $J_{n,n+1} = J = \pm 500 \text{ cm}^{-1}$ for H and J aggregates, respectively. For each aggregate type, we consider two types of boundary conditions: open chain (OC) with $J_{N,1} = J_{1,N} = 0 \text{ cm}^{-1}$, and the closed chain (CC) with $J_{N,1} = J_{1,N} = J$. The purely excitonic absorption spectrum of this CC aggregate consists of a single peak due to the super-radiant excitonic state with $\varepsilon_n + 2J$ energy. The OC aggregate, besides having the main peak at $\approx \varepsilon_n + 2J$, also has many lower amplitude peaks.

Next, we include one intramolecular vibrational mode per site with frequency $\omega_{kj} = 500 \text{ cm}^{-1}$ and Huang-Rhys (HR) factor $S = f_{kj}^2 = 1$, which defines the electron-vibrational coupling strength. Site electronic transition dipole moment vectors are identical and set to $\mu_n = (1, 0, 0)$. The vibrational mode initial thermal energy is set to $k_B T = \omega_{kj}/2$, which corresponds to the temperature of $T = 360 \text{ K}$. Note, that rescaling all energy parameters by a constant would give exactly the same spectrum.

Absorption spectra of the model H aggregate, computed with an increasing mD₂ Ansatz depth M , both in OC and CC arrangement, are shown in Fig. 1. In both cases, the absorption spectrum converges with $M = 7$ multiples, and higher multiplicity spectra have been computed and are identical up to $M = 11$. Absorption of the $M = 1$ case, which is equivalent to using the Davydov D₂ Ansatz, has peaks in the same frequencies as the converged spectrum, however, their intensities are incorrect, and some are even negative. By increasing the number of multiples considered, peak amplitudes become strictly positive. The 0-0 electronic peak can be clearly identified. Vibrational side-peaks to the higher energy side are due to 0-n vibronic transitions, while on the lower energy side reside the n-0 transition peaks, permitted by the non-zero temperature. Finite vibronic peak widths originate from vibrational dephasing, due to finite temperature and aggregate environment fluctuations. Both the OC and CC aggregates have similar line-shapes, and a slightly finer vibronic structure can be observed in the CC system, due to the greater amount of symmetry and, therefore, effectively lower broadening.

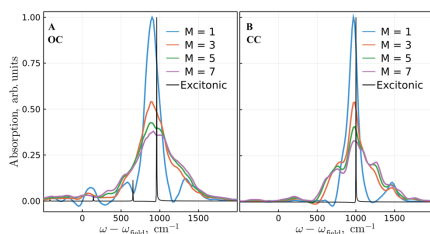


Fig. 1 Absorption spectrum of the model H aggregate in (A) OC and (B) CC configurations, computed with mD₂ Ansatz depth M . The purely excitonic spectra are also shown.

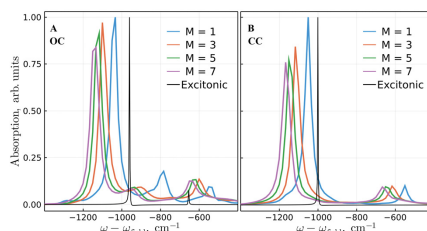


Fig. 2 Absorption spectrum of the model J aggregate in (A) OC and (B) CC configurations, computed with mD₂ Ansatz depth M . The purely excitonic spectra are also shown.

The absorption spectrum of the model J aggregate is shown in Fig. 2. In the CC aggregate, the visible side-peak, on the higher energy side of the strong 0-0 transition, is the first term of vibrational progression. The effective HR factor is thus significantly reduced (hence, the exchange narrowing) due to intermolecular couplings. It is observed to be independent of Ansatz depth considered in both OC and CC arrangements. By increasing M , the absorption spectrum redshifts to lower energies, while qualitatively maintaining the same shape, however, slight differences emerge. For the OC aggregate, peak intensities change, while for the CC aggregate, mostly only the main peak intensity changes. Apparent energy splitting between electronic transitions is considerably reduced, implying that vibronic states do not maintain excitonic intraband gaps due to the strong intramolecular vibrational coupling. In contrast to the H aggregate, all absorption peaks are positive, even with $M = 1$ multiplicity.

In order to quantify the convergence of the H aggregate absorption spectrum with increasing mD₂ Ansatz depth, we calculate the normalized discrepancy⁴¹

$$D(M) = \frac{1}{\mathcal{N}} \int d\omega \sqrt{(A(\omega, M) - \bar{A}(\omega))^2}, \quad (17)$$

where $A(\omega, M)$ is the absorption spectrum with multiplicity M , where $\bar{A}(\omega) = A(\omega, M = 11)$ is the converged reference spectra and

$$\mathcal{N} = \max_{\text{over } M} \int d\omega \sqrt{(A(\omega, M) - \bar{A}(\omega))^2}, \quad (18)$$

is the normalization factor. In Fig. 3 we show $D(M)$ for the H aggregate for various values of the nearest neighbor coupling J , vibrational mode thermal energy $k_B T$, and Ansatz depth $M = 1, \dots, 8$.

We observe that for CC and OC H aggregates, the discrepancy significantly depends on J and $k_B T$, even at the same depth M . We observe, that in the case of $M = 1$, independent of model parameters and site arrangement, spectrum discrepancy is always high. By increasing the depth to just $M = 2$, for some parameters, the discrepancy is reduced significantly. By inspecting higher depths ($M = 2-4$), a general observation can be made. Mainly, the CC H aggregate requires a larger depth at higher temperatures, while for the OC H aggregate, two

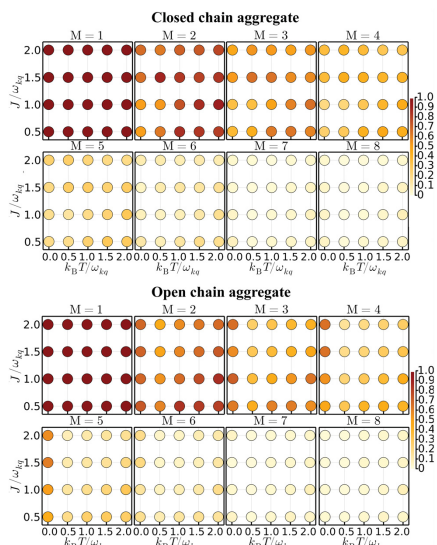


Fig. 3 Normalized discrepancy $D(M)$ of the H aggregate in CC and OC configurations for a range of J and $k_B T$ values, computed with mD_2 Ansatz depth M .

parameter regions of high discrepancy can be discerned: at low temperatures, independent of the coupling strength, and at high temperatures at weak coupling. The high temperature cases can be rationalized as needing more CS to represent thermally excited QHO eigenstates with quantum numbers $n > 0$, which are more probable at higher temperatures. The reasoning for the low temperature case is more subtle. Aggregate excitation *via* an external field shifts oscillators away from their equilibrium considerably (HR factor $S = 1$), then the molecular wavepacket relaxes *via* vibronic state energy surfaces, which induce wavepacket shape changes and/or wavepacket splitting between vibronic surfaces. Either of these two effects would necessitate the molecular aggregate wavepacket to be represented by the mD_2 Ansatz with depth $M > 1$.

As seen in Fig. 2, by considering a larger depth, the J aggregate absorption spectrum line-shape redshifts with minimal changes to the overall shape of the spectrum, therefore, the use of discrepancy estimate in eqn (17) is not necessary. By visually inspecting the spectrum of the J aggregate with various nearest neighbor couplings and temperatures (shown in the ESI†), we find a depth of $M = 7$ to again give a well converged result.

IV Discussion

The total energy of a single QHO, represented by the D_2 Ansatz, is proportional to the CS displacement λ from the origin,

$E_{D_2}^{(\text{osc})} \propto |\lambda|^2$, and the wavepacket shape is that of the lowest energy QHO eigenstate with quantum number $n = 0$, *i.e.*, a simple Gaussian. On the other hand, using the representation of the mD_2 Ansatz, the oscillation energy is proportional to the sum of products of CS displacements, $E_{mD_2}^{(\text{osc})} \propto \sum_{ij} \lambda_i^* \lambda_j$, and the

wavepacket now is not necessarily a Gaussian due to the interference of multiple CS. This allows mD_2 Ansatz to represent more complicated QHO eigenstate wavepackets with quantum numbers $n > 0$. It should be noted, that CS can be used to represent an arbitrary wavepacket using the unity operator expression

$$\hat{I} = \pi^{-1} \iint d\text{Re}\lambda d\text{Im}\lambda |\lambda\rangle\langle\lambda|, \quad (19)$$

and consequently, mD_2 Ansatz with an infinite depth would allow for a complete and exact description of a quantum system. It thus becomes important to obtain the lower limit at which the vibronic dynamics is properly described for *e.g.* absorption spectroscopy.

Using either of the D_2 or mD_2 representations, oscillators can have an equal energy, $E_{D_2}^{(\text{osc})} = E_{mD_2}^{(\text{osc})}$, however, their wavepacket shape must not be equivalent. It is therefore interesting to look at the vibrational mode wavepacket transition from being represented by the D_2 to a more complex mD_2 Ansatz. This transition occurs naturally in eqn (10), for the computation of the linear response function, when an upward transition dipole operator acts on the aggregate ground state, as given by eqn (11). One way to track wavepacket changes is to consider its coordinate and momentum variances, given by

$$\sigma_x^2(t) = \langle \hat{x}^2(t) \rangle - \langle \hat{x}(t) \rangle^2, \quad (20)$$

$$\sigma_p^2(t) = \langle \hat{p}^2(t) \rangle - \langle \hat{p}(t) \rangle^2, \quad (21)$$

where $\langle \mathcal{O}(t) \rangle = \langle \Psi_{mD_2}^{(e)}(t) | \hat{\mathcal{O}} | \Psi_{mD_2}^{(e)}(t) \rangle$ is an expectation value of operator $\hat{\mathcal{O}}$, and their average variance

$$\overline{\sigma_{x,p}^2}(t) = \frac{1}{2}(\sigma_x^2(t) + \sigma_p^2(t)). \quad (22)$$

For an independent QHO, the average variance is $\overline{\sigma_{x,p}^2} = n + \frac{1}{2}$, where n is the QHO occupation number. In Fig. 4 we display coordinate, momentum and their average variances of vibrations coupled to the 1st and 6th sites of the J aggregate in both OC and CC configurations with depth $M = 10$. In the OC configuration, the 1st site is the outermost and the 6th site is in the middle of the aggregate, while in the CC, these modes are translationally invariant and represent two modes with the largest separation.

In both configurations, we observe coordinate and momentum variance oscillations in an out-of-phase manner, while at the same time, the average variance also increases, slightly more in a CC. Instead of considering the superposition of CS to capture such oscillatory behavior, squeezed coherent states (SCS) could be used,⁴²⁻⁴⁵ which are able to produce similar variance oscillations intrinsically. The downside of using SCS

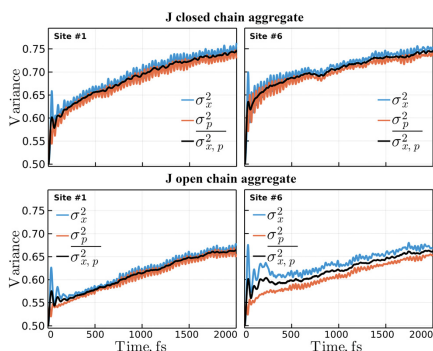


Fig. 4 Coordinate, momentum and their average variances of a 1st and 6th site vibrational mode of a J aggregate in ring and chain configurations with multiplicity $M = 11$.

would be the need to additionally propagate variables describing squeezing amplitude and phase for each vibrational mode. In the Davydov D_2 type Ansatz with SCS, the overall increase of variance would not be captured, yet, for low temperatures, this might serve as a sufficient approximation. For high temperatures, multi-Davydov D_2 type Ansatz with SCS would be required.

In a CC configuration, due to the 10-fold symmetry of the aggregate, no difference between variance changes of vibrational modes is to be expected, while slight differences are observed due to the finite size of the thermal ensemble considered. Meanwhile, in the OC, the difference between variances of the outer and inner modes can be seen. The outer vibrational mode, again, shows increasing, but oscillatory dynamics, while the inner mode coordinate and momentum variance values differ, *i.e.*, wavepacket becomes permanently more stretched along the momentum axis as compared to the coordinate axis.

We see that vibrational mode variance changes without any explicit coupling term between the vibrational DOF. Previously we have proposed a simplified version of the mD_2 Ansatz, termed sD_2 ,⁶ by considering the multiplicity only of vibrational mode states. We have observed that the energy transfer between vibrational modes required the inclusion of quadratic or higher order Hamiltonian coupling terms between oscillators, which deformed the initially quadratic oscillator potential energy surfaces. Energy transfer between vibrational modes manifested itself as an increase of vibrational mode variance. In the presented case of the mD_2 Ansatz, the vibrational mode variance increased without introducing any explicit Hamiltonian coupling terms, implying that the multiplicity of the vibronic states implicitly changes the parabolic potential energy surfaces into non-parabolic. This can be understood by solving for vibronic energy surfaces the eigenstates $E(x_1, \dots, x_0)$. *E.g.*, for a dimer aggregate, the vibronic aggregate Hamiltonian \hat{H}

characteristic polynomial equation is equal to

$$0 = \left(\varepsilon_1 + \omega f^2 - x_1 \omega f + \frac{\omega}{2}(x_1^2 + x_2^2) - E(x_1, x_2) \right) \times \left(\varepsilon_2 + \omega f^2 - x_2 \omega f + \frac{\omega}{2}(x_1^2 + x_2^2) - E(x_1, x_2) \right) - J^2, \quad (23)$$

the solution of which, $E(x_1, x_2)$, is not a quadratic function of vibrational mode coordinates x_1 and x_2 .

In conclusion, by inspecting the absorption spectrum of a wide range of J and H molecular aggregates, in both CC and OC site configurations, with various nearest neighbor coupling strength and temperature values, we find the mD_2 Ansatz with a depth of $M = 7$ to be required for accurate aggregate absorption spectra simulation, while the regular Davydov D_2 Ansatz is not sufficient. For H aggregates, multiplicity is required to obtain absorption lineshape positivity and correct peak intensities. For J aggregates, increasing the number of mD_2 Ansatz depth, mostly redshifts the absorption spectrum, keeping the overall lineshape qualitatively the same, especially in the CC aggregate. However, the very exchange narrowing effect is captured by the simple Davydov D_2 Ansatz. Due to the vibronic energy level structure of an aggregate, we find the molecular wavefunction to exhibit an out-of-phase oscillatory behavior along the coordinate and momentum axes and an overall broadening, which again is not captured by the Davydov D_2 Ansatz.

Conflicts of interest

There are no conflicts to declare.

Appendix A: Multi-Davydov D_2 equations of motion and numerical implementation

Following the TDVP procedure, we derived vibronic molecular aggregate EOMs, given by

$$\sum_j (\dot{\alpha}_{j,n} S_{ij} + \alpha_{j,n} S_{ij} K_{ij}) = -i\Theta_{i,n}, \quad (A1)$$

for each pair of indices $\{i, n\}$, and

$$\sum_{j,n} \left(\alpha_{i,n}^* \dot{\alpha}_{j,n} S_{ij} \dot{\lambda}_{j,kh} + P_{ij,n} \dot{\lambda}_{j,kh} \right) + \sum_{j,n} P_{ij,n} \dot{\lambda}_{j,kh} K_{ij} = -i\Omega_{i,kh}, \quad (A2)$$

for pair of $\{i, k, h\}$ indices. These constitute a system of equations needed to solve to propagate the mD_2 Ansatz, shown in eqn (8). Dot notation is used, where \dot{x} is the time derivative of x .

The right-hand side terms of the given EOMs are

$$\Theta_{i,n} = \sum_{j,m} \alpha_{j,m} S_{ij} J_{nm} + \sum_j \alpha_{j,n} S_{ij} \sum_h \left(C_{ij,nh} + \sum_k A_{ij,kh} \right), \quad (\text{A3})$$

$$\begin{aligned} \Omega_{i,kh} = & \sum_{j,m} G_{ij,mm} \lambda_{j,kh} J_{mm} + \sum_{j,n} P_{ij,n} \lambda_{j,kh} \sum_q \left(C_{ij,nq} + \sum_f A_{ij,fq} \right) \\ & + \sum_j P_{ij,k} \int_{kh} \omega_{kh} - i \sum_{j,n} P_{ij,n} \omega_{kh} \lambda_{j,kh}, \end{aligned} \quad (\text{A4})$$

where auxiliary definitions are

$$G_{ij,mm} = \alpha_{i,n}^* \alpha_{j,m} S_{ij}, \quad (\text{A5})$$

$$P_{ij,n} = G_{ij,mm}, \quad (\text{A6})$$

$$A_{ij,kh} = \omega_{kh} \lambda_{i,n}^* \lambda_{j,kh}, \quad (\text{A7})$$

$$C_{ij,nh} = -f_{nh} \omega_{nh} (\lambda_{i,nh}^* + \lambda_{j,nh}), \quad (\text{A8})$$

$$K_{ij} = \sum_{m,h} \lambda_{j,mh} \left(\lambda_{i,mh}^* - \frac{1}{2} \lambda_{j,mh}^* \right) - \sum_{m,h} \frac{1}{2} \lambda_{j,mh}^* \lambda_{j,mh}. \quad (\text{A9})$$

We solved the presented system of EOMs in terms of variable $\alpha_{i,n}$, $\lambda_{i,kh}$ real and imaginary parts, which are ordered in a column state vector, $\mathbf{x} = \{\alpha_{i,n}^R, \alpha_{i,n}^I, \lambda_{i,kh}^R, \lambda_{i,kh}^I\}$. This doubles the amount of variables, however, it removes consistency problems regarding the treatment of complex variables $\lambda_{j,mh}^*$, $\lambda_{j,mh}$.

Numerical propagation of the mD₂ Ansatz is a two-step process. First, the time derivative of a state vector, $\dot{\mathbf{x}}$, is found by writing eqn (A1) and (A2) in a matrix form

$$\mathbf{M} \dot{\mathbf{x}} = \mathbf{f}, \quad (\text{A10})$$

and solving for $\dot{\mathbf{x}}$ using the Generalized Minimal Residual Method (GMRES) with Lower–Upper (LU) decomposition as a preconditioner. We found the GMRES method to provide a more accurate and stable solution than using the Moore–Penrose pseudo inverse or the solely LU decomposition method. Second, the state vector now can be propagated using a variety of ordinary differential equation solvers.⁴⁶ We found an adaptive-order adaptive-time Adams–Moulton method (VCABM)⁴⁷ to provide just as accurate solution as a typical Runge–Kutta fourth-order method, however, with less computational effort.

During time evolution of the mD₂ Ansatz, two or more multiplicity wavepackets can approach each other and highly overlap, which results in an ill-conditioned coefficient matrix, \mathbf{M} , with no consistent solution of eqn (A10). To remedy this, we have implemented a programmed removal (apoptosis) of overlapping multiples of the mD₂ Ansatz, with the minimal distance for apoptosis to occur $d = 0.05$, as defined in ref. 38.

Establishing the scaling factor of the numerical effort required to propagate mD₂ Ansatz with the increasing model size is not straightforward. The total number of complex variables, V , describing mD₂ Ansatz is easy to find, $V = M \cdot (N + KQ)$, however, due to first having to compute the time derivative of a state vector, $\dot{\mathbf{x}}$, which involves non-linear and/or iterative methods, the actual numerical effort is difficult to quantify.

Empirical estimation, which would compare scaling factors of several computation approaches, is an interesting future research avenue.

Acknowledgements

We thank the Research Council of Lithuania for the financial support (grant no: SMIP-20-47). Computations were performed on resources at the High Performance Computing Center, ‘‘HPC Sauletekis’’ in Vilnius University Faculty of Physics.

References

- 1 A. S. Davydov, *Phys. Scr.*, 1979, **20**, 387–394.
- 2 A. C. Scott, *Phys. D*, 1991, **51**, 333–342.
- 3 J. Sun, B. Luo and Y. Zhao, *Phys. Rev. B: Condens. Matter Mater. Phys.*, 2010, **82**, 014305.
- 4 V. Chorošajev, O. Rancova and D. Abramavičius, *Phys. Chem. Chem. Phys.*, 2016, **18**, 7966–7977.
- 5 M. Jakuėionis, V. Chorošajev and D. Abramavičius, *Chem. Phys.*, 2018, **515**, 193–202.
- 6 M. Jakuėionis, T. Mancal and D. Abramavičius, *Phys. Chem. Chem. Phys.*, 2020, **22**, 8952–8962.
- 7 K. W. Sun, M. F. Gelin, V. Y. Chernyak and Y. Zhao, *J. Chem. Phys.*, 2015, **142**, 212448.
- 8 N. Zhou, L. Chen, Z. Huang, K. Sun, Y. Tanimura and Y. Zhao, *J. Phys. Chem. A*, 2016, **120**, 1562–1576.
- 9 V. Chorošajev, T. Marėiulionis and D. Abramavičius, *J. Chem. Phys.*, 2017, **147**, 074114.
- 10 M. Jakuėionis, I. Gaizunas, J. Sulskus and D. Abramavičius, *J. Phys. Chem. A*, 2022, **126**, 180–189.
- 11 R. J. Glauber, *Phys. Rev.*, 1963, **131**, 2766–2788.
- 12 M. Jakuėionis and D. Abramavičius, *Phys. Rev. A*, 2021, **103**, 032202.
- 13 N. Zhou, L. Chen, Z. Huang, K. Sun, Y. Tanimura and Y. Zhao, *J. Phys. Chem. A*, 2016, **120**, 1562–1576.
- 14 N. Zhou, L. Chen, D. Mozyrsky, V. Chernyak and Y. Zhao, *Phys. Rev. B: Condens. Matter Mater. Phys.*, 2014, **90**, 155135.
- 15 L. Wang, L. Chen, N. Zhou and Y. Zhao, *J. Chem. Phys.*, 2016, **144**, 024101.
- 16 L. Chen, M. F. Gelin and W. Domcke, *J. Chem. Phys.*, 2019, **150**, 24101.
- 17 L. Gao, K. Sun, H. Zheng and Y. Zhao, *Adv. Theory Simul.*, 2021, **4**, 2100083.
- 18 L. Wang, F. Zheng, J. Wang, F. Großmann and Y. Zhao, *J. Phys. Chem. B*, 2021, **125**, 3184–3196.
- 19 K. Sun, X. Liu, W. Hu, M. Zhang, G. Long and Y. Zhao, *Phys. Chem. Chem. Phys.*, 2021, **23**, 12654–12667.
- 20 K. Sun, C. Dou, M. F. Gelin and Y. Zhao, *J. Chem. Phys.*, 2022, **156**, 024102.
- 21 Y. Zhao, K. Sun, L. Chen and M. Gelin, *WIREs Comput. Mol. Sci.*, 2021, e1589.
- 22 E. G. McRae and M. Kasha, *J. Chem. Phys.*, 1958, **28**, 721–722.
- 23 M. Kasha, *Radiat. Res.*, 1963, **20**, 55–70.

- 24 M. Kasha, H. R. Rawls and M. A. El-Bayoumi, *Pure Appl. Chem.*, 1965, **11**, 371–392.
- 25 F. C. Spano, *Acc. Chem. Res.*, 2009, **43**, 429–439.
- 26 M. Schröter, S. D. Ivanov, J. Schulze, S. P. Polyutov, Y. Yan, T. Pullerits and O. Kühn, *Phys. Rep.*, 2015, **567**, 1–78.
- 27 N. J. Hestand and F. C. Spano, *Chem. Rev.*, 2018, **118**, 7069–7163.
- 28 A. Eisfeld and J. S. Briggs, *Chem. Phys.*, 2006, **324**, 376–384.
- 29 P. B. Walczak, A. Eisfeld and J. S. Briggs, *J. Chem. Phys.*, 2008, **128**, 044505.
- 30 J. Roden, A. Eisfeld and J. S. Briggs, *Chem. Phys.*, 2008, **352**, 258–266.
- 31 L. Valkunas, D. Abramavicius and T. Mančal, *Molecular Excitation Dynamics and Relaxation*, Wiley-VCH Verlag GmbH, 2013.
- 32 C. J. Bardeen, *Annu. Rev. Phys. Chem.*, 2014, **65**, 127–148.
- 33 H. van Amerongen, R. van Grondelle and L. Valkunas, *Photosynthetic Excitons*, World Scientific, 2000.
- 34 M. Schröter, S. Ivanov, J. Schulze, S. Polyutov, Y. Yan, T. Pullerits and O. Kühn, *Phys. Rep.*, 2015, **567**, 1–78.
- 35 S. Mukamel, *Principles of nonlinear optical spectroscopy*, Oxford University Press, 1995.
- 36 J. Frenkel, *Phys. Rev.*, 1931, **37**, 17–44.
- 37 V. Bargmann, P. Butera, L. Girardello and J. R. Klauder, *Rep. Math. Phys.*, 1971, **2**, 221–228.
- 38 M. Werther and F. Großmann, *Phys. Rev. B: Condens. Matter Mater. Phys.*, 2020, **101**, 174315.
- 39 L. Wang, Y. Fujihashi, L. Chen and Y. Zhao, *J. Chem. Phys.*, 2017, **146**, 124127.
- 40 Q. Xie, H. Zhong and M. T. Batchelor, *J. Phys. A: Math. Theor.*, 2017, **51**, 014001.
- 41 A. Gelzinis, D. Abramavicius and L. Valkunas, *J. Chem. Phys.*, 2015, **142**, 154107.
- 42 Y. Tsue and Y. Fujiwara, *Prog. Theor. Phys.*, 1991, **86**, 443–467.
- 43 D. Abramavicius and T. Marčiulionis, *Lith. J. Phys.*, 2018, **58**, 307–317.
- 44 V. Chorošajev, T. Marčiulionis and D. Abramavicius, *J. Chem. Phys.*, 2017, **147**, 074114.
- 45 J. Zeng and Y. Yao, *J. Chem. Theory Comput.*, 2022, **18**, 1255–1263.
- 46 C. Rackauckas and Q. Nie, *J. Open Res. Softw.*, 2017, **5**, 15.
- 47 E. Hairer, G. Wanner and S. P. Nørsett, *Solving Ordinary Differential Equations I*, Springer Berlin Heidelberg, 1993.

A4

Inspecting molecular aggregate quadratic vibronic coupling effects using
squeezed coherent states

M. Jakučionis, A. Žukas, D. Abramavičius

Physical Chemistry Chemical Physics, **25**, 1705-1716 (2023)

Reproduced with permission from the Royal Society of Chemistry.



Cite this: DOI: 10.1039/d2cp04212f

Inspecting molecular aggregate quadratic vibronic coupling effects using squeezed coherent states

Mantas Jakučionis, Agnius Žukas and Darius Abramavičius*

We present a systematic comparison of three quantum mechanical approaches describing excitation dynamics in molecular complexes using the time-dependent variational principle (TDVP) with increasing sophistication trial wavefunctions (ansätze): Davydov D_2 , squeezed D_2 (sq D_2) and a numerically exact multiple D_2 (m D_2) ansatz in order to characterize validity of the sq D_2 ansatz. Numerical simulations of molecular aggregate absorption and fluorescence spectra with intra- and intermolecular vibrational modes, including quadratic electronic–vibrational (vibronic) coupling term, which is due to vibrational frequency shift upon pigment excitation are presented. Simulated absorption and fluorescence spectra of a J type molecular dimer with high frequency intramolecular vibrational modes obtained with D_2 and sq D_2 ansätze match the spectra of m D_2 ansatz only in the single pigment model without quadratic vibronic coupling. In general, the use of m D_2 ansatz is required to model an accurate dimer and larger aggregate's spectra. For a J dimer aggregate coupled to a low frequency intermolecular phonon bath, absorption and fluorescence spectra are qualitatively similar using all three ansätze. The quadratic vibronic coupling term in both absorption and fluorescence spectra manifests itself as a lineshape peak amplitude redistribution, static frequency shift and an additional shift, which is temperature dependent. Overall the squeezed D_2 model does not result in a considerable improvement of the simulation results compared to the simplest Davydov D_2 approach.

Received 9th September 2022,
Accepted 30th October 2022

DOI: 10.1039/d2cp04212f

rsc.li/pccp

1 Introduction

A fundamental aspect of the physics of optically excited molecules and their complexes is the transport of excitation energy. Electronic and vibronic couplings are two aspects that are crucial to this process.¹ Complex quantum dynamics of electronic and vibrational excitations are produced as a result of intermolecular interactions right after optical excitation. Their interplay is essential for effective photosynthetic machinery in a natural setting where energy transfer, relaxation, and charge transfer play a crucial role in the initial stages of solar energy conversion.^{2,3}

The wavefunction-based TDVP method can be used to simulate molecular aggregate excitation dynamics as well as their optical spectra with respect to an ansatz (or parameterization form), which should be sufficiently sophisticated to describe the aggregate's essential vibronic features. One family of wavefunctions is called Davydov's ansätze,^{4–6} which utilize Gaussian wavepackets, also known as coherent states (CS), to represent vibronic states of molecular aggregates. It has been extensively used to compute spectra of molecules as well as to examine excitation relaxation dynamics in single molecules and their molecular aggregates.^{7–14}

The trial wavefunction's selection greatly influences how accurate the method is. It has been shown that in some cases for precise modeling of molecular aggregates, the D_2 ansatz falls short,¹⁵ however, the accuracy of vibrational mode representation can be improved by expanding the available parameter space. The most potent approach is to consider a superposition of multiple D_2 ansätze, known as the multi-Davydov D_2 ansatz. It considerably increases the accuracy, making TDVP with m D_2 a numerically exact method. Spin-boson models,¹⁶ nonadiabatic molecular dynamics,^{10,17} and linear and nonlinear spectra of molecular aggregates^{11,15,18} have all been investigated using TDVP with m D_2 .

Instead of considering the superposition of ansätze, which is equivalent to complete quantum treatment, one can expand the available state space of the D_2 ansatz incrementally. One approach is to replace the CS with squeezed coherent states (sqCS), which have additional degrees of freedom (DOFs) which allow the wavepacket to contract and expand along the coordinate and momentum axes in its phase space. Presumably this should allow sqCS to better represent the complicated structure of realistic vibrational mode wavepackets, which become non-Gaussian due to both electronic¹⁸ and quadratic vibronic^{10,13,19} couplings.

In this work, we aim to compare the accuracy of TDVP with three increasing sophistication ansätze: the regular Davydov

Institute of Chemical Physics, Vilnius University, Sauletekio Ave. 9-III, LT-10222, Vilnius, Lithuania. E-mail: darius.abramavicius@ff.vu.lt

D₂, sqD₂ with sqCS and an exact mD₂ ansatz by analysing the simulated absorption and fluorescence spectra of a J-type dimer coupled to high frequency (intra-) and low frequency intermolecular vibrational modes. In addition, we also consider the quadratic vibronic coupling term, which induces wavepacket non-Gaussianity.

The rest of the paper is organized as follows: in Section II A we describe the quadratic vibronic molecular aggregate model, considered ansatz and shortly mention an approach to include finite temperature into the model. In Section II B we present theory of the absorption and fluorescence spectra using the TDVP approach. In Section III we analyze and compare J aggregate absorption and fluorescence spectra in three vibrational mode regimes. Results are discussed and conclusions are given in Section IV.

II Theory

A Electron-vibronic molecular aggregate model theory

The generic model system is a molecular aggregate made of N chromophores with a resonant interaction between them. Each chromophore corresponds to a single pigment molecule (site) which is a two-level electronic quantum system with ground and excited states. Moreover, each pigment is coupled to a set of vibrational degrees of freedom (DOF) corresponding to either intra- or intermolecular vibrational modes. Vibrations are explicitly modeled by quantum harmonic oscillators (QHO). The total system Hamiltonian can then be written as^{1,3,20,21}

$$\hat{H} = \hat{H}_S + \hat{H}_V + \hat{H}_{S-V} + \hat{H}_{S-V^2} \quad (1)$$

where \hat{H}_S represents site Hamiltonian, \hat{H}_V is a vibrational Hamiltonian, \hat{H}_{S-V} is a first-order interaction term between sites and vibrational modes, and \hat{H}_{S-V^2} is the quadratic site-vibration coupling term. All of the above are explicitly expressed as

$$\hat{H}_S = \sum_n e_n \hat{a}_n^\dagger \hat{a}_n + \sum_{n,m}^{n \neq m} V_{nm} \hat{a}_n^\dagger \hat{a}_m, \quad (2)$$

$$\hat{H}_V = \sum_{k,q} \omega_{kq}^e \hat{b}_{kq}^\dagger \hat{b}_{kq}, \quad (3)$$

$$\hat{H}_{S-V} = - \sum_n \hat{a}_n^\dagger \hat{a}_n \sum_q \omega_{nq}^e f_{nq} \left(\hat{b}_{nq}^\dagger + \hat{b}_{nq} \right), \quad (4)$$

$$\hat{H}_{S-V^2} = \frac{1}{4} \sum_n \hat{a}_n^\dagger \hat{a}_n \sum_q \left(\omega_{nq}^e - \omega_{nq}^g \right) \left(\hat{b}_{nq}^\dagger + \hat{b}_{nq} \right)^2, \quad (5)$$

where e_n denotes the n th site electronic excitation energy, which includes molecular reorganization energy, equal to $\Lambda_n = \sum_q \omega_{nq}^e f_{nq}^2$. Where summation index q runs over vibrational modes. V_{nm} is the resonant coupling between the n th and m th site, \hat{a}_n^\dagger (\hat{a}_n) are the creation (annihilation) operators of chromophore electronic excitation, \hat{b}_{nq}^\dagger (\hat{b}_{nq}) are creation (annihilation) operators of vibrational excitations. The linear

vibronic coupling strength is given by dimensionless amplitude f_{nq} . The quadratic vibronic coupling term, \hat{H}_{S-V^2} , becomes relevant once the vibrational mode frequencies in the electronic ground state, ω_{nq}^g , are different from the ones in the excited state, ω_{nq}^e , otherwise this term does not contribute.^{10,13,22–26}

To obtain linear absorption and fluorescence spectrum of the presented vibronic model, we will be using the TDVP method, which will be applied to three parameterized wavefunction ansatz with increasing sophistication. All of them are based on the Davydov D₂ ansatz. First, the least sophisticated ansatz we will be testing is the Davydov D₂ ansatz. It considers a superposition of singly excited aggregate configurations $|n\rangle = |1\rangle_n \prod_{m \neq n} |0\rangle$,^{1,27} with time-dependent amplitudes $\alpha_n(t)$, while vibrational QHO states are expanded in terms of CS. These are obtained by applying the translation operator

$$\hat{D}(\lambda_{kq}(t)) = \exp\left(\lambda_{kq}(t) \hat{b}_{kq}^\dagger - \text{h.c.}\right) \quad (6)$$

with complex time-dependent displacement parameters, λ_{kq} , to the QHO vacuum state denoted by $|0\rangle_{kq}$. Then the D₂ ansatz is defined as

$$|\Psi_{D_2}(t)\rangle = \sum_n \alpha_n(t) |n\rangle \prod_{k,q} |\lambda_{kq}(t)\rangle. \quad (7)$$

In order to increase the complexity of ansatz to better represent complicated vibronic model states, in addition to the translation operator, we can additionally apply the squeeze operator

$$\hat{S}(\zeta_{kq}(t)) = \exp\left(\frac{1}{2}(\zeta_{kq}^*(t) \hat{b}_{kq}^2 - \text{h.c.})\right), \quad (8)$$

with complex-valued squeeze parameter $\zeta_{kq}(t)$, which squeezes the Gaussian wavepacket and only then shifts the resulting squeezed state along the coordinate and momentum axes. The resulting state

$$\hat{D}(\lambda_{kq}(t)) \hat{S}(\zeta_{kq}(t)) |0\rangle_{kq} = |\lambda_{kq}(t), \zeta_{kq}(t)\rangle \quad (9)$$

is called an sqCS. For convenience, we express complex squeeze parameter $\zeta_{kq}(t)$ in its polar form $\zeta_{kq}(t) = r_{kq}(t) e^{i\theta_{kq}(t)}$ where squeeze amplitude $r_{kq}(t)$ and squeeze angle $\theta_{kq}(t)$ are now real time-dependent parameters. Then the squeezed sqD₂ ansatz is defined as

$$|\Psi_{\text{sqD}_2}(t)\rangle = \sum_n \alpha_n(t) |n\rangle \prod_{k,q} |\lambda_{kq}(t), \zeta_{kq}(t)\rangle. \quad (10)$$

An even more general approach for constructing the ansatz is to consider a superposition of multiple copies of D₂ ansatz. It has been termed by the multiple Davydov D₂, mD₂ ansatz, and is defined as

$$|\Psi_{\text{mD}_2}(t)\rangle = \sum_{i=1}^M \left(\sum_n \alpha_{i,n}(t) |n\rangle \prod_{k,q} |\lambda_{i,kq}(t)\rangle \right), \quad (11)$$

where each i th multiple corresponds to a superposition of electronic state excitations accompanied by the vibrational state of an aggregate. By increasing the number of multiples

considered, M , the ansatz state space is expanded accordingly. Note, that the mD_2 ansatz with $M = 1$ simplifies to the D_2 ansatz, while an arbitrary wavefunction can be expressed when $M \rightarrow \infty$, making the approach exact.

Time evolutions of the considered ansätze are obtained by solving their respective equations of motion (EOM), which are given in Appendix A. A more in-depth discussion of mD_2 ansatz EOM numerical implementation can be found in ref. 18 and 28.

The inclusion of additional statistical physics concepts is required in order to simulate finite temperature of the model. The thermal ensemble will be constructed by considering independent wavefunction trajectories γ , each with different initial conditions, and thus energies. Note that the time propagation of the wavefunction fully conserves the total energy of each trajectory.

Considering the excitation process, prior to molecular aggregate excitation *via* an external field, the aggregate is in its electronic ground state $|0\rangle$, while vibrational DOFs are thermally excited. Thus QHO modes follow statistics of the canonical ensemble with respect to the aggregate ground electronic state. Characterization of the vibrational manifold is straightforward because all oscillators in the electronic ground state are uncoupled. The diagonal density operator of a single QHO can be written on the basis of CS with quasiprobability distribution function^{8,29–31}

$$\mathcal{P}^{(s|e)}(\lambda) = \mathcal{Z}^{-1} \exp\left(-|\lambda|^2 \left(\frac{\omega_{elc}}{e k_B T} - 1\right)\right), \quad (12)$$

where \mathcal{Z} is the partition function of QHO, k_B is the Boltzmann constant and T is the temperature. By sampling the $\mathcal{P}^{(s|e)}$ distribution, ground state vibrational mode initial displacements $\lambda(0)$ are obtained. Then, by taking the average of observable A over ensemble of trajectories γ , one obtains thermally averaged observable.

In the case of D_2 ansatz, distributions $\mathcal{P}^{(s|e)}$ fully describe CS initial displacements without ambiguity. For the sqD_2 ansatz, we again sample $\mathcal{P}^{(s|e)}$ to deduce displacements $\lambda_{kq}(0)$ and set the squeeze parameters to $r_{kq} = 1$, $\theta_{kq} = 0$ (no squeezing). This is still the complete description of the thermal equilibrium state due to eqn (12). Finally, in the case of the mD_2 ansatz, we have M equivalent ways to set $\lambda_{i,kq}(0)$ values. Therefore, we chose to initially populate the first multiple, $i = 1$, according to values sampled from $\mathcal{P}^{(s|e)}$, and set the rest, $i \neq 1$, terms to $\lambda_{i \neq 1}(0) = 0$.¹⁸

B Absorption and fluorescence spectra theory using TDVP

Two spectroscopic signals, the linear absorption and fluorescence are the most widely employed spectroscopy tools used to infer information on molecular systems. Assuming that the lifetime of the excited state is longer than the excited state thermal equilibration, it is well known^{1,32} that the absorption/fluorescence spectrum can be obtained by taking Fourier transform of the corresponding time domain response function

$$A_{\text{abs}/\text{flor}}(\omega) = \text{Re} \int_0^{\infty} d\tau e^{i\omega\tau - \gamma_{\text{dep}}\tau} S_{\text{abs}/\text{flor}}^{(1)}(\tau). \quad (13)$$

In the rotating wave and instantaneous aggregate-field interaction approximations,^{18,32} the absorption-related response

function is given by linear response

$$S_{\text{abs}}^{(1)}(t) = \frac{1}{T} \sum_{\gamma=1}^T \left\langle \Psi^{(s|e)}(0) \left| \hat{\mu}_- e^{iHt} \hat{\mu}_+ e^{-iH_G t} \right| \Psi^{(s|e)}(0) \right\rangle_{\gamma}, \quad (14)$$

where the ground state Hamiltonian is equal to $\hat{H}_G = \hat{H}_V$. Sum over γ trajectories describes ensemble averaging over the incoherent ensemble of electronic ground states $|\Psi^{(s|e)}(0)\rangle_{\gamma}$ (for all ansätze) before excitation *via* the external field, where each trajectory has different initial bath conditions, as described previously in Section (II A). T is the total number of trajectories of thermal ensemble.

$$\hat{\mu}_+ = \sum_n (e \cdot \mu_n) \hat{a}_n^{\dagger}, \quad (15)$$

$$\hat{\mu}_- = \sum_n (e \cdot \mu_n) \hat{a}_n, \quad (16)$$

are the aggregate excitation and deexcitation operators, e is the external field polarization vector, μ_n is the n th molecule electronic transition dipole vector. In eqn (13) we include the phenomenological dephasing rate, γ_{dep} , to account for the decay of coherence due to explicitly unaccounted dephasing effects.

To describe fluorescence response function $S_{\text{flor}}^{(1)}(t)$, a more general, third-order, time-resolved fluorescence (TRF) response function^{32,33}

$$S_{\text{flor}}^{(3)}(\tau, t) = \frac{1}{T} \sum_{\gamma=1}^T \left\langle \Psi^{(s|e)}(0) \left| \hat{\mu}_+ e^{-iH(\tau+t)} \hat{\mu}_- \times e^{-iH_G t} \hat{\mu}_- e^{-iH\tau} \hat{\mu}_+ \right| \Psi^{(s|e)}(0) \right\rangle_{\gamma} \quad (17)$$

must be used. Initially, first two aggregate-field interactions create the nonequilibrium density matrix configuration among electronic excited states. Then the aggregate evolves for waiting time, τ , after which, deexcitation transition takes place by spontaneous emission from the excited to the ground electronic state, defined by delay time interval, t .

We assume spontaneous emission to occur only from the lowest energy excited aggregate vibronic state. After initial excitation by an external field, due to non-radiative relaxation processes and interaction with an environment, during the sufficiently long waiting time, $\tau \rightarrow \infty$, aggregate relaxes towards the minimal energy $E_0^{(e)}$ excited aggregate vibronic state, $|\Psi_{E_0}^{(e)}(\tau)\rangle$. From the TRF response function in eqn (17) now follows that the fluorescence response function can be written as

$$S_{\text{flor}}^{(1)}(t) = \left\langle \Psi_{E_0}^{(e)}(0) \left| e^{-iHt} \hat{\mu}_+ e^{-iH_G t} \hat{\mu}_- \right| \Psi_{E_0}^{(e)}(0) \right\rangle, \quad (18)$$

where, for convenience, we set the long waiting time to $\tau = 0$. Note, that eqn (18) does not contain summation over thermal ensemble trajectories γ , as the minimal energy $E_0^{(e)}$ and initial state $|\Psi_{E_0}^{(e)}(0)\rangle$ does not depend on initial vibrational conditions (temperature), but is solely a function of Hamiltonian and chosen ansatz.

The lowest energy state $|\Psi_{E_0}^{(e)}(0)\rangle$ is obtained by numerical optimization of the excited state energy. That is obtained using heuristic adaptive particle swarm optimization algorithm^{34,35} by minimizing the total aggregate energy $E = \langle \Psi | \hat{H} | \Psi \rangle$, as a function of respective ansatz free parameters. For a given model of interest, optimization has to be performed once and can be reused afterwards.

At finite temperature T , due to thermal energy fluctuations, the resulting thermal ensemble in the excited aggregate state has larger average energy $\langle E_0^{(e)} \rangle_T \geq E_0^{(e)}$. Therefore, after waiting time τ the aggregate can be in any one of the thermal ensemble states. Now fluorescence response function $S_{\text{flor}}^{(1)}(t)$ is obtained by averaging over an ensemble of thermal excited states $|\Psi_{E_\gamma}^{(e)}(0)\rangle_\gamma$, where γ is a trajectory number.

In order to find $|\Psi_{E_\gamma}^{(e)}(0)\rangle_\gamma$ states, we cannot use the same algorithm as for the electronic ground state since all vibrational modes in the electronic excited state are now indirectly coupled. Additionally, their frequencies are shifted if the quadratic vibronic coupling contributes.

For each trajectory γ , thermal excited states $|\Psi_{E_\gamma}^{(e)}(0)\rangle_\gamma$ is obtained by perturbing $|\Psi_{E_0}^{(e)}(0)\rangle$ free parameters in such a way as to increase its total energy by the energy fluctuation $\delta E_\gamma = \sum_{n,q} \omega_{nq}^{(e)} |\tilde{\lambda}_{nq}^{(\gamma)}|^2$, where $\tilde{\lambda}_{nq}^{(\gamma)}$ are sampled from the excited state $\mathcal{P}^{(e)}$ distribution in eqn (12). In order to find free parameters that correspond to energy $E_\gamma = E_0^{(e)} + \delta E_\gamma$, we perturb CS displacements $\lambda_{nq}(\tau)$ for D₂ and sqD₂ ansätze and $\lambda_{injq}(\tau)$ for the mD₂ ansatz, until the new state energy $E_\gamma^{(e)} = \langle \Psi_{E_\gamma}^{(e)}(0) | \hat{H} | \Psi_{E_\gamma}^{(e)}(0) \rangle_\gamma$ matches E_γ with 0.1 cm⁻¹ precision. The fluorescence response function at finite temperature is then equal to

$$S_{\text{flor}}^{(1)}(t) = \frac{1}{\Gamma} \sum_{\gamma=1}^{\Gamma} \langle \Psi_{E_\gamma}^{(e)}(0) | e^{-i\hat{H}t} \hat{\mu}_+ e^{-i\hat{H}t} \hat{\mu}_- | \Psi_{E_\gamma}^{(e)}(0) \rangle_\gamma, \quad (19)$$

III Results

A Model parameters

In this section we investigate the effects of intermolecular coupling and vibrational mode frequency shifts in eqn (5), on absorption and fluorescence spectroscopy. We consider three models. First model, \mathcal{M}_1 , contains a single pigment coupled to one high frequency intramolecular mode. Second, \mathcal{M}_2 , is a J-type dimer of two coupled chromophores, where excitations are coupled to a single high frequency intramolecular vibrational mode (one per pigment). Third, \mathcal{M}_3 , is again a two chromophore system, but here electronic excitations are coupled to an overdamped phonon bath.

The J-type dimers in models \mathcal{M}_2 and \mathcal{M}_3 consist of two pigments, each of which can be resonantly excited by an external electric field, thus we assume that single pigment excitation energies are resonant with the optical field, $\epsilon_n = \omega_{\text{field}}$, where ω_{field} is an external field frequency. Electronic transition dipole moment vectors of the chromophores are

identical, $\mu_n = (1, 0, 0)$, in the Cartesian coordinate system. For the \mathcal{M}_1 model, intramolecular vibrational mode frequency in the electronic ground state is $\omega_{1,1}^g = 1000$ cm⁻¹ and Huang-Rhys (HR) factor is $S = f_{1,1}^2 = 1$. For the \mathcal{M}_2 model, the resonance coupling is $J_{12} = -500$ cm⁻¹, while vibrational mode frequencies of the chromophores are $\omega_{1,1}^g = \omega_{2,1}^g = 1000$ cm⁻¹ with HR factors $S = f_{1,1}^2 = f_{2,1}^2 = 1$. For the \mathcal{M}_3 model, the resonance coupling is $J_{12} = -50$ cm⁻¹ and vibrational phonon mode frequencies $\omega_{n,q}^g$ span from 0.1 cm⁻¹ to 490.1 cm⁻¹ with a step-size of 10 cm⁻¹ for each pigment n to represent an overdamped phonon bath with a given spectral density. Here, the f_{nq} distribution is defined in terms of a discretized quasi-continuous spectral density function

$$C_n''(\omega) = \pi \sum_q f_{nq}^2 \omega_{nq}^g \delta(\omega - \omega_{nq}), \quad (20)$$

where $C_n''(\omega) = \omega / (\omega^2 + \gamma^2)$ is the Drude function with damping $\gamma = 100$ cm⁻¹. Magnitudes of f_{nq} are then normalized so that the total reorganization energy $A_n = 100$ cm⁻¹ for each pigment n .

Models \mathcal{M}_1 and \mathcal{M}_2 are typically found in synthetic pigment aggregates,³⁶⁻³⁸ while the \mathcal{M}_3 model more closely corresponds to chlorophyll aggregates found in nature.^{1,3}

When plotting the simulated absorption and fluorescence response functions according to eqn (13), we will include a phenomenological dephasing rate of $\gamma_{\text{dep}} = 50$ fs for models \mathcal{M}_1 , \mathcal{M}_2 and a rate of $\gamma_{\text{dep}} = 250$ fs for model \mathcal{M}_3 . These are to account for additional dephasing stemming from explicitly not included phonons (for models \mathcal{M}_1 , \mathcal{M}_2) and chromophore vibrational modes (for model \mathcal{M}_3).

B Absorption spectra

In all models, we vary vibrational mode frequencies in the excited state ω_{nq}^e by shifting them from frequencies in the ground state ω_{nq}^g , thus we define the difference of frequencies as $\Delta\omega_{nq} = \omega_{nq}^e - \omega_{nq}^g$. First, we start by investigating the absorption spectrum of \mathcal{M}_1 model. In Fig. (1) we present the absorption spectrum of the monomer at 300 K temperature with frequency shifts of $\Delta\omega_{1,1} \equiv \Delta\omega = -250, 0, +250$ cm⁻¹.

When $\Delta\omega = 0$, we observe the absorption spectrum with vibrational peak progression representing jumps from the ground to an arbitrary vibrational excited state. All three ansätze produce identical spectra since there is no electronic coupling and the nonlinear effects, due to quadratic vibronic coupling, are also absent. Now, when vibrational mode frequency in the excited state is higher than the ground state ($\Delta\omega = 250$ cm⁻¹), nonlinear effects become evident together with non-physical features in spectra of some ansätze. Absorption spectra of D₂ and sqD₂ ansätze have a negative peak at ≈ 2000 cm⁻¹ suggesting that they are unable to fully capture the nonlinear effects, *i.e.*, they are not exact solutions of the Schrödinger equation. Meanwhile, the mD₂ ansatz with $M = 5$ superposition terms produce strictly positive absorption spectra and thus will be considered to be the reference spectra for further comparisons. To check the validity of this claim, we compared mD₂ spectra simulated with $M = 1-10$ terms and found $M \geq 5$ spectra to be quantitatively exact (not shown).

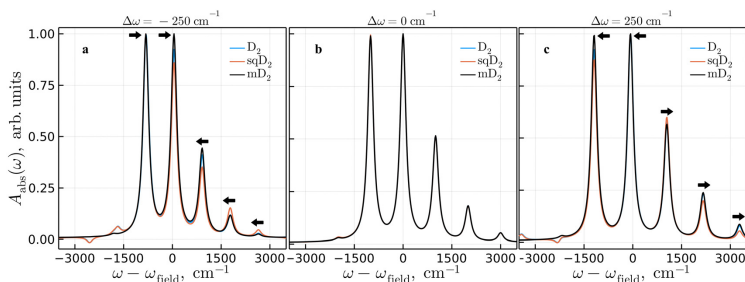


Fig. 1 Absorption spectrum of a monomer (M_1 model) at a temperature of 300 K with $\Delta\omega_{1,1}$ equal to (a) -250 cm^{-1} , (b) 0 cm^{-1} , and (c) $+250\text{ cm}^{-1}$ simulated using D_2 , sqD_2 and mD_2 ansatz. Arrows indicate the peak frequency shift direction when compared to the $\Delta\omega = 0$ case.

Besides the negative peaks, neither D_2 nor sqD_2 is able to reproduce vibrational peak progression amplitudes of the mD_2 ansatz.

By comparing mD_2 absorption spectra peak amplitude progression in all three $\Delta\omega$ cases, we find that progression peak amplitudes either increase or are reduced as compared to the $\Delta\omega = 0$ spectrum, we will refer to these qualitative changes as models having an increased or decreased effective HR factor. Therefore, effective HR is reduced when $\Delta\omega$ is positive, and is increased when $\Delta\omega$ is negative. In addition, $\Delta\omega$ also changes progression peak frequencies, however, not in a monotonic fashion. The direction of frequency change of each peak is indicated by an arrow, when compared to the $\Delta\omega = 0$ case. Absolute frequency of some peaks increase, while for others it decreases. This can also be interpreted as relative energy gap between progression peaks becoming larger when $\Delta\omega$ is positive, and gap is reduced when $\Delta\omega$ is negative.

Next, we look at the absorption spectrum of model M_2 . In Fig. (2) we present the absorption spectrum of the J dimer at a temperature of 300 K with shifts $\Delta\omega_{1,1} = \Delta\omega_{2,1} \equiv \Delta\omega = -250, 0, 250\text{ cm}^{-1}$. Now, even in the $\Delta\omega = 0$ case, when nonlinear effects are still absent, we find the mismatch between the absorption

spectrum simulated using the D_2 and sqD_2 ansatz and mD_2 . This is purely due to electronic coupling between vibronic states of sites, which was lacking in model M_1 . Also, note that the spectra of D_2 and sqD_2 ansatz are identical, since according to equations sqD_2 becomes different from D_2 only when quadratic vibronic coupling is present, *i.e.* $\Delta\omega \neq 0$. The exact mD_2 spectrum has a familiar J dimer absorption lineshape dominated by the exchange narrowing effect,³⁹ which effectively reduces the HR factor as compared to the monomer shown in Fig. (1). Absorption spectra of D_2 and sqD_2 ansatz reproduce the exchange narrowing effect, however, their spectra has additional secondary peaks not seen in the mD_2 spectrum. Their spectra also have slightly higher energy 0-0 quanta transitions peak (and 0-1, 0-2, *etc.*) as compared to the mD_2 spectrum, which implies that mD_2 is able to better represent the lower energy excited aggregate state.

When the quadratic vibronic coupling effects are present ($\Delta\omega = -250, 250\text{ cm}^{-1}$), again, in both cases, we find D_2 and sqD_2 spectra to differ from mD_2 spectra. Very slight differences can also be seen between D_2 and sqD_2 ansatz, however, without any obvious improvement from sqD_2 . In both cases, mD_2 spectra again show a J dimer exchange narrowing type lineshape with

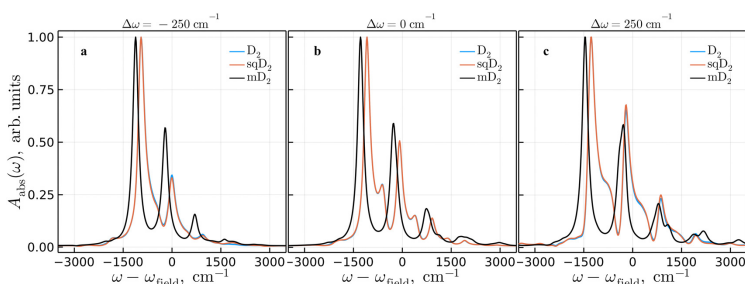


Fig. 2 Absorption spectrum of a J-type dimer (M_2 model) at 300 K temperature with $\Delta\omega_{1,1} = \Delta\omega_{2,1}$, equal to (a) -250 cm^{-1} , (b) 0 cm^{-1} , and (c) $+250\text{ cm}^{-1}$ simulated using D_2 , sqD_2 and mD_2 ansatz.

changes to peak amplitudes similar to those seen in Fig. (1) – relative energy gap between peaks become larger when $\Delta\omega$ is positive, and is reduced when $\Delta\omega$ is negative. The spectrum with $\Delta\omega = 250 \text{ cm}^{-1}$ has a more pronounced fine structure to its absorption progression peaks than those spectra with $\Delta\omega = -250 \text{ cm}^{-1}$ and 0 .

These findings suggest that neither D_2 nor a more complicated sqD₂ is able to fully capture the absorption spectrum of J dimers with high frequency intramolecular vibrational modes, not even in the simplest case ($\Delta\omega = 0 \text{ cm}^{-1}$) when the quadratic vibronic coupling is excluded.

Next, let's look at the absorption spectra of the \mathcal{M}_3 model. In this case phonon modes become thermally excited so we additionally present temperature-dependent spectra. In Fig. (3) we present absorption spectra of a J dimer coupled to the phonon bath at various temperatures. Now each chromophore couples to 50 low frequency vibrational modes, therefore, to investigate the quadratic vibronic coupling effect, we will look

at cases when all mode frequencies, ω_{nq}^e , in an excited aggregate are equal to frequencies in a ground aggregate state, ω_{nq}^g , scaled by a factor of $\gamma = 0.95, 1, 1.05$.

When $\gamma = 1$, all methods produce qualitatively identical absorption spectra over a broad range of temperatures. At low temperatures, the spectra consist of a single absorption peak. With increasing temperature, spectra broaden and slightly shift (on average) due to thermal excitation of vibrational modes in the electronic ground state and due to finite discretization at low frequencies.

Now, when phonon mode frequencies in the aggregate excited state are higher ($\gamma = 1.05$), in addition to the previously seen thermal spectra broadening, we also observe two types of spectral shifts: a static shift – the whole absorption spectra shifts to the higher energies, as compared to the $\gamma = 1$ case, and a temperature dependent absorption peak shift to higher energies. Spectrum simulated with all ansatz when $\gamma = 1.05$ are also qualitatively similar, however, the spectrum of mD₂ is

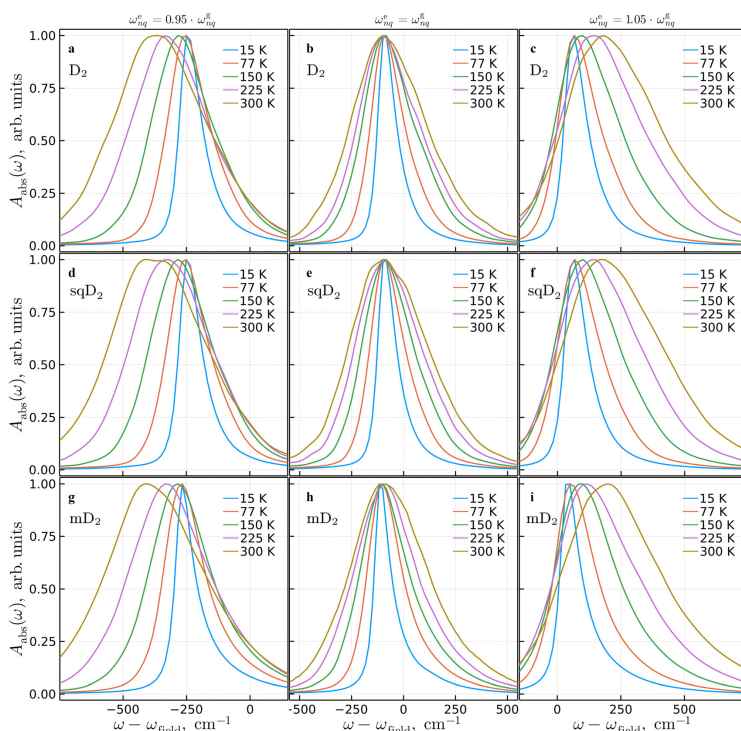


Fig. 3 Absorption spectrum of a J dimer (\mathcal{M}_3 model) coupled to the phonon bath at various temperatures with vibrational mode frequencies in aggregate excited states ω_{nq}^e equal to a) $0.95 \omega_{nq}^g$, b) ω_{nq}^g , and c) $1.05 \omega_{nq}^g$ simulated using D_2 (1st row), sqD₂ (2nd row) and mD₂ (3rd row) ansatz.

Fig. (3i) has a less straightforward temperature dependent peak shift dependence. Peak frequency changes are not as linear with temperature as in spectra simulated with D_2 and sqD₂ ansätze in Fig. (3c and f). Similarly, when phonon mode frequencies in the aggregate excited state are lower ($\gamma = 0.95$), we find all the same spectral shift effects, only now to the lower energy side. Spectra simulated with different ansätze appear qualitatively the same, therefore we conclude that to simulate absorption spectra of a J dimer coupled to low frequency phonon modes, even with quadratic vibronic coupling, it is sufficient to use the simplest D_2 ansatz fluorescence spectra.

In order to compute the fluorescence spectrum, for each considered ansatz, we first have to find the lowest energy $E_0^{(e)}$ excited aggregate state $|\Psi_{E_0^{(e)}}^{(e)}(0)\rangle$ in terms of the ansatz free parameter by minimizing the total aggregate energy $E = \langle \Psi | \hat{H} | \Psi \rangle$, as explained in Section (II B). The resulting energies $E_0^{(e)}$ for models are given in Table (1).

We see that for model \mathcal{M}_1 , when vibrational nonlinearities are absent, all ansätze give exactly the same energy, however, by including the quadratic vibronic coupling ($\Delta\omega \neq 0$ cases), both sqD₂ and mD₂ find lower energy states than the D_2 ansatz. The mD₂ ansatz further outperforms the sqD₂ ansatz, when $\Delta\omega$ is negative. Consequently, the sqD₂ model outperforms the D_2 ansatz when searching for excited state energy minimum when quadratic coupling is included.

In model \mathcal{M}_2 , when $\Delta\omega = 0$, we see that D_2 and sqD₂ again find equivalent energy state, however, now mD₂ ansatz manages to represent a significantly lower energy state, which is not accessed by any of the non-multiple ansätze and is created purely due to electronic coupling between pigments. When nonlinearities are included, the sqD₂ ansatz again outperforms D_2 , especially when $\Delta\omega$ is positive, yet mD₂ further improves in sqD₂ states.

In model \mathcal{M}_3 , we try to find the minimum point in 1020-dimensional space for mD₂, 204-dimensional for D_2 , and 404-dimensional for sqD₂, which is a difficult problem to solve. To have a fair comparison of ansätze for model \mathcal{M}_3 , we limited the

search for the $|\Psi_{E_0^{(e)}}^{(e)}(0)\rangle$ state in terms of the sqD₂ ansatz to its sqCS displacement parameters, λ_{kq} , and set squeezing parameters to $r_{kq} = 1$, $\theta_{kq} = 0$ (no squeezing). For the mD₂ ansatz, we limited the search to just one of its multiples. With these limits set, essentially both sqD₂ and mD₂ ansätze behave as D_2 , thus all three ansätze relax to the same excited aggregate state with energies equivalent to those under the D_2 column. This is confirmed by numerical results where all ansätze managed to represent states with very similar energies. The obtained numbers are also likely within the margin of error and require an improved approach for finding the actual lowest energy states.

Now, let's look at the fluorescence spectra of the same models. In Fig. (4) we display fluorescence spectra of a monomer coupled to high frequency vibration (\mathcal{M}_1 model) at a temperature of 300 K with frequency shifts of $\Delta\omega_{1,1} \equiv \Delta\omega = -250, 0, +250 \text{ cm}^{-1}$. When $\Delta\omega = 0$, we find all three ansätze to produce identical fluorescence spectra, which, as expected, has mirror symmetry with the \mathcal{M}_1 model absorption spectrum in Fig. (1b). The fluorescence spectrum consists of progression of energetically downward transition peaks.

When the quadratic vibronic coupling term is included ($\Delta\omega = -250, +250 \text{ cm}^{-1}$), simulated fluorescence spectra of the considered ansätze are different. In both cases, the fluorescence spectrum of D_2 qualitatively matches the mD₂ ansatz spectrum peak amplitudes and frequencies, while the intermediate complexity sqD₂ consistently overestimates the peak amplitudes and shows additional peaks that are not present in the mD₂ ansatz spectrum. Here, we see an example, where additional, but not sufficient, DOF (squeezing) of sqD₂ ansatz actually produces a visually worse quality spectrum than the smaller state space D_2 ansatz. This is in contrast to absorption spectra of the \mathcal{M}_1 model, where both D_2 and sqD₂ ansätze showed equivalent errors when compared to mD₂ spectra.

By comparing mD₂ fluorescence spectra with quadratic vibronic coupling to that without it, we find that fluorescence progression peak amplitudes change – effective HR factor increases when $\Delta\omega$ is positive, and decreases when $\Delta\omega$ is negative. Also, quadratic vibronic coupling shifts the whole spectra to the lower energy side when $\Delta\omega$ is positive, and to the higher side when $\Delta\omega$ is negative. In contrast to the absorption spectra in Fig. (1), energy gaps between progression peaks remain unchanged. Also, by comparing quadratic vibronic coupling absorption and fluorescence spectra of the \mathcal{M}_1 model of the mD₂ ansatz, we see that quadratic vibronic coupling breaks the mirror symmetry between the two.

Now, let's move on to the \mathcal{M}_2 model. In Fig. (5) we show its fluorescence spectrum simulated at 300 K temperature with $\Delta\omega_{1,1} = \Delta\omega_{2,1} \equiv \Delta\omega$ equal to -250 cm^{-1} , 0 cm^{-1} , and 250 cm^{-1} .

When nonlinearities are absent ($\Delta\omega = 0$), we again see that D_2 and sqD₂ ansätze yield identical fluorescence spectra, which differ from the spectrum of the mD₂ ansatz in fluorescence peak amplitudes and frequencies. The discrepancy between spectra is again a result of D_2 and sqD₂ ansätze not being able to appropriately represent vibronic states created by electronic coupling between J dimer pigments. The lineshape of the mD₂ fluorescence

Table 1 Energy $E_0^{(e)}$ of aggregate excited state $|\Psi_{E_0^{(e)}}^{(e)}(0)\rangle$ for models using D_2 , sqD₂ and mD₂ ansätze. mD₂ ansatz consist of $M = 5$ superposition terms. Values are in units of cm^{-1}

\mathcal{M}_1	$\Delta\omega$	D_2	sqD ₂	mD ₂
	-250	-812.5	-812.5	-816.9
	0	-1000.0	-1000.0	-1000.0
	250	-1187.5	-1190.9	-1190.9
\mathcal{M}_2	$\Delta\omega$	D_2	sqD ₂	mD ₂
	-250	-956.3	-959.9	-1119.2
	0	-1125.0	-1125.0	-1284.7
	250	-1131.9	-1302.0	-1460.9
\mathcal{M}_3	ω_{kq}^e	D_2	sqD ₂	mD ₂
	0.95 ω_{kq}^e	-265.09	-265.1	-265.0
	1.0 ω_{kq}^e	-112.5	-112.2	-111.7
	1.05 ω_{kq}^e	41.1	40.4	41.1

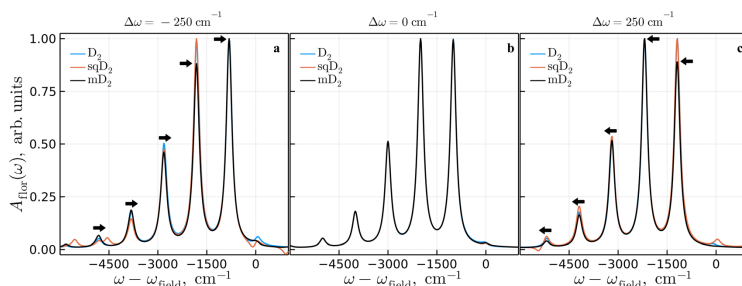


Fig. 4 Fluorescence spectrum of a monomer (\mathcal{M}_1 model) at 300 K temperature with $\Delta\omega_{1,1}$ equal to (a) -250 cm^{-1} , (b) 0 cm^{-1} , and (c) $+250\text{ cm}^{-1}$ simulated using D_2 , sqD_2 and mD_2 ansatz. Arrows indicate the peak frequency shift direction when compared to the $\Delta\omega = 0$ case.

spectrum is dominated by the exchange narrowing effect and does not have mirror symmetry with the absorption spectrum.

From the fluorescence spectra of the \mathcal{M}_2 model with the quadratic vibronic coupling term ($\Delta\omega = -250, +250\text{ cm}^{-1}$), we draw the same conclusions as in the \mathcal{M}_1 model: the D_2 spectrum matches mD_2 spectrum better than does sqD_2 ; effective HR factor increases when $\Delta\omega$ is positive, and decreases when $\Delta\omega$ is negative; quadratic vibronic coupling shift the spectra to the lower energy side when $\Delta\omega$ is positive, and to the higher side when $\Delta\omega$ is negative; energy gaps between progression peaks remain unchanged from the $\Delta\omega = 0$ spectrum.

Overall, the fluorescence spectrum of the J dimer coupled to the high frequency vibrational modes is accurately captured only by the mD_2 ansatz, while sqD_2 yields a visually slightly worse quality spectrum than the D_2 ansatz, however, neither is a match to mD_2 accuracy.

Next, let's look at the fluorescence spectra of the \mathcal{M}_3 model. In Fig. (6) we show the fluorescence spectra of a J dimer coupled to low frequency phonon bath modes at various temperatures. We see that all ansatz produce qualitatively similar fluorescence spectra with all vibrational mode scaling factors $\gamma = 0.95, 1, \text{ and } 1.05$. As in the absorption spectra of the \mathcal{M}_3 model in Fig. (3), we find analogous effects of spectral broadening with increasing

temperature, as well as two type of spectral shifts: a static shift – the whole spectrum shifts to the higher energies when γ is positive, and to the lower energies when γ is negative, as compared to the $\gamma = 1$ case, and an additional temperature dependent fluorescence peak shift to the higher energy side when γ is positive, and to the lower side when γ is negative. In addition to these, we now observe fluorescence peak drift to the lower energies with increasing temperature when the frequency scale factor is $\gamma = 1$, regardless of the ansatz used.

All in all, spectra simulated with considered ansatz appear qualitatively equivalent, thus we conclude that to simulate fluorescence spectra of the J dimer coupled to low frequency phonon modes, even with quadratic vibronic coupling, it is sufficient to use the simplest D_2 ansatz.

IV Discussion

Natural progression in constructing more and more sophisticated Davydov type ansatz, would be to write down ansatz as a superposition of sqD_2 ansatz – the multi- sqD_2 ansatz. This was recently done by Zeng *et al.*,⁴⁰ where they used it to simulate dynamics and absorption spectra of pyrazine and the 2-pyridone dimer aggregate,

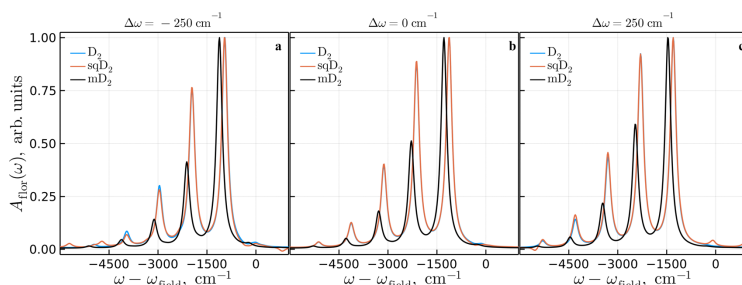


Fig. 5 Fluorescence spectrum of a J dimer (\mathcal{M}_2 model) at 300 K temperature with $\Delta\omega_{1,1} = \Delta\omega_{2,1}$ equal to (a) -250 cm^{-1} , (b) 0 cm^{-1} , and (c) 250 cm^{-1} simulated using D_2 , sqD_2 and mD_2 ansatz.

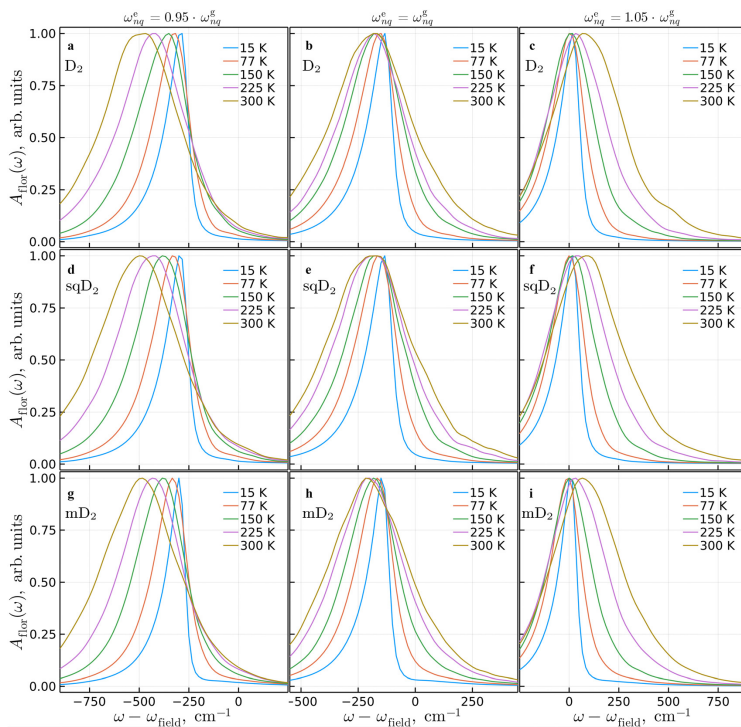


Fig. 6 Fluorescence spectrum of a J dimer (M_3 model) coupled to the bath at various temperatures with vibrational mode frequencies in aggregate excited states ω_{vib}^0 equal to (a) $0.95 \omega_{\text{ag}}^0$, (b) ω_{ag}^0 , (c) $1.05 \omega_{\text{ag}}^0$ simulated using D_2 (1st row), $\text{sq}D_2$ (2nd row) and mD_2 (3rd row) ansatz.

and found a great match with the state-of-the-art multi-configuration time-dependent Hartree (MCTDH) method results. In fact, the presented approach of using Davydov type ansatz is closely related to the Gaussian-MCTDH with frozen Gaussians functions for D_2 , mD_2 ansatz, and $\text{sq}D_2$ with thawed Gaussian functions.^{6,41–43}

Our analysis presented in Section (III), shows that using sqCS , instead of regular CS , does not provide any significant improvement in the simulated absorption and fluorescence spectra of J dimers, even when the quadratic vibronic coupling is used. Therefore one has to wonder if an additional numerical effort needed to propagate multi- $\text{sq}D_2$ ansatz is worth, since any arbitrary wavefunction can be already exactly expanded using the mD_2 ansatz using the unity operator expression

$$\hat{I} = \pi^{-1} \iint d\text{Re}\lambda d\text{Im}\lambda |\lambda\rangle\langle\lambda|. \quad (21)$$

It would be interesting to see if the multi- $\text{sq}D_2$ ansatz would require less terms in its superposition than the mD_2 ansatz to obtain equivalent spectra. However, this is outside the topic of this paper.

We looked at the quadratic vibronic coupling effects for low and high frequency modes. For the high frequency modes, we looked at large nonlinearities by increasing and decreasing the mode frequency by 25%, which is much larger than what is observed in molecules.¹⁴ This was chosen to investigate the limits of all ansatz, however, for smaller nonlinearities we expect the same conclusion, *i.e.*, that multiple-type ansatz are required to simulate aggregate spectra. This is because we considered strong electronic coupling between pigments, which eventually splits the wavepacket into several discrete packets and move quasi-independent along separate vibronic state energy surfaces, while the quadratic vibronic coupling introduces only the secondary effects, which were not captured by non-multiple ansatz.

For the low frequency modes, we considered small nonlinearities by changing frequencies by 5%, more in line with what is observed, with small electronic coupling between pigments, and found all considered ansatz to produce qualitatively identical spectra. This implies that even when quadratic vibronic coupling is the main source of nonlinearity, for realistic frequency shifts, sqCS does not

provide any significant improvement. However, it is worth mentioning that the sqD₂ model outperforms the D₂ ansatz when searching for excited state energy minimum when quadratic coupling is included. This improvement may be important for other types of processes such as charge separation and internal conversion.

In conclusion, we compared the absorption and fluorescence spectra of the vibronic J dimer model with quadratic vibronic coupling simulated using three increasing sophistication wavefunction ansatz: D₂, sqD₂ and mD₂. We found that it is necessary to use the mD₂ ansatz whenever molecular aggregate electronic DOFs are coupled to higher frequency intramolecular vibrational modes. If they are coupled to low frequency phonon bath modes, all three ansatz produce qualitatively the same spectra. The quadratic vibronic coupling term manifests itself in both absorption and fluorescence spectra as a lineshape peak amplitude redistribution, static frequency shift and an additional shift, which is dependent on the temperature.

Conflicts of interest

There are no conflicts of interest to declare.

Appendix

A Time-dependent variational principle

Will be using time-dependent Dirac–Frenkel variational principle to obtain a set of equations of motion of the D₂, sqD₂ and mD₂ ansatz free parameters: $\Gamma_{D_2} = \{\alpha_n(t), \lambda_{kq}(t)\}$, $\Gamma_{sqD_2} = \{\alpha_n(t), \lambda_{kq}(t), r_{kq}(t)\}$ and $\Gamma_{mD_2} = \{\alpha_{i,n}(t), \lambda_{i,kq}(t)\}$. Solution of the set of equations will result in ansatz time evolution, such that the deviation from an exact solution of the Schrödinger equation will be minimized. As a first step, we write down model Lagrangian in the form of

$$\mathcal{L}(t) = \frac{i}{2}(\langle \dot{\Psi}(t) | \dot{\Psi}(t) \rangle - \langle \dot{\Psi}(t) | \Psi(t) \rangle) - \langle \Psi(t) | \hat{H} | \Psi(t) \rangle \quad (\text{A1})$$

where $\dot{x}(t)$ is the time derivative of $x(t)$. For the sqD₂ ansatz, Lagrangian can be expressed as (hereafter, we omit explicitly writing parameter time dependence)

$$\begin{aligned} \mathcal{L}_{sqD_2} = & \frac{i}{2} \sum_n \alpha_n^* \dot{\alpha}_n - \frac{i}{2} \sum_m \alpha_m \dot{\alpha}_m^* \\ & + \frac{i}{2} \sum_{n,h,q} |\alpha_n|^2 (\dot{\lambda}_{hq} \lambda_{hq}^* - \dot{\lambda}_{hq}^* \lambda_{hq} + i \dot{\theta}_{hq} \sinh^2(r_{hq})) \\ & - \sum_n |\alpha_n|^2 \epsilon_n - \sum_{n,m} V_{nm} \alpha_n \alpha_m^* \\ & - \sum_{n,m,q} |\alpha_n|^2 \omega_{nq}^s (\sinh^2(r_{nq}) + |\lambda_{nq}|^2) \\ & + 2 \sum_{n,q} |\alpha_n|^2 \omega_{nq}^e f_{nq} \text{Re} \lambda_{nq} \\ & - \sum_{n,q} |\alpha_n|^2 \Delta \omega_{nq} \\ & \times (\cos h(2r_{nq}) - \sin h(2r_{nq}) \cos(\theta_{nq}) + (2\text{Re} \lambda_{nq})^2) \end{aligned} \quad (\text{A2})$$

and for mD₂, Lagrangian reads

$$\begin{aligned} \mathcal{L}_{mD_2} = & i \sum_{ij} \sum_n \alpha_{i,n}^* \dot{\alpha}_{j,n} S_{ij} \\ & + i \sum_{ij} \sum_n \alpha_{i,n}^* \alpha_{j,n} S_{ij} K_{ij} \\ & - \sum_{ij} \sum_n \alpha_{i,n}^* \alpha_{j,n} S_{ij} \epsilon_n - \sum_{ij} \sum_{n,m} \alpha_{i,n}^* \alpha_{j,m} S_{ij} J_{nm} \\ & - \sum_{ij} \sum_n \alpha_{i,n}^* \alpha_{j,n} S_{ij} \sum_h \omega_{nh} \lambda_{i,nh}^* \lambda_{j,nh} \\ & + \sum_{ij} \sum_n \alpha_{i,n}^* \alpha_{j,n} S_{ij} \sum_h \omega_{nh} f_{nh} (\tilde{\lambda}_{i,nh}^* + \tilde{\lambda}_{j,nh}) \\ & - \sum_{ij} \sum_n \alpha_{i,n}^* \alpha_{j,n} S_{ij} \sum_h \Delta \omega_{nh} \left(1 + (\lambda_{i,nh}^* + \lambda_{j,nh})^2 \right), \end{aligned} \quad (\text{A3})$$

where the Debye–Waller factor is

$$S_{ij} = \exp \left\{ \sum_{k,q} \lambda_{i,kq}^* \lambda_{j,kq} - \frac{1}{2} (|\lambda_{i,kq}|^2 + |\lambda_{j,kq}|^2) \right\}, \quad (\text{A4})$$

and

$$K_{ij} = \sum_{kq} \lambda_{i,kq}^* \dot{\lambda}_{j,kq} - \frac{1}{2} \frac{d}{dt} |\lambda_{j,kq}|^2. \quad (\text{A5})$$

Now, for each Lagrangian \mathcal{L}_β , where $\beta = \text{sqD}_2, \text{mD}_2$, we apply the Euler–Lagrange equation

$$\frac{d}{dt} \left(\frac{\partial \mathcal{L}_\beta}{\partial \dot{\gamma}_\beta} \right) - \frac{\partial \mathcal{L}_\beta}{\partial \gamma_\beta} = 0, \quad (\text{A6})$$

to each free parameter $\gamma_\beta \in \Gamma_\beta$ of the ansatz in order to obtain the equation of motion.

For the sqD₂ ansatz, this procedure results in a system of differential equations:

$$\begin{aligned} \dot{\alpha}_n = & -\frac{i}{2} \alpha_n \sum_{h,q} (\dot{\lambda}_{hq} \lambda_{hq}^* - \dot{\lambda}_{hq}^* \lambda_{hq}) \\ & - \frac{i}{2} \alpha_n \sum_{h,q} \dot{\theta}_{hq} \sinh^2(r_{hq}) \\ & - i \alpha_n \epsilon_n - i \sum_{m}^{n \neq m} V_{nm} \alpha_m \\ & - i \alpha_n \sum_{m,q} \omega_{m,q}^s (\sinh^2(r_{mq}) + |\lambda_{mq}|^2) \\ & + i 2 \alpha_n \sum_q \omega_{n,q}^e f_{nq} \text{Re} \lambda_{nq} \\ & - i \alpha_n \sum_q \Delta \omega_{nq} \cosh(2r_{nq}) \\ & + i \alpha_n \sum_q \Delta \omega_{nq} \sinh(2r_{nq}) \cos(\theta_{nq}) + (2\text{Re} \lambda_{nq})^2, \end{aligned} \quad (\text{A7})$$

for each index n , and

$$\dot{\lambda}_{kh} = -i\omega_{kh}^g \lambda_{kh} + \frac{i}{\rho} |\alpha_k|^2 \omega_{ikf/kh}^g - 4 \frac{i}{\rho} |\alpha_k|^2 \Delta\omega_{kh} \text{Re} \lambda_{kh}, \quad (\text{A8})$$

$$\dot{r}_{kh} = \frac{2}{\rho} |\alpha_k|^2 \Delta\omega_{kh} \sin(\theta_{kh}), \quad (\text{A9})$$

$$\dot{\theta}_{kh} = -2\omega_{kh}^g - 4 \frac{|\alpha_k|^2}{\rho} \Delta\omega_{kh} (1 - \coth(2r_{kh}) \cos(\theta_{kh})), \quad (\text{A10})$$

for each pair of $\{k, h\}$ indices.

We denote $\rho = \sum_n |\alpha_n|^2$ as the total population. Only the last two terms r_{kh} and θ_{kh} , which make up the complex squeezing parameter $\zeta = r_{kh} e^{i\theta_{kh}}$, depend on $\Delta\omega$. Now, if we look back at Hamiltonian terms eqn (2)–(5), we see straightaway that only the quadratic vibronic term depends on $\Delta\omega$, thus squeezing is generated only by this term. Otherwise, if $\Delta\omega = 0$, squeezing amplitude r_{kh} becomes time independent, while squeezing angle θ_{kh} changes at a constant rate of $-2\omega_{kh}^g$.

For the mD₂ ansatz, variational principle yields a system of implicit differential equations:

$$\begin{aligned} & \sum_j (\dot{x}_{j,n} S_{ij} + x_{j,n} S_{ij} K_{ij}) \\ &= -i \sum_{j,m} \alpha_{j,m} S_{ij} J_{nm} \\ & - i \sum_j \alpha_{j,n} S_{ij} (A_{ij} + B_{ij,n} + C_{ij,n}), \end{aligned} \quad (\text{A11})$$

for each pair of indices $\{i, n\}$, and

$$\begin{aligned} & \sum_{j,n} (\alpha_{i,n}^* \dot{x}_{j,n} S_{ij} \lambda_{j,kh}^2 + P_{ij,n} \dot{\lambda}_{j,kh} + P_{ij,n} \dot{\lambda}_{j,kh} K_{ij}) \\ &= -i \sum_{j,n,m} G_{ij,nm} \lambda_{j,kh} J_{nm} \\ & - i \sum_{j,n} P_{ij,n} \lambda_{j,kh} (A_{ij} + B_{ij,n} + C_{ij,n}) \\ & - i \sum_{j,n} P_{ij,n} \omega_{kh}^g \lambda_{j,kh}^2 + i \sum_j P_{ij,k} f_{kh} \omega_{kh}^g \\ & - 2i \sum_j P_{ij,k} \Delta\omega_{kh} (\lambda_{i,kh}^* + \lambda_{j,kh}), \end{aligned} \quad (\text{A12})$$

for a pair of $\{i, k, h\}$ indices, which we additionally defined

$$G_{ij,nm} = \alpha_{i,n}^* \alpha_{j,m} S_{ij} \quad (\text{A13})$$

$$P_{ij,n} = G_{ij,nm} \quad (\text{A14})$$

$$A_{ij} = \sum_{k,q} \omega_{kh}^g \lambda_{i,kh}^* \lambda_{j,kh} \quad (\text{A15})$$

$$B_{ij,n} = - \sum_h f_{nh} \omega_{nh}^g (\lambda_{i,nh}^* + \lambda_{j,nh}), \quad (\text{A16})$$

$$C_{ij,n} = \sum_h \Delta\omega_{nh} \left(1 + (\lambda_{i,nh}^* + \lambda_{j,nh})^2 \right), \quad (\text{A17})$$

For the D₂ ansatz, we can once again explicitly compute equations of motions following TDVP, however, we do not have

to, since the D₂ ansatz is a simplified version of the mD₂ ansatz, when multiplicity number is set to $M = 1$.

Calculation of linear response functions $S_{\text{abs/flor}}^{(1)}$ requires evaluation of two distinct coherent states. In the case of D₂ and mD₂ ansätze, the overlap between two distinct a and b coherent state are given by

$$\langle \lambda_a | \lambda_b \rangle = \exp \left(\lambda_a^* \lambda_b - \frac{1}{2} (|\lambda_a|^2 + |\lambda_b|^2) \right). \quad (\text{A18})$$

Meanwhile, overlap of two squeezed coherent states, as used in the sqD₂ ansatz, is given by expression¹³

$$\begin{aligned} \langle \lambda_a, \zeta_a | \lambda_b, \zeta_b \rangle &= \frac{1}{\sqrt{\zeta_{ab}}} \exp \left(- \frac{|\lambda_a|^2 + |\lambda_b|^2}{2} \right) \\ & \times \exp \left(\frac{\lambda_a^* \lambda_b}{\zeta_{ab}} + \frac{\zeta_a^2}{2\zeta_{ab}} \eta_{ab} + \frac{\zeta_b^2}{2\zeta_{ab}} \eta_{ba} \right), \end{aligned} \quad (\text{A19})$$

where

$$\eta_{ab} = e^{-i\theta_b} \cos h(r_b) \sin h(r_a) - e^{-i\theta_a} \cos h(r_a) \sin h(r_b), \quad (\text{A20})$$

$$\zeta_{ab} = \cos h(r_a) \cos h(r_b) - e^{i(\theta_b - \theta_a)} \sin h(r_a) \sin h(r_b) \quad (\text{A21})$$

Acknowledgements

Theory developments were supported by the framework of the CERN RD50 collaboration and were funded by the Lithuanian Academy of Sciences, grant No CERN-VU-2021-2022. Computations were performed on resources at the High Performance Computing Center, "HPC Sauletekis" in Vilnius University Faculty of Physics.

References

- 1 L. Valkunas, D. Abramavicius and T. Mančal, *Molecular Excitation Dynamics and Relaxation*, Wiley-VCH Verlag GmbH, 2013.
- 2 R. E. Blankenship, *Molecular Mechanisms of Photosynthesis*, Blackwell Science Ltd; Oxford, UK, 2002.
- 3 H. van Amerongen, R. van Grondelle and L. Valkunas, *Photosynthetic Excitons*, World Scientific; 2000.
- 4 A. S. Davydov, *Phys. Scr.*, 1979, 20, 387–394.
- 5 A. C. Scott, *Phys. D*, 1991, 51, 333–342.
- 6 Y. Zhao, K. Sun, L. Chen and M. Gelin, *Wiley Interdiscip. Rev.: Comput. Mol. Sci.*, 2022, 12, e1589.
- 7 J. Sun, B. Luo and Y. Zhao, *Phys. Rev. B: Condens. Matter Mater. Phys.*, 2010, 82, 014305.
- 8 V. Chorošajev, O. Rancova and D. Abramavicius, *Phys. Chem. Chem. Phys.*, 2016, 18, 7966–7977.
- 9 M. Jakučionis, V. Chorošajev and D. Abramavičius, *Chem. Phys.*, 2018, 515, 193–202.
- 10 M. Jakučionis, T. Mančal and D. Abramavičius, *Phys. Chem. Chem. Phys.*, 2020, 22, 8952–8962.
- 11 K. W. Sun, M. F. Gelin, V. Y. Chernyak and Y. Zhao, *J. Chem. Phys.*, 2015, 142, 212448.

- 12 N. Zhou, L. Chen, Z. Huang, K. Sun, Y. Tanimura and Y. Zhao, *J. Phys. Chem. A*, 2016, **120**, 1562–1576.
- 13 V. Chorošajev, T. Marčiulionis and D. Abramavicius, *J. Chem. Phys.*, 2017, **147**, 074114.
- 14 M. Jakucionis, I. Gaiziunas, J. Sulskus and D. Abramavicius, *J. Phys. Chem. A*, 2022, **126**, 180–189.
- 15 N. Zhou, L. Chen, Z. Huang, K. Sun, Y. Tanimura and Y. Zhao, *J. Phys. Chem. A*, 2016, **120**, 1562–1576.
- 16 L. Wang, L. Chen, N. Zhou and Y. Zhao, *J. Chem. Phys.*, 2016, **144**, 024101.
- 17 L. Chen, M. F. Gelin and W. Domcke, *J. Chem. Phys.*, 2019, **150**, 24101.
- 18 M. Jakučionis, A. Žukas and D. Abramavičius, *Phys. Chem. Chem. Phys.*, 2022, **24**, 17665–17672.
- 19 D. Abramavičius and T. Marčiulionis, *Lith. J. Phys.*, 2018, **58**, 307–317.
- 20 C. J. Bardeen, *Annu. Rev. Phys. Chem.*, 2014, **65**, 127–148.
- 21 M. Schröter, S. Ivanov, J. Schulze, S. Polyutov, Y. Yan, T. Pullerits and O. Kühn, *Phys. Rep.*, 2015, **567**, 1–78.
- 22 T. Steffen and Y. Tanimura, *J. Phys. Soc. Jpn.*, 2000, **69**, 3115–3132.
- 23 Y. Tanimura and T. Steffen, *J. Phys. Soc. Jpn.*, 2000, **69**, 4095–4106.
- 24 J. Zhang, R. Borrelli and Y. Tanimura, *J. Chem. Phys.*, 2020, **152**, 214114.
- 25 B. L. Hu, J. P. Paz and Y. Zhang, *Phys. Rev. D: Part. Fields*, 1993, **47**, 1576–1594.
- 26 R.-X. Xu, Y. Liu, H.-D. Zhang and Y. Yan, *J. Chem. Phys.*, 2018, **148**, 114103.
- 27 J. Frenkel, *Phys. Rev.*, 1931, **37**, 17–44.
- 28 M. Werther and F. Großmann, *Phys. Rev. B*, 2020, **101**, 174315.
- 29 R. J. Glauber, *Phys. Rev.*, 1963, **131**, 2766–2788.
- 30 L. Wang, Y. Fujihashi, L. Chen and Y. Zhao, *J. Chem. Phys.*, 2017, **146**, 124127.
- 31 Q. Xie, H. Zhong and M. T. Batchelor, *et al.*, *J. Phys. A: Math. Theor.*, 2017, **51**, 014001.
- 32 S. Mukamel, *Principles of nonlinear optical spectroscopy*, Oxford University Press, 1995.
- 33 V. Balevičius, L. Valkunas and D. Abramavicius, *J. Chem. Phys.*, 2015, **143**, 074101.
- 34 Z. H. Zhan, J. Zhang, Y. Li and H. S. Chung, *IEEE transactions on systems, man, and cybernetics. Part B, Cybernetics: a publication of the IEEE Systems, Man, and Cybernetics Society*, 2009, **39**, 1362–1381.
- 35 P. K. Mogensen and A. N. Riseth, *J. Open Source Software*, 2018, **3**, 615.
- 36 J. Lim, D. Paleček, F. Caycedo-Soler, C. N. Lincoln, J. Prior, H. von Berlepsch, S. F. Huelga, M. B. Plenio, D. Zigmantas and J. Hauer, *Nat. Commun.*, 2015, **6**, 7755.
- 37 N. Christensson, F. Milota, J. Hauer, J. Sperling, O. Bixner, A. Nemeth and H. F. Kauffmann, *J. Phys. Chem. B*, 2011, **115**, 5383–5391.
- 38 A. S. Bondarenko, T. L. C. Jansen and J. Knoester, *J. Chem. Phys.*, 2020, **152**, 194302.
- 39 N. J. Hestand and F. C. Spano, *Chem. Rev.*, 2018, **118**, 7069–7163.
- 40 J. Zeng and Y. Yao, *J. Chem. Theory Comput.*, 2022, **18**, 1255–1263.
- 41 M. Beck, *Phys. Rep.*, 2000, **324**, 1–105.
- 42 G. A. Worth and I. Burghardt, *Chem. Phys. Lett.*, 2003, **368**, 502–508.
- 43 G. A. Worth, H.-D. Meyer, H. Köppel, L. S. Cederbaum and I. Burghardt, *Int. Rev. Phys. Chem.*, 2008, **27**, 569–606.

A5


Temperature-controlled open-quantum-system dynamics using a
time-dependent variational method

M. Jakučionis, D. Abramavičius

Physical Review A, **103**, 032202 (2021)

Reproduced with permission from the American Physical Society.

Temperature-controlled open-quantum-system dynamics using a time-dependent variational method

Mantas Jakučiūnis  and Darius Abramavičius*Institute of Chemical Physics, Vilnius University, Sauletekio al. 9-III, LT-10222 Vilnius, Lithuania* (Received 17 July 2020; revised 29 January 2021; accepted 8 February 2021; published 1 March 2021)

The Dirac-Frenkel variational method with Davydov D_2 trial wavefunction is extended by introducing a thermalization algorithm and applied to simulate dynamics of a general open quantum system. The algorithm allows to control temperature variations of a harmonic finite-size bath when in contact with the quantum system. Thermalization of the bath vibrational modes is realized via stochastic scatterings, implemented as a discrete-time Bernoulli process with Poisson statistics. It controls bath temperature by steering vibrational modes' evolution towards their canonical thermal equilibrium. Numerical analysis of the exciton relaxation dynamics in a small molecular cluster reveals that thermalization additionally provides significant calculation speedup due to the reduced number of vibrational modes needed to obtain the convergence.

DOI: [10.1103/PhysRevA.103.032202](https://doi.org/10.1103/PhysRevA.103.032202)

I. INTRODUCTION

Obtaining dynamics of open quantum systems, i.e., quantum systems that are identified as separate from their environment yet remain in thermal contact with it, is one of the most general non-equilibrium statistical physics problem. Its applicability ranges from excited state relaxation in optical response [1,2], energy transport in molecular aggregates [3–8], photosynthetic complexes [9–12], to others [13–17]. Prevalent theoretical description is given in terms of a system-bath model in constant-temperature bath conditions [18,19], where the *system* degrees of freedom are coupled to the bath-induced thermal fluctuations representing the environment, e.g., phonons or vibrational motion of surrounding molecules. Fluctuations are modeled by an infinite number of quantum harmonic oscillators constituting the *quantum bath* at thermal equilibrium.

These conditions can be fulfilled using the reduced density matrix approach [2,7]. Second order perturbation theory, with respect to the system-bath coupling, leads to the reduced equations of motion of the system-only variables, while the bath is averaged out. Then the system variables indirectly depend on the bath degrees of freedom via fluctuation correlation functions, which are well-behaved analytical functions. At the second perturbation order [7,18], equations of motion are reminiscent of the Pauli master equation with relaxation coefficients calculated with respect to the thermal equilibrium. However, now the resulting equations can lead to unphysical results, e.g., negative probabilities [20]. The more complicated fourth-order equations of motion include divergent parameters and are often avoided [21]. A nonperturbative, numerically exact approach of hierarchical equations of motion for the exponential fluctuation correlation functions is available to obtain the exact dynamics [22–24], and chain-mapping techniques together with the time-dependent density matrix renormalization group are alternatively possible for struc-

tured environments [25,26]. However, computational costs limit these methods to models with just few degrees of freedom. A well-known method of stochastic Schrödinger equation requires averaging over many entangled trajectories to obtain dynamics at finite temperature [27–32]. Its hierarchical realization [33] improves convergence; meanwhile, the thermofield dynamics approach tries to directly compute thermally averaged dynamics by mapping the initial thermal density matrix onto a fictitious bath vacuum state and then coupling the system to it [34–37]. Alternatively, dissipative dynamics can be obtained by straightforward addition of a linear friction coefficient to the model Hamiltonian [38]; however, it only applies at zero temperature. Yet, in all these cases, the thermal state of the nearest surrounding is not under control.

An important aspect of the bath, or more explicitly of the finite number of bath oscillators, is its heat capacity. For a single quantum harmonic oscillator the heat capacity in the limit of weak system-bath coupling is given by

$$c(\beta^{-1}) = (\beta\omega)^2 \frac{\exp(\beta\omega)}{[\exp(\beta\omega) - 1]^2}, \quad (1)$$

where throughout the paper $\hbar = 1$, $\beta = (k_B T)^{-1}$ is an inverse temperature, and ω is the oscillator frequency. When the system exchanges energy with a bath made of such oscillators, its temperature may be affected. If the system-bath energy exchange is excessively large, the thermal energy can accumulate in the bath oscillators and this will effectively change the thermostat temperature [39]. In most cases, the bath heating effect is undesirable as, in the system-bath models, the bath is generally supposed to represent a constant-temperature thermostat.

On the other hand, the bath heating effect could be related to the natural phenomenon of molecular local heating [40,41]; i.e., if a molecule quickly dissipates a large amount

of thermal energy to its environment, e.g., due to exciton-exciton annihilation [42–44] or ultrafast molecular internal conversion [45,46], the local heating of the molecule nearest the surrounding takes place and the further cooling process, the quantum thermalization [47,48], becomes an important ingredient to consider when describing the corresponding experiments.

In this work, we introduce the thermalization algorithm to the time-dependent variational theory that allows explicit control over the bath temperature. By varying the bath size and the thermalization rate, both the degree of bath heating and the cooling time can be adjusted. These properties allow to mimic realistic physical conditions, making the presented approach superior to the density-operator-based approaches, where the bath heating is excluded, and to the explicit bath models, where the bath temperature is not controlled.

II. FLUCTUATING EXCITON MODEL

We consider a molecular aggregate made of N coupled chromophores at specific sites. In the simplest case, the sites represent distinct molecules that can be electronically excited by, e.g., laser or sunlight irradiation in the visible spectral region. Vibrational normal modes of molecules and of the surrounding medium will be treated as the baths of harmonic oscillators. Each chromophore is directly affected only by its own intramolecular vibrations and of its closest environment; therefore, a separate and uncorrelated (local) manifold of vibrational modes $q = 1, 2, \dots, Q$ is associated with each chromophore. Such a model is characterized by a Hamiltonian $\hat{H} = \hat{H}_S + \hat{H}_B + \hat{H}_{SB}$, with system, bath, and system-bath-coupling terms being

$$\hat{H}_S = \sum_n \varepsilon_n \hat{a}_n^\dagger \hat{a}_n + \sum_{n,m}^{n \neq m} J_{nm} \hat{a}_n^\dagger \hat{a}_m, \quad (2)$$

$$\hat{H}_B = \sum_{n,q} \omega_{nq} \hat{b}_{nq}^\dagger \hat{b}_{nq}, \quad (3)$$

$$\hat{H}_{SB} = - \sum_n \hat{a}_n^\dagger \hat{a}_n \sum_q \omega_{nq} g_{nq} (\hat{b}_{nq}^\dagger + \hat{b}_{nq}). \quad (4)$$

Here ε_n denotes the n th chromophore electronic excitation energy, J_{nm} is the resonant coupling between n th and m th chromophores, and \hat{a}_n^\dagger and \hat{a}_n are the corresponding electronic excitation creation and annihilation bosonic operators. The frequency of the q th vibrational mode in the n th bath is ω_{nq} , the electron-vibrational coupling is characterized by g_{nq} , and \hat{b}_{nq}^\dagger and \hat{b}_{nq} are the creation and annihilation bosonic operators of the q th mode in the n th bath.

In the following we consider only a single electronic excitation in the aggregate. The time evolution of a nonequilibrium state is described by the Davydov D_2 wavefunction [49,50]

$$|\Psi_{D_2}\rangle = \sum_n \alpha_n(t) \hat{a}_n^\dagger \hat{a}_n |0\rangle_{el} \times \prod_{m,q} |\lambda_{mq}(t)\rangle, \quad (5)$$

where $\alpha_n(t)$ is the electronic excitation amplitude, and $|0\rangle_{el} = \prod_n |0\rangle_n$ is the global ground state, when all sites are in their electronic ground states. $|\lambda_{mq}(t)\rangle$ is the coherent state of the

q th mode in the m th bath [51,52]. It is fully described by the time-dependent complex displacements, $\lambda_{mq}(t)$. The time-dependent Dirac-Frenkel variational method allows to obtain equations of motion for parameters α_n and λ_{mq} [3,6,53,54]:

$$\begin{aligned} \frac{d\alpha_n(t)}{dt} &= -i\alpha_n(t)\varepsilon_n - i \sum_m^{m \neq n} \alpha_m(t) J_{nm} \\ &\quad + i\alpha_n(t) \sum_q \omega_{nq} (2g_{nq} - h_q) \text{Re}(\lambda_{nq}(t)), \end{aligned} \quad (6)$$

$$\frac{d\lambda_{mq}(t)}{dt} = -i\omega_{mq}(\lambda_{mq}(t) - h_q(t)). \quad (7)$$

Here $h_q(t) = \sum_i^N g_{iq} |\alpha_i(t)|^2$ is the site population-weighted electron-vibrational coupling strength. The first line in Eq. (6) describes the dynamics of an isolated system. Accordingly, the first term on the right-hand side of Eq. (7) describes isolated oscillator. Other terms are due to the system-bath interaction.

Description of the model at a given temperature T requires creation of a statistical ensemble. This is achieved by Monte Carlo sampling over a statistical thermal ensemble, i.e., over initial bath oscillator displacements $\lambda_{mq}(0)$, sampled from the Glauber-Sudarshan probability distribution [55]

$$\mathcal{P}(\lambda_{mq}) = \mathcal{Z}^{-1} \exp(-|\lambda_{mq}|^2 [e^{\beta\omega_{mq}} - 1]). \quad (8)$$

The ensemble describes canonical statistics of quantum harmonic oscillators, which applies to our model prior to external perturbations. The ensemble-averaged quantities will be denoted by $\langle \dots \rangle_{th}$. The ensemble of exciton trajectories allows to describe irreversible excitation energy relaxation. While the initial thermal state before excitation can be properly defined, the bath accepts energy during exciton relaxation and the state of the bath *after* relaxation steers away from equilibrium. Equations of motion guarantee energy conservation; hence the combined system-bath cannot thermalize. In order to thermalize the bath, we extend the original model by introducing the *secondary* bath (we will refer to the local baths as the *primary* baths). The effective heat capacity of the secondary bath is infinite; hence, the bath can be characterized by a constant temperature T_∞ . The secondary bath will not be treated explicitly; modes of the primary baths interact with the secondary bath via stochastic scattering events, or quantum jumps [56,57], which affect the kinetic energy of primary bath modes.

The scattering statistics follows the Poisson distribution $P_{mq}(\theta, \tau) = \frac{1}{\theta!} (\tau v_{mq})^\theta e^{-\tau v_{mq}}$, which defines the probability of observing θ scattering events per time interval τ with individual event scattering rate v_{mq} . Poisson statistics is obtained by simulating a discrete-time Bernoulli process [58,59] in a limit of $\tau \rightarrow 0$ and $v_{mq}\tau \ll 1$. This is realized in simulations by dividing the total evolution time t_{total} into equidistant length τ intervals. At the end of each interval, for each mode in the primary bath, we flip a biased coin with probability $v_{mq}\tau$ of landing “heads.” If the coin lands heads, we shift the momentum of the mode $p_{mq}(kt) = \sqrt{2\text{Im}\lambda_{mq}(kt)}$ to a value drawn from the Glauber-Sudarshan distribution [see Eq. (8)], while the coordinate remains unchanged. Otherwise, if coin lands “tails,” no changes are done. To obtain converged statistics,

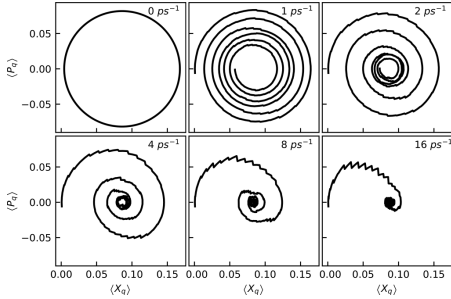


FIG. 1. Phase-space trajectory of one specific bath mode $\omega_q = 100 \text{ cm}^{-1}$ for a single excited chromophore calculated with various scattering rates ν . The initial temperature of the primary bath is $T_1(0) = 300 \text{ K}$ and the secondary bath is at a constant temperature $T_\infty = 200 \text{ K}$. The scattering step size is $\tau = 0.01 \text{ ps}$. Wiggles in dynamics are due to finite-size ensemble averaging (5000 trajectories).

we apply the thermalization algorithm to every trajectory of the thermal ensemble.

III. SIMULATION RESULTS

We first demonstrate control of the primary bath temperature of the simplest possible system, a single, $N = 1$, chromophore unit. For demonstration we set up artificial conditions: the initial primary bath temperature is $T_1(0) = 300 \text{ K}$, and the secondary bath is at $T_\infty = 200 \text{ K}$. The primary bath consists of $Q = 750$ vibrational modes with frequencies $\omega_q = \omega_0 + (q - 1)\Delta\omega$. An offset by $\omega_0 = 0.01 \text{ cm}^{-1}$ is introduced for stability and a step size $\Delta\omega = 1 \text{ cm}^{-1}$. The coupling parameters g_{mq} follow the super-Ohmic spectral density function $C''(\omega) = \omega^s \exp(-\omega/\omega_c)$ with $s = 2$ and $\omega_c = 100 \text{ cm}^{-1}$ [3,60]. The number of modes and discretization parameters are sufficient to obtain convergent model dynamics. For thermalization, we consider scattering rates of all modes to be equal, $\nu_{mq} \rightarrow \nu$, and the scattering step size is $\tau = 0.01 \text{ ps}^{-1}$. The thermal ensemble consists of 5000 trajectories.

In Fig. 1 the coordinate $\langle x_{1q} \rangle_{\text{th}} = \langle \sqrt{2} \text{Re} \lambda_{1q} \rangle_{\text{th}}$ and momentum $\langle p_{1q} \rangle_{\text{th}} = \langle \sqrt{2} \text{Im} \lambda_{1q} \rangle_{\text{th}}$ phase-space trajectory of a single 100 cm^{-1} frequency vibrational mode, calculated with various scattering rates ν , is presented. The oscillator, in the absence of thermalization, evolves along a closed trajectory around $x_{1q}^{\text{min}} = \sqrt{2}g_{1q}$. Applying the thermalization procedure, a dissipative-type trajectory is observed. The coordinate $\langle x_{1q} \rangle_{\text{th}}$ equilibrates to x_{1q}^{min} (equilibrium is shifted from zero due to coupling with the system), while momentum $\langle p_{1q} \rangle_{\text{th}}$ approaches zero. The thermalization time can be adjusted by changing the scattering rate, ν . Both weakly damped and overdamped regimes become available.

The transient temperature of the primary bath can be estimated [39] by computing the average kinetic energy $\langle K_{mq}(t, \epsilon) \rangle_{\text{th}}$ over the time interval ϵ . The parameter ϵ then implies the resolution. For the whole primary bath the tran-

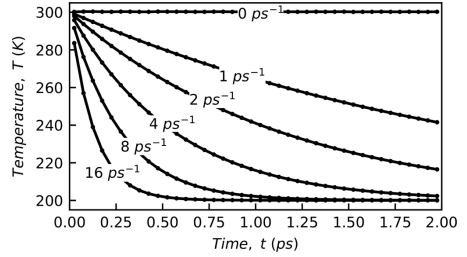


FIG. 2. The primary bath temperature $T_1(t)$ calculated with various scattering rates ν . The initial temperature of the primary bath is $T_1(0) = 300 \text{ K}$ and the secondary bath is at a constant temperature $T_\infty = 200 \text{ K}$. The scattering step size is $\tau = 0.01 \text{ ps}$.

sient temperature is then given by

$$T_m(t) = \frac{1}{k_B Q} \sum_{q=1}^Q \omega_{mq} \ln \left(1 + \frac{\omega_{mq}}{2 \langle K_{mq}(t, \epsilon) \rangle_{\text{th}}} \right)^{-1}. \quad (9)$$

In Fig. 2 we present the primary bath temperature calculated with $\epsilon = 50 \text{ fs}$ and various scattering rates, ν . In the absence of thermalization, the primary bath temperature remains at the initial value of $T_1(0) = 300 \text{ K}$. Meanwhile, thermalization introduces cooling of the primary bath down to the temperature of the secondary bath. The scattering rate, ν , allows to control the thermalization time.

The temperature control and stability considerably affect the electronic excitation dynamics. To demonstrate the sensitivity of the excitation evolution to the thermalization, we consider a linear $N = 3$ chromophore aggregate, with chromophore transition energies 0, 250, and 500 cm^{-1} , and nearest-neighbor coupling $J = 100 \text{ cm}^{-1}$. Excited states of such chromophore aggregate are *excitons* [7,61]. They represent electronic excitations delocalized over several sites with time-dependent delocalization length [62]. Hence, we switch to the eigenstate basis (exciton representation, defined by $\hat{H}_S \psi^{(\text{exc})} = \epsilon \psi^{(\text{exc})}$): $\rho_e^{(\text{exc})}(t) = \sum_{n,m} (\psi_{ne}^{(\text{exc})})^* (\alpha_n^*(t) \alpha_m(t))_{\text{th}} \psi_{me}^{(\text{exc})}$. The initial electronic state corresponds to the optically excited highest-energy exciton eigenstate. The parameters of the primary baths of chromophores are the same as above; however, now the initial primary bath temperature and the secondary bath temperature are the same: $T_m(0) = T_\infty = 77 \text{ K}$. The thermal ensemble consists of 240 trajectories. In Fig. 3 we present exciton state populations $\rho_e^{(\text{exc})}(t)$ and the primary bath temperatures $T_m(t)$ calculated in (i) the *dense* primary bath discretization regime without thermalization (the bath discretization step size is $\Delta\omega = 1 \text{ cm}^{-1}$, $Q = 750$ vibrational modes per site), (ii) the *sparse* discretization regime without thermalization ($\Delta\omega = 50 \text{ cm}^{-1}$, $Q = 15$), and (iii) the sparse discretized bath with thermalization ($\nu = 2.5 \text{ ps}^{-1}$).

Consider the excitation dynamics without thermalization. In models (i) and (ii) exciton populations sequentially relax to lower-energy exciton states, eventually reaching the lowest energy state [63–65]. The final population distribution in

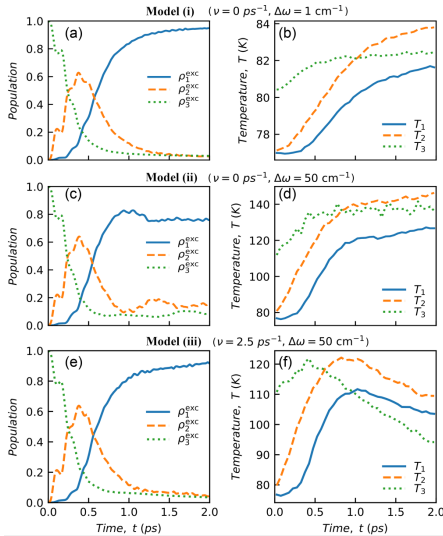


FIG. 3. Multisite bath model excitation state populations $\rho_n^{\text{exc}}(t)$ and local bath temperatures $T_m(t)$ calculated in model (i), the *dense* primary bath discretization regime without thermalization, in model (ii), the *sparse* discretization regime without thermalization, and in model (iii), the sparsely discretized bath with thermalization ($\nu = 2.5 \text{ ps}^{-1}$).

the sparse regime, model (ii), significantly differs from the dense case. The origin of the discrepancy is twofold: the bath recursion time $t_{\text{rec}} = 2\pi/\Delta\omega$ for model (ii) is shorter than the calculation time $t_{\text{rec}} < t_{\text{total}}$, and the sparse primary bath shows significant growth of the bath temperature [compare Figs. 3(b) and 3(d)]. Both of these drawbacks are addressed by introducing the bath thermalization in model (iii). Looking at Fig. 3(e), we see that the exciton population dynamics and steady-state values for model (iii) become quantitatively comparable to the case of model (i).

IV. DISCUSSION

A single quantum harmonic oscillator is characterized by a specific heat $c(\beta^{-1}) < k_B$, which depends on temperature as given by Eq. (1). For a given set of bath oscillators the specific heat at a given temperature can be estimated; however, the harmonic oscillators of the bath as defined by Eq. (3) do not exchange energy. Accordingly, as the system relaxes, only a few in-resonant oscillators accept the energy and diverge

away from equilibrium [66]. Hence, the temperature at which excitation dynamics occurs no longer matches the initial bath temperature; local heating takes place.

A straightforward approach to avoid heating is to increase the bath density of states until the dynamics of interest converges (in our model, this is achieved by increasing the number of bath oscillators). However, this is acceptable only for small systems, since computation effort scales quadratically with both number of sites and bath oscillators. Thermalization can be utilized to steer the bath to the required temperature. An additional merit of thermalization is the significant reduction of the number of vibrational modes needed per bath. Our simulations show convergence with just 15 modes per bath while maintaining comparable exciton relaxation dynamics (Fig. 3).

In an effort to reduce the computational effort, Wang *et al.* [67] used a logarithmic bath discretization. However, high-frequency representation of the continuous spectral density becomes poor. Our model is in line with the explicit surrogate Hamiltonian [68] and its stochastic realization [69–71]; while our approach does not require the explicit modeling of the secondary bath, it still maintains proper quantum dynamics in the system.

The time-dependent variational approach with the Davydov D_2 *Ansatz* can be improved by considering more complex Davydov *Ansätze* family members, e.g., multitude of D_1 *Ansatz* (multi- D_1) and multi- D_2 [53,67,72,73] or its Born-Oppenheimer approximated variant [74], sD_2 . Either way, they all suffer from finite bath heating capacity, in most cases, even stronger than the D_2 *Ansatz*, because of the significantly increased computational effort needed to propagate numerous bath oscillators. Work is in progress on adapting the presented thermalization algorithm to these more intricate *Ansätze*.

In conclusion, we present a system-bath model with stochastic bath thermalization using the time-dependent variational approach with Davydov D_2 *Ansatz*. Thermalization allows to steer the bath vibrational mode evolution towards an equilibrium thermal state of selected temperature in a controlled way, and at the same time for the bath to still maintain an aspect of being coupled to the system. In addition, by analyzing exciton relaxation dynamics of a chromophore aggregate with thermalization, we found the exciton dynamics to converge with a much smaller number of bath modes, significantly speeding up numerical computation.

ACKNOWLEDGMENTS

We thank the Research Council of Lithuania for financial support (Grant No. S-MIP-20-47). Computations were performed on resources at the High Performance Computing Center “HPC Sauletekis” in the Vilnius University Faculty of Physics.

[1] K. E. Dorfman, F. Schlawin, and S. Mukamel, *Rev. Mod. Phys.* **88**, 045008 (2016).

[2] S. S. Mukamel, *Principles of Nonlinear Optical Spectroscopy* (Oxford University Press, New York, 1995).

- [3] M. Jakuciūnis, V. Chorošajev, and D. Abramavičius, *Chem. Phys.* **515**, 193 (2018).
- [4] V. Chorošajev, T. Marčiulionis, and D. Abramavičius, *J. Chem. Phys.* **147**, 74114 (2017).
- [5] M. Schröter, S. Ivanov, J. Schulze, S. Polyutov, Y. Yan, T. Pullerits, and O. Kühn, *Phys. Rep.* **567**, 1 (2015).
- [6] V. Chorošajev, A. Gelzinis, L. Valkunas, and D. Abramavičius, *J. Chem. Phys.* **140**, 244108 (2014).
- [7] L. Valkunas, D. Abramavičius, and T. Mančal, *Molecular Excitation Dynamics and Relaxation* (Wiley-VCH, Weinheim, Germany, 2013).
- [8] V. May and O. Kühn, *Charge and Energy Transfer Dynamics in Molecular Systems* (Wiley-VCH, Weinheim, Germany, 2011).
- [9] S. J. Jang and B. Mennucci, *Rev. Mod. Phys.* **90**, 035003 (2018).
- [10] E. Thyrgaug, C. N. Lincoln, F. Branchi, G. Cerullo, V. Perlik, F. Šanda, H. Lokstein, and J. Hauer, *Photosynth. Res.* **135**, 45 (2018).
- [11] P. Malý, J. M. Gruber, R. J. Cogdell, T. Mančal, and R. Van Grondelle, *Proc. Natl. Acad. Sci. USA* **113**, 2934 (2016).
- [12] A. Chenu and G. D. Scholes, *Annu. Rev. Phys. Chem.* **66**, 69 (2015).
- [13] J. Sjakste, K. Tanimura, G. Barbarino, L. Perfetti, and N. Vast, *J. Phys. Condens. Matter* **30**, 353001 (2018).
- [14] A. Flesch, M. Cramer, I. P. McCulloch, U. Schollwöck, and J. Eisert, *Phys. Rev. A* **78**, 033608 (2008).
- [15] F. C. Lombardo and G. J. Turiaci, *Phys. Rev. D* **87**, 084028 (2013).
- [16] H. Yu and J. Zhang, *Phys. Rev. D* **77**, 024031 (2008).
- [17] J. Ruostekoski and D. F. Walls, *Phys. Rev. A* **58**, R50 (1998).
- [18] H.-P. Breuer and F. Petruccione, *The Theory of Open Quantum Systems* (Oxford University Press, New York, 2007).
- [19] U. Weiss, *Quantum Dissipative Systems* (World Scientific, Singapore, 2012).
- [20] A. Montoya-Castillo, T. C. Berkelbach, and D. R. Reichman, *J. Chem. Phys.* **143**, 194108 (2015).
- [21] S. Jang, J. Cao, and R. J. Silbey, *J. Chem. Phys.* **116**, 2705 (2002).
- [22] Y. Tanimura, *Phys. Rev. A* **41**, 6676 (1990).
- [23] Y. Tanimura, *J. Phys. Soc. Jpn.* **75**, 82001 (2006).
- [24] R.-X. Xu and Y. J. Yan, *Phys. Rev. E* **75**, 031107 (2007).
- [25] D. Tamascellì, A. Smirne, J. Lim, S. F. Huelga, and M. B. Plenio, *Phys. Rev. Lett.* **123**, 090402 (2019).
- [26] J. Prior, A. W. Chin, S. F. Huelga, and M. B. Plenio, *Phys. Rev. Lett.* **105**, 050404 (2010).
- [27] V. Abramavičius and D. Abramavičius, *J. Chem. Phys.* **140**, 065103 (2014).
- [28] H. Appel and M. Di Ventura, *Phys. Rev. B* **80**, 212303 (2009).
- [29] R. Biele and R. D'Agosta, *J. Phys. Condens. Matter* **24**, 273201 (2012).
- [30] L. Diósi and W. T. Strunz, *Phys. Lett. A* **235**, 569 (1997).
- [31] I. de Vega, D. Alonso, and P. Gaspard, *Phys. Rev. A* **71**, 023812 (2005).
- [32] V. Link and W. T. Strunz, *Phys. Rev. Lett.* **119**, 180401 (2017).
- [33] R. Hartmann and W. T. Strunz, *J. Chem. Theory Comput.* **13**, 5834 (2017).
- [34] C. S. Reddy and M. D. Prasad, *Mol. Phys.* **113**, 3023 (2015).
- [35] G. Ritschel, D. Suess, S. Möbius, W. T. Strunz, and A. Eisfeld, *J. Chem. Phys.* **142**, 034115 (2015).
- [36] R. Borrelli and M. F. Gelin, *J. Chem. Phys.* **145**, 224101 (2016).
- [37] L. Chen and Y. Zhao, *J. Chem. Phys.* **147**, 214102 (2017).
- [38] R. Martinazzo, M. Nest, P. Saalfrank, and G. F. Tantarini, *J. Chem. Phys.* **125**, 194102 (2006).
- [39] D. Abramavičius, V. Chorošajev, and L. Valkunas, *Phys. Chem. Chem. Phys.* **20**, 21225 (2018).
- [40] Z. Chen and R. S. Sorbello, *Phys. Rev. B* **47**, 13527 (1993).
- [41] M. Ichikawa, H. Ichikawa, K. Yoshikawa, and Y. Kimura, *Phys. Rev. Lett.* **99**, 148104 (2007).
- [42] V. Gulbinas, L. Valkunas, D. Kuciauskas, E. Katilius, V. Liuolia, W. Zhou, and R. E. Blankenship, *J. Phys. Chem.* **100**, 17950 (1996).
- [43] L. Valkunas and V. Gulbinas, *Photochem. Photobiol.* **66**, 628 (1997).
- [44] V. Gulbinas, R. Karpicz, G. Garab, and L. Valkunas, *Biochemistry* **45**, 9559 (2006).
- [45] V. Balevičius, C. N. Lincoln, D. Viola, G. Cerullo, J. Hauer, and D. Abramavičius, *Photosynth. Res.* **135**, 55 (2018).
- [46] V. Balevičius, Jr., T. Wei, D. Di Tommaso, D. Abramavičius, J. Hauer, T. Polívka, and C. D. P. Duffy, *Chem. Sci.* **10**, 4792 (2019).
- [47] J. Choi, H. Zhou, S. Choi, R. Landig, W. W. Ho, J. Isoya, F. Jelezko, S. Onoda, H. Sumiya, D. A. Abanin, and M. D. Lukin, *Phys. Rev. Lett.* **122**, 043603 (2019).
- [48] V. Scarani, M. Ziman, P. Štelmachovič, N. Gisin, and V. Bužek, *Phys. Rev. Lett.* **88**, 097905 (2002).
- [49] I. Frenkel and J. Frenkel, *Wave Mechanics: Elementary Theory* (Oxford University Press, New York, 1936).
- [50] J. Sun, B. Luo, and Y. Zhao, *Phys. Rev. B* **82**, 014305 (2010).
- [51] W.-M. Zhang, D. H. Feng, and R. Gilmore, *Rev. Mod. Phys.* **62**, 867 (1990).
- [52] S. Kais and R. D. Levine, *Phys. Rev. A* **41**, 2301 (1990).
- [53] L. Chen, M. Gelin, and Y. Zhao, *Chem. Phys.* **515**, 108 (2018).
- [54] Y. Yan, L. Chen, J. Y. Luo, and Y. Zhao, *Phys. Rev. A* **102**, 023714 (2020).
- [55] R. J. Glauber, *Phys. Rev.* **131**, 2766 (1963).
- [56] M. B. Plenio and P. L. Knight, *Rev. Mod. Phys.* **70**, 101 (1998).
- [57] K. Luoma, W. T. Strunz, and J. Piilo, *Phys. Rev. Lett.* **125**, 150403 (2020).
- [58] V. N. Kampen, *Stochastic Processes in Physics and Chemistry* (Elsevier, Amsterdam, 2007).
- [59] D. Bertsekas and J. Tsitsiklis, *Introduction to Probability* (Athena Scientific, Belmont, 2008).
- [60] A. Kell, X. Feng, M. Reppert, and R. Jankowiak, *J. Phys. Chem. B* **117**, 7317 (2013).
- [61] H. van Amerongen, R. van Grondelle, and L. Valkunas, *Photosynthetic Excitons* (World Scientific, Singapore, 2000).
- [62] V. Chorošajev, O. Rancova, and D. Abramavičius, *Phys. Chem. Chem. Phys.* **18**, 7966 (2016).
- [63] J. M. Moix, Y. Zhao, and J. Cao, *Phys. Rev. B* **85**, 115412 (2012).
- [64] Y. Subasi, C. H. Fleming, J. M. Taylor, and B. L. Hu, *Phys. Rev. E* **86**, 061132 (2012).
- [65] A. Gelzinis and L. Valkunas, *J. Chem. Phys.* **152**, 51103 (2020).
- [66] A. W. Chin, J. Prior, R. Rosenbach, F. Caycedo-Soler, S. F. Huelga, and M. B. Plenio, *Nat. Phys.* **9**, 113 (2013).
- [67] L. Wang, L. Chen, N. Zhou, and Y. Zhao, *J. Chem. Phys.* **144**, 024101 (2016).
- [68] R. Baer and R. Kosloff, *J. Chem. Phys.* **106**, 8862 (1997).
- [69] G. Katz, D. Gelman, M. A. Ratner, and R. Kosloff, *J. Chem. Phys.* **129**, 034108 (2008).
- [70] E. Torrontegui and R. Kosloff, *New J. Phys.* **18**, 093001 (2016).

- [71] F. Habecker, R. Röhse, and T. Klüner, *J. Chem. Phys.* **151**, 134113 (2019).
- [72] N. Zhou, Z. Huang, J. Zhu, V. Chernyak, and Y. Zhao, *J. Chem. Phys.* **143**, 014113 (2015).
- [73] N. Zhou, L. Chen, Z. Huang, K. Sun, Y. Tanimura, and Y. Zhao, *J. Phys. Chem. A* **120**, 1562 (2016).
- [74] M. Jakučionis, T. Mancal, and D. Abramavičius, *Phys. Chem. Chem. Phys.* **22**, 8952 (2020).


A6

Thermalization of open quantum systems using the multiple-Davydov-D2

M. Jakučionis, D. Abramavičius

Physical Review A, **107**, 062205 (2023)

Reproduced with permission from the American Physical Society.

Thermalization of open quantum systems using the multiple-Davydov- D_2 variational approachMantas Jakučionis  and Darius Abramavičius*Institute of Chemical Physics, Vilnius University, Sauletekio Avenue 9-III, 10222 Vilnius, Lithuania*

(Received 3 March 2023; accepted 31 May 2023; published 8 June 2023)

Numerical implementation of an explicit phonon bath requires a large number of oscillator modes in order to maintain oscillators at the initial temperature when modeling energy relaxation processes. An additional thermalization algorithm may be useful in controlling the local temperature. In this paper we extend our previously proposed thermalization algorithm [M. Jakučionis and D. Abramavičius, *Phys. Rev. A* **103**, 032202 (2021)] to be used with the numerically exact multiple-Davydov- D_2 trial wave function for simulation of relaxation dynamics and spectroscopic signals of open quantum systems using the time-dependent Dirac-Frenkel variational principle. By applying it to the molecular aggregate model, we demonstrate how the thermalization approach significantly reduces the numerical cost of simulations by decreasing the number of oscillators needed to explicitly simulate the aggregate's environment fluctuations while maintaining correspondence to the exact population relaxation dynamics. Additionally, we show how the thermalization can be used to find the equilibrium state of the excited molecular aggregate, which is necessary for simulation of the fluorescence and other spectroscopic signals. The thermalization algorithm we present offers the possibility to investigate larger system-bath models than was previously possible using the multiple-Davydov- D_2 trial wave function and local heating effects in molecular complexes.

DOI: [10.1103/PhysRevA.107.062205](https://doi.org/10.1103/PhysRevA.107.062205)**I. INTRODUCTION**

Open-quantum-system models are widely used to describe properties of molecular aggregates [1,2]. The system usually consists of molecular electronic states. Intramolecular vibrational degrees of freedom (DOFs), which play a major role in the relaxation process of the systems of interest, can also be included in the quantum-system model. The rest of the DOFs are treated as an environment of a constant temperature: the bath. The bath is modeled as a collection of quantum harmonic oscillators (QHOs) and is characterized by a continuous-fluctuation spectral density function [2–5]. Separation into the system and the bath parts is mostly a formality as the system-bath coupling has to be included to account for molecular environment-induced decoherence and temperature effects; hence the quantum dynamics penetrates into the bath and the bath also changes its state.

When using wave-function-based simulation approaches, it can be challenging to maintain a precise representation of the bath as a constant temperature thermostat, because energy exchange between the system and the bath can alter thermal properties of the bath. Generally, a large number of explicitly modeled QHO modes have to be included to minimize the negative effects of thermal energy accumulation in the bath, but this is numerically expensive. Therefore, one always has to balance between the size of the model, the accuracy of the chosen numerical method, and the method's numerical cost. Alternatively, one could numerically change the wave-function variables during its time evolution in a way so as to prevent accumulation of the thermal energy in the bath and to maintain it at a desired temperature, i.e., perform thermalization.

It is challenging to accurately simulate the dynamics of quantum systems that exchange energy and (quasi)particles with their surroundings, i.e., of the open quantum systems [6,7], because the numerical cost needed to propagate the corresponding dynamical equations in time increases exponentially with the number of DOFs. The wave-function approach based on the multiple-Davydov- D_2 trial wave function (multiple-Davydov- D_2 *Ansatz*) [8–12], along with the time-dependent variational principle, has been shown to be an excellent tool for accurately simulating the dynamics of system-bath models [8,13–19] and spectroscopic signals [10,18–21]. Despite relying on an adaptive time-dependent state basis set, the problem of rapidly growing numerical costs remains.

In a previous study we proposed the thermalization algorithm [22] to be used with the Davydov- D_2 *Ansatz* [13,23–28], which restricts QHOs to their lowest uncertainty states: coherent states [29,30] with Gaussian wave packets in their coordinate-momentum phase space. We demonstrated how the thermalization algorithm regulates the temperature of the environment and enables the electronically excited molecular system to relax into its equilibrium state at a given temperature [31–33] even when using a reduced number of bath oscillators, which greatly reduces numerical costs. The characteristics of the resulting equilibrium state are essential for modeling fluorescence, excited-state emission, excited-state absorption, and other spectroscopic signals [1]. However, the Davydov- D_2 *Ansatz* is a crude approximation of the actual system-bath model eigenstates and thus is unable to completely capture electronic population relaxation dynamics [10].

Meanwhile, the system-bath dynamics obtained using the multiple-Davydov *Ansätze* is consistent with the results from

other state-of-the-art methods, such as hierarchical equations of motion [9–11], the quasiadiabatic path integral [14], and the multiconfiguration time-dependent Hartree method [15,34], even when the number of bath oscillators is large. Due to the more complicated wave-function structure of the multiple-Davydov-D₂ ansatz, straightforward application of the D₂ Ansatz thermalization algorithm is not possible. In this work we extend the thermalization algorithm for the multiple-Davydov-D₂ Ansatz by introducing an additional state projection algorithm and adopting the coarse-grained scattering approximation.

In Sec. II we describe the thermalization algorithm for the multiple-Davydov-D₂ Ansatz. In Sec. III we provide a theoretical description of its application to simulating the fluorescence spectra. In Sec. IV we demonstrate its capabilities by simulating the excitation relaxation dynamics of an H-type molecular aggregate and its fluorescence spectrum. In Sec. V we discuss changes made to adapt the thermalization algorithm of the D₂ Ansatz for the multiple-Davydov-D₂ Ansatz.

II. THERMALIZATION OF THE MULTIPLE-DAVYDOV-D₂ ANSATZ

We consider a molecular aggregate model, where each molecule $n = 1, 2, \dots, N$ couples to its own local reservoir $k = 1, 2, \dots, N$, each of which consists of $q = 1, 2, \dots, Q$ QHO modes. The model is given by the Hamiltonian $\hat{H} = \hat{H}_S + \hat{H}_B + \hat{H}_{SB}$ with the system, the bath, and the system-bath coupling terms defined as

$$\hat{H}_S = \sum_n \varepsilon_n \hat{a}_n^\dagger \hat{a}_n + \sum_{n \neq m} J_{nm} \hat{a}_n^\dagger \hat{a}_m, \quad (1)$$

$$\hat{H}_B = \sum_{k,q} \omega_{kq} \hat{b}_{kq}^\dagger \hat{b}_{kq}, \quad (2)$$

$$\hat{H}_{SB} = - \sum_n \hat{a}_n^\dagger \hat{a}_n \sum_q \omega_{nq} g_{nq} (\hat{b}_{nq}^\dagger + \hat{b}_{nq}), \quad (3)$$

with the reduced Planck's constant set to $\hbar = 1$. Here ε_n is the n th molecule electronic excitation energy, J_{nm} denotes the resonant coupling between the n th and m th molecules, ω_{nq} denotes the frequency of the q th QHO in the n th local reservoir, and g_{nq} is the coupling strength between the q th oscillator in the n th local reservoir and the n th molecule. The operators \hat{a}_n^\dagger and \hat{a}_n represent the creation and annihilation operators for electronic excitations, respectively, while \hat{b}_{nq}^\dagger and \hat{b}_{nq} represent the creation and annihilation bosonic operators for QHOs.

In addition, we implicitly couple the system-bath model to the secondary bath characterized by a fixed temperature T . The coupling between the secondary and primary baths occurs via the scattering events that allow the system-bath model to exchange energy with the secondary bath and thermalize local reservoirs, as is described below.

The state of the system-bath model is given by the multiple-Davydov-D₂ wave function

$$|\Psi(t)\rangle = \sum_{i,n} \alpha_{i,n}(t) |n\rangle \otimes |\lambda_i(t)\rangle, \quad (4)$$

where $\alpha_{i,n}(t)$ is the i th multiple complex amplitude associated with a singly excited electronic state $|n\rangle$ localized on the n th molecule, $|n\rangle = \hat{a}_n^\dagger |0\rangle_{\text{el}}$. Here $|0\rangle_{\text{el}}$ is the electronic ground state. The complexity and accuracy of the multiple-Davydov-D₂ Ansatz can be adjusted by varying the multiplicity number M . The states of the QHO modes are represented by multidimensional coherent states

$$|\lambda_i(t)\rangle = \exp \sum_{k,q} [\lambda_{i,kq}(t) \hat{b}_{kq}^\dagger - \lambda_{i,kq}^*(t) \hat{b}_{kq}] |0\rangle_{\text{vib}}, \quad (5)$$

where $\lambda_{i,kq}(t)$ is the i th multiple complex displacement parameter and $|0\rangle_{\text{vib}} = \otimes_{k,q} |0\rangle_{k,q}$ is the global vibrational ground state of all QHOs.

The multiple-Davydov-D₂ wave function describes a state of the system-bath model as a superposition of M multidimensional coherent state terms, which allows it to represent a wide range of system-bath model states beyond the Born-Oppenheimer and Gaussian approximations. The thermalization algorithm for the multiple-Davydov-D₂ Ansatz is realized by stochastic scattering events [35,36] during time evolution of the wave function. These events change the momenta p_{kq} of all the q th QHO modes of the k th local reservoir at once. We assume that the scattering probability $P_k(\theta, \tau_{\text{sc}})$ of θ scattering events occurring per time interval τ_{sc} with a scattering rate ν_k is given by a Poisson distribution

$$P_k(\theta, \tau_{\text{sc}}) = \frac{1}{\theta!} (\tau_{\text{sc}} \nu_k)^\theta e^{-\tau_{\text{sc}} \nu_k}. \quad (6)$$

Numerically, Poisson statistics are realized by simulating Bernoulli processes [37,38] in the limit of $\tau_{\text{sc}} \rightarrow 0$ while maintaining the condition that $\nu_k \tau_{\text{sc}} \ll 1$. To simulate the scattering events, we divide wave-function propagation into equal time length τ_{sc} intervals

$$t_i = (i\tau_{\text{sc}}, (i+1)\tau_{\text{sc}}], \quad i = 0, 1, \dots \quad (7)$$

At the end of each interval, for each local reservoir, we flip a biased coin with the probability $\nu_k \tau_{\text{sc}}$ of landing heads for all local reservoirs. If the k th coin lands heads, we change the momenta of all oscillator modes of that k th reservoir; otherwise, no changes are made. A list of scattering moments at which the numerical simulation is paused to perform the scatterings can be precomputed prior to starting the simulation by drawing probabilities for all local reservoir and all time intervals t_i from Eq. (6).

We assume that during the scattering event the local bath, which experiences the scattering, acquires thermal-equilibrium kinetic energy. Such a state is given by a single coherent state for one specific QHO. In order to set the new momentum values of the scattered reservoir oscillator modes, we first project the multiple-Davydov-D₂ wave function of Eq. (4) to its single-multiple Davydov-D₂ form

$$|\psi(t)\rangle = \sum_n \beta_n(t) |n\rangle \otimes |\tilde{\lambda}(t)\rangle, \quad (8)$$

where β_n are the projected complex electronic amplitudes and $|\tilde{\lambda}(t)\rangle$ is the projected multidimensional coherent state, which is defined later. This follows the decoherence idea [39], where the macroscopic environment performs a collapse of

the wave function into a set of preferred states, in our case, the electronic-vibrational states $|n\rangle \otimes |\tilde{\lambda}(t)\rangle$. The projected complex electronic amplitudes are equal to

$$\beta_n(t) = \sum_i^M \alpha_{i,n}(t) \langle \tilde{\lambda}(t) | \lambda_i(t) \rangle, \quad (9)$$

while the projected multidimensional coherent state

$$|\tilde{\lambda}(t)\rangle = \exp \sum_{k,q}^{N,Q} [\tilde{\lambda}_{kq}(t) \hat{b}_{kq}^\dagger - \tilde{\lambda}_{kq}^*(t) \hat{b}_{kq}] |0\rangle_{\text{vib}} \quad (10)$$

is defined in terms of the complex displacements

$$\tilde{\lambda}_{kq}(t) = \frac{1}{\sqrt{2}} [x_{kq}(t) + i p_{kq}(t)], \quad (11)$$

where $x_{kq}(t)$ and $p_{kq}(t)$ are QHO coordinate and momentum expectation values

$$x_{kq} = \frac{1}{\sqrt{2}} \sum_{i,j,n}^{M,M,N} \alpha_{i,n}^* \alpha_{j,n} \langle \lambda_i | \lambda_j \rangle \sum_{k,q}^{N,Q} (\lambda_{i,kq}^* + \lambda_{j,kq}), \quad (12)$$

$$p_{kq} = \frac{i}{\sqrt{2}} \sum_{i,j,n}^{M,M,N} \alpha_{i,n}^* \alpha_{j,n} \langle \lambda_i | \lambda_j \rangle \sum_{k,q}^{N,Q} (\lambda_{i,kq}^* - \lambda_{j,kq}) \quad (13)$$

calculated from the multiple-Davydov-D₂ Ansatz, where $\langle \lambda_i | \lambda_j \rangle$ is the overlap of two coherent states

$$\langle \lambda_i | \lambda_j \rangle = \exp \sum_{k,q}^{N,Q} \left[\lambda_{i,kq}^* \lambda_{j,kq} - \frac{1}{2} (|\lambda_{i,kq}|^2 + |\lambda_{j,kq}|^2) \right]. \quad (14)$$

This completes the projection operation of the multiple-Davydov-D₂ state, given by Eq. (4), into its simplified D₂ form in Eq. (8).

Once the projected wave function is deduced, we modify the momenta of the scattered oscillators by sampling the QHO diagonal density operator distribution in the coherent state representation at temperature T , known as the Glauber-Sudarshan distribution [14,40–42]

$$\mathcal{P}(\tilde{\lambda}_{kq}) = \mathcal{Z}_{kq}^{-1} \exp[-|\tilde{\lambda}_{kq}|^2 (e^{\omega_{kq}/k_B T} - 1)]. \quad (15)$$

For scattered modes, we set the momentum values in Eq. (11) to

$$p_{kq}(t) = \sqrt{2} \text{Im}(\tilde{\lambda}_{kq}^{\mathcal{P}}), \quad (16)$$

where $\tilde{\lambda}_{kq}^{\mathcal{P}}$ is a sample drawn from the Glauber-Sudarshan distribution. In addition, \mathcal{Z}_{kq}^{-1} and ω_{kq} are partition functions and frequencies of the QHO, respectively, and k_B is the Boltzmann constant. During the scattering events, coordinates x_{kq} of both the scattered and nonscattered modes remain unchanged. Notice that the local baths, which do not experience scattering, remain unaffected by the scattering of other modes.

Now that the wave function of the system-bath model after scattering is known [given by Eq. (8)] we rewrite it in the multiple-Davydov-D₂ wave-function form of Eq. (4) by populating amplitudes and displacements of the first multiple

$i = 1$ as

$$\alpha_{1,n}(t) = \beta_n(t), \quad (17)$$

$$\lambda_{1,kq}(t) = \tilde{\lambda}_{kq}(t). \quad (18)$$

The amplitudes of the unpopulated multiples are set to $\alpha_{j=2,\dots,M,n}(t) = 0$, while the unpopulated displacements are positioned in a layered hexagonal pattern around the populated coherent state [18]

$$\lambda_{j=2,\dots,M,kq}(t) = \lambda_{1,kq}(\tau) + \frac{1}{4} [1 + \lfloor \beta(j) \rfloor] e^{i2\pi[\beta(j)+(1/12)\lfloor \beta(j) \rfloor]}, \quad (19)$$

where $\beta(j) = (j-2)/6$ is the coordination function and $\lfloor x \rfloor$ is the floor function. The exact arrangement of displacements of the unpopulated multiples is not critical as long as the distance in the phase space to the populated multiple coherent state is not too large; otherwise, the initially unpopulated multiples will not contribute to further dynamics [16,43].

Once the scattered multiple-Davydov-D₂ wave function is determined and the scattering event is finalized, further simulation of multiple-Davydov-D₂ dynamics according to equations of motion (EOMs) proceeds. This procedure generates a stochastic wave-function trajectory, where the system-bath model at each time moment is described by a pure state, which is a single member of a statistical ensemble [14,41]. The thermalized model dynamics is obtained by averaging observables over an ensemble of wave-function trajectories γ , which differ by their initial amplitudes $\alpha_{i,n}(0)$, initial coherent state displacements $\lambda_{i,kq}(0)$, and a sequence of scattering events. Ensemble averaging is performed in a parallelized Monte Carlo scheme.

III. THERMALIZED FLUORESCENCE SPECTRA

Wave-function trajectories allow calculation of an arbitrary observable. Calculation of the equilibrium fluorescence spectrum requires us to know the thermally equilibrated state of the excited model. The presented thermalization procedure allows us to obtain such a state and calculate the fluorescence spectrum.

In general, the frequency-domain spectrum of a quantum system can be written as a Fourier transform

$$F(\omega) = \text{Re} \int_0^\infty dt e^{i\omega t} S(t) \quad (20)$$

of the corresponding time-domain response function $S(t)$. The fluorescence response function $S_{\text{fl}}(t)$ is a specific case of the more general time-resolved fluorescence (TRF) response function [1,44]

$$S_{\text{TRF}}(\tau_{\text{eq}}, t) = \frac{1}{\Gamma} \sum_{\gamma=1}^{\Gamma} \langle \Psi_G(0) | \gamma \hat{\rho}_- \hat{V}_{\text{E}}^\dagger(\tau_{\text{eq}} + t) \hat{\rho}_+ \times \hat{V}_{\text{G}}(t) \hat{\rho}_- \hat{V}_{\text{E}}(\tau_{\text{eq}}) \hat{\rho}_+ | \Psi_G(0) \rangle_\gamma, \quad (21)$$

where \hat{V}_{E} and \hat{V}_{G} are the excited- and ground-state system-bath propagators

$$\hat{V}_A(t_1) | \Psi_A(t_2) \rangle = | \Psi_A(t_1 + t_2) \rangle, \quad (22)$$

$\hat{\mu}_+ = \sum_n^N (\mathbf{e} \cdot \boldsymbol{\mu}_n) \hat{a}_n^\dagger$ and $\hat{\mu}_- = \sum_n^N (\mathbf{e} \cdot \boldsymbol{\mu}_n) \hat{a}_n$ are the excitation creation and annihilation operators of the system [18], respectively, $\boldsymbol{\mu}_n$ is the electronic transition dipole moment vector, \mathbf{e} is the external field polarization vector, and $|\Psi_G(0)\rangle_\gamma$ is a model ground state with an initial condition of the γ th trajectory. The EOMs for propagating the multiple-Davydov-D₂ wave function, as well as the approach to solving them, are described in detail in Refs. [18,43].

Here $S_{\text{TRF}}(\tau_{\text{eq}}, t)$ is a function of two times: the equilibration time τ_{eq} and the coherence time t . During the equilibration time, the system evolves in its excited state and, due to the system-bath interaction, relaxes to an equilibrium state. After this, during the coherence time, spontaneous emission occurs.

We will apply thermalization during the equilibration time to facilitate the relaxation of the system-bath model into the lowest-energy equilibrium state by removing excess thermal energy from local reservoirs. We denote by $\hat{G}_{E,\gamma}$ the excited-state propagator \hat{V}_E but with thermalization. Then the thermalized TRF (TTRF) response function can be written as

$$\begin{aligned}
 \tilde{S}_{\text{TRF}}(\tau_{\text{eq}}, t) = & \frac{1}{\Gamma} \sum_{\gamma=1}^{\Gamma} \langle \Psi_G(0) |_\gamma \hat{\mu}_- \hat{G}_{E,\gamma}^*(\tau_{\text{eq}}) \hat{V}_E^\dagger(t) \hat{\mu}_+ \\
 & \times \hat{V}_G(t) \hat{\mu}_- \hat{G}_{E,\gamma}(\tau_{\text{eq}}) \hat{\mu}_+ | \Psi_G(0) \rangle_\gamma. \quad (23)
 \end{aligned}$$

By considering the equilibration time to be long enough to reach the equilibrium state of the system-bath model, we define the fluorescence response function as

$$S_{\text{fl}}(t) = \lim_{\tau_{\text{eq}} \rightarrow \infty} S_{\text{TRF}}(\tau_{\text{eq}}, t) \quad (24)$$

and the thermalized fluorescence (TF) response function as

$$\tilde{S}_{\text{fl}}(t) = \lim_{\tau_{\text{eq}} \rightarrow \infty} \tilde{S}_{\text{TRF}}(\tau_{\text{eq}}, t). \quad (25)$$

The spectra obtained using the fluorescence response function without and with thermalization will be compared in the next section. For the numerical simulation, the required equilibration time interval has to be deduced by increasing τ_{eq} until the resulting fluorescence spectra converge.

IV. RESULTS

To investigate the thermalization algorithm for the multiple-Davydov-D₂ Ansatz, we will analyze the linear trimer model, which we previously used to study thermalization of the Davydov-D₂ Ansatz [22]. The model consists of $N = 3$ coupled molecules, with excited-state energies ε_n being equal to 0, 250, and 500 cm^{-1} , forming an energy funnel. The nearest-neighbor couplings are set to $J_{1,2} = J_{2,3} = 100 \text{ cm}^{-1}$ and $J_{3,1} = 0$. The electronic dipole moment vectors of molecules are $\boldsymbol{\mu}_n = (1, 0, 0)$ in the Cartesian coordinate system. This classifies the trimer as the H-type molecular aggregate [45].

The QHOs of local molecular reservoirs are characterized by the super-Ohmic [46] spectral density function $C''(\omega) = \omega(\omega/\omega_c)^{s-1} \exp(-\omega/\omega_c)$ with an order parameter $s = 2$ and a cutoff frequency $\omega_c = 100 \text{ cm}^{-1}$. The QHO frequencies are $\omega_{kq} = \omega_0 + (q-1)\Delta\omega$, where the frequency offset is $\omega_0 = 0.01 \text{ cm}^{-1}$. The reorganization energy of

each local reservoir is $\Lambda_k = \sum_q \omega_{kq} g_{kq}^2 = 100 \text{ cm}^{-1}$. The scattering time step size is set to $\tau_{\text{sc}} = 0.01 \text{ ps}$. Finally, the ensemble consists of 900 wave-functions trajectories, which we found to be sufficient to obtain the converged model dynamics. The multiple-Davydov-D₂ Ansatz multiplicity $M = 5$ is used as the results with a higher multiplicity quantitatively match the $M = 5$ case.

We will be considering three bath models: the dense bath model, where the spectral density function $C''(\omega)$ is discretized into $Q = 75$ oscillators per local reservoir with a step size of $\Delta\omega = 10 \text{ cm}^{-1}$; the sparse bath model, where the number of modes is reduced by a factor of 5 to just $Q = 15$ oscillators per local reservoir with $\Delta\omega = 50 \text{ cm}^{-1}$; and the sparse bath with thermalization model, where $C''(\omega)$ is discretized according to the sparse bath model and thermalization is used.

In the absence of the bath, the system has three single-excitation stationary exciton states with energies $E_1^{\text{exc}} \approx -37.23 \text{ cm}^{-1}$, $E_2^{\text{exc}} = 250 \text{ cm}^{-1}$, and $E_3^{\text{exc}} \approx 537.23 \text{ cm}^{-1}$, satisfying the time-independent Schrödinger equation

$$\hat{H}_S \Phi_n^{\text{exc}} = E_n^{\text{exc}} \Phi_n^{\text{exc}}, \quad (26)$$

with the system Hamiltonian given by Eq. (1). The exciton eigenstates [24] Φ_n^{exc} have their excitations delocalized over multiple molecules [41]. Therefore, it is convenient to analyze molecular aggregate excitation relaxation dynamics in terms of excitons as they are natural quasiparticles of the aggregate. We define the probability of finding the aggregate in its n th excitonic state as the population, given by

$$\rho_n^{\text{exc}}(t) = \sum_{k,l,i,j} (\Phi_k^{\text{exc}})_n^* (\alpha_{i,k}^*(t) \alpha_{j,l}(t) S_{i,j}(t))_{\text{th}} (\Phi_l^{\text{exc}})_n, \quad (27)$$

where $(\dots)_{\text{th}}$ is the averaging over an ensemble of wave-function trajectories. Using the multiple-Davydov-D₂ Ansatz, we proceed with the following analysis.

First, we study the electronic excitation dynamics. The initial excitonic-state populations correspond to the optically excited highest-energy states $\rho_3^{\text{exc}} = 1$ and $\rho_{1,2}^{\text{exc}} = 0$, while the initial QHO displacements $\lambda_{i,kq}(0)$ are sampled from the Glauber-Sudarshan distribution in Eq. (15) to account for the initial temperatures of $T_k = 77 \text{ K}$.

In Fig. 1 we display the trimer model exciton-state populations $\rho_n^{\text{exc}}(t)$ and average temperatures [47] $T_k(t)$ of local reservoirs for all three bath models. The aggregate environment causes dephasing between excitonic states and induces irreversible population relaxation [1,2]. The population dynamics of the dense bath models exhibits a sequential relaxation from the initially populated highest-energy excitonic state to the lowest-energy state via the intermediate state. Eventually, the population distribution reaches the equilibrium state. The majority of the excitation energy is transferred to oscillators of local reservoirs. We observe an increase of temperatures [47–49] due to the finite number of oscillators in local reservoirs. An infinite number of oscillators would have to be included to maintain a constant temperature at the initial value. The initial rapid rise in temperature is due to oscillator reorganization in the aggregate's electronic excited-state manifold, while the following slow rise is due to energy transfer from the system to local reservoirs.

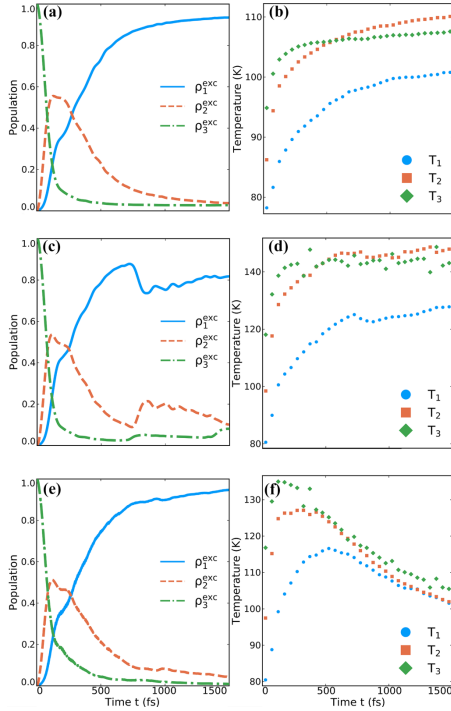


FIG. 1. Exciton-state populations $\rho_i^{\text{exc}}(t)$ and the average temperatures $T_i(t)$ of local reservoirs of the trimer in (a) and (b) the dense bath model, (c) and (d) the sparse bath model, and (e) and (f) the sparse bath model with thermalization.

In the sparse bath model, we observe that if the number of vibrational modes is reduced, the population dynamics become skewed due to an insufficiently dense representation of the spectral density function. Furthermore, the temperature increase is higher than that for the dense bath model, which further changes the characteristics of the resulting equilibrium state.

When the thermalization algorithm is applied to the sparse bath model with a scattering rate $\nu_k = 1.25 \text{ ps}^{-1}$, the population dynamics is restored and qualitatively matches that of the dense model. Although the initial temperatures of the local reservoirs exceed those of the dense bath model, they gradually decrease due to thermalization, and this rate can be adjusted by changing the scattering rate.

Next we turn our attention to simulating the fluorescence spectrum of the linear trimer with the dense bath model with scattering rate $\nu_k = 1 \text{ ps}^{-1}$. The initial excitonic-state population distribution is now calculated in terms of the system-field interaction, as described in Ref. [18].

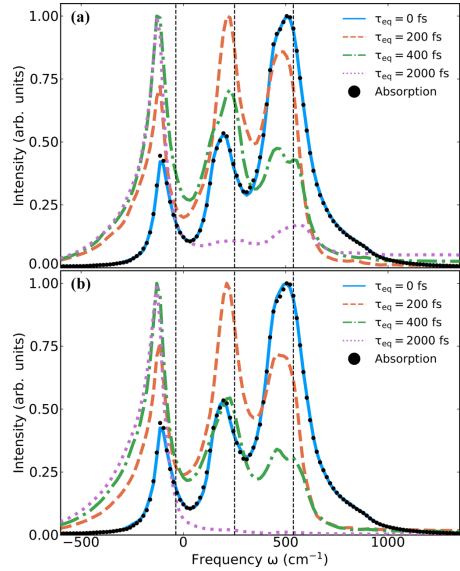


FIG. 2. The (a) TRF and (b) TTRF spectra of the trimer in the dense bath model, simulated with increasing equilibration time τ_{eq} . The absorption spectrum is also shown. Vertical dashed lines show energies E^{exc} of the excitonic states.

In Fig. 2 we compare the TRF and TTRF spectra with increasing equilibration times τ_{eq} . When $\tau_{\text{eq}} = 0$, both the TRF and TTRF spectra are equivalent and exactly match the absorption spectrum, which consists of three peaks due to a transition involving the combined excitonic-vibronic (vibronic) states and cannot be regarded as purely excitonic. For reference, vertical dotted lines indicate energies E^{exc} of excitonic states. These do not match the three peak energies exactly due to the system being coupled to the environment.

By allowing equilibration to occur, $\tau_{\text{eq}} > 0$, both the TRF and TTRF spectra show a peak intensity shift towards lower energies as excitation relaxes towards the equilibrated state during the equilibration time. After equilibrating for $\tau_{\text{eq}} = 2 \text{ ps}$, we find that both spectra have converged and do not change with longer τ_{eq} . Therefore, the TRF and TTRF spectra at $\tau_{\text{eq}} = 2 \text{ ps}$ can be considered as the fluorescence and TF spectra of the trimer model as defined in Eqs. (24) and (25).

Both spectra exhibit their highest intensities at the energies of the lowest vibronic states. However, the fluorescence spectrum also has considerable intensities at energies of the intermediate and highest vibronic states. Surprisingly, the higher-energy peak is more intense than the intermediate peak. The TF spectrum intensities at these energies are negligible, which indicates that the thermalization allows the trimer model to reach a lower-energy equilibrium state, which is no

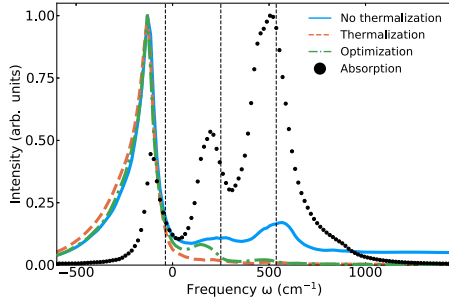


FIG. 3. Comparison of the fluorescence spectra of the trimer with the dense bath model obtained without thermalization, with thermalization, and using the optimization approach. The equilibration time is $\tau_{\text{eq}} = 2$ ps. The absorption spectrum is also shown. Vertical dashed lines show energies E^{exc} of the excitonic states.

longer hindered by the excess thermal energy accumulation in QHOs of local reservoirs.

In Fig. 3 we also compare the obtained fluorescence and TF spectra with the fluorescence spectrum simulated using a previously proposed excited-state numerical optimization approach [19,50,51]. It relies on finding the model's lowest-energy excitonic state in terms of the multiple-Davydov-D₂ *Ansatz* parameters and then applying thermal fluctuations to effectively generate the model in a lowest-energy equilibrium state at a temperature of 77 K. We see that all three methods produce a similar lowest vibronic peak, but the TF spectrum has a higher-intensity tail towards the low-energy side and almost no intensities at energies of the intermediate and the highest vibronic states, while the fluorescence spectrum simulated using the optimization approach has a low intensity at the energy of the intermediate vibronic states. The optimization approach spectrum more closely resembles that of the thermalized model than the nonthermalized spectrum.

V. DISCUSSION

Starting from an arbitrary nonequilibrium initial condition, a closed quantum system will not equilibrate due to energy conservation. The thermalization procedure is necessary to guarantee proper thermal equilibrium in the long run for all bath oscillators. This requires introducing the concept of primary and secondary baths. In our model the primary bath is a part of explicit quantum DOFs, while the secondary bath is a thermal reservoir with infinite thermal capacity, i.e., it maintains a constant temperature in any energy exchange process. In this case, the secondary bath cannot be described by mechanical equations; only statistical or thermodynamical concepts apply. Our statistical algorithm performs energy exchange between the primary and secondary baths using the statistical scattering idea: The primary bath state is reset to the thermally equilibrated state, thus giving up excess energy to or drawing additional energy from the secondary bath. This is a major extension of the explicit quantum time-dependent

variational principle (TDVP) theory: The extended model covers a broader range of phenomena, i.e., local heating and cooling, as well as bath oscillator dynamic localization, which are not available in the standard TDVP theory.

In order to adapt the Davydov-D₂ *Ansatz* thermalization algorithm for the multiple-Davydov-D₂ *Ansatz*, several extensions were made. During the time evolution of the system-bath model, the multiple-Davydov-D₂ *Ansatz* multiples become correlated, leading to a non-Gaussian bath wave function. It becomes impossible to represent a new Gaussian wave function of scattered QHO modes, sampled from Eq. (15), without changing the wave function of the rest of the nonscattered oscillators at the same time. Therefore, we chose to project the multiple-Davydov-D₂ *Ansatz* into the Davydov-D₂ *Ansatz* whenever scattering occurred, allowing us to correctly represent the newly sampled Gaussian wave function of scattered oscillators. This idea requires consideration of a few aspects.

The projected Davydov-D₂ wave function accurately maintains average coordinates and momenta of the multiple-Davydov-D₂ *Ansatz* QHO states, while variances and higher-order moments are affected. This causes variation of excitation relaxation dynamics compared to the standard multiple-Davydov-D₂ *Ansatz*. However, system-bath models mostly rely only on the linear coupling between the system and average coordinates of QHO modes; therefore, as seen in Fig. 1, the discrepancy is minimal. The higher-order couplings become necessary when anharmonic vibrational modes or changes to their frequencies upon excitation are considered [19,52].

To maintain the close correspondence to the standard multiple-Davydov-D₂ *Ansatz*, the projection should not occur too often. This is because, after scattering, it takes time for the wave function to again become correlated between its many multiples, i.e., to take advantage of the unpopulated multiple-Davydov-D₂ *Ansatz* multiples after projection. If the repopulation time is shorter than the time between projection operations, the model population dynamics becomes similar to that of the Davydov-D₂ *Ansatz*, even though the multiple-Davydov-D₂ *Ansatz* is being used. The average time interval between projection operations is determined by the scattering rate ν_k , a property of the physical system, while the scattering time τ_{sc} is a parameter of the model and must be as small as necessary to ensure the Bernoulli-to-Poisson statistics transition condition $\nu_k \tau_{\text{sc}} \ll 1$.

To increase the average time between projection operations, we adopt a coarser scattering approach for the multiple-Davydov-D₂ *Ansatz* compared to the Davydov-D₂ *Ansatz*. Instead of considering scattering events of individual oscillators, we consider events where all oscillators of certain local reservoirs are scattered at once, requiring only a single projection operation to scatter many oscillators at once. This approach allows the multiple-Davydov-D₂ *Ansatz* to continue utilizing all its multiples for the improved accuracy over the Davydov-D₂ *Ansatz* while reducing the number of explicitly modeled oscillators needed to maintain the local reservoirs' temperatures close to initial values, thereby reducing the numerical cost.

Using the multiple-Davydov-D₂ *Ansatz* to simulate the population dynamics of the trimer model, it took an average of 166 min per trajectory using the dense bath model, but

only 1.3 min using the sparse bath model and 2 min using the sparse bath model with thermalization. The computational overhead of thermalization is small compared to the overall time savings when switching from using the dense bath to the sparse bath. The numerical cost reduction is also greater for the multiple-Davydov- D_2 Ansatz than for the Davydov- D_2 Ansatz in Ref. [22], because the multiple-Davydov- D_2 Ansatz EOMs constitute an implicit system of differential equations, which require a more involved two-step numerical approach to find a solution [18,43]. By considering fewer oscillators in each local reservoir, simulations of the dynamics and spectroscopic signals of aggregates made up of more molecules become possible.

Computing a single trajectory of the TTRF response function in Eq. (23) with an equilibration time of $\tau_{\text{eq}} = 2$ ps took an average of 79 min. The previously proposed optimization method [19] for simulating fluorescence spectra does not require propagation during the equilibration time interval of the TRF response function and has to be computed only once, but it takes 193 min. In general, we find that the computation of TTRF is more reliable and numerically stable. The optimization approach struggles to consistently find the lowest-energy excitonic state of the model due to its heuristic nature, requiring many attempts to find the solution and eventually having to choose the lowest-energy one. This is particularly apparent when a wide range of oscillator frequencies are included.

For elementary system-bath models without Hamiltonian parameter disorder, the optimization approach can be a

good starting point for fluorescence spectra simulation. However, a more accurate spectrum most likely will be obtained using the TTRF approach. For models with Hamiltonian disorder, e.g., static molecule excitation energy disorder [53–55], the optimization approach would require finding the model's lowest-energy excitonic state for each realization of the Hamiltonian, negating its advantage of having to perform the optimization procedure only once.

In conclusion, the thermalization algorithm presented for the numerically exact multiple-Davydov- D_2 Ansatz allows us to reduce the numerical cost of system-bath model simulations by having to explicitly include fewer bath oscillators while maintaining a correspondence with the exact relaxation dynamics. The thermalization algorithm efficiently controls molecular heating effects due to the reduced number of oscillators. Furthermore, the application of thermalization to the simulation of fluorescence spectra demonstrates a lower computation time, greater numerical stability, and higher accuracy compared to the numerical optimization approach.

ACKNOWLEDGMENTS

We thank the Research Council of Lithuania for financial support (Grant No. S-MIP-23-48). Computations were performed on resources at the High Performance Computing Center, HPC Sauletekis, of the Faculty of Physics, Vilnius University.

- [1] S. Mukamel, *Principles of Nonlinear Optical Spectroscopy* (Oxford University Press, Oxford, 1995).
- [2] L. Valkunas, D. Abramavičius, and T. Mančal, *Molecular Excitation Dynamics and Relaxation* (Wiley-VCH, Weinheim, 2013).
- [3] C. J. Bardeen, The structure and dynamics of molecular excitons, *Annu. Rev. Phys. Chem.* **65**, 127 (2014).
- [4] H. van Amerongen, R. van Grondelle, and L. Valkunas, *Photosynthetic Excitons* (World Scientific, Singapore, 2000).
- [5] M. Schröter, S. Ivanov, J. Schulze, S. Polyutov, Y. Yan, T. Pullerits, and O. Kühn, Exciton-vibrational coupling in the dynamics and spectroscopy of Frenkel excitons in molecular aggregates, *Phys. Rep.* **567**, 1 (2015).
- [6] H.-P. Breuer and F. Petruccione, *The Theory of Open Quantum Systems* (Oxford University Press, Oxford, 2007).
- [7] U. Weiss, *Quantum Dissipative Systems* (World Scientific, Singapore, 2012).
- [8] N. Zhou, Z. Huang, J. Zhu, V. Chernyak, and Y. Zhao, Polarons dynamics with a multitude of Davydov D_2 trial states, *J. Chem. Phys.* **143**, 014113 (2015).
- [9] L. Wang, L. Chen, N. Zhou, and Y. Zhao, Variational dynamics of the sub-Ohmic spin-boson model on the basis of multiple Davydov D_1 states, *J. Chem. Phys.* **144**, 024101 (2016).
- [10] N. Zhou, L. Chen, Z. Huang, K. Sun, Y. Tanimura, and Y. Zhao, Fast, Accurate simulation of polaron dynamics and multidimensional spectroscopy by multiple Davydov trial states, *J. Phys. Chem. A* **120**, 1562 (2016).
- [11] L. Chen, M. Gelin, and Y. Zhao, Dynamics of the spin-boson model: A comparison of the multiple Davydov D_1 , $D_{1.5}$, D_2 Ansätze, *Chem. Phys.* **515**, 108 (2018).
- [12] Y. Zhao, K. Sun, L. Chen, and M. Gelin, The hierarchy of Davydov's Ansätze and its applications, *WIRES Comput. Mol. Sci.* **12**, e1589 (2022).
- [13] Z. Huang, L. Chen, N. Zhou, and Y. Zhao, Transient dynamics of a one-dimensional Holstein polaron under the influence of an external electric field, *Ann. Phys. (Berlin)* **529**, 1600367 (2017).
- [14] L. Wang, Y. Fujihashi, L. Chen, and Y. Zhao, Finite-temperature time-dependent variation with multiple Davydov states, *J. Chem. Phys.* **146**, 124127 (2017).
- [15] L. Chen, M. F. Gelin, and W. Domcke, Multimode quantum dynamics with multiple Davydov D_2 trial states: Application to a 24-dimensional conical intersection model, *J. Chem. Phys.* **150**, 024101 (2019).
- [16] M. Jakučionis, T. Mančal, and D. Abramavičius, Modeling irreversible molecular internal conversion using the time-dependent variational approach with sD_2 ansatz, *Phys. Chem. Chem. Phys.* **22**, 8952 (2020).
- [17] L. Wang, F. Zheng, J. Wang, F. Großmann, and Y. Zhao, Schrödinger-cat states in Landau-Zener-Stückelberg-Majorana interferometry: A multiple Davydov Ansatz approach, *J. Phys. Chem. B* **125**, 3184 (2021).
- [18] M. Jakučionis, A. Žukas, and D. Abramavičius, Modeling molecular J and H aggregates using multiple-Davydov D_2 ansatz, *Phys. Chem. Chem. Phys.* **24**, 17665 (2022).
- [19] M. Jakučionis, A. Žukas, and D. Abramavičius, Inspecting molecular aggregate quadratic vibronic coupling effects using squeezed coherent states, *Phys. Chem. Chem. Phys.* **25**, 1705 (2023).
- [20] K. W. Sun, M. F. Gelin, V. Y. Chernyak, and Y. Zhao, Davydov Ansatz as an efficient tool for the simulation of nonlinear optical

- response of molecular aggregates, *J. Chem. Phys.* **142**, 212448 (2015).
- [21] Y. Zhao, The hierarchy of Davydov's Ansatz: From guesswork to numerically "exact" many-body wave functions, *J. Chem. Phys.* **158**, 080901 (2023).
- [22] M. Jakučionis and D. Abramavičius, Temperature-controlled open-quantum-system dynamics using a time-dependent variational method, *Phys. Rev. A* **103**, 032202 (2021).
- [23] J. Sun, B. Luo, and Y. Zhao, Dynamics of a one-dimensional Holstein polaron with the Davydov ansätze, *Phys. Rev. B* **82**, 014305 (2010).
- [24] B. Luo, J. Ye, C. Guan, and Y. Zhao, Validity of time-dependent trial states for the Holstein polaron, *Phys. Chem. Chem. Phys.* **12**, 15073 (2010).
- [25] M. Jakučionis, V. Chorošajev, and D. Abramavičius, Vibrational damping effects on electronic energy relaxation in molecular aggregates, *Chem. Phys.* **515**, 193 (2018).
- [26] M. Jakučionis, I. Gaiziunas, J. Sulskus, and D. Abramavičius, Simulation of ab initio optical absorption spectrum of β -carotene with fully resolved S_0 and S_2 vibrational normal modes, *J. Phys. Chem. A* **126**, 180 (2022).
- [27] A. S. Davydov, Solitons in molecular systems, *Phys. Scr.* **20**, 387 (1979).
- [28] A. C. Scott, Davydov's soliton revisited, *Physica D* **51**, 333 (1991).
- [29] W.-M. Zhang, D. H. Feng, and R. Gilmore, Coherent states: Theory and some applications, *Rev. Mod. Phys.* **62**, 867 (1990).
- [30] S. Kais and R. D. Levine, Coherent states for the Morse oscillator, *Phys. Rev. A* **41**, 2301 (1990).
- [31] J. M. Moix, Y. Zhao, and J. Cao, Equilibrium-reduced density matrix formulation: Influence of noise, disorder, and temperature on localization in excitonic systems, *Phys. Rev. B* **85**, 115412 (2012).
- [32] Y. Subaşı, C. H. Fleming, J. M. Taylor, and B. L. Hu, Equilibrium states of open quantum systems in the strong coupling regime, *Phys. Rev. E* **86**, 061132 (2012).
- [33] A. Gelzinis and L. Valkunas, Analytical derivation of equilibrium state for open quantum system, *J. Chem. Phys.* **152**, 051103 (2020).
- [34] J. Zeng and Y. Yao, Variational squeezed Davydov ansatz for realistic chemical systems with nonlinear vibronic coupling, *J. Chem. Theory Comput.* **18**, 1255 (2022).
- [35] M. B. Plenio and P. L. Knight, The quantum-jump approach to dissipative dynamics in quantum optics, *Rev. Mod. Phys.* **70**, 101 (1998).
- [36] K. Luoma, W. T. Strunz, and J. Pilo, Diffusive Limit of Non-Markovian Quantum Jumps, *Phys. Rev. Lett.* **125**, 150403 (2020).
- [37] V. N. Kampen, *Stochastic Processes in Physics and Chemistry* (Elsevier, Amsterdam, 2007).
- [38] D. P. Bertsekas and J. N. Tsitsiklis, *Introduction to Probability* (IOP, Bristol, 2008).
- [39] M. Schlosshauer, *Decoherence and the Quantum-To-Classical Transition* (Springer, Berlin, 2007).
- [40] R. J. Glauber, Coherent and incoherent states of the radiation field, *Phys. Rev.* **131**, 2766 (1963).
- [41] V. Chorošajev, O. Rancova, and D. Abramavičius, Polaronic effects at finite temperatures in the B850 ring of the LH2 complex, *Phys. Chem. Chem. Phys.* **18**, 7966 (2016).
- [42] Q. Xie, H. Zhong, M. T. Batchelor, and C. Lee, The quantum Rabi model: Solution and dynamics, *J. Phys. A: Math. Theor.* **50**, 113001 (2017).
- [43] M. Werther and F. Großmann, Apoptosis of moving nonorthogonal basis functions in many-particle quantum dynamics, *Phys. Rev. B* **101**, 174315 (2020).
- [44] V. Balevičius, Jr., L. Valkunas, and D. Abramavičius, Modeling of ultrafast time-resolved fluorescence applied to a weakly coupled chromophore pair, *J. Chem. Phys.* **143**, 074101 (2015).
- [45] N. J. Hestand and F. C. Spano, Expanded theory of H- and J-molecular aggregates: The effects of vibronic coupling and intermolecular charge transfer, *Chem. Rev.* **118**, 7069 (2018).
- [46] A. Kell, X. Feng, M. Reppert, and R. Jankowiak, On the shape of the phonon spectral density in photosynthetic complexes, *J. Phys. Chem. B* **117**, 7317 (2013).
- [47] D. Abramavičius, V. Chorošajev, and L. Valkunas, Tracing feed-back driven exciton dynamics in molecular aggregates, *Phys. Chem. Chem. Phys.* **20**, 21225 (2018).
- [48] V. Scarani, M. Ziman, P. Štelmachovič, N. Gisin, and V. Bužek, Thermalizing Quantum Machines: Dissipation and Entanglement, *Phys. Rev. Lett.* **88**, 097905 (2002).
- [49] A. W. Chin, J. Prior, R. Rosenbach, F. Caycedo-Soler, S. F. Huelga, and M. B. Plenio, The role of non-equilibrium vibrational structures in electronic coherence and recoherence in pigment-protein complexes, *Nat. Phys.* **9**, 113 (2013).
- [50] P. K. Mogensen and A. N. Riseth, Optim: A mathematical optimization package for Julia, *J. Open Source Softw.* **3**, 615 (2018).
- [51] Z. H. Zhan, J. Zhang, Y. Li, and H. S. Chung, Adaptive particle swarm optimization, *IEEE Trans. Syst. Man Cy. B* **39**, 1362 (2009).
- [52] V. Chorošajev, T. Marčulionis, and D. Abramavičius, Temporal dynamics of excitonic states with nonlinear electron-vibrational coupling, *J. Chem. Phys.* **147**, 074114 (2017).
- [53] D. Abramavičius and L. Valkunas, Geminate pair recombination in molecular systems with correlated disorder, *Phys. Rev. B* **68**, 245203 (2003).
- [54] A. Eisfeld, S. M. Vlamings, V. A. Malyshev, and J. Knoester, Excitons in Molecular Aggregates with Lévy-Type Disorder: Anomalous Localization and Exchange Broadening of Optical Spectra, *Phys. Rev. Lett.* **105**, 137402 (2010).
- [55] O. Rancova, M. Jakučionis, L. Valkunas, and D. Abramavičius, Origin of non-Gaussian site energy disorder in molecular aggregates, *Chem. Phys. Lett.* **674**, 120 (2017).

Vilniaus universiteto leidykla
Saulėtekio al. 9, III rūmai, LT-10222 Vilnius
El. p. info@leidykla.vu.lt, www.leidykla.vu.lt
bookshop.vu.lt, journals.vu.lt
Tiražas 15 egz.

NOTES

NOTES

NOTES